Design of High-Performance Delayed Fluorescence Materials and Their Application in Organic Light-Emitting Diodes

朴, 仁燮

https://doi.org/10.15017/1806987

2017

Doctoral Dissertation

Design of High-Performance Delayed Fluorescence Materials and Their Application in Organic Light-Emitting Diodes

In Seob Park

Department of Chemistry and Biochemistry

Graduate School of Engineering

Kyushu University

Table of Contents

Chapter 1

General Introduction

1. 1. Introduction

Organic light-emitting diodes (OLEDs) have attracted a great deal of attention, interest in their practical applications for full-color, flat-panel displays and lighting owing to virtue of their unique advantages such as the high electroluminescence (EL) efficiency, high contrast, light weight, flexibility, and potentially low manufacturing cost.[1] In OLEDs, electrically injected holes and electrons are recombined to form 25% singlet excitons (antiparallel spins, ↑↓) and 75% triplet excitons (parallel spins, ↑↑), according to spin statistics.[2] As shown in **Figure 1-1**, the operation of OLEDs involves charge injection from the electrodes, transport of charge carriers, and recombination of holes and electrons as the excitons under electrical-excitation, resulting in the emission of either fluorescence or phosphorescence in accordance with different radiative decay processes.

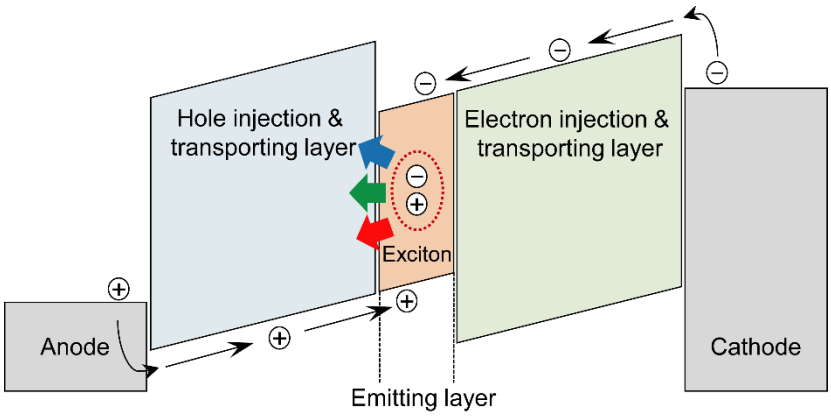

Figure 1-1. Schematic energy-diagram of OLEDs.

The first electroluminescence (EL) in an organic material was reported from an anthracene single crystal by recombination of electrons and holes in 1965 by Helfrich and Schneider.[3] This discovery was not thought to be useful because rather high driving voltages are necessary for light emission from the single crystal. After that, Tang and VanSlyke demonstrated the first efficient organic light-emitting diode (OLED) based on tris(8-hydroxyquinolinato)aluminum (Alq_3, **Figure 1-2**) with a luminance of over 1000 cd m^{-2} at a voltage of 10 V and an external EL quantum efficiency (η_{ext}) of nearly 1% utilizing an organic multilayer structure in 1987.[4] In 1990, Friend and coworkers exhibited the first polymer OLED based on poly(*p*-phenylene vinylene) (PPV, **Figure 1-2**).[5] Since these seminal reports have been truly spectacular, the developments for highly efficient OLEDs have been conducted in countless organic materials and device architectures.[6]

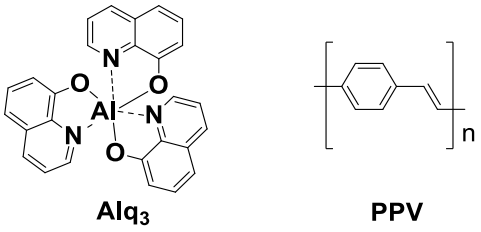

Figure 1-2. Molecular structures of tris(8-hydroxyquinolinato)aluminum (Alq_3, left) and poly(*p*-phenylene vinylene) (PPV, right).

1. 2. Photophysical Processes of Organic Materials

Excited organic molecules by photo- or electrical-excitation return to their original ground states with undergoing various deactivation processes (**Figure 1-3**).

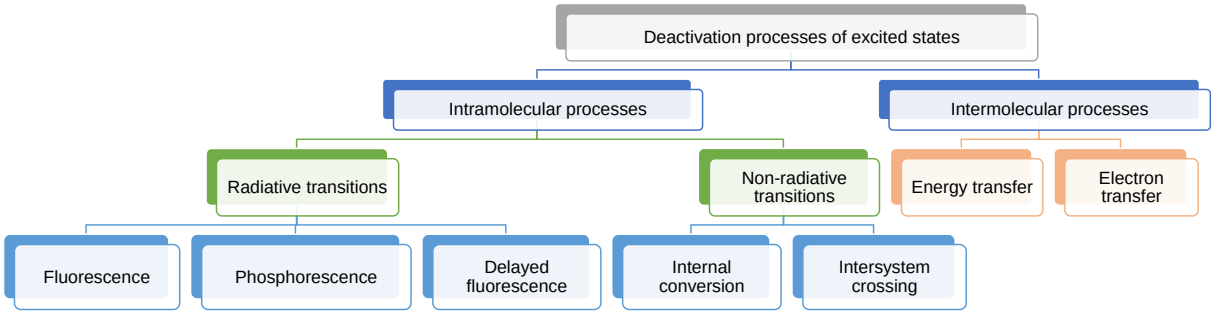

Figure 1-3. Possible physical deactivation processes of excited organic molecules.

1. 2. 1. Intramolecular Processes

The electronic energy levels and electronic transitions of organic molecules can be shown using a Jablonski energy level diagram (**Figure 1-4**), which is convenient for visualizing in a simple way the possible deactivation processes. When a molecule has excited by photon absorption, the transition from its ground state (S_0) to a lowest excited singlet state (S_1) or higher excited singlet states (S_2–S_n) occurs with transient time of 10^{-13} to 10^{-15} s. As shown **Figure 1-4**, the electron transfers from lowest vibrational level of S_0 to the third vibrational level of the second excited singlet level (S_2) and causes the electron-collision of excited molecules with surrounding molecules. The electron then degrades to the lowest vibrational level of the same electronic energy level because of vibration energy loss. This process is known as vibrational relaxation (vr). Another degradation to the lowest vibrational level of a lower electronic energy level is called internal conversion (IC). These processes are so fast (10^{-13} to 10^{-14} s) that after molecules have excited by photon absorption, so they almost all instantly jump and down to the lowest vibration level of S_1. Subsequently, the following processes can occur:

i) fluorescence: fluorescence is light emission of photons corresponding $S_1 \rightarrow S_0$ relaxation with transition time ranging from 10^{-5} to 10^{-9} s.

ii) intersystem crossing (ISC): ISC is the non-radiative transition from the excited singlet state to the excited triplet state. This process is slower (10^{-8} to 10^{-10}) than the IC process because of accompanying a spin transition.

iii) phosphorescence: phosphorescence is the radiative transition from the T_1 to the S_0 states with a change in spin direction with transition time ranging from 10 to 10^{-6} s.

iv) reverse intersystem crossing (RISC): RISC is a non-radiative transition from the excited to singlet states, which can occur when molecules possessing a small energy difference (ΔE_{ST}) between the excited singlet and triplet states.

v) delayed fluorescence: delayed fluorescence is the radiative transition from the S_1 to S_0 states involving the ISC and RISC processes. This process displays the same spectral distribution with conventional fluorescence. However, its decay time is longer than that of conventional fluorescence because a molecule emits as light emission after accompanying the ISC and RISC processes.

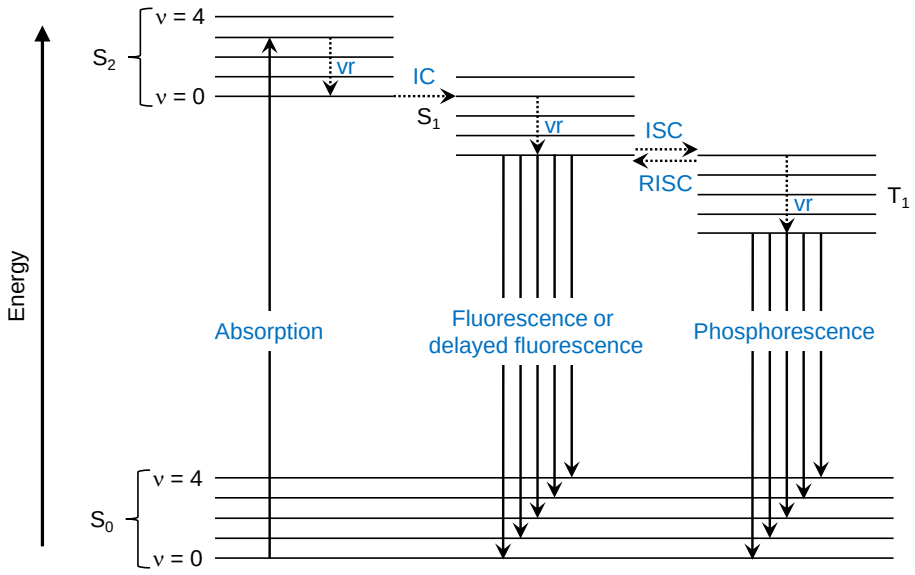

Figure 1-4. Jabloski energy level diagram. Vibrational relaxation (vr), internal conversion (IC), intersystem crossing (ISC), and reverse ISC (RISC) are non-radiative processes and fluorescence (lowest excited singlet state (S_1) → ground state (S_0)), delayed fluorescence (S_1 → lowest excited triplet state (T_1) → S_1 → S_0), and phosphorescence (T_1 → S_0) are radiative processes.

As shown in **Figure 1-5**, organic molecules show difference luminescence processes by excitation sources. Under the photo-excitation, nearly 100% excited singlet energies of organic

molecules are generated, and then occur various transition processes as mentioned earlier. On the contrary, under electrical-excitation, singlet and triplet excitons are formed by recombination of electrons and holes, each of them carrying spin 1/2. The probability of forming a triplet exciton is statistically three times higher than that of forming a singlet exciton. Therefore, internal EL quantum efficiencies (η_{int}) are believed to have a value of 25% for conventional fluorescence-based OLEDs as only the S_1 excitons can be utilized for light emission (**Figure 1-6a**).[7] In this case, the T_1 excitons undergo a spin-forbidden transition, resulting in non-radiative deactivation. But in contrary to this, precious metal-containing organometallic phosphorescent materials are capable of harvesting both S_1 and T_1 excitons for light emission (**Figure 1-6b**).[2] this is because of the enhanced ISC mediated by a spin–orbit coupling of the heavy metals such as iridium (Ir), platinum (Pt), and osmium (Os), which results in η_{int} of up to 100%.[8] Despite their desirable EL characteristics, the rarity, high cost, and toxicity of these precious metals, as well as the poor stability of blue phosphors would hamper the widespread applications of these OLEDs in the future. As an alternative, thermally activated delayed fluorescence (TADF, **Figure 1-6c**), which occurs by converting the excited T_1 states to emissive S_1 states via an efficient RISC using purely organic emitters without any precious metal elements, has attracted great attention in recent years.[9–14] Owing to efficient up-conversion from the T_1 to S_1 states, highly efficient TADF-OLEDs with η_{int} of nearly 100% have been successfully realized,[9a] and hence TADF is expected as a key technology for the next-generation OLEDs.

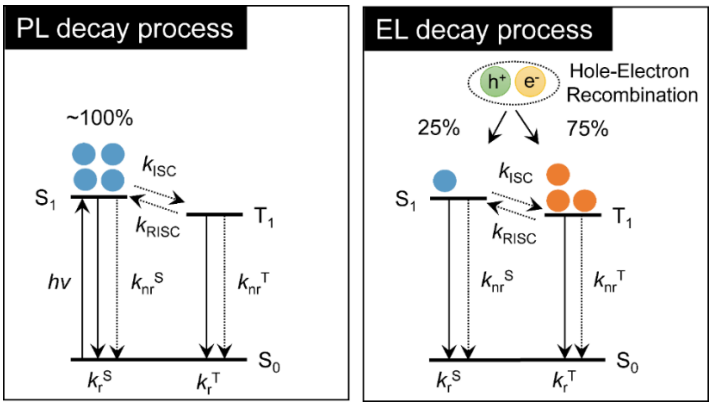

Figure 1-5. Schematic representation for PL (left) and EL (right) decay processes. k_n^S and k_{nr}^S are the radiative and non-radiative decay rate constants of S_1, respectively. k_n^T and k_{nr}^T are the radiative and non-radiative decay rate constants of T_1, respectively. k_{ISC} and k_{RISC} are the non-radiative decay rate constants of ISC and RISC, respectively.

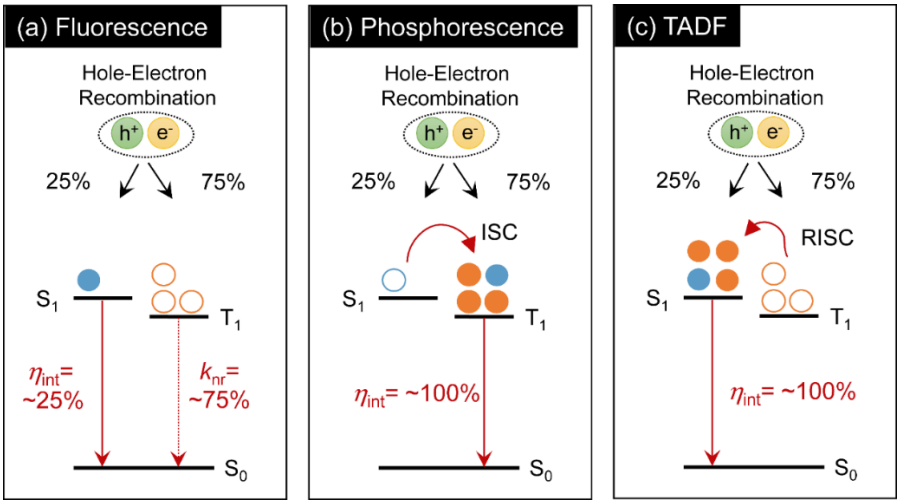

Figure 1-6. Schematic representation for (a) fluorescence, (b) phosphorescence, and (c) TADF mechanisms under electrical-excitation. η_{int} is the internal EL quantum efficiency.

1. 2. 2. Intermolecular Processes

1. 2. 2. 1. Long-Range Energy Transfer (Förster Energy Transfer)

Förster energy transfer is long-range dipole–dipole (Coulombic) energy transfer in the range of up to 10 nm, which is a consequence of electron–electron repulsions of a donor molecule (D) and an acceptor molecule (A).[15] Energy transfer occurs from the excited state of a donor molecule (D*) to the S_0 state of an acceptor molecule (A), according to D* + A → D + A* (**Figure 1-7**). There are physical parameters to occur the efficient energy transfer as follows, i) there should be the good spectral overlap between the emission spectrum of the donor and the absorption spectrum of the acceptor and ii) the relative orientation between the emission dipole moment of the donor and the absorption dipole moment of the acceptor. This energy transfer is only allowed singlet–singlet energy transfer (^{1}D* + ^{1}A → ^{1}D + ^{1}A*) between the donor and acceptor without a change in spin multiplicity, resulting in the creation of significant transition dipoles, whereas triplet–triplet energy transfer (^{3}D* + ^{1}A → ^{1}D + ^{3}A*) cannot occur because this is required to a change in spin multiplicity.

The efficiency of the Förster energy transfer process depends on the increase sixth power of the distance between the donor and acceptor pair (r) given by following equation:

$$E_F = R_0^6/(R_0^6 + r^6) \qquad \textbf{(1-1)}$$

where R_0 is Förster radius at which the efficiency of energy transfer is 50%, which can be determined from photophysical data by employing following equation:

$$R_0^6 = \frac{9(\ln 10)\kappa^2 \Phi_D}{128\pi^5 N_A n^4} J \quad \textbf{(1-2)}$$

where κ^2 is the dipole orientation factor, Φ_D is the PL quantum efficiency of the donor in the absence of transfer, N_A is the Avogadro's number, n is the refractive index of the medium, and J is the spectral overlap integral calculated as

$$J = \int f_D(\lambda)\varepsilon_A(\lambda)d\lambda \quad \textbf{(1-3)}$$

where f_D is normalized emission spectrum of the donor and ε_A is molar extinction coefficient from the absorption spectrum of the acceptor.

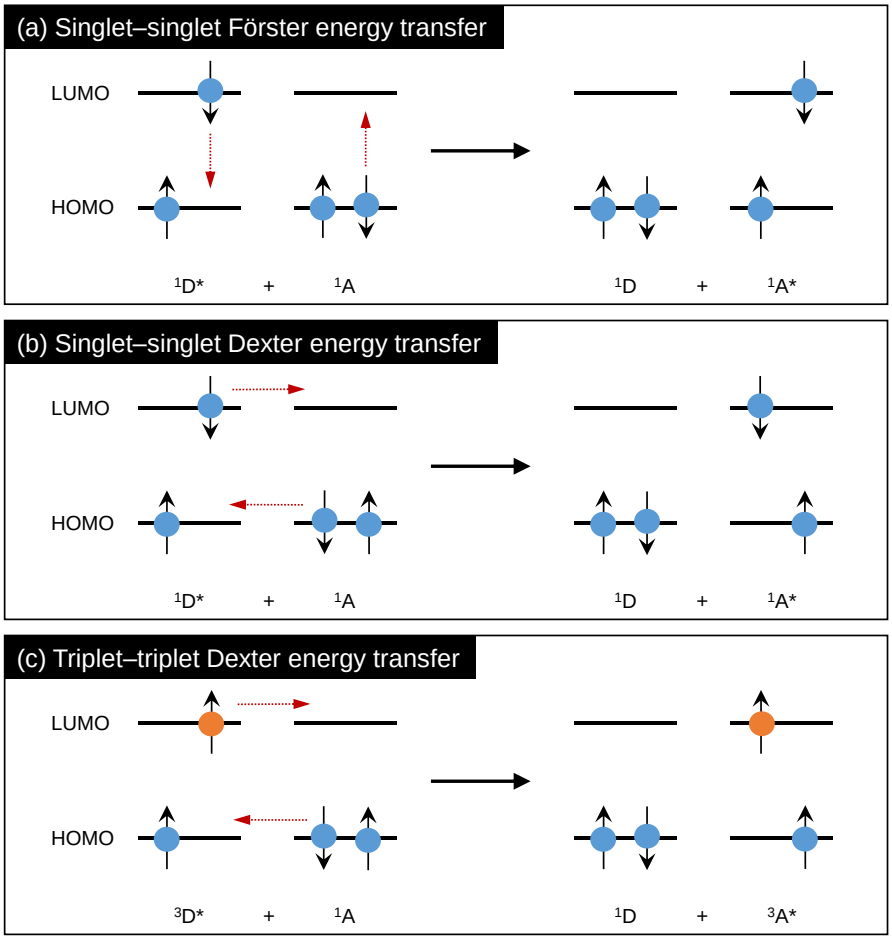

Figure 1-7. Schematic representation for (a) singlet–singlet Förster energy transfer, (b) singlet–singlet Dexter energy transfer, and (c) triplet–triplet Dexter energy transfer.

1. 2. 2. 2. Short-Range Energy Transfer (Dexter Energy Transfer)

Dexter energy transfer is short-range energy transfer by an emission quenching mechanism in which an excited electron of the donor is transferred to that of the acceptor through a non-radiative path at short distances (~ 1 nm) of the donor and acceptor. This process

is allowed both singlet–singlet ($^1D^* + {}^1A \rightarrow {}^1D + {}^1A^*$) and triplet–triplet ($^3D^* + {}^1A \rightarrow {}^1D + {}^3A^*$) energy transfer (**Figure 1-7**).[16] Therefore, the wavefunction overlap between the donor and acceptor is required for efficient Dexter energy transfer. The rate constant of Dexter energy transfer is given by following equation:

$$k_D = \left(\frac{2\pi}{h}\right)\kappa^2 \exp\left(\frac{-2R_{DA}}{L}\right)J \qquad \textbf{(1-4)}$$

where R_{DA} is the distance between the donor and acceptor, L is the sum of the Van der Waals radii of the donor and acceptor, and J is the spectral overlap integral calculated as the eqn. **1-3**.

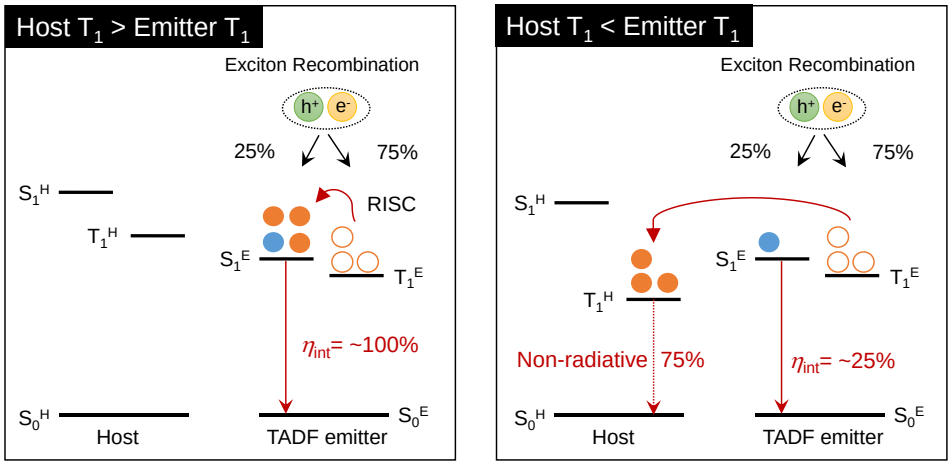

Figure 1-8. Schematic representation for energy transfer between a host material and a TADF emitter under electrical-excitation. S_0^H and S_0^E are the ground states, S_1^H and S_1^E are the lowest excited singlet states, and T_1^H and T_1^E are the lowest excited triplet states of the host and TADF materials, respectively.

1. 2. 2. 3. Energy Transfer in Host–Guest System

Emitting materials have to be dispersed into a suitable host matrix at a low concentration (1–10 wt.%) to reduce concentration quenching and avoid self-absorption of emitting materials in OLEDs to realize the high EL efficiency.[17] In addition, triplet harvesting emitters (phosphorescent and TADF materials) should be required to employ a host material with high triplet energy (E_T) to prevent backward energy transfer from the triplet state of the emitter to that of the host material, because both Förster and Dexter energy transfer occur in phosphorescence and TADF molecules in a host matrix. As exemplified **Figure 1-8**, 75% triplet excitons of a TADF emitter transferred to the triplet state of a host material, and hence dissipated as the non-radiative process when using a host material with a lower triplet state than that of a TADF emitter. Therefore, it is important to select suitable host materials for the high

EL efficiency in OLEDs. Design of highly efficient host materials for TADF emitters will be discussed in **Chapter 8**.

1. 3. Thermally Activated Delayed Fluorescence (TADF) Process

1. 3. 1. Design Principle for TADF Molecules

The efficient TADF emission is usually observed organic materials with a small ΔE_{ST} ($k_B T \approx 25.6$ meV) because the RISC process can be strongly accelerated by the thermal energy at 300 K, in accordance with Fermi's Golden rule, in which k_{RISC} is expressed by the following equation:[18]

$$k_{\mathrm{RISC}} = \frac{2\pi}{\hbar} < \Psi^1 | H_{SO} | \Psi^2 >^2 \frac{1}{\sqrt{4\pi\lambda k_B T}} exp\left(-\frac{(\Delta E_{ST}+\lambda)^2}{4\pi\lambda k_B T}\right) \qquad \textbf{(1-5)}$$

where, $\hbar$ and H_{SO} are the Planck constant and spin–orbit coupling between two states ($\Psi^1 \rightarrow \Psi^2$), respectively. λ and k_B are the mixing coefficient between two states ($\Psi^1 \rightarrow \Psi^2$) and the Boltzmann constant, respectively. T is the absolute temperature. The RISC process in purely organic materials with a negligible small H_{SO} can be accelerated by realizing a small ΔE_{ST}, which is due entirely to electron–electron repulsions. Generally, electron–electron repulsion energies are distributed as two types of the repulsions (K) between negative charge distributions of electrons and the electron exchange energy (J) between the different states. In a single molecule, the S_1 and T_1 states have the same K, whereas J in the T_1 state is lower than that of the S_1 state because there are electrons of parallel (↑↑) and antiparallel (↑↓) spins in the S_1 and T_1 states, respectively. Such a parallel spin has the tendency of electrons to avoid each other, which lead to a lower energy than that of an antiparallel spin. Therefore, assuming the S_0 energy (E_0) is zero, the S_1 energy (E_S), T_1 (E_T) energy, and ΔE_{ST} of a molecule are given by the following equations:

$$E_0 = 0 \qquad \textbf{(1-6)}$$

$$E_S = E_0 + K + J \qquad \textbf{(1-7)}$$

$$E_T = E_0 + K - J \qquad \textbf{(1-8)}$$

$$\Delta E_{ST} = 2J > 0 \qquad \textbf{(1-9)}$$

Thus, the ΔE_{ST} depends only on the electron exchange energy and is precisely equal to $2J$. J, which is associated with the Pauli principle, is expressed by the following equation of the overlap integral between the highest occupied molecular orbital (HOMO) and the lowest unoccupied molecular orbital (LUMO):

$$J = \iint \Phi_{\mathrm{H}}(1)\Phi_{\mathrm{L}}(2)\left(\frac{e^2}{r_{12}}\right)\Phi_{\mathrm{L}}(2)\Phi_{\mathrm{H}}(1)dr_1dr_2 \qquad \textbf{(1-10)}$$

where, Φ_{H} and Φ_{L} are the wavefuctions of the HOMO and LUMO, respectively. e is the charge on an electron and r_{12} is the distance separating the electrons. From these equations, the ΔE_{ST} value can be controlled by the overlap integral between the two states. The energy diagram of benzophenone (H_2C=O) shown in **Figure 1-9** serves as an exemplified case. The π–π* transition of benzophenone has relatively a large ΔE_{ST}, resulting from their large orbital overlap, whereas the n–π* transition has relatively a small ΔE_{ST} owing to their small orbital overlap. Therefore, the major design principle for TADF molecules is to minimize the overlap between the HOMO and LUMO by localizing them on different moieties in a molecule, leading to a small ΔE_{ST}, as a consequence of reduced electron exchange interactions. Under this condition, the RISC process can be strongly accelerated. However, a weak frontier orbital overlap is a prerequisite for an efficient light emission, because a negligible spatial overlap of the wavefunctions results in the loss of transition probability according to Fermi's Golden rule. Therefore, both these conditions should be met for designing novel efficient TADF molecules.

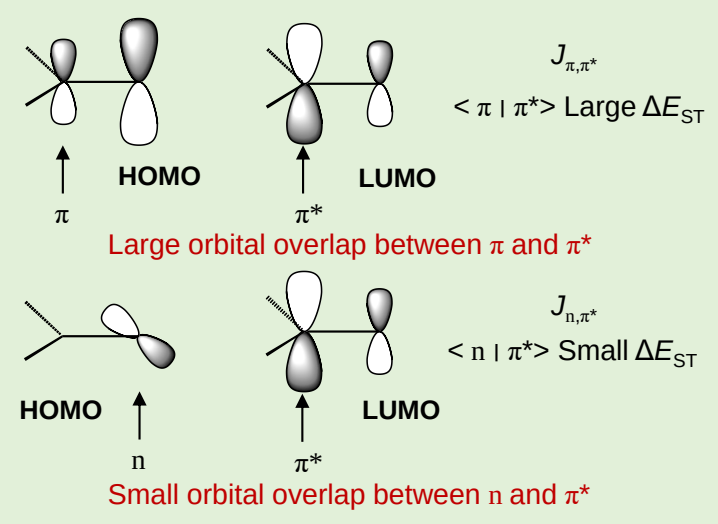

Figure 1-9. π–π* (upper) and n–π* (lower) orbital overlap in benzophenone.

1. 3. 2. Determination of Rate Constants for TADF

The PL quantum efficiencies (Φ_{PL}) of the prompt (Φ_{p}) and delayed (Φ_{d}) components can be experimentally obtained from the transient PL decay curves (**Figure 1-10**) and the absolute Φ_{PL}. The lifetimes of the prompt (τ_{p}) and delayed (τ_{d}) components were determined by fitting the transient PL decay curves by the following equation:

$$\mathrm{y} = y_0 + A_{\mathrm{p}}e^{-x/\tau_{\mathrm{p}}} + A_{\mathrm{d}}e^{-x/\tau_{\mathrm{d}}} \qquad \textbf{(1-11)}$$

where, A_p and A_d are the area of the prompt and delayed components. In the presence of ISC and RISC between the S_1 and T_1 states, the rate constants of the prompt (k_p) and delayed (k_d) components can be expressed by the following formulas:[19]

$$k_p = \frac{1}{\tau_p} = k_r^S + k_{nr}^S + k_{ISC} \quad \textbf{(1-12)}$$

$$k_d = \frac{1}{\tau_d} = k_{nr}^T + \left(1 - \frac{k_{ISC}}{k_r^S + k_{nr}^S + k_{ISC}}\right) k_{RISC} \quad \textbf{(1-13)}$$

where k_r^S and k_{nr}^S are the radiative and non-radiative decay rate constants of the S_1 state, respectively, and k_{ISC} and k_{RISC} are the ISC ($S_1 \rightarrow T_1$) and RISC ($T_1 \rightarrow S_1$) rate constants, respectively. k_r^S and k_{ISC} are assumed to be much faster than k_{nr}^T and k_{RISC}. The Φ_p, Φ_d, and Φ_{ISC} are given by the following formulas:

$$\Phi_p = \frac{k_r^S}{k_r^S + k_{nr}^S + k_{ISC}} = \frac{k_r^S}{k_p} \quad \textbf{(1-13)}$$

$$\Phi_d = \sum_{k=1}^{\infty} (\Phi_{ISC}\, \Phi_{RISC})^k\, \Phi_p = \frac{\Phi_{ISC}\, \Phi_{RISC}}{1 - \Phi_{ISC}\, \Phi_{RISC}} \cdot \Phi_p \quad \textbf{(1-14)}$$

$$\Phi_{ISC} = \frac{k_{ISC}}{k_r^S + k_{nr}^S + k_{ISC}} = \frac{k_{ISC}}{k_p} \quad \textbf{(1-15)}$$

From Eqs. **1-12–1-15**, the following equation for k_{RISC} can be obtained.

$$k_{RISC} = \frac{k_p k_d}{k_{ISC}} \frac{\Phi_d}{\Phi_p} \quad \textbf{(1-16)}$$

Since the Φ_p exhibits almost negligible temperature dependence, we assume that $k_{nr}^S \approx 0$ at 300 K. Based on Eqs. **1-12–16**, the radiative and non-radiative rate constants corresponding decay efficiencies can be estimated for TADF materials.

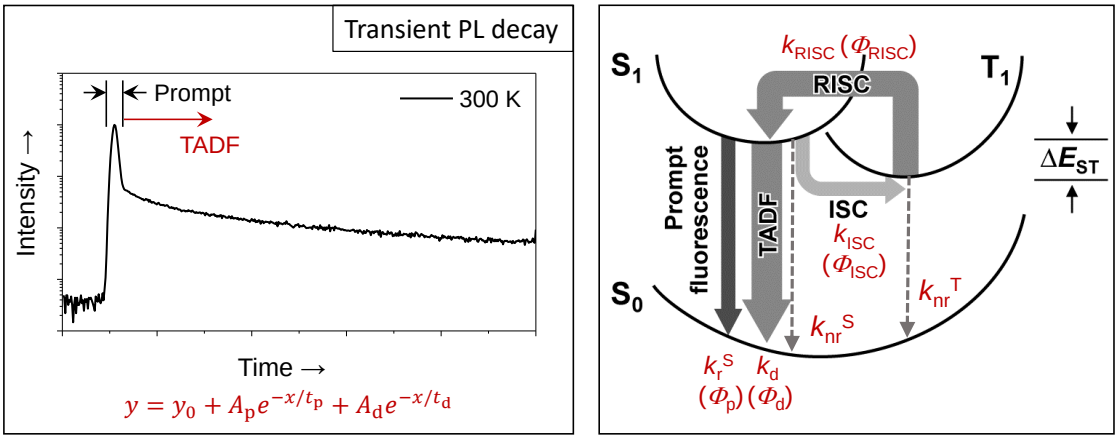

Figure 1-10. Transient PL decay of TADF (left) and Postulated PL decay processes for TADF materials (right). k_r^S and k_{nr}^S are the radiative and non-radiative decay rate constants of the S_1 state, k_{ISC} and k_{RISC} are the ISC ($S_1 \rightarrow T_1$) and RISC ($T_1 \rightarrow S_1$) rate constants, respectively, k_d is the radiative decay rate constant of the S_1 state involving the ISC and RISC process, and k_{nr}^T is the non-radiative rate constant of the T_1 state. Φ are corresponding PL quantum efficiencies

1. 3. 3. Efficiency of TADF-Based OLEDs

In OLEDs, the most critical parameter is η_{ext}, which describes the ratio between the number of emitted photons that are extracted to air per injected electrons and injected charge carriers:

$$\eta_{ext} = (\gamma \times \eta_{ST} \times \Phi_{PL}) \times \eta_{out} = \eta_{int} \times \eta_{out} \quad \textbf{(1-18)}$$

where γ is the fraction of holes and electrons recombination to form excitons in an emitting layer (EML). η_{ST} is the exciton production efficiency resulting in the radiative transition according to the spin selection rules. Φ_{PL} is the PL quantum efficiency for radiative decay of the excitons and η_{out} is the light out-coupling efficiency which is the fraction of the radiated photons from the device into air. γ and Φ_{PL} are able to realize up to 100% by the advanced device architectures and well-designed molecules by suppressed non-radiative activation,[6] respectively. η_r can be changed by emission mechanisms (fluorescence = ~25% and phosphorescence = ~100%). Therefore, assuming η_{out} of 20%, η_{ext} of fluorescence-based OLEDs are limited to 5%,[7] whereas phosphorescence-based OLEDs can be achieved high η_{ext} of up to 20%.[9] In contrary to both fluorescence and phosphorescence-based OLEDs, the directly generated T_1 excitons by carrier recombination in TADF-based OLEDs are converted into the S_1 state via the efficient RISC. Accordingly, the theoretical maxima of η_{int} for TADF-based OLEDs can be given by the following equation:[10a]

$$\eta_{int} = \eta_S \times \Phi_p + \eta_S \times \Phi_d + \eta_T \times \Phi_d/\Phi_{ISC} \quad \textbf{(1-19)}$$

where η_S and η_T denote the singlet exciton and triplet exciton production rates (25% and 75%, respectively) and Φ_d is the ISC efficiency ($1 - \Phi_p$). Therefore, the theoretical maxima of η_{ext} for TADF-based OLEDs can be estimated and achieved up to 20%, assuming η_{out} of 20%.

1. 4. Efficiency Roll-Off in OLEDs

The efficiency of OLEDs is typically decreased with increasing current density by exciton quenching, which is drawback for practical lighting applications.[20] This so-called efficiency roll-off that is attributed to several bimolecular annihilation processes in excited states as follows (**Figure 1-11**):

i) singlet–singlet annihilation (SSA): SSA is firstly observed in anthracene crystals by dipole–dipole interactions because the SSA process occurs through Förster energy transfer.[21] Therefore, crystalline materials more easily undergo the SSA process than

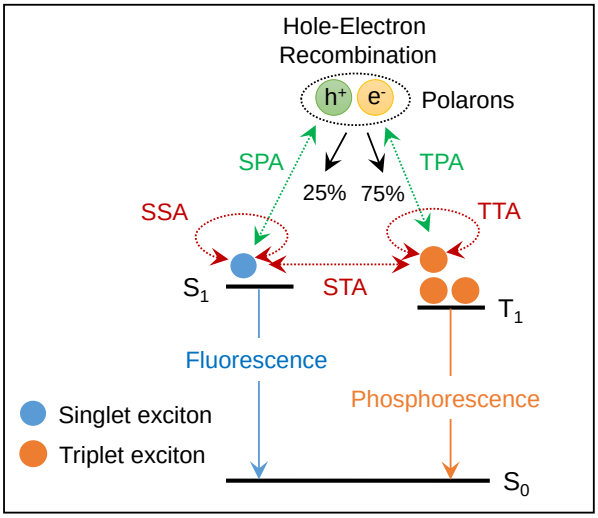

Figure 1-11. Schematic illustration of possible mechanisms of efficiency roll-off in OLEDs. SSA: singlet–singlet annihilation, TTA: triplet–triplet annihilation, STA: singlet–triplet annihilation, SPA: singlet–polaron annihilation, TPA: triplet–polaron annihilation.

that of amorphous materials, resulting from the higher diffusion constant of ordered materials.[22]

ii) triplet–triplet annihilation (TTA): TTA is mostly relevant to the efficiency roll-off in phosphorescence- and TADF-based OLEDs because both emitters utilize 75% triplet excitons for light emission. Despite the high η_{int} of nearly 100% in phosphorescence- and TADF-based OLEDs, more serious efficiency roll-off of both devices are usually observed than that of conventional fluorescence-based OLEDs because of triplet excitons possessing long emission lifetimes ranging up to the millisecond range, which lead to higher probability of exciton annihilation than that of singlet excitons having nanosecond scale-emission lifetimes.[2] Moreover, the emitters are usually required the suitable host materials to confine exciton within emitters for the high EL efficiency as mentioned Section **1. 2. 2. 3.**. However, such a host–guest system induces guest–guest TTA as well as host–guest[23] and host–host[24] TTA.

iii) singlet–triplet annihilation (STA): STA, which is usually observed in conventional fluorescence[25] and TADF[26]-based OLEDs because of utilizing singlet excitons for light emission, can occur by interactions between the singlet and triplet excited states.

iv) exciton–polaron interaction: the interactions between excitons and electron polarons (e^-) or hole polarons (h^+) by free or trapped charge carriers induces singlet–polaron annihilation (SPA)[22] and triplet–polaron annihilation (TPA)[21a,23,27].

Several strategies, to realize the high efficiency at high current density by reducing annihilation, have been introduced, including decreasing the exciton lifetime[28] and reducing molecular aggregation[29] of emitters, broadening of the recombination zone in the EML,[30] and reducing the Förster radius[31].

1. 5. Motivation and Outline of This Dissertation

Full-color flat-panel displays and solid-state lighting sources based on organic light-emitting diodes (OLEDs) have attracted considerable research interest for over 30 years, because of their high contrast, flexibility, and potentially low manufacturing costs as well as bright and full-color light emissions from thin organic layers. In general, the light emission of excited organic molecules is classified as either fluorescence or phosphorescence. Although fluorescence materials have attracted attention because of their high color purity and high reliability, the internal quantum efficiency of conventional fluorescent OLEDs is limited to 25%, as the recombination of injected electrons and holes generates the lowest excited triplet (T_1) and singlet (S_1) states at a ratio of 3:1. This spin-statistical requirement limits the maximum external electroluminescence (EL) quantum efficiency of fluorescent OLEDs to less than 5%. Meanwhile, phosphorescence organometallic materials incorporating an iridium or platinum metal center are promising emitters for OLEDs because the internal quantum efficiency of nearly 100% can be attained by harvesting both 25% S_1 and 75% T_1 excitons for EL emission by accelerated intersystem crossing from the S_1 to T_1 states, owing to a strong spin–orbit coupling. As an alternative way, thermally activated delayed fluorescence (TADF) has recently gained increasing interest to produce highly efficient OLEDs since the achievement of the internal quantum efficiency close to unity by Uoyama et al. in 2012. Until this discovery, only phosphorescence organometallic materials were regarded as the sole candidates as emitters in high-efficiency OLEDs because phosphorescent OLEDs can achieve external EL quantum efficiency of over 20%. However, these phosphorescence materials still have some drawbacks: the rarity of the precious metals required for fabrication, toxicity, and difficulty in color rendering of the three primary colors (blue, green, and red), especially for blue emission. Purely organic TADF materials can utilize both S_1 and T_1 excitons for light emission without the use

of any precious metal. Thus, TADF molecules can act as a class of next-generation organic light-emitting materials. Therefore, this dissertation focuses on molecular design for highly efficient TADF materials and their application in OLEDs.Outline of this dissertation is as follows.

Chapter 2 deals with a design way for efficient full-color TADF molecules by employing donor and acceptor units with the different electron-donating and electron-withdrawing abilities, respectively. Full-color OLEDs utilizing a new series of wedge-shaped TADF materials as emitters achieved high electroluminescence efficiencies compared with conventional fluorescence-based OLEDs. **Chapter 3** and **Chapter 4** provide design strategies for highly efficient pyrimidine-based blue TADF molecules employing highly twisted D–A and D–A–D molecular architectures. The newly designed and synthesized series of pyrimidine-based blue TADF materials were investigated their photophysical properties and completely applied to blue TADF-OLEDs. **Chapter 5** describes a new high-efficiency blue TADF luminophore based on phenazaborin, and its photophysical properties and potential for application of OLED was investigated. **Chapter 6** describes the effect of combining TADF with horizontally oriented dipoles of molecules on both pure thin and doped films in a host matrix as well as OLEDs utilizing a new series of linear-shaped TADF materials as emitters. **Chapter 7** deals with a design concept of bipolar host materials having high thermal stabilities as well as high lowest excited triplet energies to realize high efficiency TADF-OLEDs with reduced efficiency roll-off. Finally, **Chapter 8** summarizes this dissertation.

References

[1] a) J. Kido, M. Kimura, K. Nagai, *Science* **1995**, *267*, 1332; b) S. Reineke, F. Lindner, G. Schwartz, N. Seidler, K. Walzer, B. Lüssem, K. Leo, *Nature* **2009**, *459*, 234; c) M. A. McCarthy, B. Liu, E. P. Donghue, I. Kravchenko, D. Y. Kim, F. So, A. G. Rinzler, *Science* **2011**, *332*, 570.

[2] M. A. Baldo, D. F. O'Brien, Y. You, A. Shoustikov, S. Sibley, M. E. Thompson, S. R. Forrest, *Nature* **1998**, *395*, 151.

[3] W. Helfrich, W. G. Schneider, *Phys. Rev. Lett.* **1965**, *14*, 229.

[4] C. W. Tang, S. A. VanSlyke, *Appl. Phys. Lett.* **1987**, *51*, 913.

[5] J. H. Burroughes. D. D. Bradley, A. R. Brown, R. N. Marks, K. Mackay, R. H. Friend, P. L. Burns, A. B. Holmes, *Nature* **1990**, *347*, 539.

[6] a) L. Xiao, Z. Chen, B. Qu, J. Luo, S. Kong, Q. Gong, J. Kido, *Adv. Mater.* **2011**, *23*, 926; b) M. Zhu, C. Yang, *Chem. Soc. Rev.* **2013**, *42*, 4963; c) H. Xu, R. Chen, Q. Sun, W. Lai, Q. Su, W. Huang, X. Liu, *Chem. Soc. Rev.* **2014**, *43*, 3259; d) W. Brütting, J. Frischeisen, T. D. Schmidt, B. J. Scholz, C. Mayr, *Phys. Stasus Solidi A* **2013**, *210*, 44; e) J.-H. Jou, S. Kumar, A. Agrawal, T.-H. Li, S. Sahoo, *J. Mater. Chem. C* **2015**, *3*, 2974.

[7] L. J. Rothberg, A. J. Lovinger, *J. Mater. Res.* **1996**, *11*, 3174.

[8] a) C. Adachi, M. A. Baldo, M. A. Thompson, S. R. Forrest, *J. Appl. Phys.* **2001**, *90*, 5048; b) C. Adachi, M. A. Baldo, S. R. Forrest, M. E. Thompson, *Appl. Phys. Lett.* **2000**, *77*, 904.

[9] For cyanobenzene-based TADF emitters: a) H. Uoyama, K. Goushi, H. Nomura, C. Adachi, *Nature* **2012**, *492*, 234; b) T. Nishimoto, T. Yasuda, S. Y. Lee, R. Kondo, C. Adachi, *Mater. Horiz.* **2014**, *1*, 264; c) Y. J. Cho, K. S. Yook, J. Y. Lee, *Sci. Rep.* **2015**, *5*, 7859; d) Y. J. Cho, B. D. Chin, S. K. Jeon, J. Y. Lee, *Adv. Mater.* **2015**, *25*, 6786; e) Y. J. Cho, S. K. Jeon, B. D. Chin, E. Yu, J. Y. Lee, *Angew. Chem. Int. Ed.* **2015**, *54*, 5201; f) S. Wang, X. Yan, Z. Cheng, H. Zhang, Y. Liu, Y. Wang, *Angew. Chem. Int. Ed.* **2015**, *54*, 13068.

[10] For triazine-based TADF emitters: a) S. Y. Lee, T. Yasuda, H. Nomura, C. Adachi, *Appl. Phys. Lett.* **2012**, *101*, 093306; b) A. Endo, K. Sato, K. Yoshimura, T. Kai, A. Kawada, H. Miyazaki, C. Adachi, *Appl. Phys. Lett.* **2011**, *98*, 083302; c) K. Sato, K. Shizu, K. Yoshimura, A. Kawada, H. Miyazaki, C. Adachi, *Phys. Rev. Lett.* **2013**, *110*, 247401; d) H. Tanaka, K. Shizu, H. Miyazaki, C. Adachi, *Chem. Commun.* **2012**, *48*, 11392; e)

S. Hirata, Y. Sakai, K. Masui, H. Tanaka, S. Y. Lee, H. Nomura, N. Nakamura, M. Yasumatsu, H. Nakanotani, Q. Zhang, K. Shizu, H. Miyazaki, C. Adachi, *Nat. Mater.* **2015**, *14*, 330; f) M. Kim, S. K. Jeon, S.-H. Hwang, J. Y. Lee, *Adv. Mater.* **2015**, *27*, 2515; g) D. Y. Lee, M. Kim, S. K. Jeon, S.-H. Hwang, C. W. Lee, J. Y. Lee, *Adv. Mater.* **2015**, *27*, 5861; h) W.-L. Tsai, M.-H. Huang, W.-K. Lee, Y.-J. Hsu, K.-C. Pan, Y.-H. Huang, H.-C. Ting, M. Sarma, Y.-Y. Ho, H.-C. Hu, C.-C. Chen, M.-T. Lee, K.-T. Wong, C.-C. Wu, *Chem. Commun.* **2015**, *51*, 13662; i) J. W. Sun, J. Y. Baek, K.-H. Kim, C.-K. Moon, J.-H. Lee, S.-K. Kwon, Y.-H. Kim, J.-J. Kim, *Chem. Mater.* **2015**, *27*, 6675.

[11] For sulfone-based TADF emitters: a) Q. Zhang, J. Li, K. Shizu, S. Huang, S. Hirata, H. Miyazaki, C. Adachi, *J. Am. Chem. Soc.* **2012**, *134*, 14706; b) Q. Zhang, B. Li, S. Huang, H. Nomura, H. Tanaka, C. Adachi, *Nat. Photon.* **2014**, *8*, 326; c) F. B. Dias, K. N. Bourdakos, V. Jankus, K. C. Moss, K. T. Kamtekar, V. Bhalla, J. Santos, M. R. Bryce, A. P. Monkman, *Adv. Mater.* **2013**, *25*, 3707; d) H. Wang, L. Xie, Q. Peng, L. Meng, Y. Wang, Y. Yi, P. Wang, *Adv. Mater.* **2014**, *26*, 5198; Z. Xie, C. Chen, S. Xu, J. Li, Y. Zhang, S. Liu, J. Xu, Z. Chi, *Angew. Chem. Int. Ed.* **2015**, *54*, 7181.

[12] For benzophenone-based TADF emitters: a) S. Y. Lee, T. Yasuda, Y. S. Yang, Q. Zhang, C. Adachi, *Angew. Chem. Int. Ed.* **2014**, *126*, 6520; b) S. Y. Lee, T. Yasuda, I. S. Park, C. Adachi, *Dalton Trans.* **2015**, *44*, 8356; c) Q. Zhang, D. Tsang, H. Kuwabara, Y. Hatae, B. Li, T. Takahashi, S. Y. Lee, T. Yasuda, C. Adachi, *Adv. Mater.* **2015**, *27*, 2096.

[13] For spirofluorene-based TADF emitters: a) G. Méhes, H. Nomura, Q. Zhang, T. Nakagawa, C. Adachi, *Angew. Chem. Int. Ed.* **2012**, *51*, 11311; b) K. Nasu, T. Nakagawa, H. Nomura, C.-J. Lin, C.-H. Cheng, M.-R. Tseng, T. Yasuda, C. Adachi, *Chem. Commun.* **2013**, *49*, 10385; c) H. Ohkuma, T. Nakagawa, K. Shizu, T. Yasuda, C. Adachi, *Chem. Lett.* **2014**, *43*, 1017.

[14] For heteraborin-based TADF emitters: M. Numata, T. Yasuda, C. Adachi, *Chem. Commun.* **2015**, *51*, 9443.

[15] a) T. Förster, *Discuss Farada Soc.* **1959**, *27*, 7; b) B. P. Lyons, A. P. Monkman, *Phys. Rev. B* **2005**, *71*, 235201.

[16] D. L. Dexter, *J. Chem. Phys.* **1953**, *21*, 836.

[17] a) Y. Tao, C. Yang, J. Qin, *Chem. Soc. Rev.* **2011**, *40*, 2943; b) L. Xiao. Z. Chen, B. Qu, J. Luo, S. Kong, Q. Gong, J. Kido, *Adv. Mater.* **2011**, *23*, 926; c) A. Chaskar, H.-F. Chen, K. T. Wong, *Adv. Mater.* **2011**, *23*, 3876; d) K. S. Yook, J. Y. Lee, *Adv. Mater.* **2012**, *24*, 3169.

[18] a) N. J. Turro, V. Ramamurthy, J. C. Scaiano, *Modern Molecular Photochemistry of Organic Molecules*, University Science Books, Sausalito, **2010**; b) Y. Tao, K. Tuan, T. Chen, P. Xu, H. Li, R. Chen, C. Zheng, L. Zhang, W. Huang, *Adv. Mater.* **2014**, *26*, 7931.

[19] K. Goushi, K. Yoshida, K. Sato, C. Adachi, *Nat. Photon.* **2012**, *6*, 253.

[20] C. Murawshk, K. Leo, M. C. Gather, *Adv. Mater.* **2013**, *25*, 6801.

[21] a) M. Pope, C. E. Swenberg, *Electric Processes in Organic Crystals*, *Clarendon Press*, Oxford University Press, **1982**; b) S. D. Babenko, V. A. Bendershkii, V. I. Gol'Danskii, A. G. Lavrushko, V. P. Tychinskii, *Chem, Phys, Lett.* **1971**, 8, 598.

[22] M. A. Baldo, R. J. Homes, S. R. Forrest, *Phys. Rev. B* **2002**, *66*, 035321.

[23] M. A. Baldo, C. Adachi, S. R. Forrest, *Phys, Rev. B* **2000**, *62*, 10967.

[24] a) Y. Sun, N. C. Giebink, H. Kanno, B. Ma, M. E. Thompson, S. R. Forrest, *Nature* **2006**, *440*, 908; b) G. Schwartz, S. Reineke, T. C. Rosenow, K. Walzer, K. Leo, *Adv. Funct. Mater.* **2009**, *19*, 1319; c) T. C. Rosenow, M. Furno, S. Reineke, S. Olthof, B. Lüssem, K. Leo, *J. Appl. Phys.* **2010**, *108*, 11331133.

[25] a) J. Fourny, G. Delacote, *Phys. Rev. Lett.* **1968**, *21*, 1085; b) Y. Zhang, M. Whited, M. E. Thompson, S. R. Forrest, *Chem. Phys. Lett.* **2010**, *495*, 161; c) D. Kasemann, R. Brückner, H. Fröb, K. Leo, *Phys. Rev. B* **2011**, *84*, 115208.

[26] K. Masui, H. Nakanotani, C. Adachi, *Org. Electron.* **2013**, *14*, 2721.

[27] a) S Reineke, K. Walzer, K. Leo, *Phys. Rev. B* **2007**, *75*, 125328; b) J. Kalinowski, W. Stampor, J. Mezyk, M. Cocchi. D. Virgili, V. Fattori. P. Di Marco, *Phys. Rev. B* **2002**, *66*, 235321.

[28] a) H. Yersin, A. F. Rausch, R. Czerwieniec, T. Hofbeck, T. Fischer, *Coord. Chem. Rev.* **2011**, *255*, 2622; b) L. Han, D. Yang, W. Li, B. Chu, Y. Chen, Z. Su, D. Zhang, F. Yan, Z. Hu, Z. Zhang, *Appl. Phys. Lett.* **2008**, *93*, 153303; c) D. Yang, L. Han, W. Li, B. Chu, Z. Su, D. Zhang, T. Li, G. Zhang, J. Zhu, *J. Phys. D Appl. Phys.* **2010**, *43*, 105101; d) D. Song, S. Zhao, H. Aziz, *Adv. Funct. Mater.* **2011**, *21*, 2311; e) Q. Huang, S. Reineke, K. Walzer, M. Pfeiffer, K. Leo, *Appl. Phys. Lett.* **2006**, *89*, 263512; f) W. Ji, L. Zhang, W. Xie, *Opt. Lett.* **2012**, *37*, 2019.

[29] a) Y. Kawamura, L. Brooks, J. J. Brown, H. Sasabe, C. Adachi. *Phys. Rev. Lett.* **2006**, *96*, 17404; b) S. Reineke, T. C. Rosenow, B. Lussem, K. Leo, *Adv. Mater.* **2010**, *22*, 3189.

[30] a) J. Lee, J.-I. Lee, J. Y. Lee, H. Y. Chu, *Org. Electron.* **2009**, *10*, 1529; b) G. He, M. Pfeiffer, K. Leo, M. Hofmann, J. Birnstock, R. Pudzich, J. Salbeck, *Appl. Phys. Lett.* **2004**, *85*, 3911; c) M.-T. Lee, J.-S. Lin, M-T. Chu, M.-R. Tseng, *Appl. Phys. Lett.* **2009**, *94*, 083506; d) J.-W. Kang, S.-H. Lee, H.-D. Park, W.-I. Jeong, K.-M. Yoo, Y.-S. Park, J.-J. Kim, *Appl. Phys. Lett.* **2007**, *90*, 223508; e) S. H. Kim, J. Jang, K. S. Yook, J. Y. Lee, *Appl. Phys. Lett.* **2008**, *92*, 023513; f) Z. M. Hudson, Z. Wang, M. G. Helander, Z.-H. Lu, S. Wang, *Adv. Mater.* **2012**, *24*, 2922; g) S. Gong, Y. Chen, C. Yang, C. Zhong, J. Qin, D. Ma, *Adv. Mater.* **2010**, *22*, 5370.

[31] a) W. Staroske, M. Pfeiffer, K. Leo, M. Hoffmann. *Phys. Rev. Lett.* **2007**, *98*, 197402; b) Y. Divayana. X. Sun, *Phys. Rev. Lett.* **2007**, *99*, 143003.

Chapter 2

Wedge-Shaped Delayed Fluorescence Materials Based on Phthalonitriles and Dicyanopyrazines for Full-Color Electroluminescence

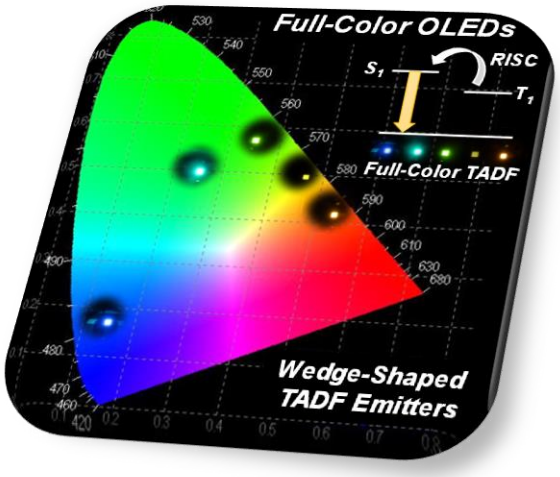

2. 1. Introduction

Various purely organic TADF emitters have been developed to date based on aforementioned design principle in General Introduction,[1–6] most of them adopt a twisted intramolecular charge transfer (ICT) design, in which the electron donor and acceptor units are incorporated to be orthogonal to each other. Among the reported TADF emitters, 1,2,3,5-tetrakis(carbazol-9-yl)-4,6-dicyanobenzene (4CzIPN)[1a] combined with an electron-withdrawing isophthalonitrile (i.e., 1,3-dicyanobenzene) with four-fold electron-donating carbazole units is one of the most efficient TADF emitters, exhibiting a maximum external EL quantum efficiency (η_{ext}) of almost 20%[1a] or even higher.[7] It has also been reported that by changing the position of cyano groups and the number of carbazole units, the emission spectra of the TADF materials can be tuned. ICT of these molecules has crucial effects on their band gap and luminescence. For the realization of full-color TADF-OLEDs, it is vital to modulate the TADF characteristics and the emission colors systematically using a versatile donor–acceptor (D–A) system.

In this chapter, a series of wedge-shaped D–A–D molecules (**Figure 2-1**), comprising of a central phthalonitrile (VPN) or 2,3-dicyanopyrazine (CNP) acceptor core coupled with various donor units (i.e., 1-methylcarbazole (Cz), 9,9-dimethylacridan (Ac), and phenoxazine (Px)), are reported. π-Conjugated phenylene linkers are introduced between the donor and acceptor units to enhance the radiative decay constant of the S_1 state to some degree, meanwhile maintaining a small ΔE_{ST}. These new systems allow a systematic fine-tuning of their band gap and TADF emissions to cover the entire visible range. Full-color EL with a high η_{ext} of up to 18.9% can be achieved using wedge-shaped phthalonitrile and dicyanopyrazine derivatives as TADF emitters in OLEDs.

2. 2. Molecular Geometric and Electronic Structures

To understand the effect of variation of the D–A–D structures on the geometric and optoelectronic properties, quantum chemical calculations were performed on the designed phthalonitrile- and dicyanopyrazine-based molecules. The calculated energy levels of the HOMO and LUMO and the respective frontier orbital distributions are presented in **Figure 2-1**. The energy levels and molecular geometries in the ground state were optimized by density functional theory (DFT) calculations. The excited S_1 and T_1 states were computed using the optimized structures with time-dependent DFT (TD-DFT) calculations. It is found that the calculated HOMO–LUMO energy gaps (E_g) can be modulated systematically from 3.2 eV (Cz-

VPN) to 1.9 eV (Px-CNP) by a rational combination of donor and acceptor units. The decrease in the E_g from Cz-VPN to Px-VPN follows the increasing order of the electron-donating ability of their donor units (Cz < Ac < Px) which consequently affects their HOMO energy levels. Ac-CNP and Px-CNP containing a strong electron-withdrawing dicyanopyrazine core tend to have a lower LUMO energy and a narrower E_g than the phthalonitrile-based counterparts do. This trend indicates that the donor and acceptor strengths have a great influence on the resulting optoelectronic functionality since the HOMO–LUMO electronic transition dominates the S_1 excitation with ICT characteristics.

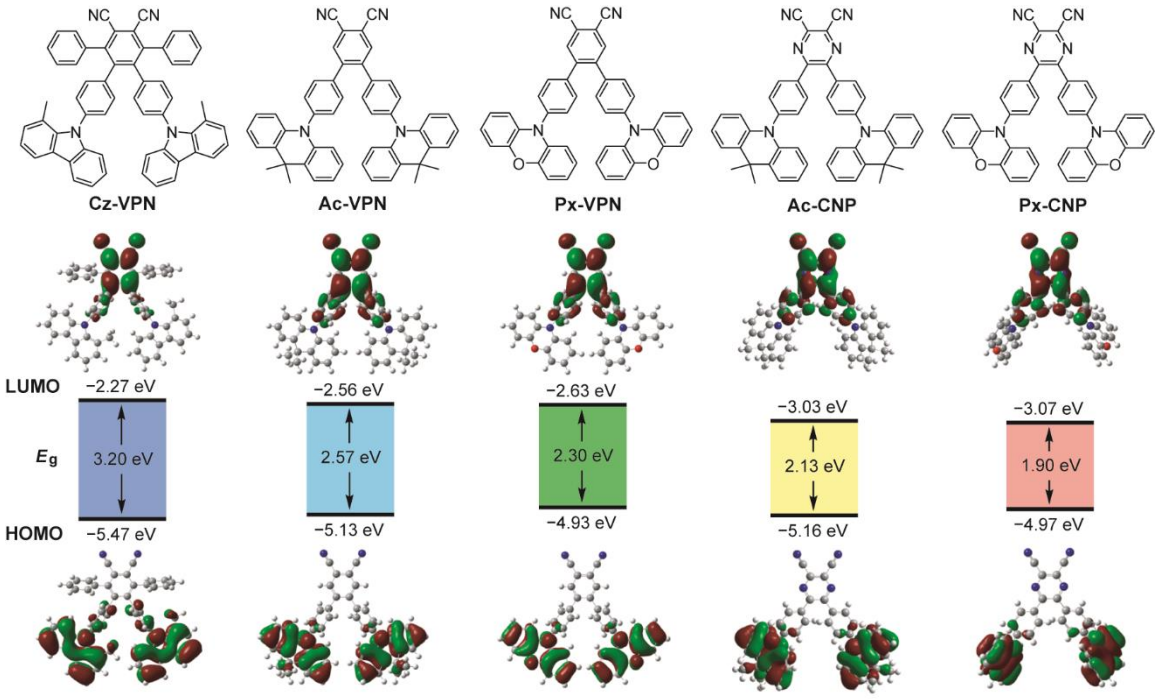

Figure 2-1. Molecular structures (upper), energy levels and Kohn–Sham orbitals of the HOMO and LUMO (lower) of wedge-shaped phthalonitrile- and dicyanopyrazine-based TADF molecules characterized by DFT and TD-DFT calculations at the B3LYP/6-31G(d,p) level.

The HOMOs of these molecules are predominantly located on the peripheral donor units, whereas the LUMOs are distributed over the phenylene linkers as well as the central acceptor core (**Figure 2-1**). For Cz-VPN, the HOMO is extended slightly to the neighboring phenylene linkers, owing to the less steric hindrance of the Cz donor units, compared with the Ac and Px units. The clear spatial separation of the frontier orbitals of all these molecules resulted in small calculated ΔE_{ST} values of less than 0.04 eV (**Table 2-1**), suggesting the high potential as TADF emitters. It is also evident that, in the optimized ground-state structures, the dihedral angles between the peripheral donor units and the nearby phenylene linkers increase in the order of Cz

(53–54°) < Px (74–77°) < Ac (87–90°). Such highly distorted geometries of these molecules should arise from the steric effects of the hydrogen atoms and/or methyl groups at the *peri*-positions in the donor units, contributing to the decrease of the electron exchange energy for the ICT transitions. In contrast, the dihedral angles between the central phthalonitrile or dicyanopyrazine acceptor unit and the phenylene linkers are relatively small (51–54° for Ac-VPN and Px-VPN; 34–35° for Ac-CNP and Px-CNP). These results suggest that the phenylene linker has a stronger conjugation with the central acceptor core than the outermost donor units. The detail calculated results are summarized in **Table 2-1**.

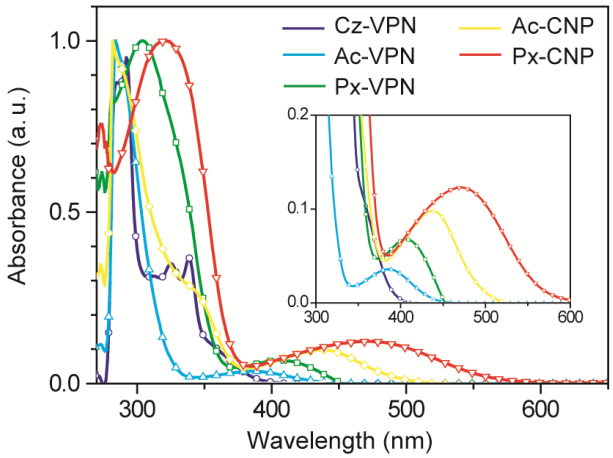

Figure 2-2. UV–vis absorption spectra of phthalonitrile- and dicyanopyrazine-based D–A–D type molecules in toluene. The inset shows a magnified view of lower-energy ICT absorptions.

2. 3. Photophysical Properties

The molecular orbital distributions are reflected in the photophysical properties of the phthalonitrile- and dicyanopyrazine-based materials. Basic photophysical parameters have been collected from steady-state UV–vis absorption and photoluminescence (PL) spectra and time-resolved transient PL analyses for toluene solutions and as doped thin films, and the results are summarized in **Table 2-2**. As shown in **Figure 2-2**, these compounds exhibit a broad and weak absorption band at longer wavelengths in the absorption spectra, which can be assigned to the ICT transitions from the peripheral donor units to the acceptor core. The ICT absorption band shifts to lower energies with increasing donor and acceptor strengths, which is well in accordance with the calculation results.

Table 2-1. Triplet and singlet excitation energies (vertical transition), oscillator strength (*f*), and transition configurations of the phthalonitrile and dicyanopyrazine derivatives calculated by TD-DFT at the B3LYP/6-31G(d,p).

Compound	State	*E* (eV)	*f*	Main configuration[a)]		ΔE_{ST} (eV)
Cz-VPN	S_1	2.836	0.0181	H → L	0.702	0.039
	S_2	2.904	0.0124	H−1 → L	0.703	
	T_1	2.797	0	H → L	0.662	
				H−1 → L	0.112	
	T_2	2.877	0	H → L	0.673	
				H−1 → L	−0.143	
Ac-VPN	S_1	2.183	0	H → L	0.703	0.002
	S_2	2.185	0	H−1 → L	0.703	
	T_1	2.181	0	H → L	0.703	
	T_2	2.183	0	H−1 → L	0.703	
Px-VPN	S_1	1.934	0.0099	H → L	0.703	0.015
	S_2	1.958	0.0118	H−1 → L	0.704	
	T_1	1.919	0	H → L	0.700	
	T_2	1.941	0	H−1 → L	0.701	
Ac-CNP	S_1	1.736	0	H → L	0.692	0.003
				H−1 → L+1	−0.129	
	S_2	1.736	0.0001	H−1 → L	0.692	
				H → L+1	−0.129	
	T_1	1.733	0	H → L	0.691	
				H−1 → L+1	−0.133	
	T_2	1.733	0	H−1 → L	0.691	
				H → L+1	−0.134	
Px-CNP	S_1	1.524	0.0336	H → L	0.698	0.040
	S_2	1.547	0.0318	H−1 → L	0.703	
	T_1	1.484	0	H−1 → L	0.687	
				H−1 → L+1	0.144	
	T_2	1.493	0	H−1 → L	0.687	
				H → L+1	0.150	

[a)] H → L represents the HOMO to LUMO transition. Excitation configurations with the highest contributions are presented, together with the corresponding transition symmetry and nature of the involved orbitals.

Table 2-2. Photophysical data of phthalonitrile- and dicyanopyrazine-based TADF materials.

Compound	λ_{asb} [nm] sol[a)]	λ_{PL} [nm] sol[a)] / film[b)]	Φ_{PL}[%][c)] sol[a)] / film[b)]	τ_p [ns][d)] / τ_d [μs][d)]	HOMO [eV][e)]	LUMO [eV][f)]	E_S / E_T [eV][g)]	ΔE_{ST} [eV][h)]
Cz-VPN	292,325,339[i)]	440 / 450	78 / 63	41 / 173	−6.1	−2.9	3.08 / 2.72	0.36
Ac-VPN	282,384	532 / 499	59 / 86	35 / 5.1	−5.8	−3.1	2.90 / 2.70	0.20
Px-VPN	304,406	577 / 540	42 / 77	27 / 2.3	−5.7	−3.3	2.64 / 2.56	0.08
Ac-CNP	282,342[i)],436	620 / 570	20 / 67	30 / 3.3	−5.4	−3.1	2.33 / 2.24	0.09
Px-CNP	321,473	—[j)] / 610	<1 / 15	21 / 1.5	−5.2	−3.2	2.45 / 2.41	0.04

[a)]Measured in oxygen-free toluene solution at room temperature; [b)] 6 wt%-doped thin film in a host matrix (host = PPF for Cz-VPN; mCBP for others); [c)]Absolute PL quantum yield evaluated using an integrating sphere under a nitrogen atmosphere; [d)]PL lifetimes of prompt (τ_p) and delayed (τ_d) decay components for the 6 wt%-doped film measured using a streak camera at 300 K; [e)]Determined by photoelectron yield spectroscopy in pure neat films; [f)]Deduced from the HOMO and optical energy gap (E_g); [g)]Singlet (E_S) and triplet (E_T) energies estimated from onset wavelengths of the emission spectra at 300 and 50 K in the doped films, respectively; [h)]$\Delta E_{ST} = E_S - E_T$; [i)]Shoulder peak; [j)]Not determined (see ref. 10).

For further investigation of the photophysical and TADF properties, doped thin films of the phthalonitrile- and dicyanopyrazine-based emitters in a host matrix were prepared in order to avoid concentration quenching. For the blue emitter Cz-VPN, 2,8-bis(diphenylphosphoryl)dibenzofuran (PPF)[8] possessing a high T_1 energy (E_T) value of 3.1 eV was selected as a host to prevent the backward energy transfer from the excited Cz-VPN to the host material and to confine the T_1 excitons within the Cz-VPN molecules. For other emitters, 3,3'-bis(carbazol-9-yl)-1,1'-biphenyl (mCBP)[9] with an E_T of 2.9 eV was adopted as a suitable host material. As can be seen from **Figure 2-3**, the emission colors of the doped films range from blue (Cz-VPN: λ_{PL} = 450 nm) to green (Px-VPN: λ_{PL} = 540 nm), and even red (Px-CNP: λ_{PL} = 610 nm), covering the entire visible light. The absolute PL quantum yields (Φ_{PL}) of these emitters in the doped films lie in the range of 63–86%, with the exception for the red-emitting Px-CNP film (Φ_{PL} = 15%).[10] The reason for such a low Φ_{PL} of Px-CNP may be ascribed to the energy-gap law, which suggests that the Φ_{PL} decreases as the energy gap is reduced, owing to the vibrational overlap of the ground and the excited states.[11] Thus, the experimental PL observations confirm the expected trend that the multi-color tuning of TADF can be accomplished by systematic structural variations.

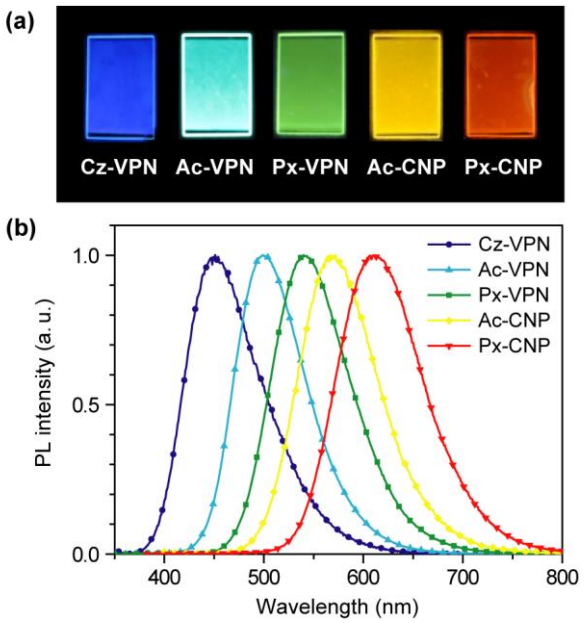

Figure 2-3. (a) Photographs showing PL emission under UV irradiation and (b) steady-state PL spectra of 6 wt%-doped thin films of the phthalonitrile- and dicyanopyrazine-based emitters in a PPF or mCBP host matrix.

The transient PL characteristics of the emitters were also examined to reveal the TADF behavior. As exemplified in **Figure 2-4**, the transient PL curve of the 6 wt%-Ac-VPN:mCBP doped film obviously indicated a nanosecond-order prompt decay component and a microsecond-order delayed decay component in the time range of 10 μs, which can be fitted with a biexponential model. While the prompt component had a lifetime (τ_p) of 35 ns with a quantum efficiency (Φ_p) of 8%, the delayed component had a lifetime (τ_d) of 5.1 μs with an efficiency (Φ_d) of 78% at 300 K. Moreover, the delayed component is appeared with a similar spectral distribution as the prompt one; hence, the delayed emission can be ascribed to the singlet emission through RISC processes. Temperature-dependence of the transient PL was also studied for the 6 wt%-Ac-VPN:mCBP doped film in the temperature range of 50–300 K (**Figure 2-4a**). Apparently, the delayed emission was intensified when temperature was increased from 50 to 300 K, demonstrating that the $T_1 \rightarrow S_1$ RISC process was enhanced by the thermal energy, which is a direct evidence of TADF. Similar temperature-dependent transient PL behavior was observed for all the phthalonitrile- and dicyanopyrazine-based emitters (**Figure 2-5**). The delayed emission lifetime of the green-emitting Px-VPN film (τ_d = 2.3 μs) is found to be much shorter than those of the blue-emitting Cz-VPN and light-blue-emitting Ac-VPN films (τ_d = 173 and 5.1 μs, respectively), suggesting a more efficient $T_1 \rightarrow S_1$ up-conversion arising from smaller ΔE_{ST} (**Table 2-2**). From the room-temperature fluorescence

and the low-temperature phosphorescence (5 K) spectra of the doped films (**Figure 2-6**), the experimental ΔE_{ST} values are found to be in the order of Cz-VPN (0.36 eV) > Ac-VPN (0.20 eV) > Px-VPN (0.08 eV) ≈ Ac-CNP (0.09 eV) > Px-CNP (0.04 eV), which are in good agreement with the trend of the delayed emission lifetimes.

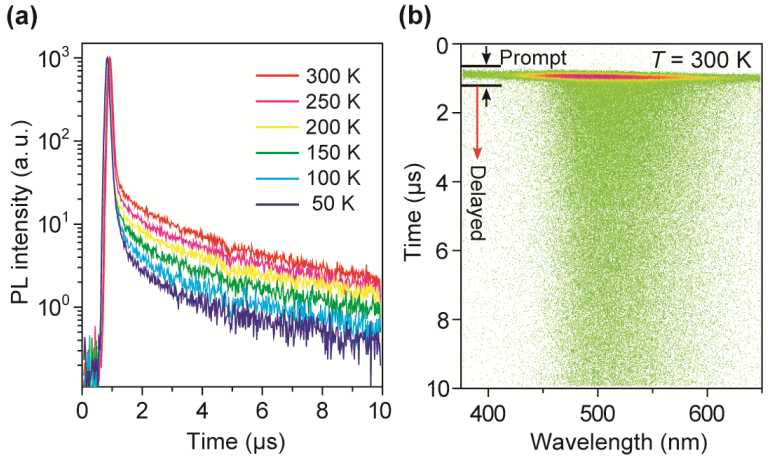

Figure 2-4. (a) Temperature dependence of transient PL decay of a 6 wt%-Ac-VPN:mCBP doped film. (b) Streak image of the doped film measured at 300 K under vacuum, in which green dots represent PL photon counts.

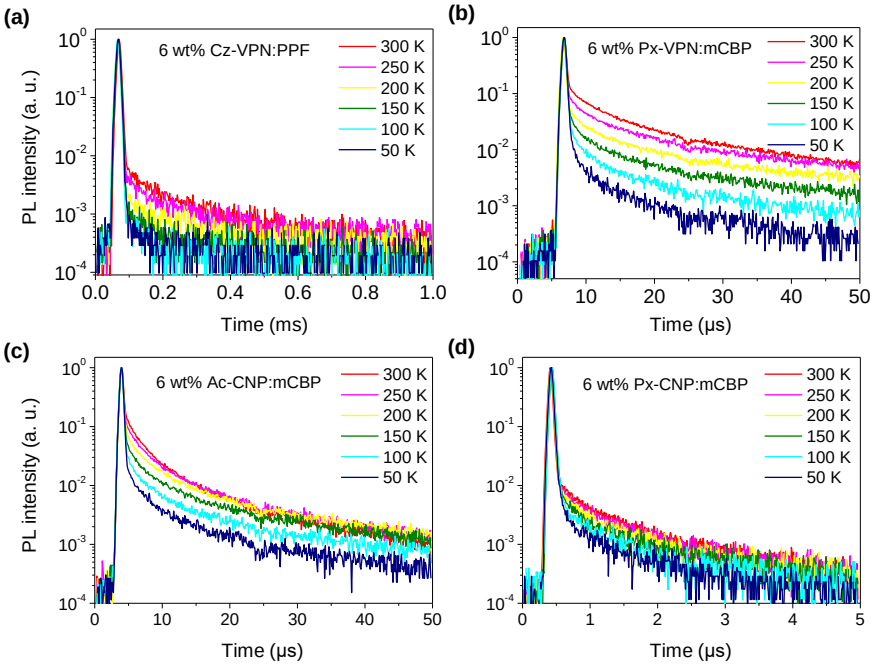

Figure 2-5. Temperature dependence of transient PL decay of 6 wt%-doped films in a host matrix measured from 50 to 300 K: (a) Cz-VPN:PPF, (b) Px-VPN:mCBP, (c) Ac-CNP:mCBP, and (d) Px-CNP:mCBP.

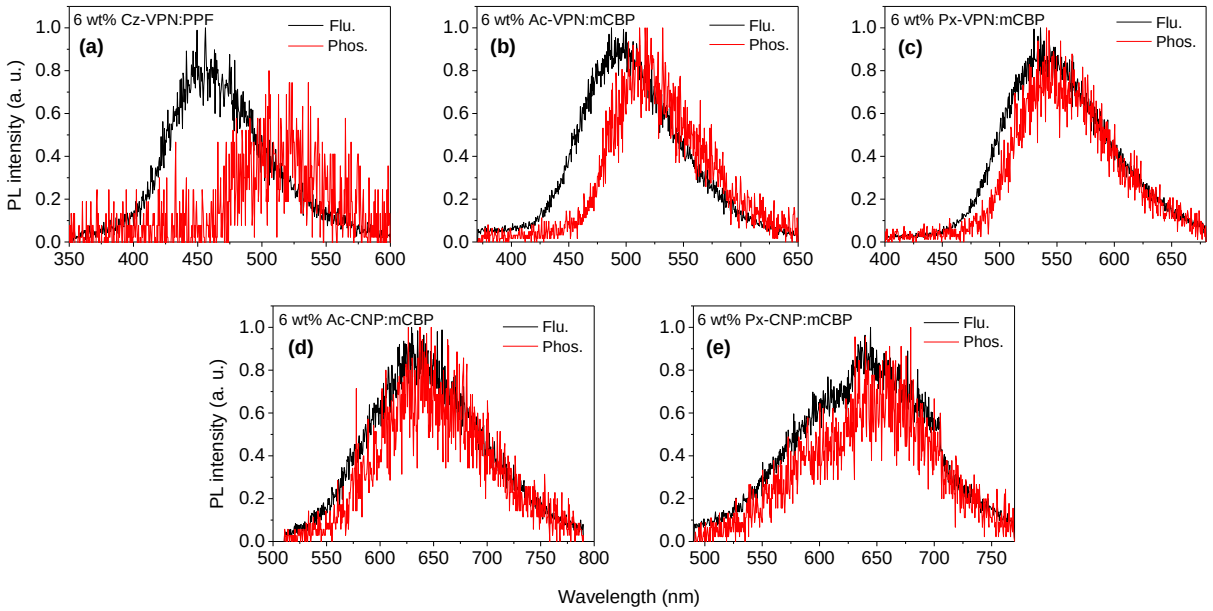

Figure 2-6. PL spectra for prompt fluorescence in the range of 0–300 ns at 300 K (black) and phosphorescence in the range of 1–10 ms at 50 K (red) for 6 wt%-doped films in a host matrix: (a) Cz-VPN:PPF, (b) Ac-VPN:mCBP (c) Px-VPN:mCBP, (d) Ac-CNP:mCBP, and (e) Px-CNP:mCBP. The lowest excited singlet (S_1) and triplet energy (T_1) levels of the TADF emitters were determined from the high energy onsets of the fluorescence and phosphorescence, respectively.

2. 4. Electroluminescence Performance

Color-tunable TADF characteristics with high Φ_{PL} enable these emitters to be adopted in high-efficiency full-color TADF-OLEDs. To investigate the EL performance, multilayer OLEDs were fabricated using 6 wt%-emitter:host doped films as the emitting layer (EML). The structure of the fabricated devices was as follows: indium-tin-oxide (ITO, 110 nm)/α-NPD (40 nm)/mCP (10 nm)/EML (20 nm)/PPF (10 nm)/TPBi (30 nm)/LiF (0.8 nm)/Al (100 nm), where 4,4'-bis[*N*-(1-naphthyl)-*N*-phenylamino]-1,1'-biphenyl (α-NPD) and 1,3,5-tris(*N*-phenylbenzimizazol-2-yl)benzene (TPBi) served as a hole-transporting layer (HTL) and electron-transporting layer (ETL), respectively. To prevent the energy transfer and to confine T_1 excitons in the EML, thin layers of 1,3-bis(carbazol-9-yl)benzene (mCP) and PPF with high T_1 energies were inserted at the EML/HTL and EML/ETL interfaces. The current density–voltage–luminance (*J*–*V*–*L*) and η_{ext} versus luminance characteristics of the devices are shown in **Figure 2-7**, and the key device parameters are summarized in **Table 2-3**.

All the devices employing phthalonitrile- and dicyanobenzene-based emitters displayed EL spectra similar to the corresponding PL spectra, confirming that EL emission was generated solely from the emitters via the same radiative decay process. These devices indicated similar

turn-on voltages (V_{on}) in the range of 4.4–5.5 V. For the Cz-VPN-based device, a blue EL emission at a maximum wavelength (λ_{EL}) of 465 nm and Commission Internationale de l'Éclairage (CIE) color coordinates of (0.15, 0.18) were obtained. The EL efficiency of the blue-emitting Cz-VPN device is drastically decreased with increasing luminance. This severe efficiency roll-off of the device is mainly attributed to the relatively longer T_1 excited-state lifetime of the Cz-VPN emitter, which undergoes exciton quenching such as triplet–triplet annihilation and/or triplet–polaron annihilation.[12] Another possible reason can be the poor hole-transport property of the PPF host. PPF is a unipolar electron-transporting material and the hole/electron carrier balance is disrupted at high current densities. We anticipate that the performance and roll-off behavior of the blue TADF device can further be improved by using suitable bipolar hosts with high T_1 values and blue TADF emitters with shorter excited-state lifetimes.

Table 2-3. EL performance of the TADF-based OLEDs.[a)]

TADF emitter	Host	λ_{EL} [nm]	V_{on} [V]	L_{max} [cd m^{-2}]	η_{ext} [%]	η_c [cd A^{-1}]	η_p [lm W^{-1}]	CIE (x, y)
Cz-VPN	PPF	465	4.4	13,590	8.7	18.0	12.3	(0.15, 0.18)
Ac-VPN	mCBP	504	4.5	65,720	18.9	51.7	34.1	(0.23, 0.50)
Px-VPN	mCBP	537	4.7	44,380	14.9	45.4	26.7	(0.35, 0.57)
Ac-CNP	mCBP	580	4.7	70,630	13.3	38.1	26.1	(0.47, 0.51)
Px-CNP	mCBP	606	5.5	101,860	3.0	5.8	3.1	(0.53, 0.44)

[a)]Abbreviations: λ_{EL} = EL emission maximum, V_{on} = turn-on voltage at 1 cd m^{-2}, L_{max} = maximum luminance, η_{ext} = maximum external EL quantum efficiency, η_c = maximum current efficiency, η_p = maximum power efficiency, CIE = Commission Internationale de l'Éclairage color coordinates measured at 10 mA cm^{-2}, PPF = 2,8-bis(diphenylphosphoryl)dibenzofuran, mCBP = 3,3'-bis(carbazol-9-yl)-1,1'-biphenyl.

High EL efficiencies with η_{ext} of 18.9%, 14.9%, and 13.3% are attained for the devices containing Ac-VPN, Px-VPN, and Ac-CNP, respectively (corresponding power efficiencies (η_p) are 34.1, 26.7, and 26.1 lm W^{-1}), and their EL emissions are located in the light-blue, green, and yellow regions, respectively. It is noteworthy that the Ac-VPN- and Px-VPN-based devices showed very small efficiency roll-off, hence, the η_{ext} of the devices were still high (12.4% and 10.4%, respectively), even at a high luminance of 10,000 cd m^{-2}. For the red-emitting Px-CNP-based device, the η_{ext} was inferior compared to those of the other devices because of the relatively lower Φ_{PL} of 15% in its doped film. However, the Px-CNP-based device exhibited only a slight efficiency roll-off owing to its short T_1 exciton lifetime of 1.5 μs, compared to

other TADF emitters (**Table 2-2**). The detail EL performances of full-color TADF-OLEDs are summarized in **Table 2-4**.

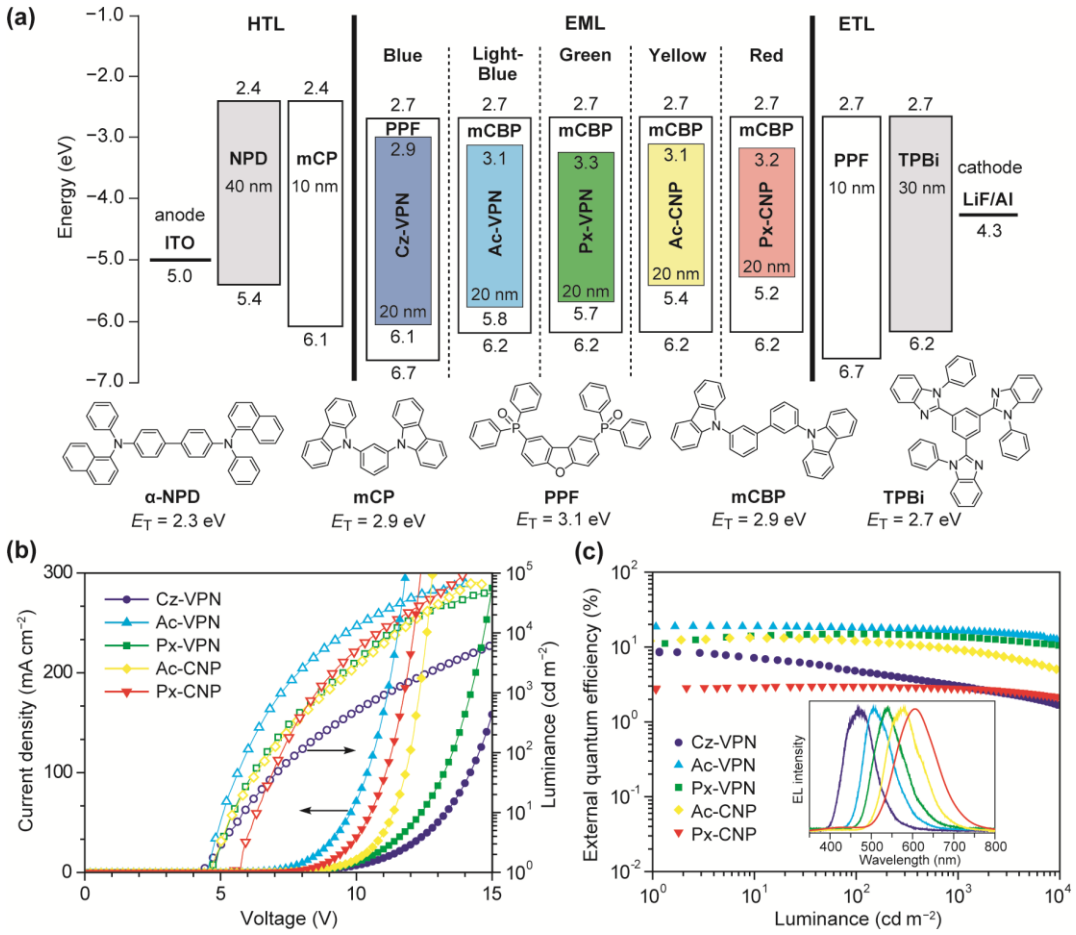

Figure 2-7. (a) Energy level diagram and molecular structures of materials used for TADF-OLEDs. (b) Current density–voltage–luminance (*J*–*V*–*L*) characteristics and (c) external EL quantum efficiency (η_{ext}) versus luminance plots of the TADF-OLEDs. The inset of (c) represents normalized EL spectra of the devices measured at 10 mA cm^{-2}.

Under electrical excitation in TADF-OLEDs, the T_1 excitons are directly generated by carrier recombination and are subsequently converted into the S_1 state via an efficient RISC. Accordingly, the theoretical maxima of η_{int} and η_{ext} can be estimated by equations **1-18** and **1-19.** The theoretical maxima of η_{ext} for Cz-VPN, Ac-VPN, Px-VPN, Ac-CNP, and Px-CNP-based devices are estimated to be approximately 9%, 17%, 14%, 13%, and 3%, respectively, by assuming that η_{out} is ~20%.[13] These theoretical values are consistent with the experimentally obtained η_{ext} values (**Table 2-3**), implying that the appropriate carrier balance and effective exciton confinement are indeed achieved in the EML for the full-color TADF-OLEDs.

Table 2-4. Summary of EL performances of TADF-OLEDs in this study.[a)]

TADF emitter	η_{ext} [%] / η_c [cd A^{-1}] / η_p [lm W^{-1}]		
	Maximum	At 100 cd m^{-2}	At 1000 cd m^{-2}
Cz-VPN	8.7 / 18.0 / 12.3	4.8 / 10.0 / 3.8	3.1 / 6.4 / 1.7
Ac-VPN	18.9 / 51.7 / 34.1	18.0 / 45.5 / 27.1	16.4 / 41.5 / 22.3
Px-VPN	14.9 / 45.4 / 26.7	14.9 / 43.0 / 19.9	13.6 / 33.2 / 11.8
Ac-CNP	13.3 / 38.1 / 26.1	12.0 / 34.1 / 15.3	9.1 / 26.0 / 9.1
Px-CNP	3.0 / 5.8 / 3.1	3.0 / 5.8 / 2.9	2.8 / 5.1 / 1.7

[a)]Abbreviations: η_{ext} = external EL quantum efficiency, η_c = current efficiency, η_p = power efficiency.

2. 5. Experimental Section

2. 5. 1 General Methods

NMR spectra were recorded on an Avance III 500 or Avance III 400 spectrometer (Bruker). Chemical shifts of ^{1}H and ^{13}C NMR signals were quoted to tetramethylsilane (δ = 0.00), $CDCl_3$ (δ = 77.0) as internal standards, respectively. Matrix-assisted laser desorption ionization time-of-flight (MALDI-TOF) mass spectra were collected on an Autoflex III spectrometer (Bruker Daltonics) using dithranol as the matrix. Elemental analyses were carried out with a Yanaco MT-5 CHN corder. UV–vis absorption and photoluminescence (PL) spectra were measured with a UV-2550 spectrometer (Shimadzu) and a Fluoromax-4 spectrophotometer (Horiba Scientific), respectively, using degassed spectral grade solvents. The PL quantum yields were measured using an integration sphere system C9920-02 coupled with a PMA-11 photonic multichannel analyzer (Hamamatsu Photonics). The transient PL measurements of doped thin films were performed using a C4334 Streak camera (Hamamatsu Photonics) with a N_2 gas laser (λ = 337 nm, pulse width = 500 ps, repetition rate = 20 Hz) under vacuum ($< 4 \times 10^{-1}$ Pa). The HOMO energy levels of thin films were determined using an AC-3 ultraviolet photoelectron spectrometer (Riken-Keiki). The LUMO energy levels were estimated by subtracting the optical energy gap (E_g) from the measured HOMO energies; E_g values were determined from the onset position of the PL spectra of thin films. All quantum chemical calculations were performed using the Gaussian 09 program package. Geometries in the ground state were optimized using the B3LYP functional with the 6-31G(d,p) basis set. Low-lying excited singlet and triplet states were computed using the optimized structures with time-dependent density functional theory (TD-DFT) at the same level.

2. 5. 2. Preparation of Materials

All regents and solvents for the synthesis were purchased from Sigma-Aldrich, Tokyo Chemical Industry, or Wako Pure Chemical Industries, and were used as received unless otherwise stated. 9,9-Dimethylacridan (Ac)[14] and PPF[8] were prepared according to the reported procedures. Other OLED materials were purchased from Luminescence Technology Corp. All reactions were performed under nitrogen atmospheres in dry solvents. All final products were purified by temperature-gradient sublimation under vacuum before the measurements and device fabrication.

2. 5. 3. Synthesis

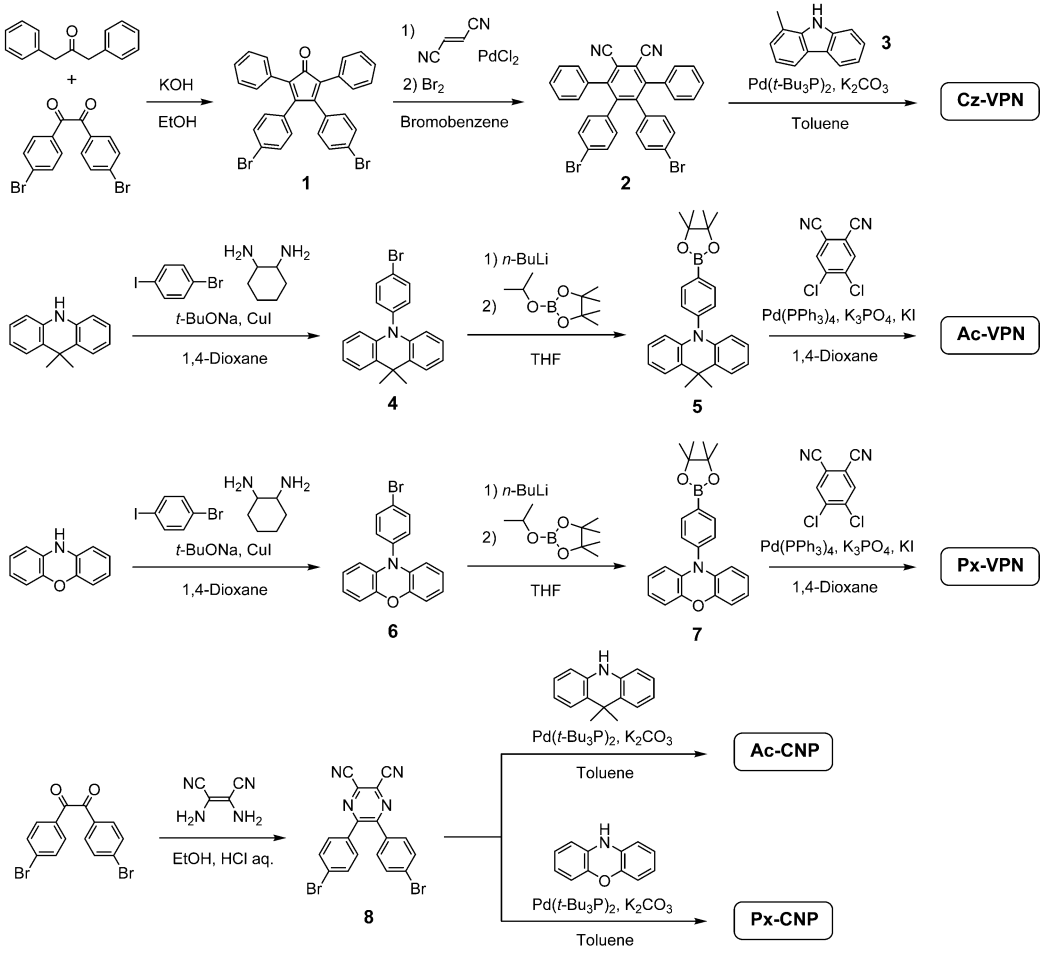

Scheme 2-1. Synthetic routes for phthalonitrile- and dicyanopyrazine-based TADF molecules.

The synthetic schemes are outlined in **Schemes 2-1** and **2-2**. The key intermediate **2** was synthesized from tetraphenylcyclopentadienone **1** and fumaronitrile.[15] Then, the Buchwald–Hartwig amination of **2** with 1-methylcarbazole in the presence of Pd(*t*-Bu$_3$P)$_2$ as a catalyst

afforded Cz-VPN with a high yield. The syntheses of Ac-VPN and Px-VPN were achieved by Suzuki–Miyaura cross-coupling reactions between 4,5-dichlorophthalnitrile and the corresponding boronic esters (**5** and **7**, respectively). For the synthesis of Ac-CNP and Px-CNP, the dibromo precursor **8** was initially prepared, and the Buchwald–Hartwig aminations with 9,9-dimethylacridan or phenoxazine were carried out. All final products were purified by temperature-gradient sublimation under vacuum after column chromatography to obtain highly pure materials, which can be used for the fabrication of OLED devices by vacuum deposition. Chemical structures of the final products were confirmed by ^{1}H and ^{13}C NMR spectroscopy, matrix-assisted laser desorption ionization time-of-flight (MALDI-TOF) mass spectrometry, and elemental analysis.

Synthesis of 3,4-bis(4-bromophenyl)-2,5-diphenylcyclopenta-2,4-dien-1-one (1): A mixture of 4,4'-dibromobenzil (20.0 g, 54.3 mmol), 1,3-diphenylpropan-2-one (11.4 g, 54.3 mmol), and potassium hydroxide (3.05 g, 54.3 mmol) in ethanol (100 mL) was stirred for 3 h at room temperature. Upon cooling to 0 °C, the formed precipitate was collected by filtration, washed with ethanol, and dried under vacuum to give **1** as a purple solid (yield = 26.0 g, 88%). ^{1}H NMR (500 MHz, $CDCl_3$, δ): 7.34 (d, J = 8.5 Hz, 4H), 7.28-7.24 (m, 6H), 7.20-7.18 (m, 4H), 6.79 (d, J = 8.5 Hz, 4H); MS (MALDI-TOF) m/z: $[M]^+$ calcd 539.97; found 539.82.

Synthesis of 4,5-bis(*p*-bromophenyl)-3,6-diphenyl-phthalonitrile (2): A solution of **1** (19.0 g, 35.0 mmol), fumaronitrile (2.73 g, 35.0 mmol), and palladium(II) chloride (0.06 g, 0.35 mmol) in bromobenzene (150 mL) was refluxed for 2 h. The reaction mixture was allowed to cool to room temperature, and then bromine (6.15 g, 38.5 mmol) in bromobenzene (50 mL) was slowly added into the mixture. The mixture was refluxed for 5 h. After cooling to room temperature, the mixture was added into an aqueous solution of sodium thiosulfate to quench the reaction, and the product was extracted with dichloromethane. The combined organic layers were washed with water, and dried over anhydrous magnesium sulfate. After filtration and evaporation, the crude product was purified by column chromatography on silica gel (hexane/dichloromethane = 5:1, v/v) to afford **2** as a white solid (yield = 13.4 g, 65%). ^{1}H NMR (500 MHz, $CDCl_3$, δ): 7.44 (d, J = 8.5 Hz, 2H), 7.29 (d, J = 7.0 Hz, 4H), 7.14 (d, J = 8.5 Hz, 2H), 7.12-7.09 (m, 4H), 6.99 (d, J = 8.5 Hz, 2H), 6.59-6.54 (m, 4H); MS (MALDI-TOF) m/z: $[M+H]^+$ calcd 588.99; found 590.07.

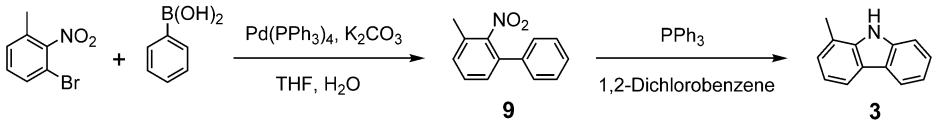

Scheme 2-2. Synthesis of 1-methyl-9*H*-carbazole (**3**).

Synthesis of 3-methyl-2-nitro-1,1'-biphenyl (9): A solution of 1-bromo-3-methyl-2-nitrobenzene (20.0 g, 92.5 mmol), phenylboronic acid (11.3 g, 92.5 mmol), and tetrakis(triphenylphosphine)palladium(0) (1.1 g, 0.95 mmol) in dry THF (200 mL) was stirred at room temperature, and then an aqueous solution of potassium carbonate (38.3 g, 277 mmol) was added to the solution. The mixture was stirred for 3 h at 60 °C. After cooling to room temperature, the reaction mixture was added into water, and then extracted with dichloromethane. The combined organic layers were washed with water, and dried over anhydrous magnesium sulfate. After filtration and evaporation, the crude product was purified by column chromatography on silica gel (hexane/dichloromethane = 5:1, v/v) to give **9** as a white solid (yield = 18.7 g, 95%). ^{1}H NMR (500 MHz, $CDCl_3$, δ): 7.48-7.38 (m, 4H), 7.37-7.35 (m, 2H), 7.32-7.27 (m, 2H), 2.39 (s, 3H); MS (MALDI-TOF) *m*/*z*: $[M]^+$ calcd 213.08; found, 213.03.

Synthesis of 1-methyl-9*H*-carbazole (3): A solution of **9** (15.0 g, 70.0 mmol) and triphenylphosphine (33.05 g, 126 mmol) in 1,2-dichlorobenzene (200 mL) was refluxed for 48 h. After cooling to room temperature, the solvent was removed under reduced pressure with heating. The crude product was purified by column chromatography on silica gel (hexane/dichloromethane = 4:1, v/v) to afford **3** as a white solid (yield = 10.8 g, 85%). ^{1}H NMR (500 MHz, $CDCl_3$, δ): 8.07 (d, J = 8.0 Hz, 1H), 7.97 (br, 1H), 7.93 (d, J = 8.0 Hz, 1H), 7.47 (d, J = 8.0 Hz, 1H), 7.41 (td, J = 7.5 Hz, 1.0 Hz, 1H), 7.25-7.21 (m, 2H), 7.16 (t, J = 7.5 Hz), 2.58 (s, 3H); MS (MALDI-TOF) *m*/*z*: $[M]^+$ calcd 181.09; found, 181.02.

Synthesis of 10-(4-bromophenyl)-9,9-dimethylacridan (4): A mixture of 9,9-dimethylacridan (11.4 g, 54.5 mmol), 1-bromo-4-iodobenzene (17.0 g, 60.0 mmol), copper iodide (0.21 g, 1.1 mmol), sodium *tert*-butoxide (10.5 g, 109 mmol), and 1,2-diaminocyclohexane (0.63 g, 5.5 mmol) in dry 1,4-dioxane (100 mL) was refluxed for 6 h. After cooling to room temperature, the reaction mixture was added into water, and then extracted with dichloromethane. The combined organic layers were dried over anhydrous magnesium

sulfate. After filtration and evaporation, the crude product was purified by column chromatography on silica gel (hexane/dichloromethane = 9:1, v/v) to give **4** as a white solid (yield = 17.6 g, 89%). ^{1}H NMR (500 MHz, $CDCl_3$, δ): 7.75 (d, J = 8.5 Hz, 2H), 7.45 (dd, J = 7.5 Hz, 2.0 Hz , 2H), 7.22 (d, J = 8.5 Hz, 2H), 6.99-6.91 (m, 4H), 6.24 (dd, J = 8.2 Hz, 1.5 Hz, 2H), 1.54 (s, 6H); MS (MALDI-TOF) m/z: $[M]^+$ calcd 363.06; found, 362.90.

Synthesis of 9,9-dimethyl-10-(4-(4,4,5,5-tetramethyl-1,3,2-dioxaborolan-2-yl)-phenyl-acridan (5): To a solution of **4** (10.0 g, 27.5 mmol) in dry THF (100 mL) was added dropwise *n*-butyllithium (2.6 M, 12.0 mL, 31.8 mmol) at −78 °C. The mixture was stirred for 1 h at that temperature. Then, 2-isopropoxy-4,4,5,5-tetramethyl-1,3,2-dioxaborolane (6.12 g, 32.9 mmol) was added dropwise to the mixture at −78 °C. The reaction mixture was further stirred for 3 h at room temperature. The resulting mixture was added into water, and then extracted with chloroform. The combined organic layers were washed with water, and dried over anhydrous magnesium sulfate. After filtration and evaporation, the crude product was purified by column chromatography on silica gel (hexane/dichloromethane = 4:1, v/v) to afford **5** as a white solid (8.10 g, 72%). ^{1}H NMR (500 MHz, $CDCl_3$, δ): 8.06 (d, J =8.0 Hz, 2H), 7.44 (dd, J = 7.5 Hz, 1.5 Hz, 2H), 7.34 (d, J = 8.5 Hz, 2H), 6.95-6.90 (m, 4H), 6.25 (dd, J = 8.0 Hz, 1.5 Hz, 2H), 1.69 (s, 6H), 1.40 (s, 12H); MS (MALDI-TOF) m/z: $[M]^+$ calcd 411.24; found, 411.18.

Synthesis of 10-(4-bromophenyl)-phenoxazine (6): Compound **6** was synthesized according to the same procedure as described above for the synthesis of **4**, except that phenoxazine (10.0 g, 54.5 mmol) was used as the reactant instead of 9,9-dimethylacridan, yielding a white solid (yield = 15.0 g, 81%). ^{1}H NMR (500 MHz, $CDCl_3$, δ): 7.72 (d, J = 9.0 Hz, 2H), 7.23 (d, J = 8.5 Hz, 2H), 6.71-6.63 (m, 4H), 6.60 (td, J = 7.5 Hz, 1.5 Hz, 2H), 5.91 (dd, J = 7.5 Hz, 1.5 Hz, 2H); MS (MALDI-TOF) m/z: $[M]^+$ calcd 337.01; found, 337.18.

Synthesis of 10-(4-(4,4,5,5-tetramethyl-1,3,2-dioxaborolan-2-yl)phenyl)-phenoxazine (7): Compound **7** was synthesized according to the same procedure as described above for the synthesis of **5**, except that **6** (9.30 g, 27.5 mmol) was used as the reactant instead of **4**, yielding a white solid (yield = 7.10 g, 67%). ^{1}H NMR (500 MHz, $CDCl_3$, δ): 8.02 (d, J = 8.0 Hz, 2H), 7.35 (d, J = 8.0 Hz, 2H), 6.68 (dd, J = 7.8 Hz, 1.4 Hz, 2H), 6.63 (t, J = 7.6 Hz, 2H), 6.56 (td, J

= 7.6 Hz, 1.5 Hz, 2H), 5.91 (d, *J* = 7.8 Hz, 2H), 1.38 (s, 12H); MS (MALDI-TOF) *m*/*z*: $[M]^+$ calcd 385.18; found, 385.08.

Synthesis of 5,6-bis(4-bromophenyl)-2,3-dicyanopyrazine (8): A mixture of 4,4'-dibromobenzil (3.00 g, 8.2 mmol), diaminomaleonitrile (0.88 g, 8.2 mmol), and hydrochloric acid (36%, 1 mL) in ethanol (60 mL) was stirred for 3h at 60 °C. After cooling to room temperature, the reaction mixture was poured into water, and then extracted with dichloromethane. The combined organic layers were washed with water, and dried over anhydrous magnesium sulfate. After filtration and evaporation, the crude product was recrystallized from dichloromethane/hexane to give **8** as a light-purple solid (3.20 g, 89%). ^{1}H NMR (500 MHz, $CDCl_3$, δ): 7.58 (d, *J* = 8.2 Hz, 4H), 7.45 (d, *J* = 8.2 Hz, 4H); MS (MALDI-TOF) *m*/*z*: $[M]^+$ calcd 437.91; found, 437.70.

Synthesis of Cz-VPN: A mixture of **2** (1.65 g, 2.8 mmol), **3** (1.05 g, 5.8 mmol), bis(tri-*tert*-butylphosphine)palladium(0) (Pd(*t*-$Bu_3P)_2$, 0.03 g, 0.06 mmol), and potassium carbonate (2.28 g, 16.5 mmol) in dry toluene (30 mL) was refluxed for 48 h. After cooling to room temperature, the reaction mixture was filtered through a Celite pad, and the filtrate was concentrated under reduced pressure. The crude product was purified by column chromatography on silica gel (hexane/dichloromethane = 4:1, v/v) to afford Cz-VPN as a white solid (yield = 1.85 g, 84%). ^{1}H NMR (500 MHz, $CDCl_3$, δ): 8.06 (t, *J* = 8.0 Hz, 2H), 7.97 (d, *J* = 7.4 Hz, 2H), 7.39-7.26 (m, 12H), 7.19-7.01 (m, 12H), 6.89 (t, *J* = 7.0 Hz, 2H), 6.73-6.61 (m, 2H), 1.70 (s, 6H); ^{13}C NMR (125 MHz, $CDCl_3$, δ): 146.54, 139.44, 138.95, 137.26, 136.02, 131.32, 129.81, 128.90, 128.86, 128.73, 128.56, 126.35, 123.99, 121.09, 120.06, 120.03, 118.16, 115.19, 109.60, 109.11, 19.92; MS (MALDI-TOF) *m*/*z*: $[M]^+$ calcd 790.31; found, 790.56. Anal. calcd for $C_{58}H_{38}N_4$: C 88.07, H 4.84, N 7.08; found: C 88.16, H 4.74, N 7.07.

Synthesis of Ac-VPN: A mixture of 4,5-dichlorophthalonitrile (0.99 g, 5.0 mmol), **5** (4.17 g, 10.1 mmol), tetrakis(triphenylphosphine)palladium(0) ($Pd(PPh_3)_4$, 0.06 g 0.05 mmol), potassium iodide (1.66 g, 10.0 mmol), and potassium phosphate (4.31 g, 20.0 mmol) in dry 1,4-dioxane (10 mL) was refluxed for 48 h. After cooling to room temperature, the reaction mixture was added into water and was extracted with dichloromethane. The combined organic layers were washed with water and dried over anhydrous magnesium sulfate. After filtration and evaporation, the crude product was purified by column chromatography on silica gel

(hexane/dichloromethane = 4:1, v/v) to give Ac-VPN as a yellow solid (yield = 1.18 g, 34%). ^{1}H NMR (500 MHz, $CDCl_3$, δ): 8.07 (s, 2H), 7.45-7.43 (m, 8H), 7.36 (d, J = 8.4 Hz, 4H), 6.87 (td, J = 7.5 Hz, 1.1 Hz, 4H), 6.79 (td, J = 7.7 Hz, 1.5 Hz, 4H) 6.20 (dd, J = 8.2 Hz, 2.2 Hz, 4H), 1.67 (s, 12H); ^{13}C NMR (125 MHz, $CDCl_3$, δ): 145.43, 142.01, 140.54, 137.35, 135.20, 131.96, 131.69, 130.39, 126.52, 125.15, 120.95, 115.18, 115.13, 113.81, 36.02, 30.80; MS (MALDI-TOF) m/z: $[M+H]^+$ calcd 695.32; found, 695.71. Anal. calcd for $C_{50}H_{38}N_4$: C 86.42, H 5.51, N 8.06; found: C 86.32, H 5.48, N 7.99.

Synthesis of Px-VPN: Px-VPN was synthesized according to the same procedure as described above for the synthesis of Ac-VPN, except that **7** (3.91 g, 10.1 mmol) was used as the reactant instead of **5**, yielding an orange solid (yield = 0.98 g, 31%). ^{1}H NMR (500 MHz, $CDCl_3$, δ): 8.01 (s, 2H), 7.39 (d, J = 8.0 Hz, 4H), 7.33 (d, J = 8.0 Hz, 4H), 6.69 (d, J = 7.8 Hz, 4H), 6.65-6.54 (m, 4H), 6.48 (t, J = 7.4 Hz, 4H), 5.82 (d, J = 7.4 Hz, 4H); ^{13}C NMR (125 MHz, $CDCl_3$, δ): 145.15, 143.92, 139.87, 137.60, 135.17, 133.77, 132.13, 131.32, 123.41, 121.76, 115.69, 115.24, 115.06, 112.93; MS (MALDI-TOF) m/z: $[M]^+$ calcd 642.21; found, 642.35. Anal. calcd for $C_{44}H_{26}N_4O_2$: C 82.23, H 4.08, N 8.72; found: C 82.23, H 3.99, N 8.77.

Synthesis of Ac-CNP: A mixture of **8** (1.01 g, 2.3 mmol), 9,9-dimethylacridan (1.05 g, 5.0 mmol), bis(tri-*tert*-butylphosphine)palladium(0) ($Pd(t\text{-}Bu_3P)_2$, 0.12 g, 0.23 mmol), and potassium carbonate (0.95 g, 6.9 mmol) in dry toluene (30 mL) was refluxed for 72 h. After cooling to room temperature, the reaction mixture was filtered through a Celite pad, and the filtrate was concentrated under reduced pressure. The crude product was purified by column chromatography on silica gel (hexane/ethyl acetate = 5:1, v/v) to afford Ac-CNP as an orange solid (yield = 0.64 g, 40%). ^{1}H NMR (500 MHz, $CDCl_3$, δ): 7.86 (d, J = 8.5 Hz, 4H), 7.47-7.43 (m, 8H), 6.97-6.90 (m, 8H), 6.35 (dd, J = 7.8 Hz, 1.5 Hz, 4H), 1.66 (s, 12H); ^{13}C NMR (125 MHz, $CDCl_3$, δ): 154.77, 144.69, 140.35, 134.21, 132.33, 131.42, 130.84, 130.16, 126.47, 125.28, 121.48, 114.64, 113.04, 36.18, 30.66; MS (MALDI-TOF) m/z: $[M]^+$ calcd 696.30; found, 696.49. Anal. calcd for $C_{48}H_{36}N_6$: C 82.73, H 5.21, N 12.06; found: C 82.21, H 5.16, N 11.85.

Synthesis of Px-CNP: Px-CNP was synthesized according to the same procedure as described above for the synthesis of Ac-CNP, except that phenoxazine (0.92 g, 5.0 mmol) was used as the reactant instead of 9,9-dimethylacridan, yielding a red solid (yield = 1.03 g, 69%). ^{1}H NMR

(500 MHz, $CDCl_3$, δ): 7.81 (d, J = 8.6 Hz, 4H), 7.45 (d, J = 8.6 Hz, 4H), 6.72 (dd, J = 8.0 Hz, 1.6 Hz, 4H), 6.68 (td, J = 7.6 Hz, 1.4 Hz, 4H), 6.57 (td, J = 7.6 Hz, 1.6 Hz, 4H), 5.96 (dd, J = 8.0 Hz, 1.4 Hz, 4H); ^{13}C NMR (125 MHz, $CDCl_3$, δ): 154.53, 144.13, 142.36, 134.79, 133.42, 132.49, 131.34, 130.30, 123.39, 122.13, 115.90, 113.23, 112.92; MS (MALDI-TOF) m/z: $[M]^+$ calcd 644.20; found, 644.43. Anal. calcd for $C_{42}H_{24}N_6O_2$: C 78.25, H 3.75, N 13.04; found: C 78.33, H 3.65, N 13.13.

2. 5. 4. Device Fabrication and Measurements

ITO-coated glass substrates were cleansed with detergent, deionized water, acetone, and isopropanol. The substrates were then subjected to UV-ozone treatment for 15 min, before loading them into a vacuum evaporation system. The organic layers were thermally evaporated on the substrates under vacuum ($< 3 \times 10^{-4}$ Pa) with an evaporation rate of < 0.3 nm s^{-1}. A cathode aluminum layer was then deposited through a shadow mask. The layer thickness and the deposition rate were monitored *in situ* during deposition by an oscillating quartz thickness monitor. The current density–voltage–luminance characteristics of the devices were measured using an E5273A semiconductor parameter analyzer (Agilent) and a 1930-C optical power meter (Newport). The EL spectra were recorded using an SD2000 multi-channel analyzer (Ocean Optics).

2. 6. Conclusion

A new series of full-color TADF emitters have been designed and synthesized by combining a phthalonitrile or dicyanopyrazine acceptor core with various donor units. The photophysical properties of these materials could be tuned by a rational combination of the donor and acceptor constituents. The TADF emissions of the doped films depend on their HOMO–LUMO energy gap, and the emission occurred at wavelengths ranging from blue (450 nm) to red (610 nm) region, spanning the entire visible region. Moreover, their small ΔE_{ST} originating from the angular-linked donor–acceptor structures induces efficient TADF characteristics. The OLEDs based on these emitters exhibited a high maximum external EL quantum efficiencies of up to 18.9% and an extremely small efficiency roll-off. We believe that these results open new avenues for designing high-performance full-color TADF emitters with simple and versatile structures for OLED applications.

References

[1] For cyanobenzene-based TADF emitters: a) H. Uoyama, K. Goushi, H. Nomura, C. Adachi, *Nature* **2012**, *492*, 234; b) T. Nishimoto, T. Yasuda, S. Y. Lee, R. Kondo, C. Adachi, *Mater. Horiz.* **2014**, *1*, 264; c) Y. J. Cho, K. S. Yook, J. Y. Lee, *Sci. Rep.* **2015**, *5*, 7859; d) Y. J. Cho, B. D. Chin, S. K. Jeon, J. Y. Lee, *Adv. Mater.* **2015**, *25*, 6786; e) Y. J. Cho, S. K. Jeon, B. D. Chin, E. Yu, J. Y. Lee, *Angew. Chem. Int. Ed.* **2015**, *54*, 5201; f) S. Wang, X. Yan, Z. Cheng, H. Zhang, Y. Liu, Y. Wang, *Angew. Chem. Int. Ed.* **2015**, *54*, 13068.

[2] For triazine-based TADF emitters: a) S. Y. Lee, T. Yasuda, H. Nomura, C. Adachi, *Appl. Phys. Lett.* **2012**, *101*, 093306; b) A. Endo, K. Sato, K. Yoshimura, T. Kai, A. Kawada, H. Miyazaki, C. Adachi, *Appl. Phys. Lett.* **2011**, *98*, 083302; c) K. Sato, K. Shizu, K. Yoshimura, A. Kawada, H. Miyazaki, C. Adachi, *Phys. Rev. Lett.* **2013**, *110*, 247401; d) H. Tanaka, K. Shizu, H. Miyazaki, C. Adachi, *Chem. Commun.* **2012**, *48*, 11392; e) S. Hirata, Y. Sakai, K. Masui, H. Tanaka, S. Y. Lee, H. Nomura, N. Nakamura, M. Yasumatsu, H. Nakanotani, Q. Zhang, K. Shizu, H. Miyazaki, C. Adachi, *Nat. Mater.* **2015**, *14*, 330; f) M. Kim, S. K. Jeon, S.-H. Hwang, J. Y. Lee, *Adv. Mater.* **2015**, *27*, 2515; g) D. Y. Lee, M. Kim, S. K. Jeon, S.-H. Hwang, C. W. Lee, J. Y. Lee, *Adv. Mater.* **2015**, *27*, 5861; h) W.-L. Tsai, M.-H. Huang, W.-K. Lee, Y.-J. Hsu, K.-C. Pan, Y.-H. Huang, H.-C. Ting, M. Sarma, Y.-Y. Ho, H.-C. Hu, C.-C. Chen, M.-T. Lee, K.-T. Wong, C.-C. Wu, *Chem. Commun.* **2015**, *51*, 13662; i) J. W. Sun, J. Y. Baek, K.-H. Kim, C.-K. Moon, J.-H. Lee, S.-K. Kwon, Y.-H. Kim, J.-J. Kim, *Chem. Mater.* **2015**, *27*, 6675.

[3] For sulfone-based TADF emitters: a) Q. Zhang, J. Li, K. Shizu, S. Huang, S. Hirata, H. Miyazaki, C. Adachi, *J. Am. Chem. Soc.* **2012**, *134*, 14706; b) Q. Zhang, B. Li, S. Huang, H. Nomura, H. Tanaka, C. Adachi, *Nat. Photon.* **2014**, *8*, 326; c) F. B. Dias, K. N. Bourdakos, V. Jankus, K. C. Moss, K. T. Kamtekar, V. Bhalla, J. Santos, M. R. Bryce, A. P. Monkman, *Adv. Mater.* **2013**, *25*, 3707; d) H. Wang, L. Xie, Q. Peng, L. Meng, Y. Wang, Y. Yi, P. Wang, *Adv. Mater.* **2014**, *26*, 5198; e) Z. Xie, C. Chen, S. Xu, J. Li, Y. Zhang, S. Liu, J. Xu, Z. Chi, *Angew. Chem. Int. Ed.* **2015**, *54*, 7181.

[4] For benzophenone-based TADF emitters: a) S. Y. Lee, T. Yasuda, Y. S. Yang, Q. Zhang, C. Adachi, *Angew. Chem. Int. Ed.* **2014**, *126*, 6520; b) S. Y. Lee, T. Yasuda, I. S. Park, C. Adachi, *Dalton Trans.* **2015**, *44*, 8356; c) Q. Zhang, D. Tsang, H. Kuwabara, Y. Hatae, B. Li, T. Takahashi, S. Y. Lee, T. Yasuda, C. Adachi, *Adv. Mater.* **2015**, *27*, 2096.

[5] For spirofluorene-based TADF emitters: a) G. Méhes, H. Nomura, Q. Zhang, T. Nakagawa, C. Adachi, *Angew. Chem. Int. Ed.* **2012**, *51*, 11311; b) K. Nasu, T. Nakagawa, H. Nomura, C.-J. Lin, C.-H. Cheng, M.-R. Tseng, T. Yasuda, C. Adachi, *Chem. Commun.* **2013**, *49*, 10385; c) H. Ohkuma, T. Nakagawa, K. Shizu, T. Yasuda, C. Adachi, *Chem. Lett.* **2014**, *43*, 1017.

[6] For arylboron-based TADF emitters: a) M. Numata, T. Yasuda, C. Adachi, *Chem. Commun.* **2015**, *51*, 9443; b) K. Suzuki, S. Kubo, K. Shizu, T. Fukushima, A. Wakamiya, Y. Murata, C. Adachi, H. Kaji, *Angew. Chem. Int. Ed.* **2015**, *54*, 15231; c) I. S. Park, M. Numata, C. Adachi, T. Yasuda, *Bull. Chem. Soc. Jpn.* **2016**, *89*, 375.

[7] a) J. W. Sun, J.-H. Lee, C.-K. Moon, K.-H. Kim, H. Shin, J.-J. Kim, *Adv. Mater.* **2014**, *26*, 5684; b) D. Y. Lee, B. S. Kim, C. W. Lee, Y. Im, K. S. Yook, S.-H. Hwang, J. Y. Lee, *ACS Appl. Mater. Interfaces* **2015**, *7*, 9625.

[8] P. A. Vecchi, A. B. Padmaperuma, H. Qiao, J. S. Sapochak, P. E. Burrows, *Org. Lett.* **2006**, *8*, 4211.

[9] S. Gong, X. He, Y. Chen, Z. Jiang, C. Zhong, D. Ma, J. Qin, C. Yang, *J. Mater. Chem.* **2012**, *22*, 2894.

[10] Px-CNP exhibited no PL emission in dissolved states, but emitted intensely in a doped solid thin film.

[11] a) J. V. Caspar, E. M. Kober, B. P. Sullivan, T. J. Meyer, *J. Am. Chem. Soc.* **1982**, *104*, 630. b) S. D. Cummings, R. Eisenberg, *J. Am. Chem. Soc.* **1996**, *118*, 1949.

[12] a) C. Murawski, K. Leo, M. C. Gather, *Adv. Mater.* **2013**, *25*, 6801; b) Y. Zhang, S. R. Forrest, *Phys. Rev. Lett.* **2012**, *108*, 267404; c) M. A. Baldo, C. Adachi, S. R. Forrest, *Phys. Rev. B* **2000**, *62*, 10967; d) K. Masui, H. Nakanotani, C. Adachi, *Org. Electron.* **2013**, *14*, 2721.

[13] a) B. E. A. Saleh, M. C. Teich, *Fundamentals of Photonics*, Wiley, New York **1991**; b) S. Nowy, B. C. Krummacher, J. Frischeisen, N. A. Reinke, W. Brütting, *J. Appl. Phys.* **2008**, *104*, 123109; c) J.-S. Kim, P. K. H. Ho, N. C. Greenham, R. H. Friend, *J. Appl. Phys.* **2000**, *88*, 1073.

[14] T. Takahashi, K. Shizu, T. Yasuda, K. Togashi, C. Adachi, *Sci. Technol. Adv. Mater.* **2014**, *15*, 034202.

[15] R. F. Doering, R. S. Miner Jr., L. Rothman, E. I. Becker, *J. Org. Chem.* **1958**, *23*, 520.

Chapter 3

Twisted Donor−Acceptor−Donor Delayed Fluorescence Materials Based on Pyrimidine for High-Performance Blue Organic Light-Emitting Diodes

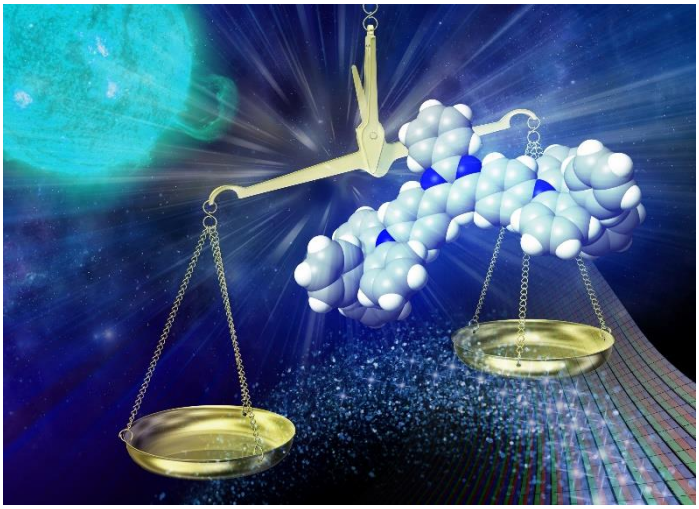

3. 1. Introduction

A variety of purely organic TADF materials, including benzonitrile,[1] triazine,[2] pyrimidine,[3] dibenzosulfone,[4] aryl ketone,[5] and aryl boron[6] derivatives, have been reported up to date. However, high-performance blue TADF materials are still very limited, and only a few of them realize η_{ext} over 20%.[2g,6a,6f]

In this chapter, novel pure blue TADF materials, 2DPAc-MPM and 2DPAc-PPM, possessing donor–acceptor–donor (D–A–D) electronic structures (**Figure 3-1a**), in which a central pyrimidine unit serves as an electron-accepting moiety and peripheral diphenylacridan (DPAc) units as electron-donating moieties linked through phenylene units, were reported. Solid-state thin films of 2DPAc-MPM and 2DPAc-PPM doped in a host matrix displayed bright blue TADF emissions with the peaks at 458 and 462 nm, respectively, and photoluminescence (PL) quantum efficiencies (Φ_{PL}) exceeding 90%. Remarkably, the 2DPAc-PPM-based blue TADF-OLED achieved an extremely high maximum η_{ext} of 20.8 %, power efficiency (η_p) of 31.5 lm W^{-1}, and current (η_c) efficiencies of 38.1 cd A^{-1}.

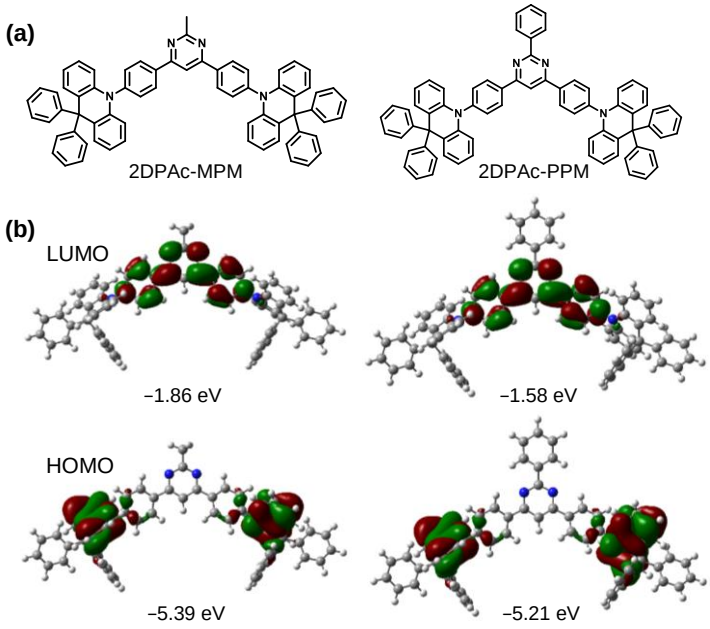

Figure 3-1. (a) Molecular structures and (b) HOMO and LUMO distributions of pyrimidine-based TADF molecules, 2DPAc-MPM and 2DPAc-PPM, calculated at the PBE1PBE 6-31G(d) level.

3. 2. Molecular Geometric and Electronic Structures

To investigate the geometric and electronic structures of the designed pyrimidine-based D−A−D type molecules, quantum-chemical calculations were performed by means of time-dependent density functional theory (TD-DFT) calculations with the PBE1PBE functional and the 6-31G(d) basis set in a gas phase. The calculations for 2DPAc-MPM and 2DPAc-PPM provide their S_1 and T_1 states as well as the ground state (S_0) geometries, and the respective energy levels. As shown **Figure 3-1b**, the HOMOs of these molecules are predominantly located on the peripheral DPAc donor units, whereas the LUMOs are distributed over the central pyrimidine acceptor core and the adjacent phenylene linkers. Large dihedral angles (82–87°) between the DPAc units and nearby phenylene linkers offer such obvious spatial separation of the frontier orbitals. This highly distorted geometric feature leads to small ΔE_{ST} values of 0.15–0.16 eV, indicating that 2DPAc-MPM and 2DPAc-PPM can function as TADF emitters, as the RISC rate constant (k_{RISC}) is expressed by the following Boltzmann relationship: $k_{RISC} \propto \exp(-\Delta E_{ST}/k_B T)$. The detail calculated results are summarized in **Table 3-1**.

Table 3-1. TD-DFT calculation results. The lowest excited singlet (S_1) and triplet (T_1) energies, oscillator strength (*f*), and transition configurations of the pyrimidine derivatives calculated by TD-DFT at the PBE1PBE/6-31G(d) level.

Compound	State	*E* (eV)	*f*	Main configuration		ΔE_{ST} (eV)
2DPAc-MPM	S_1	2.62	0.0002	H → L	0.693	0.16
	T_1	2.46	0	H−1 → L	0.557	
				H−5 → L	0.290	
				H−7 → L	−0.145	
				H−1 → L+1	−0.133	
2DPAc-PPM	S_1	2.60	0.0010	H → L	−0.694	0.15
	T_1	2.45	0	H−1 → L	0.559	
				H−3 → L	−0.235	
				H−10 → L	0.184	
				H−13 → L	−0.149	

H → L represents the HOMO to LUMO transition. Excitation configurations with the highest contributions are presented, together with the corresponding transition symmetry and nature of the involved orbitals.

3. 3. Photophysical Properties

Figure 3-2 depicts the UV−vis absorption and PL spectra of 2DPAc-MPM and 2DPAc-PPM in toluene. Both compounds showed a strong absorption originating from π-π^* transitions at around 300 nm, and a broad and weak absorption at 370 nm, which can be assigned to intramolecular charge-transfer (ICT) transitions from the peripheral DPAc donor moieties to

the central pyrimidine acceptor moiety. The ICT excited states of the 2DPAc-MPM and 2DPAc-PPM molecules lead to pure blue PL emissions with the peak at 453 and 456 nm, respectively, whose absolute Φ_{PL} values were determined to be 54% and 50% in oxygen-free toluene solutions.

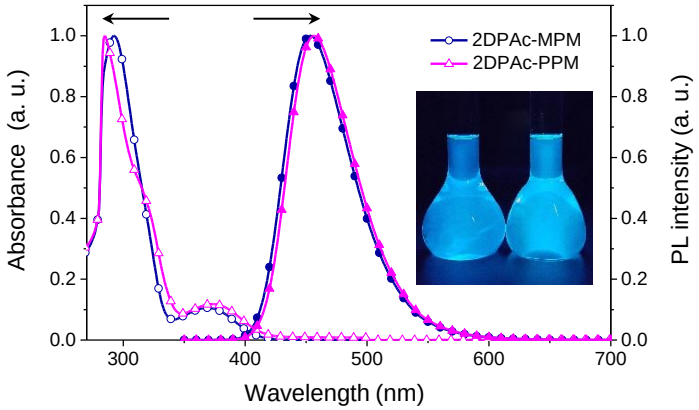

Figure 3-2. UV−vis absorption and PL spectra of 2DPAc-MPM and 2DPAc-PPM in toluene (10^{-5} M). The inset shows photographs of pure blue emissions from the 2DPAc-MPM (left) and 2DPAc-PPM (light) solutions under UV irradiation at 365 nm.

The photophysical properties of 2DPAc-MPM and 2DPAc-PPM in doped thin films were examined to understand the solid state nature of them (see **Table 3-2**). 2,8-Bis(diphenylphosphine oxide)dibenzofuran (PPF)[7] with a high T_1 energy (E_T) of 3.1 eV was employed as a host matrix of the doped films, in order to prevent the reverse energy transfer from the T_1 state of the blue emitter to that of the PPF host. As displayed in Figure 3a, the doped thin films also exhibited intense pure blue PL emissions with the peak at 458 nm for 2DPAc-MPM and 462 nm for 2DPAc-PPM, corresponding to Commission Internationale de I'Éclairage (CIE) color coordinates of (0.15, 0.14) and (0.14, 0.15), respectively. The PL emissions from these doped films are obtained solely from the emitters themselves, implying that efficient Förster energy transfer from the PPF host to the blue emitter occurs effective in the host-guest systems. The absolute Φ_{PL} values of the doped thin films are found to be exceeding 90%, which are nearly twice higher than those measured in dilute solutions (**Table 3-2**). This PL enhancement in the rigid host matrix can be ascribed to restriction of non-radiative relaxation processes caused by intramolecular torsional and vibrational motions.[8]

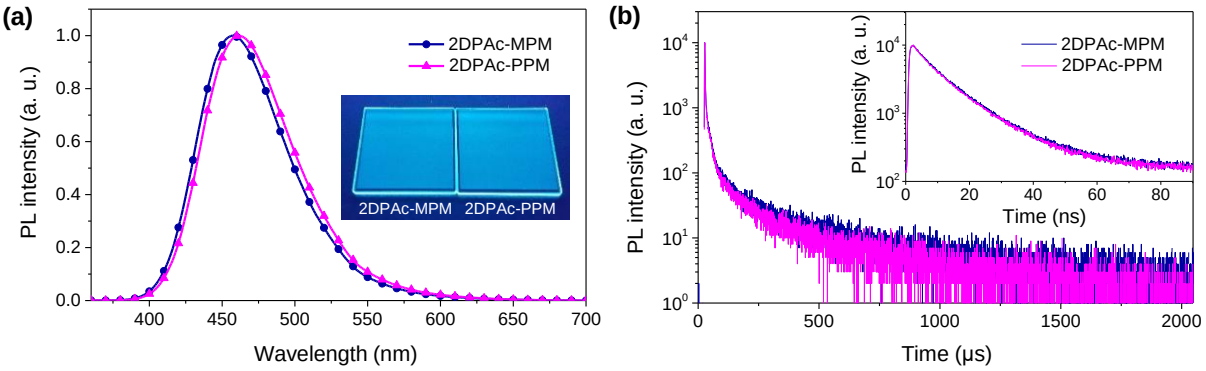

Figure 3-3. (a) Steady-state PL spectra (inset: blue TADF emissions under UV irradiation) and (b) transient PL decay curves for 18 wt%-2DPAc-MPM:PPF and 2DPAc-PPM:PPF doped films.

Table 3-2. Photophysical properties of pyrimidine-based TADF materials.

Compound	λ_{abs} [nm] sol[a]	λ_{PL} [nm] sol[a] / film[b]	Φ_{PL}[%][c] sol[a] / film[b]	τ_p [ns][d] / τ_d [μs][d]	HOMO[e] [eV]	LUMO[f] [eV]	E_S / E_T [eV][g]	ΔE_{ST} [eV][h]
2DPAc-MPM	293,370	453 / 458	54 / 92	11 / 330	−6.04	−3.04	3.09 / 2.83	0.26
2DPAc-PPM	285,373	456 / 462	50 / 94	11 / 210	−6.04	−3.07	3.01 / 2.77	0.24

[a]Measured in 10^{-5} M toluene solution at room temperature. [b]18 wt%-doped thin film in a PPF host matrix. [c]Absolute PL quantum yield evaluated using an integrating sphere under a nitrogen atmosphere. [d]PL lifetimes of prompt (τ_p) and delayed (τ_d) decay components for the 18 wt%-doped films measured at room temperature. [e]Determined by photoelectron yield spectroscopy in neat films. [f]Deduced from the HOMO and optical energy gap (E_g). [g]Singlet (E_S) and triplet (E_T) energies estimated from onset wavelengths of the emission spectra at 300 and 5 K in the doped thin films, respectively. [h]$\Delta E_{ST} = E_S - E_T$. [i]Calculated by TD-DFT at PBE1PBE/6-31G(d).

Next, the experiment was focused on transient PL decay characteristics of the doped thin films to further verify TADF properties of 2DPAc-MPM and 2DPAc-PPM. As can be seen from **Figure 3-3b**, these doped films clearly indicate a nanosecond-scale prompt decay component and a microsecond-scale delayed decay component at room temperature in the time range of 2000 μs, which can be fitted by a biexponential model. Both materials give the same prompt emission lifetime (τ_p) of 11 ns, whereas the delayed emission lifetime (τ_d) of 2DPAc-PPM (210 μs) is slightly shorter than that of 2DPAc-MPM (330 μs) (**Table 3-2**). As shown in **Figures 3-4a,b**, the delayed PL emissions (red curves) from the doped films of 2DPAc-MPM and 2DPAc-PPM exhibit similar spectral distributions with their prompt PL emissions (black curves), indicating that the delayed PL emission should originate from the emissive S_1 state as a result of efficient up-conversion from T_1 to S_1 states. Temperature dependence of transient PL characteristics of the doped films were also analyzed in the temperature range of 5–300 K (**Figures 3-4c**,**d**). The PL intensity for the delayed component gradually increased with

increasing temperature from 5 to 300 K through the efficient RISC process by thermal activation, which is direct evidence of TADF. The experimental ΔE_{ST} values of 2DPAc-MPM and 2DPAc-PPM were estimated to be 0.26 and 0.24 eV, respectively, from the highest-energy onset positions of the room-temperature fluorescence (time range: 0–100 ns) and low-temperature (5 K) phosphorescence (time range: 100–10000 μs) spectra of the doped films (**Figure 3-5**). Detail photophysical parameters of 2DPAc-MPM and 2DPAc-PPM as pure blue TADF emitters are listed in **Table 3-2.**

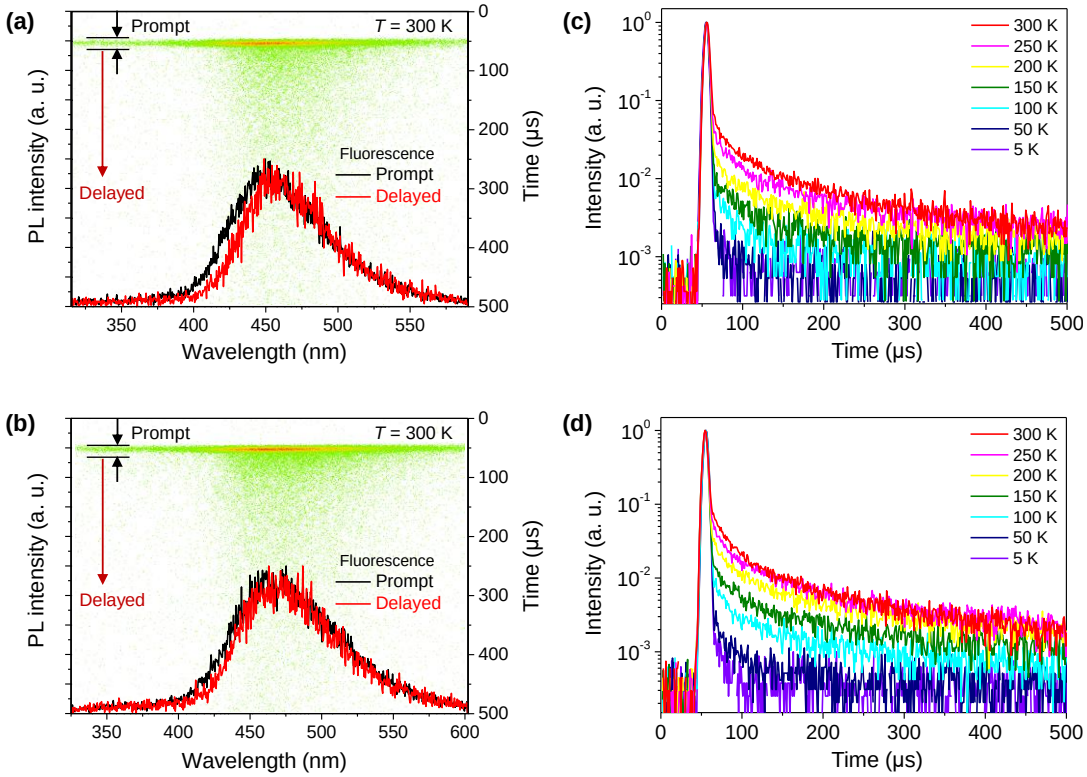

Figure 3-4. (a,b) Streak images and prompt and delayed PL spectra taken at 300 K, in which green dots represent PL photon counts, and (c,d) temperature dependence of transient PL decay in the range of 5–300 K under vacuum for 6 wt%-2DPAc-MPM:PPF (top panels) and 2DPAc-PPM:PPF doped films (bottom panels).

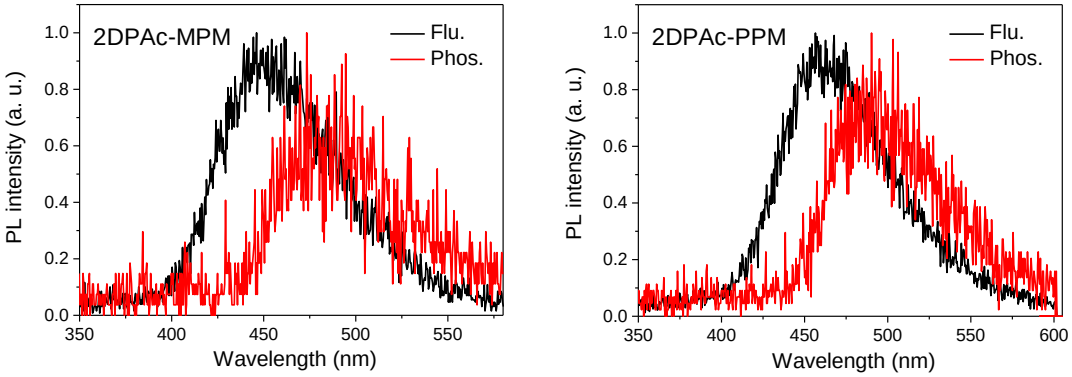

Figure 3-5. PL spectra of prompt fluorescence in the range of 1–100 ns at 300 K (black) and phosphorescence at 5 K in the range of 100–10000 μs (red) for 2DPAc-MPM:PPF (left) and 2DPAc-PPM:PPF (right) doped thin films. The lowest excited singlet (S_1) and triplet energy (T_1) levels of the TADF emitters were determined from the high energy onsets of the fluorescence and phosphorescence spectra, respectively.

Table 3-3. Rate constants and quantum efficiencies of the pyrimidine derivatives in doped thin films.[a)]

Compound	k_r^S [s^{-1}]	k_{ISC} [s^{-1}]	k_{RISC} [s^{-1}]	Φ_p [%]	Φ_d [%]	Φ_{ISC} [%]	Φ_{RISC} [%]
2DPAc-MPM	4.4×10^6	1.6×10^7	8.7×10^3	22	70	78	90
2DPAc-PPM	1.8×10^6	1.1×10^7	2.5×10^4	14	80	86	93

[a)]Abbreviations: k_r^S, radiative rate constant ($S_1 \rightarrow S_0$); k_{ISC}, intersystem-crossing (ISC) rate constant ($S_1 \rightarrow T_1$); k_{RISC}, reverse ISC rate constant ($T_1 \rightarrow S_1$); Φ_p, quantum efficiency for prompt fluorescence component; Φ_d, quantum efficiency for delayed fluorescence component; Φ_{ISC}, ISC quantum efficiency; Φ_{RISC}, RISC quantum efficiency.

3. 4. Electroluminescence Performance

To verify potentials of the pyrimidine-based TADF materials as blue emitters, we fabricated TADF-OLEDs with the following device configuration (**Figure 3-6a**): ITO (100 nm)/HAT-CN (10 nm)/α-NPD (40 nm)/CCP (5 nm)/18 wt%-emitter:PPF (20 nm)/PPF (10 nm)/TPBi (30 nm)/Liq (1 nm)/Al (100 nm). In these devices, HAT-CN (2,3,6,7,10,11-hexacyano-1,4,5,8,9,12-hexaazatriphenylene) and α-NPD (4,4'-bis[*N*-(1-naphthyl)-*N*-phenylamino]-1,1'-biphenyl) serve as a hole-injection layer and hole-transporting layer, whereas TPBi (1,3,5-tris(*N*-phenylbenzimidazol-2-yl)benzene) and Liq (8-hydroxyquinoline lithium) are used as an electron-transporting layer and electron-injection material, respectively. In addition, thin layers of CCP (9-phenyl-9*H*-3,9'-bicarbazole) and PPF with high T_1 energies were inserted to suppress the triplet exciton quenching at the neighboring interfaces and to confine the excitons within the emitting layer.

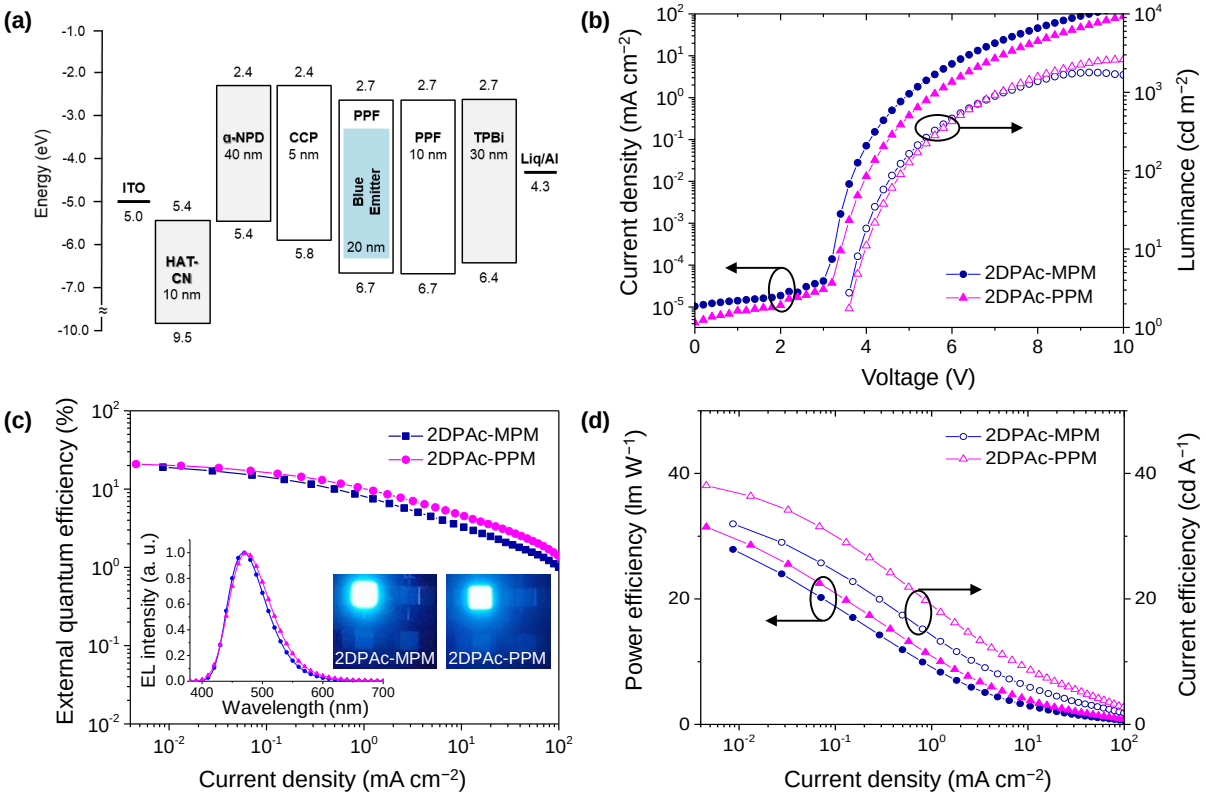

Figure 3-6. (a) Energy-level diagram for TADF-OLEDs based on 2DPAc-MPM and 2DPAc-PPM as blue emitters (b) Current density–voltage–luminance (*J*–*V*–*L*) plots, (c) external EL quantum efficiency (η_{ext}) versus current density plots (inset: EL spectra measured at 10 mA cm^{-2} (left) and photographs displaying blue EL emissions (right)), and (d) power efficiency (η_p) and current efficiency (η_c) plots for the blue TADF-OLEDs

Figure 3-6b shows the current density–voltage–luminance (*J*–*V*–*L*) plots of the fabricated TADF-OLEDs. Both devices exhibited the same low turn-on voltages (V_{on}) of 3.6 V and similar *J*–*V*–*L* characteristics. Bright blue EL emissions with a peak (λ_{EL}) at 468 and 472 nm and CIE color coordinates of (0.16, 0.21) and (0.16, 0.24) were obtained for the 2DPAc-MPM and 2DPAc-PPM-based devices, respectively (**Figure 3-6c** and **Table 3-4**). It should be noted that both devices exhibited high maximum η_{ext} of 19.0% for 2DPAc-MPM and 20.8% for 2DPAc-PPM at low current density without any light out-coupling enhancements. These excellent EL performances can be attributed to their high Φ_{PL} values of 92–94% and RISC efficiencies (Φ_{RISC}) of 90–93%. (see **Tables 3-2** and **3-3**). However, the η_{ext} of these devices decreased with increasing current densities. This severe efficiency roll-off behavior should originate from the relatively long exciton lifetimes of 2DPAc-MPM (330 μs) and 2DPAc-PPM (210 μs) in doped films, because the long-lived T_1 excitons undergo exciton quenching such as triplet-triplet annihilation and/or triplet-polaron annihilation.[9] In spite of such efficiency roll-

off behavior, the η_{ext} values were still rather high, even at a high luminance of 100 cd m^{-2} (**Table 3-4**). Moreover, the 2DPAc-PPM-based device demonstrated extremely high maximum η_p and η_c of 31.5 lm W^{-1} and 38.1 cd A^{-1}, respectively. To the best of our knowledge, these η_p and η_c values are the highest among the blue TADF-OLEDs ever reported.[8d,9c,9g,11a–11c,12a,12g,13a–13b,13f]

As mentioned in the General Introduction, T_1 excitons are directly generated by carrier recombination under electrical excitation and then up-converted into the emissive S_1 state through the efficient RISC process. Consequently, the theoretical maxima of η_{int} and η_{ext} for TADF-OLEDs can be estimated by the equations **1-18** and **1-19**. the light out-coupling efficiency is considered to be approximately 20% because of the difference in refractive index (n) of the organic layers and ITO (n = 1.7–1.8), the glass substrate and air (n = 1.5).[10] Thus, by assuming $\eta_{out} \approx 20\%$ in this experiment, theoretical maxima of η_{ext} for the 2DPAc-MPM and 2DPAc-PPM-based OLEDs are estimated to be 18% and 19%, respectively. These theoretical values are reasonably consistent with the experimentally obtained η_{ext} values (19.0% and 20.8%, respectively), suggesting that the appropriate recombination balance of holes and electrons within the emitting layer results in the high EL efficiencies.

Table 3-4. Electroluminescence Performances of blue TADF-OLEDs.[a)]

Emitter	λ_{EL} [nm]	V_{on} [V]	η_{ext} [%] Max / @10 cd m^{-2} / @100 cd m^{-2}	η_c [cd A^{-1}] Max / @10 cd m^{-2} / @100 cd m^{-2}	η_p [lm W^{-1}] Max / @10 cd m^{-2} / @100 cd m^{-2}	CIE (x, y)
2DPAc-MPM	468	3.6	19.0 / 16.5 / 9.4	32.0 / 28.2 / 16.5	27.9 / 23.0 / 11.1	(0.16, 0.21)
2DPAc-PPM	472	3.6	20.8 / 18.9 / 12.4	38.1 / 34.4 / 23.5	31.5 / 26.0 / 14.6	(0.16, 0.24)

[a)]Abbreviations: λ_{EL}, EL emission maximum; V_{on}, turn-on voltage at 1 cd m^{-2}; η_{ext}, external EL quantum efficiency; η_c, current efficiency; η_p, power efficiency; CIE, Commission Internationale de l'Éclairage color coordinates measured at 10 mA cm^{-2}.

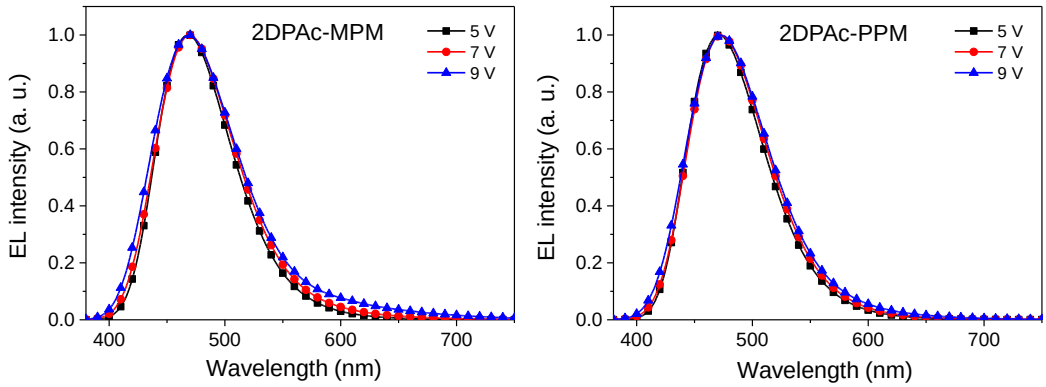

Figure 3-7. Normalized EL spectra of TADF-OLEDs based on 2DPAc-MPM (left) and 2DPAc-PPM (right) measured at different voltages.

3. 5. Experimental Section

3. 5. 1. General Methods

Density functional theory (DFT) calculations for the pyrimidine-based molecules were performed using the Gaussian 09 program package. Geometries in the ground state were optimized using the PBE1PBE functional with the 6-31G(d) basis set. The lowest singlet and triplet excited states were computed using the optimized structures with time-dependent DFT (TD-DFT) at the same level. NMR spectra were recorded on Bruker Avance III 400 and 500 spectrometers. Chemical shifts of ^{1}H and ^{13}C NMR signals were quoted to tetramethylsilane (δ = 0.00), $CDCl_3$ (δ = 77.0), and DMSO-d_6 (δ = 39.5) as internal standards, respectively. Matrix-assisted laser desorption ionization time-of-flight (MALDI-TOF) mass spectra were collected on a Bruker Daltonics Autoflex III spectrometer using dithranol as the matrix. Elemental analyses were carried out with a Yanaco MT-5 CHN corder. Density functional theory (DFT) calculations for the pyrimidine-based molecules were performed using the Gaussian 09 program package. Geometries in the ground state were optimized using the PBE1PBE functional with the 6-31G(d) basis set. The lowest singlet and triplet excited states were computed using the optimized structures with time-dependent DFT (TD-DFT) at the same level. Organic thin films for photophysical measurements were prepared by vacuum deposition under high vacuum (~ 7×10^{-5} Pa) onto a quartz glass or Si(100) substrate. UV−vis absorption and photoluminescence (PL) spectra were measured with a Jasco V-670 spectrometer and a Jasco FP-8600 spectrophotometer, respectively, using degassed spectral grade solvents. The absolute PL quantum yields (Φ_{PL}) were measured using a Jasco ILF-835 integrating sphere system. The transient PL characteristics of the doped thin films were performed using a Quantaurus-Tau C11367-01 (λ_{ex} = 340 nm, pulse width = 100 ps, and repetition rate = 20 Hz) under N_2 atmosphere, and a Hamamatsu Photonics C9300 streak camera with an N_2 gas laser (λ_{ex} = 337 nm, pulse width = 500 ps, and repetition rate = 20 Hz) under vacuum (< 4×10^{-1} Pa). The HOMO energy levels of the materials in thin films were determined using a Riken-Keiki AC-2 ultraviolet photoelectron spectrometer. The LUMO energy levels were estimated by subtracting the optical energy gap (E_g) from the measured HOMO energies; E_g values were determined from the high energy onset position of the PL spectra of the thin films.

3. 5. 2. Preparation of Materials

All regents and solvents were purchased from Sigma-Aldrich, Tokyo Chemical Industry (TCI), or Wako Pure Chemical Industries, and used as received unless otherwise noted. Methyl-

2-(phenylamino)benzoate,[11] 9-phenyl-9*H*-3,9'-bicarbazole (CCP),[6a] and 2,8-bis(diphenylphosphine oxide)dibenzofuran (PPF)[7] were prepared according to the literature procedure, and were further purified by temperature-gradient vacuum sublimation twice. 1,4,5,8,9,11-Hexaazatriphenylene-hexacarbonitrile (HAT-CN) was donated from Nippon Soda Corporation, and was then purified by vacuum sublimation before use. Other OLED materials were purchased from E-Ray Optoelectronics Technology corporation, and used for the device fabrication without further purification. The detailed synthetic procedures and characterization data for compounds **1–3** are described in **Schemes 3-1** and **3-2**.

3. 5. 3. Synthesis

The synthetic routes for 2DPAc-MPM and 2DPAc-PPM are outlined in **Scheme 3-2**. The boronic ester **3** was prepared from **1** through the Ullmann coupling reaction, followed by borylation. The final compounds were synthesized by Suzuki-Miyaura cross-coupling reactions of **3** with 4,6-dichloro-2-methylpyrimidine for 2DPAc-MPM or fenclorim for 2DPAc-PPM in the presence of $Pd(PPh_3)_4$ and K_2CO_3. These final products were purified by temperature-gradient vacuum sublimation. Chemical structures of these compounds were characterized by ^1H and ^{13}C nuclear magnetic resonance (NMR) spectroscopy, matrix-assisted laser desorption ionization time-of-flight (MALDI-TOF) mass spectrometry, and elemental analysis.

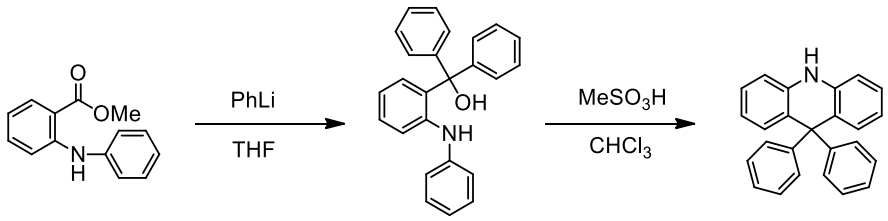

4 **1**

Scheme 3-1. Synthesis of 9,9-diphenyl-9,10-dihydroacridine (**1**).

Synthesis of 9,9-diphenyl-9,10-dihydroacridine (1): To a solution of methyl-2-(phenylamino)benzoate[11] (18.0 g, 79.2 mmol) in dry THF (300 mL) was added dropwise phenyllithium (1.6 M, 148.5 mL, 237.6 mmol) at −78 °C under a nitrogen atmosphere. The mixture was stirred for 1 h at −78 °C, and then further reacted for 2 h at 0 °C. After heating up to room temperature, the mixture was reacted for 4 h at room temperature, and then quenched by addition of a large amount of water. The product was extracted with chloroform and dried

over anhydrous Na_2SO_4. After filtration and evaporation, the crude product was used in the next reaction without further purification.

To a solution of **4** in chloroform (300 mL) was added methanesulfonic acid (8.4 g, 87.1 mmol) at room temperature. The mixture was refluxed for 1 h under air, and then further reacted for 12 h at room temperature. The reaction mixture was concentrated under reduced pressure. Then, the residue was purified by column chromatography on silica gel (hexane/chloroform = 3:1, v/v) to give **1** as a white solid (yield = 18.5 g, 70%). ^{1}H NMR (500 MHz, $CDCl_3$): δ 7.26-7.19 (m, 4H), 7.17-7.16 (m, 4H), 6.96-6.94 (m, 4H), 6.90-6.87 (m, 2H), 6.83 (dd, *J* = 7.8 Hz, 1.5 Hz, 2H), 6.80 (dd, *J* = 7.9 Hz, 1.1 Hz, 2H), 6.28 (s, 1H); MS (MALDI-TOF) *m*/*z* $[M]^+$ calcd 333.15; found, 333.97.

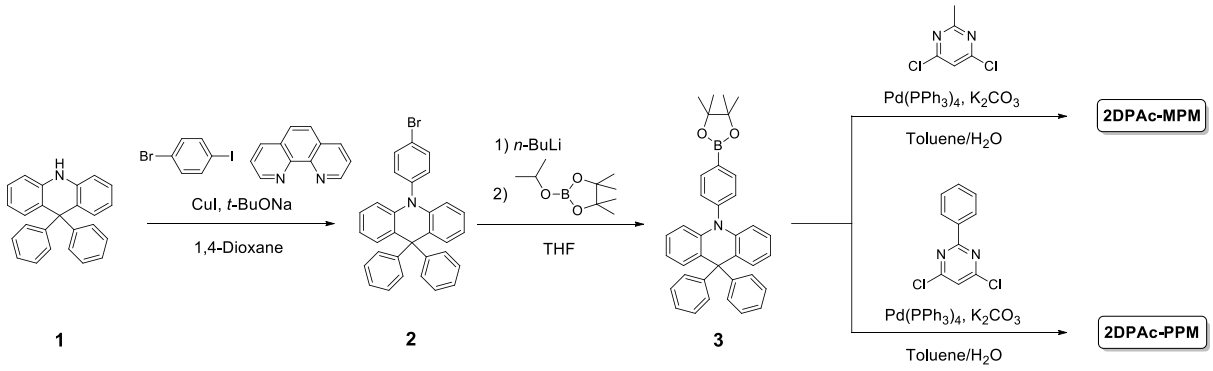

Scheme 3-2. Synthetic routes for 2DPAc-MPM and 2DPAc-PPM.

Synthesis of 10-(4-bromophenyl)-9,9-diphenyl-9,10-dihydroacridine (2): A solution of **1** (15.0 g, 44.9 mmol) in 1,4-dioxane (150 mL) was added slowly sodium *tert*-butoxide (8.6 g, 89.8 mmol) at room temperature under a nitrogen atmosphere. After stirred for 30 min, copper (I) iodide (0.85 g, 4.5 mmol), 1,10-phenanthroline (0.81 g, 4.5 mmol), and 4-bromoiodobenzene (15.2 g, 53.9 mmol) were added to the reaction mixture. The mixture was refluxed for 12 h. After cooling to room temperature, water (150 mL) was added to the reaction mixture. After filtered through a Celite pad, the product was extracted with chloroform and dried over anhydrous Na_2SO_4. After filtration and evaporation, the product was purified by column chromatography on silica gel (hexane/chloroform = 10:1, v/v) to give **2** as a white solid (yield = 18.6 g, 85%). ^{1}H NMR (400 MHz, DMSO-d_6, δ): 7.84-7.80 (m, 2H), 7.34-7.30 (m, 6H), 7.12-7.08 (m, 2H), 7.04-7.01 (m, 2H), 6.94-6.88 (m, 6H), 6.77 (dd, *J* = 8.0 Hz, 1.6 Hz, 2H), 6.34 (dd, *J* = 8.3 Hz, 1.0 Hz, 2H); MS (MALDI-TOF) *m*/*z*: $[M+H]^+$ calcd 487.09; found, 487.18.

Synthesis of 9,9-diphenyl-10-(4-(4,4,5,5-tetramethyl-1,3,2-dioxaborolan-2-yl)phenyl)-9,10-dihydroacridine (3): To a solution of **2** (5.0 g, 10.2 mmol) in dry THF (400 mL) was added dropwise *n*-butyllithium (2.6 M, 4.7 mL, 12.3 mmol) at −78 °C under a nitrogen atmosphere. The mixture was stirred for 1 h at that temperature. Then, 2-isopropoxy-4,4,5,5-tetramethyl-1,3,2-dioxaborolane (2.3 g, 12.3 mmol) was added dropwise to the mixture at −78 °C. The reaction mixture was further stirred for 3 h at room temperature. The resulting mixture was added into water, and then extracted with chloroform. The combined organic layers were washed with water, and dried over anhydrous Na_2SO_4. After filtration and evaporation, the crude product was purified by column chromatography on silica gel (hexane/ethyl acetate = 10:1, v/v) to afford **3** as a white solid (yield = 4.0 g, 73%). ^{1}H NMR (400 MHz, DMSO-d_6, δ): 7.92 (d, J = 8.0 Hz, 2H), 7.35-7.25 (m, 6H), 7.11-7.04 (m, 4H), 6.92-6.88 (m, 6H), 6.77 (dd, J = 7.6 Hz, 1.6 Hz, 2H), 6.29 (dd, J = 6.8 Hz, 0.8 Hz, 2H), 1.33 (s, 12H); MS (MALDI-TOF) m/z: $[M]^+$ calcd 535.27; found, 535.88.

Synthesis of 2DPAc-MPM: A mixture of **3** (2.00 g, 3.74 mmol), 4,6-dichloro-2-methylpyrimidine (0.24 g, 1.47 mmol), and $Pd(PPh_3)_4$ (0.13 g, 0.11 mmol) in dry toluene (80 mL) was stirred under a nitrogen atmosphere. An aqueous solution (30 mL) of potassium carbonate (1.55 g, 11.22 mmol) was added to the mixture, and then the mixture was refluxed for 48 h. After cooling to room temperature, the reaction mixture was filtered through a Celite pad. After extracting with chloroform and drying over anhydrous sodium sulfate, the solvent was removed under reduced pressure. The crude product was purified by column chromatography on silica gel (hexane/ethyl acetate/chloroform = 10:1:3, v/v/v) to afford 2DPAc-MPM as a light-yellow solid (yield = 1.94 g, 57%). This compound was further purified by temperature-gradient sublimation under vacuum. ^{1}H NMR (400 MHz, DMSO-d_6, δ): 8.60 (d, J = 8.0 Hz, 5H), 7.37-7.25 (m, 16H), 7.12 (t, J = 7.2 Hz, 4H), 6.95-6.92 (m, 12H), 6.80 (d, J = 6.8 Hz, 4H), 6.44 (d, J = 8.4 Hz, 4H), 2.81 (s, 3H); ^{13}C NMR (125 MHz, $CDCl_3$, δ): 168.95, 164.33, 146.38, 143.31, 141.94, 137.26, 131.95, 130.39, 130.14, 129.71, 129.52, 127.65, 126.88, 126.30, 120.40, 114.08, 110.35, 56.76, 26.54; MS (MALDI-TOF) m/z: $[M+H]^+$ calcd 909.40; found, 909.65. Anal. calcd for $C_{67}H_{48}N_4$: C 88.52, H 5.32, N 6.16; found: C 88.35, H 5.12, N 6.16.

Synthesis of 2DPAc-PPM: This compound was synthesized according to the same procedure as described above for the synthesis of 2DPAc-MPM, except that fenclorim (0.34 g, 1.5 mmol)

was used as the reactant instead of 4,6-dichloro-2-methylpyrimidine. 2DPAc-PPM was obtained as a light-yellow solid (yield = 2.36 g, 65%), and was further purified by temperature-gradient sublimation under vacuum. ^{1}H NMR (400 MHz, DMSO-d_6, δ): 8.77 (d, J = 8.4 Hz, 4H), 8.74-8.71 (m, 3H), 7.64-7.61 (m, 3H), 7.38-7.28 (m, 16H), 7.13 (t, J = 8.0 Hz, 4H), 6.96-6.93 (m, 12H), 6.81 (d, J = 8.0 Hz, 4H), 6.48 (d, J = 8.4 Hz, 4H); ^{13}C NMR (125 MHz, $CDCl_3$, δ): 164.22, 146.38, 143.42, 141.96, 137.81, 137.25, 131.90, 130.95, 130.41, 130.13, 129.79, 129.53, 128.58, 128.50, 127.67, 126.93, 126.32, 120.42, 114.10, 110.54, 56.79, 30.94; MS (MALDI-TOF) m/z: $[M+H]^+$ calcd 971.41; found, 971.51. Anal. calcd for $C_{72}H_{50}N_4$: C 89.04, H 5.19, N 5.77; found: C 89.13, H 5.09, N 5.84.

3. 5. 4. OLED Fabrication and Measurements

Indium tin oxide (ITO)-coated glass substrates were cleaned with detergent, deionized water, acetone, and isopropanol, and then subjected to UV-ozone treatment for 30 min, before loading into a vacuum evaporation system. The organic layers and a cathode aluminum layer were thermally evaporated through shadow masks under vacuum (< 6×10^{-5} Pa) with an evaporation rate of < 0.3 nm s^{-1}. The layer thickness and deposition rate were monitored in situ during deposition by an oscillating quartz thickness monitor. OLED properties were measured using a Keithley 2400 source meter and a Konica Minolita CS-2000 spectroradiometer.

3. 6. Conclusion

Highly efficient pure blue TADF materials, 2DPAc-MPM and 2DPAc-PPM, comprising of a pyrimidine acceptor core and diphenylacridan donor moieties linked through phenylene units, have been developed. These donor-acceptor-donor intramolecular charge-transfer systems lead to high Φ_{RISC} of 90–93%, together with high Φ_{PL} of 92–94%. OLEDs employing 2DPAc-MPM and 2DPAc-PPM as blue TADF emitters have achieved extremely high maximum η_{ext} of up to 20.8%. Also, high η_p of 31.5 lm W^{-1} and η_c of 38.1 cd A^{-1} were attained. These results provide a promising strategy for designing efficient pure blue TADF luminophores for the next-generation optoelectronic applications.

References

[1] a) H. Uoyama, K. Goushi, K. Shizu, H. Nomura, C. Adachi, *Nature* **2012**, *492*, 234; b) T. Nishimoto, T. Yasuda, S. Y. Lee, R. Kondo, C. Adachi, *Mater. Horiz.* **2014**, *1*, 264; c) Y. J. Cho, S. K. Jeon, B. D. Chin, E. Yu, J. Y. Lee, *Angew. Chem. Int. Ed.* **2015**, *54*, 5201; d) S. Wang, X. Yan, Z. Cheng, H. Zhang, Y. Liu, Y. Wang, *Angew. Chem. Int. Ed.* **2015**, *54*, 13068; e) I. S. Park, S. Y. Lee, C. Adachi, T. Yasuda, *Adv. Funct. Mater.* **2016**, 26, 1813.

[2] a) S. Y. Lee, T. Yasuda, H. Nomura, C. Adachi, *Appl. Phys. Lett.* **2012**, *101*, 093306; b) H. Tanaka, K. Shizu, H. Miyazaki, C. Adachi, *Chem. Commun.* **2012**, *48*, 11392; c) S. Hirata, Y. Sakai, K. Masui, H. Tanaka, S. Y. Lee, H. Nomura, N. Nakamura, M. Yasumatsu, H. Nakanotani, Q. Zhang, K. Shizu, H. Miyazaki, C. Adachi, *Nat. Mater.* **2015**, *14*, 330; d) H. Kaji, H. Suzuki, T. Fukushima, K. Shizu, K. Suzuki, S. Kubo, T. Komino, H. Oiwa, F. Suzuki, A. Wakamiya, Y. Murata, C. Adachi, *Nat. Commun.* **2015**, *6*, 8476; e) M. Kim, S. K. Jeon, S.-H. Hwang, J. Y. Lee, *Adv. Mater.* **2015**, *27*, 2515; f) W. -L. Tsai, M.-H. Huang, W.-K. Lee, Y.-J. Hsu, K.-C. Pan, Y.-H. Huang, H.-C. Ting, M. Sarma, Y.-Y. Ho, H.-C. Hu, C.-C. Chen, M.-T. Lee, K.-T. Wong, C.-C. Wu, *Chem. Commun.* **2015**, *51*, 13662; g) J. W. Sun, J. Y. Baek, K.-H. Kim, C.-K. Moon, J.-H. Lee, S.-K. Kwon, Y.-H. Kim, J.-J. Kim, *Chem. Mater.* **2015**, *27*, 6675.

[3] R. Komatsu, H. Sasabe, Y. Seino, K. Nakao, J. Kido, *J. Mater. Chem. C* **2016**, 4, 2274.

[4] a) Q. Zhang, J. Li, K. Shizu, S. Huang, S. Hirata, H. Miyazaki, C. Adachi, *J. Am. Chem. Soc.* **2012**, *134*, 14706–14709; b) S. Wu, M. Aonuma, Q. Zhang, S. Huang, T. Nakagawa, K. Kuwabara, C. Adachi, *J. Mater. Chem. C* **2014**, *2*, 421; c) Q. Zhang, B. Li, S. Huang, H. Nomura, H. Tanaka, C. Adachi, *Nat. Photon.* **2014**, *8*, 326; d) F. B. Dias, K. N. Bourdakos, V. Jankus, K. C. Moss, K. T. Kamtekar, V. Bhalla, J. Santos, M. R. Bryce, A. P. Monkman, *Adv. Mater.* **2013**, *25*, 3707; e) H. Wang, L. Xie, Q. Peng, L. Meng, Y. Wang, Y. Yi, P. Wang, *Adv. Mater.* **2014**, *26*, 5198.

[5] a) S. Y. Lee, T. Yasuda, Y. S. Yang, Q. Zhang, C. Adachi, *Angew. Chem. Int. Ed.* **2014**, *53*, 6520; b) S. Y. Lee, T. Yasuda, I. S. Park, C. Adachi, *Dalton Trans.* **2015**, *44*, 8356; c) Q. Zhang, D. Tsang, H. Kuwabara, Y. Hatae, B. Li, T. Takahashi, S. Y. Lee, T. Yasuda, C. Adachi, *Adv. Mater.* **2015**, *27*, 2096; d) K. Nasu, T. Nakagawa, H. Nomura, C.-J. Lin, C.-H. Cheng, M.-R. Tseng, T. Yasuda, C. Adachi, *Chem. Commun.* **2013**, *49*, 10385; e) Q. Zhang, H. Kuwabara, W. J. Potscavage, Jr, S. Huang, Y. Hatae, T. Shibata, C. Adachi, *J. Am. Chem. Soc.* **2014**, *136*, 18070; f) P. Rajamalli, N. Senthilkumar, P.

Gandeepan, P.-Y. Huang, M.-J. Huang, C.-Z. Ren-Wu, C.-Y. Yang, M.-J. Chiu, L.-K. Chu, H.-W. Lin, C.-H. Cheng, *J. Am. Chem. Soc.* **2016**, *138*, 628; g) W. Liu, C. J. Zheng, K. Wang, Z. Chen, D. Y. Chen, F. Li, X.-M. Ou, Y. P. Dong, X.-H. Zhang, *ACS Appl. Mater. Interfaces* **2015**, *7*, 18930.

[6] a) M. Numata, T. Yasuda, C. Adachi, *Chem. Commun.* **2015**, *51*, 9443; b) I. S. Park, M. Numata, C. Adachi, T. Yasuda, *Bull. Chem. Soc. Jpn.* **2016**, 89, 375; c) K. Suzuki, S. Kubo, K. Shizu, T. Fukushima, A. Wakamiya, Y. Murata, C. Adachi, H. Kaji, *Angew. Chem. Int. Ed.* **2015**, *54*, 15231; d) H. Hirai, K. Nakajima, S. Nakatsuka, K. Shiren, J. Ni, S. Nomura, T. Ikuta, T. Hatakeyama, *Angew. Chem. Int. Ed.* **2015**, *54*, 13581; e) Y. Kitamoto, T. Namikawa, D. Ikemizu, Y. Miyata, T. Suzuki, H. Kita, T. Sato, S. Oi, *J. Mater. Chem. C* **2015**, *3*, 9122; f) T. Hatakeyama, K. Shiren, K. Nakajima, S. Nomura, S. Nakatsuka, K. Kinoshita, J. Ni, Y. Ono, T. Ikuta. *Adv. Mater.* **2016**, *26*, 2777.

[7] P. A. Vecchi, A. B. Padmaperuma, H. Qiao, L. S. Sapochak, P. E. Burrows, *Org. Lett.* **2006**, *8*, 4211.

[8] Y. Hong, J. W. Y. Lam, B. Z. Tang, *Chem. Commun.* **2009**, 4332.

[9] a) C. Murawski, K. Leo, M. C. Gather, *Adv. Mater.* **2013**, *25*, 6801; b) M. A. Baldo, C. Adachi, S. R. Forrest, *Phys. Rev. B* **2000**, *62*, 10967.

[10] J.-S. Kim, P. K. H. Ho, N. C. Greenham, R. H. Friend, *J. Appl. Phys.*, **2000**, *88*, 1073.

[11] T. Takahashi, K. Shizu, T. Yasuda, K. Togashi, C. Adachi, *Adv. Mater.* **2014**, *15*, 034202.

Chapter 4

Twisted Donor−Acceptor Delayed Fluorescence Materials Based on Pyrimidine for Highly Efficient Blue Electroluminescence

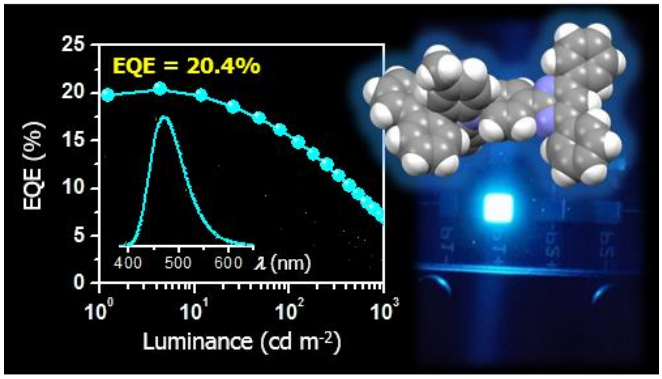

4. 1. Introduction

To produce full-color displays and white lighting devices based on OLED technologies, the three primary RGB (red, green, and blue) colors are indispensable. Up to date, red and green phosphorescent emitters based on organometallic iridium or platinum complexes primarily match the requirements of application in terms of efficiency, stability, and color purity.[1] However, the overall device performance of blue (especially deep-blue) OLEDs, based on phosphorescent emitters[2] or conventional fluorescent emitters,[3] still lags behind its red and green counterparts. Hence, further improvement in electroluminescence (EL) efficiency, operational stability, and color index should be required. Driven by such technological demands, it is vital to develop highly efficient deep-blue emitters with Commission Internationale de l'Éclairage chromaticity coordinate ($CIE_{x,y}$) values below 0.15, matching closely with the National Television System Committee (NTSC) standard pure blue coordinates of (0.14, 0.08).

Over the last few years, OLEDs utilizing various D–A and D–A–D structured blue/sky-blue TADF emitters containing triazine,[4] benzosulfone,[5] phenone,[6] benzonitrile,[7] or phenylborane[8] as the A moiety have recently been synthesized and applied to TADF-OLEDs. However, high-performance blue TADF emitters are still very rare and only a few of them can achieve both a high external EL quantum efficiency (η_{ext}) exceeding 20% and a suitable color purity with the CIE_y value below 0.25.[4c,5a,5e,5f,7d,8a,8b,9] Hence, it remains quite challenging to search for an appropriate combination of D and A moieties to simultaneously attain both excellent EL efficiency and high color purity for deep-blue TADF materials.

In this chapter, a new family of highly efficient deep-blue TADF emitters based on a simple pre-twisted D–A architecture (**Figure 4-1**) in which a pyrimidine-based acceptor moiety is connected with a spiroacridan/acridan-based donor moiety through a phenylene π-spacer, are reported. Owing to the large steric repulsion between the hydrogen atoms of the acridan unit and the adjacent phenylene spacer, this D–A system offers nearly orthogonal conformations in the ground (S_0) and S_1 states, leading to effective spatial separation of the HOMO and LUMO and a reduction in ΔE_{ST}. Hence it enables efficient upconversion from the T_1 to the S_1 state. We envisage that the pyrimidine unit can serve as a universal building block for deep-blue TADF materials as it possesses a weaker electron-accepting nature than the widely used triazine unit and thus increases the bandgap energy (E_g) and S_1 and T_1 energy levels of the resulting D–A molecules. Moreover, the pyrimidine unit can be substituted with a variety of functional groups,

and fine-tuning of the photophysical and electronic properties can be attained by simple chemical modifications.

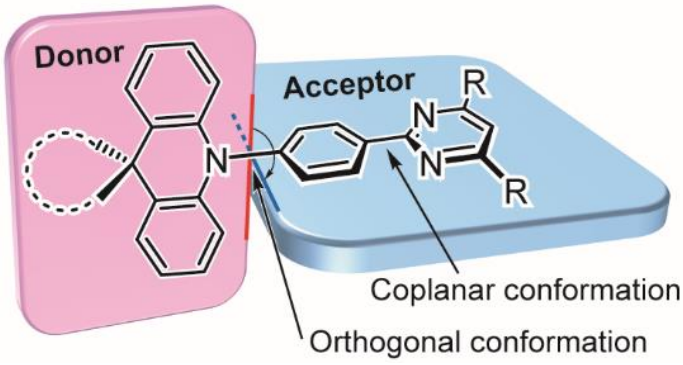

Figure 4-1. Molecular design and preferred geometry of deep-blue TADF emitters based on pre-twisted acridan–pyrimidine D–A structures.

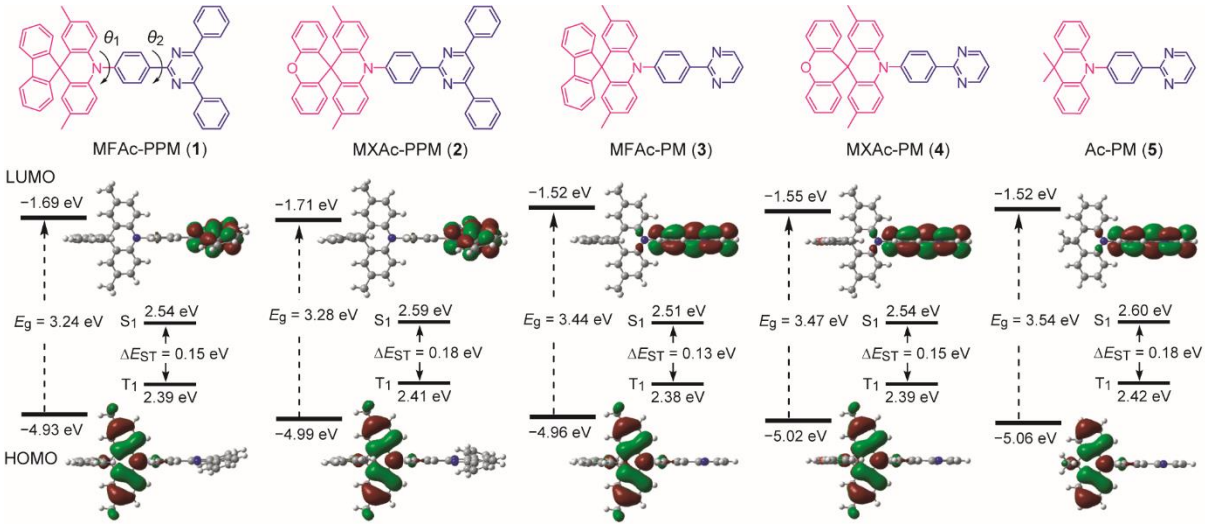

Figure 4-2 Chemical structures (upper), HOMO and LUMO distributions, and calculated singlet (S_1) and triplet (T_1) energy levels (lower) for D–A molecules **1–5** characterized by TD-DFT at the PBE1PBE/6-31G(d) level.

4. 2. Molecular Design

As shown in **Figure 4-2**, we designed a new series of D–A molecules, **1–5** consisting of 2,4,6-triphenylpyrimidine (PPM) or 2-phenylpyrimidine (PM) as an acceptor and spiro[2,7-dimethylacridan-9,9'-fluorene] (MFAc), spiro[2,7-dimethylacridan-9,9'-xanthene] (MXAc), or 9,9-dimethylacridan (Ac) as a donor. The selection of the PPM and PM units having relatively weak electron-withdrawing

characteristics and intrinsic high T_1 energies is key to producing wide-bandgap deep-blue TADF materials. Our design strategy is justified by time-dependent density functional theory (TD-DFT) calculations, which provide insights into the geometrical and electronic properties of **1–5** at the molecular level. As can be seen from **Figure 4-2**, all of these molecules adopt highly twisted D–A conformations in their optimized geometries, with dihedral angles between the acridan unit and the adjacent phenylene ring (θ_1) of 87–90° owing to the steric repulsion arising from their *peri*-hydrogen atoms. Meanwhile, the dihedral angles between the pyrimidine ring and the central phenylene ring (θ_2) were rather small (<6°). Such nearly orthogonal molecular structures formed by **1–5** can effectively break π-conjugation between the donor and acceptor moieties and cause localization of the HOMO and LUMO primarily on the acridan and PPM (or PM) units, respectively. Besides, the calculated first excited S_1 states for **1–5** were dominated by the HOMO→LUMO intramolecular charge-transfer (ICT) transition. As a result, small ΔE_{ST} values in the range of 0.13–0.18 eV were estimated for **1–5** from the calculated S_1 and T_1 energies (**Figure 4-2** and **Table 4-1**), allowing for efficient RISC and consequently resulting in TADF emission.

Table 4-1. The lowest excited singlet (S_1) and triplet (T_1) energies, oscillator strength (*f*), and transition configurations of **1–5** calculated by TD-DFT at the PBE1PBE/6-31G(d).

Compound	State	*E* (eV)	*f*	Main configuration		ΔE_{ST} (eV)
MFAc-PPM	S_1	2.54	0.0004	H → L	0.699	0.15
(**1**)	T_1	2.39	0	H → L	0.568	
				H−2 → L	0.360	
MXAc-PPM	S_1	2.59	0	H → L	0.699	0.18
(**2**)	T_1	2.41	0	H → L	0.562	
				H−3 → L	0.366	
MFAc-PM	S_1	2.51	0.0003	H → L	0.702	0.13
(**3**)	T_1	2.38	0	H → L	0.590	
				H−3 → L	0.357	
MXAc-PM	S_1	2.54	0.0005	H → L	0.702	0.15
(**4**)	T_1	2.39	0	H → L	0.583	
				H−3 → L	0.372	
Ac-PM	S_1	2.60	0	H → L	0.702	0.18
(**5**)	T_1	2.42	0	H → L	0.573	
				H−1 → L	0.381	

H → L represents the HOMO to LUMO transition. Excitation configurations with the highest contributions are presented, together with the corresponding transition symmetry and nature of the involved orbitals.

The configuration of **1** was further verified by X-ray crystallographic analysis (**Figure 4-3**). As per our designed, **1** revealed a highly twisted molecular structure with a dihedral angle between the acridan unit and the adjacent phenylene ring of 80°, reasonably consistent with the TD-DFT calculations. It is also noted that the spiro-fused fluorene substituent caused a slight bending of the acridan unit along the C9–N10 axis, on account of the sp^3 character of the C9 atom.

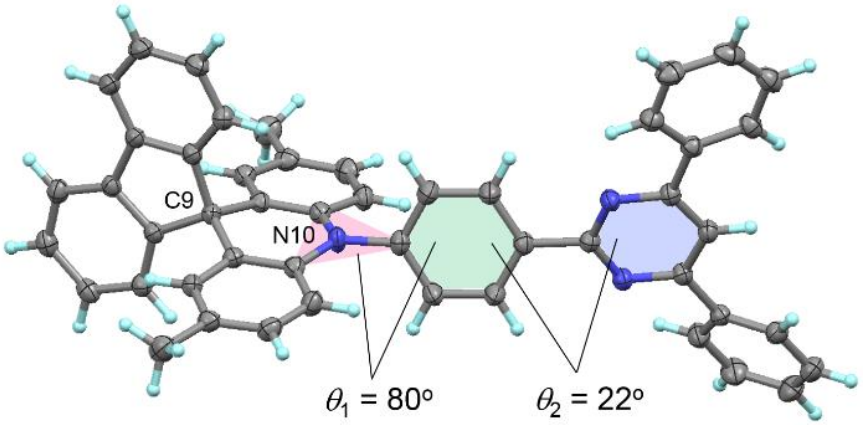

Figure 4-3. ORTEP diagram of **1** with 50% probability ellipsoids. Atom color code: C, gray; N, blue; H, light-blue.

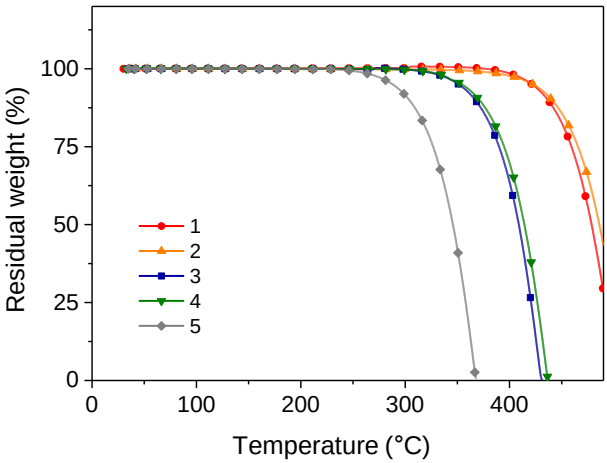

Figure 4-4. TGA curves for **1–5** recorded at a heating rate of 10 °C min^{-1} under N_2.

The thermal properties of **1–5** were examined by thermogravimetric analysis (**Figure 4-4**). Among these new compounds, **1** and **2** possessed the highest thermal stability with a decomposition temperature (T_d, corresponding to 5% weight loss) of 422 °C. Such T_d value was much higher than those of **3–5** (T_d = 351, 354, and 288 °C, respectively). The D–A molecules

bearing the spiro-fused D units (MFAC and MXAc) were found to exhibit better thermal properties than that with a non-spiro Ac unit.

4. 3. Photophysical and TADF Properties

The steady-state UV–vis absorption and photoluminescence (PL) spectra of **1–5** in dilute solutions are depicted in **Figure 4-5** and their relevant photophysical data are summarized in **Table 4-2**. All these compounds exhibit a similar spectral feature which involves two major absorption bands. While the stronger higher-energy absorptions below 330 nm are attributed to the π–π* transitions of the conjugated aromatic units, the much weaker lower-energy absorptions spanning in the range of 350–400 nm are assigned to the ICT transitions associated with electron transfer from the acridan to the pyrimidine moieties. Upon photoexcitation at the ICT absorption band, **1–5** in toluene solutions exhibited intense deep-blue PL emissions with peaks (λ_{PL}) ranging from 448 to 460 nm.

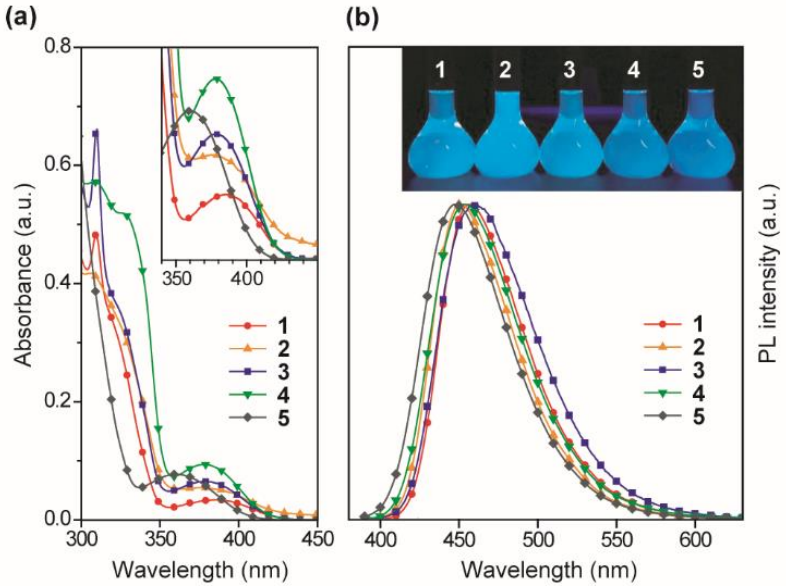

Figure 4-5. (a) UV–vis absorption and (b) PL spectra of **1–5** in toluene (10^{-5} M). The insets of (a) and (b) represent a magnified view of lower-energy ICT absorptions and a photograph of deep-blue PL emissions from their solutions under UV irradiation, respectively.

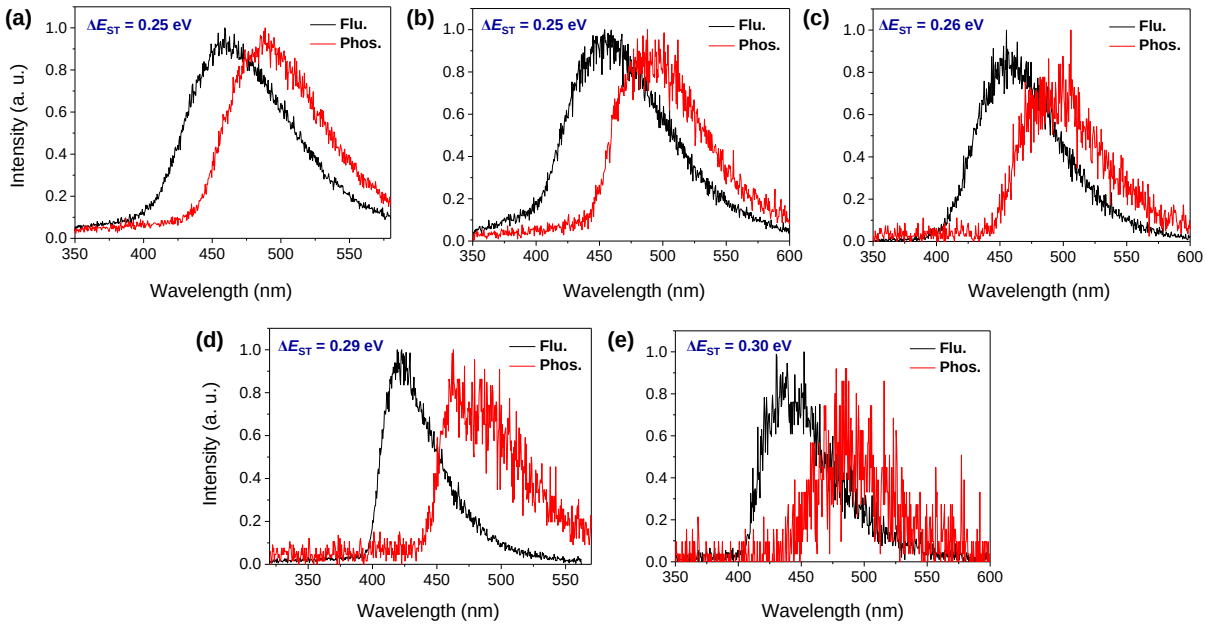

Figure 4-6. PL spectra of fluorescence in the time range of 1–100 ns at 300 K (black) and phosphorescence at 5 K in the range of 100–10000 μs (red) for doped thin films of (a) **1**, (b) **2**, (c) **3**, (d) **4**, and (e) **5** in a PPF host matrix. The lowest excited singlet (E_S) and triplet (E_T) energy levels of the TADF emitters were estimated from the high energy onsets of the fluorescence and phosphorescence spectra, respectively.

The photophysical and TADF properties of **1–5** were examined using doped thin films in a solid host matrix. The S_1 and T_1 energies (E_S and E_T, respectively) of **1–5** were determined from the onsets of the fluorescence (300 K) and phosphorescence (5 K) spectra, respectively, and thus their ΔE_{ST} values were experimentally evaluated to be between 0.25–0.30 eV (**Table 4-2** and **Figure 4-6**). Because of the high E_S and E_T values of 3.0–3.1 eV and 2.8–2.9 eV, respectively, for these wide-bandgap emitters **1–5**, we selected 2,8-bis(diphenylphosphoryl)dibenzofuran (PPF)[10] with a high E_T of 3.1 eV as a suitable host material to prevent the reverse energy transfer from the T_1 states of the guest emitter to the host material and to confine the excitons in the emitters. As shown in **Figure 4-7**, the PL emissions from these doped films thoroughly originated from their guest emitters (**1–5**), manifesting efficient host-to-guest energy transfer. Among these derivatives, MFAc-containing **1** and **3** showed slightly red-shifted PL emissions centered at 464 and 466 nm, respectively, compared with the MXAc-containing counterparts (λ_{PL} = 452 and 458 nm for **2** and **4**, respectively), presumably because of enhanced electron-donating effects caused by the conjugated spirofluorene substituent on the C9 position of the acridan unit. The absolute PL quantum yields (Φ_{PL}) of the doped films of **1–5** in PPF are as high as 87%, 69%, 91%, 90%, and 83% under N_2, respectively, which are

much higher than those obtained in dilute solutions (Φ_{PL} = 32–36% in deoxygenated toluene solution). Such PL enhancement in the solid state originates from the suppression of non-radiative deactivation processes caused by collisional and intramolecular rotational excited-energy loss. It is noteworthy that most of these derivatives exhibited $CIE_{x,y}$ values below 0.15 in those solid thin films, demonstrating their suitability as efficient deep-blue emitters in TADF-OLEDs.

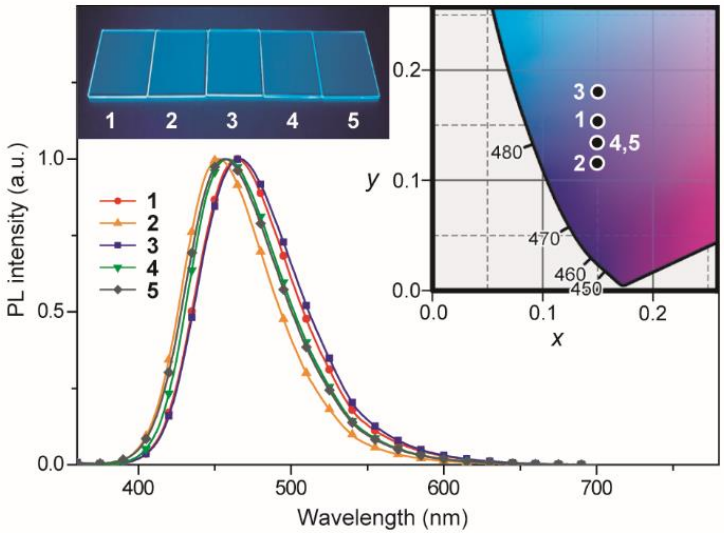

Figure 4-7. PL spectra of **1–5** in 18 wt%-emitter:PPF doped thin films. The inset shows CIE chromaticity coordinates and a photograph of deep-blue PL emissions of **1–5** in the doped films.

TADF characteristics of **1–5** in the doped films were further evidenced by investigating temperature-dependent transient PL decays. As shown in **Figure 4-7**, each of the transient PL curves displays clear double-exponential decay profile with prompt and delayed components in oxygen-free conditions. While the prompt component with the lifetime (τ_p) of 11–13 ns corresponds to conventional fluorescence ($S_1 \rightarrow S_0$), the delayed component with the lifetime (τ_d) of 38–78 μs can be assigned to TADF involving ISC and RISC processes ($S_1 \rightarrow T_1 \rightarrow S_1 \rightarrow S_0$). In comparison with **4** and **5**, the relatively shorter τ_d for **1–3** can be attributed to their smaller ΔE_{ST} values (**Figure 4-6** and **Table 4-2**). Furthermore, the transient PL profiles of the doped films reveal a typical TADF feature:[7a] the PL intensity for delayed component gradually increases when increasing temperature from 5 to 300 K. These observations unambiguously indicate that **1–5** can indeed utilize T_1 excitons for efficient light emission from the S_1 state via the $T_1 \rightarrow S_1$ thermal upconversion. From the overall Φ_{PL} value and the proportion of the integrated areas of the two components in each transient PL curve, the fractional quantum

efficiencies for the prompt (Φ_p) and delayed (Φ_d) components were evaluated for the doped films of **1–5**, as given in the insets of **Figure 4-8**. Obviously, these doped films exhibited a high ratio of Φ_d with respect to overall Φ_{PL} at ambient temperature (300 K), suggesting that a large portion of the S_1 excitons underwent efficient ISC and RISC and then decayed to emit delayed fluorescence upon photoexcitation. Indeed, for **1–5**, high RISC efficiencies (Φ_{RISC}) of 44–82% were assumed by the equation:[5f] $\Phi_{RISC} = \Phi_d/(1-\Phi_p)$ (see in General Introduction for details).

Table 4-2. Photophysical Data for Deep-Blue TADF Emitters **1–5**.

	λ_{abs}[a] (nm)	λ_{PL}[a] (nm)	λ_{PL}[b] (nm)	CIE[b),c] (x, y)	Φ_{PL}[b),d] (%)	τ_p[e] (ns)	τ_d[e] (μs)	HOMO[f] (eV)	LUMO[g] (eV)	E_S[h] (eV)	E_T[h] (eV)	ΔE_{ST}[i] (eV)
1	309, 386	458	464	(0.15, 0.15)	87	12	38	−5.62	−2.67	3.07	2.82	0.25
2	306, 378	451	452	(0.15, 0.12)	69	11	40	−5.65	−2.68	3.10	2.85	0.25
3	310, 380	461	466	(0.15, 0.18)	91	13	45	−5.60	−2.69	3.06	2.80	0.26
4	310, 379	454	458	(0.15, 0.13)	90	11	70	−5.65	−2.70	3.09	2.80	0.29
5	286, 359	448	457	(0.15, 0.13)	83	11	78	−5.68	−2.70	3.10	2.80	0.30

[a]Measured in toluene solution (10^{-5} M) at room temperature. [b]Measured in 18 wt%-doped thin films in a PPF solid host matrix at room temperature. [c]Commission Internationale de l'Éclairage (CIE) color coordinates. [d]Absolute PL quantum yield evaluated using an integrating sphere under N_2. [e]PL lifetimes of prompt (τ_p) and delayed (τ_d) decay components for the 18 wt%-doped films measured at room temperature. [f]Determined by photoelectron yield spectroscopy in neat films. [g]LUMO = HOMO + E_g, in which the optical energy gap (E_g) was derived from the absorption onset of the neat film. [h]Lowest singlet (E_S) and triplet (E_T) energies estimated from onset wavelengths of the PL spectra at 300 and 5 K in the doped films, respectively. [i]Singlet–triplet energy splitting determined experimentally using $\Delta E_{ST} = E_S - E_T$.

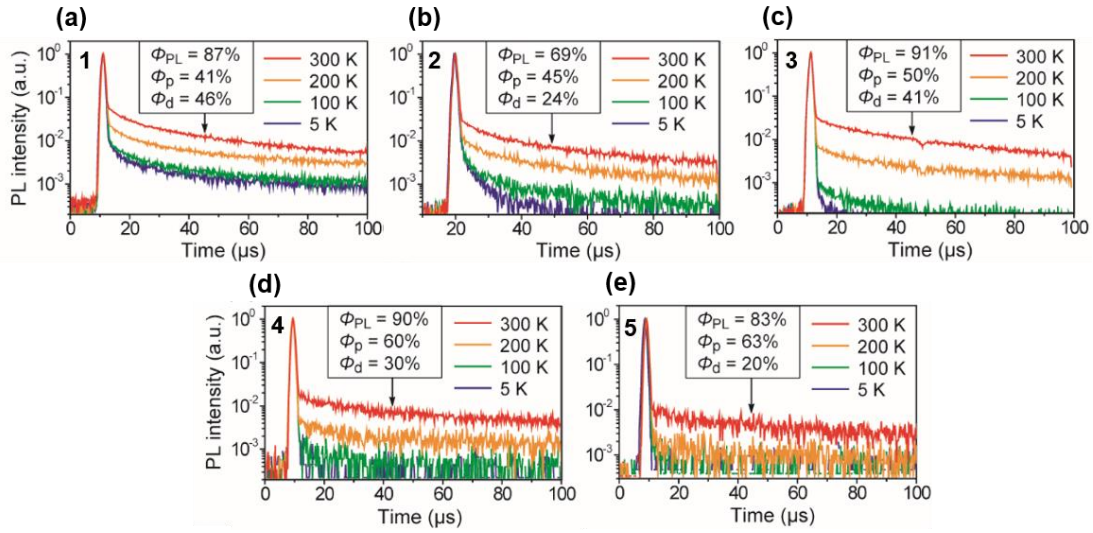

Figure 4-8. Temperature dependence of transient PL decays for **1–5** in 18 wt%-emitter:PPF doped thin films in the temperature range of 5–300 K under vacuum.

Table 4-3. Rate constants and quantum efficiencies of **1–5** in 18 wt%-doped films.[a)]

Emitter	k_r^S [s^{-1}]	k_{ISC} [s^{-1}]	k_{RISC} [s^{-1}]	Φ_p [%]	Φ_d [%]	Φ_{ISC} [%]	Φ_{RISC} [%]
1	3.4×10^7	4.9×10^7	5.0×10^4	41	46	59	78
2	4.1×10^7	5.0×10^7	2.4×10^4	45	24	55	44
3	3.8×10^7	3.8×10^7	3.6×10^4	50	41	50	82
4	5.5×10^7	3.6×10^7	1.8×10^4	60	30	40	75
5	5.7×10^7	3.4×10^6	1.1×10^4	63	20	37	54

[a)]Abbreviations: k_r^S, radiative rate constant ($S_1\rightarrow S_0$); k_{ISC}, intersystem-crossing (ISC) rate constant ($S_1\rightarrow T_1$); k_{RISC}, reverse ISC rate constant ($T_1\rightarrow S_1$); Φ_p, quantum efficiency for prompt fluorescence component; Φ_d, quantum efficiency for delayed fluorescence component; Φ_{ISC}, ISC quantum efficiency; Φ_{RISC}, RISC quantum efficiency.

4. 4. Electroluminescence Performance

To investigate the EL performance of deep-blue TADF emitters **1–5**, multilayer OLEDs were fabricated by employing thin films of **1–5** doped in a PPF host as an emitting layer (EML). We adopted the following device configuration: indium-tin-oxide (ITO, 100 nm)/HAT-CN (10 nm)/α-NPD (40 nm)/CCP (5 nm)/EML (20 nm)/PPF (10 nm)/TPBi (30 nm)/Liq (1 nm)/Al (100 nm), as illustrated in **Figure 4-9a**. In this device architecture, HAT-CN (2,3,6,7,10,11-hexacyano-1,4,5,8,9,12-hexaazatriphenylene) and α-NPD (4,4'-bis-[*N*-(1-naphthyl)-*N*-phenylamino]-1,1'-biphenyl) were used as a hole-injection layer and a hole-transporting layer, respectively; whereas, TPBi (1,3,5-tris(*N*-phenylbenzimidazol-2-yl)benzene) and Liq (8-hydroxyquinoline lithium) served as an electron-transporting layer and an electron-injection material, respectively. Additionally, thin layers of CCP[8a] (9-phenyl-3,9'-bicarbazole) and PPF[10] with high E_T of 3.0 and 3.1 eV were inserted as exciton-blocking layers to suppress the triplet exciton deactivation at the neighboring interfaces and to confine the excitons within the EML.

The EL characteristics of the fabricated TADF-OLEDs are depicted in **Figure 4-9b** and **c**, and the key device parameters are compiled in **Table 4-4**. The devices based on **1–5** displayed bright blue EL emissions peaking between the ranges of 458–470 nm, with rather low turn-on voltages (V_{on}) of 3.4–3.6 V. Their EL spectra were consistent with the corresponding PL spectra, suggesting efficient carrier injection, transport, and recombination into the EML within the device. Among the fabricated devices, the device employing **1** achieved the highest EL efficiencies with maximum η_{ext} of 20.4%, current efficiency (η_c) of 41.7 cd A^{-1}, and power efficiency (η_p) of 37.2 lm W^{-1} at low current densities without any light out-coupling enhancement. The CIE coordinates of EL from

this device were (0.16, 0.23). To our knowledge, these efficiencies are among the highest level of blue TADF-OLEDs ever reported.[4c,5a,5e,5f,8a,8b,9] So far, deep-blue TADF-OLEDs with emission maxima (λ_{EL}) below 470 nm have rarely achieved high η_{ext} exceeding 20%. Moreover, the device employing **1** also showed relatively reduced efficiency roll-off compared to the other devices; the η_{ext} value still remained as high as 15.6% at a practical luminance of 100 cd m^{-2}. The reduced roll-off behavior for **1** can be attributed to the fast RISC originating from its relatively shorter τ_d and the suppression of triplet–triplet annihilation (TTA) and singlet–triplet annihilation (STA),[11] as discussed below.

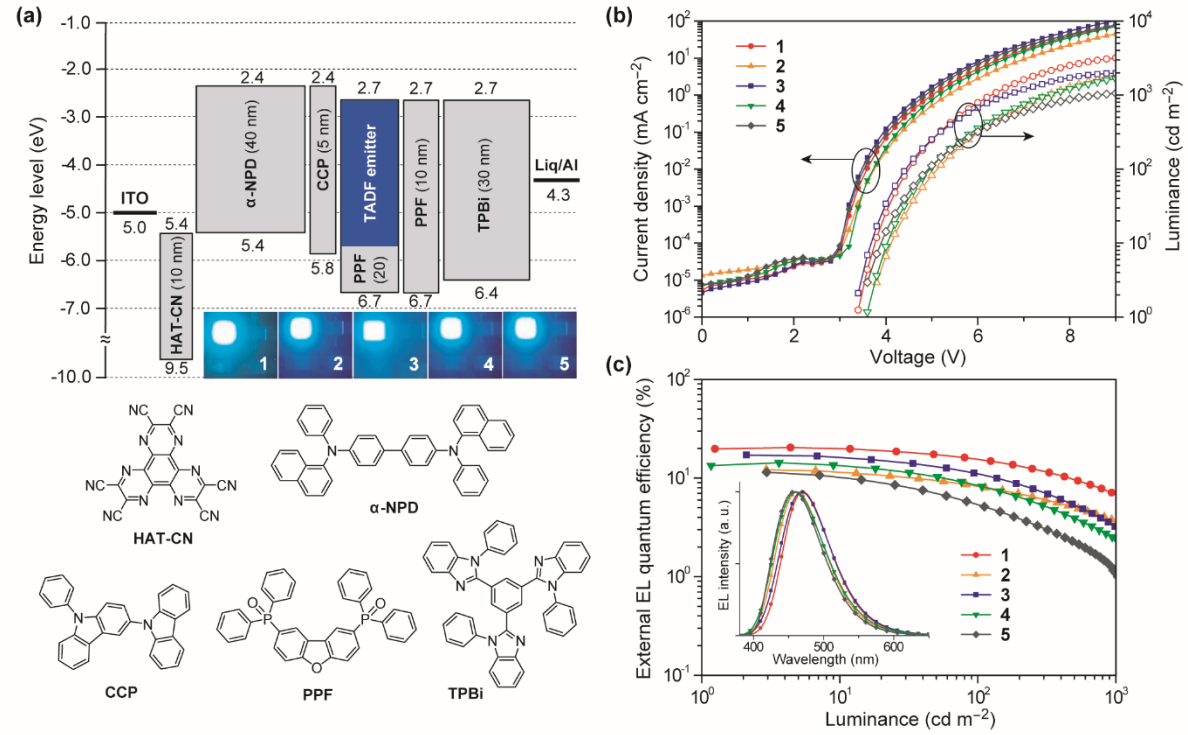

Figure 4-9. (a) Schematic energy-level diagram and photos of EL emission for blue TADF-OLEDs based on **1–5** as emitters (top) and chemical structures of the materials used in the devices (bottom). (b) Current density and luminance versus voltage (*J–V–L*) characteristics and (c) external EL quantum efficiency versus luminance (η_{ext}–*L*) characteristics of blue TADF-OLEDs. The inset of (c) represents EL spectra measured at 10 mA cm^{-2}.

Comparing performance of the TADF-OLEDs containing **1–5**, the maximum η_{ext} values were in the order of **1** (20.4%) > **3** (17.1%) > **4** (14.3%) > **2** (12.2%) > **5** (11.4%). The relatively lower efficiencies of the devices with **2** and **5** than those with **1**, **3**, and **4** can be mainly ascribed to their lower Φ_{PL} and Φ_d values. Nevertheless, η_{ext} values of **2** and **5** were more than two times higher than those expected from conventional

fluorescent emitters with the same Φ_{PL} values. These pyrimidine-based deep-blue TADF emitters could thus achieve high EL efficiencies by utilizing both the electro-generated T_1 and S_1 excitons for efficient light emission. However, the EL efficiencies for some of these TADF-OLEDs significantly decreased with increasing current density (or luminance). This severe efficiency roll-off is primarily attributed to the long-lived excited states of the T_1 excitons, which undergo exciton deactivation processes such as TTA and STA. The TTA model is here used to analyze the efficiency roll-off for the devices containing **1–5**, according to the following equation:[11,12]

$$\eta_{ext}/\eta_0 = J_0/4J\left[\sqrt{1+8J/J_0}-1\right] \qquad (\textbf{4-1})$$

where η_0 is the external EL quantum efficiency in the absence of TTA and J_0 is the critical current density at $\eta_{ext} = \eta_0/2$. The fitted curves based on the TTA model agreed well with the experimental η_{ext}–J plots for all the devices containing **1–5** with correlation coefficients greater than 0.98 (**Figure 4-10**), which indicates that the efficiency roll-off for these devices was primarily caused by TTA exciton deactivation. Indeed, the device based on **5** showed a smaller J_0 value (0.9 mA cm^{-2}) than that of **1** (2.1 mA cm^{-2}), which implies that **5** suffered from more severe TTA and efficiency roll-off as the increase of current density. This propensity arises from the relatively long TADF lifetime (τ_d) for **5** in the doped film. If efficient deep-blue TADF emitters with much shorter τ_d (<1 μs) can be realized, we can therefore expect that high η_{ext} values of over 20% can be retained even at higher current densities.

Table 4-4. EL Performance of TADF-OLEDs Based on 1–5.

Emitter[a]	**1**	**2**	**3**	**4**	**5**
λ_{EL}[b] (nm)	470	462	469	460	458
V_{on}[c] (V)	3.4	3.6	3.4	3.6	3.6
$\eta_{ext,max}$[d] (%)	20.4	12.2	17.1	14.3	11.4
$\eta_{ext,100}$[e] (%)	15.6	8.2	10.9	8.4	5.4
η_c[f] (cd A^{-1})	41.7	22.7	34.3	25.0	18.9
η_p[g] (lm W^{-1})	37.2	18.8	31.7	20.7	16.5
CIE[h] (x, y)	(0.16, 0.23)	(0.16, 0.20)	(0.16, 0.21)	(0.16, 0.19)	(0.15, 0.15)

[a]Device configuration: ITO/HAT-CN (10 nm)/α-NPD (40 nm)/CCP (5 nm)/18 wt%-emitter:PPF (20 nm)/PPF (10 nm)/TPBi (30 nm)/Liq (1 nm)/Al (100 nm). [b]EL emission maximum. [c]Turn-on voltage at a brightness of 1 cd m^{-2}. [d]Maximum external EL quantum efficiency. [e]External EL quantum efficiency at 100 cd m^{-2}. [f]Maximum current efficiency. [g]Maximum power efficiency. [h]Commission Internationale de l'Éclairage (CIE) chromaticity coordinates recorded at 10 mA cm^{-2}.

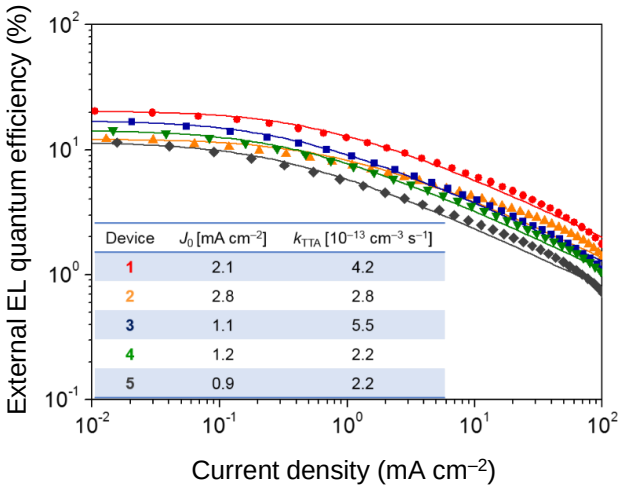

Figure 4-10. External EL quantum efficiency *verse* current density (η_{ext}–J) plots for blue TADF-OLEDs based on **1–5**. The solid lines represent the simulated η_{ext} by using the TTA model. J_0 is the critical current density at $\eta_{ext} = \eta_0/2$ and k_{TTA} is the TTA rate constant.

4. 5. Experimental Section

4. 5. 1. Materials

All commercially available reagents and solvents were used as received unless otherwise noted. 2,8-Bis(diphenylphosphoryl)dibenzofuran (PPF)[10] and 9-phenyl-3,9'-bicarbazole (CCP)[8a] were prepared according to the literature procedures, and were purified by vacuum sublimation. 2,3,6,7,10,11-Hexacyano-1,4,5,8,9,12-hexaazatriphenylene (HAT-CN) was donated by the Nippon Soda Co., Ltd. and was purified by vacuum sublimation before use. Other OLED materials were purchased from E-Ray Optoelectronics Technology Co., Ltd. and were used for the device fabrication without further purification. The synthetic routes for deep-blue TADF molecules **1–5** are outlined in **Scheme 4-1**, and detailed synthetic procedures and characterization data for other intermediates (**6–9**) are given in **Schemes 4-2–5**. 9,9-Dimethylacridan[13] (**10**) was prepared according to the literature procedure. ^{1}H and ^{13}C NMR spectra were recorded on a Bruker Avance III 400 spectrometer. Chemical shifts of ^{1}H and ^{13}C NMR signals were quoted to tetramethylsilane (δ = 0.00), $CDCl_3$ (δ = 77.0), and DMSO-d_6 (δ = 39.5) as internal standards. Matrix-assisted laser desorption ionization time-of-flight (MALDI-TOF) mass spectra were collected on an Autoflex III spectrometer (Bruker Daltonics) using dithranol as the matrix. Elemental analysis was performed using an MT-5 CHN corder (Yanaco). Single-crystal X-ray analysis was carried out using a Rigaku VariMax with Saturn 70 system with graphite monochromated Mo$K\alpha$

radiation.All final products were purified by temperature-gradient vacuum sublimation with a P-100 system (ALS Technology), before the measurements and device fabrication.

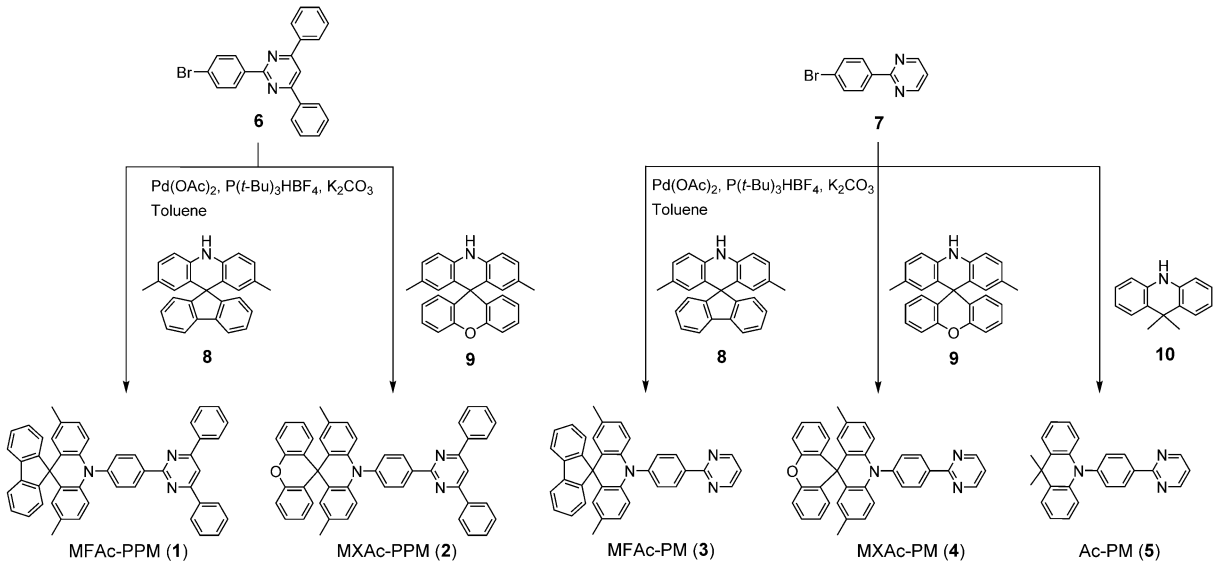

Scheme 4-1. Synthetic routes for pyrimidine-based TADF molecules **1–5**.

4. 5. 2. Synthesis

Compounds **1–5** were readily synthesized through the Buchwald–Hartwig amination of bromo-PPM (for **1** and **2**) or bromo-PM (for **3–5**) with the corresponding spiroacridan/acridan by employing a $Pd(OAc)_2/P(t\text{-}Bu)_3HBF_4$ catalytic system in high yields of over 90%. All final products were purified by temperature-gradient vacuum sublimation to obtain highly pure materials for subsequent measurements and device fabrication. The chemical structures of **1–5** were confirmed by ^1H and ^{13}C NMR spectroscopy, mass spectrometry, and elemental analysis.

MFAc-PPM (1): A mixture of **6** (1.00 g, 2.58 mmol), **8** (0.93 g, 2.59 mmol), $Pd(OAc)_2$ (0.022 g, 0.1 mmol), $P(t\text{-}Bu)_3HBF_4$ (0.03 g, 0.1 mmol), and K_2CO_3 (1.07 g, 7.7 mmol) in dry toluene (30 mL) was refluxed for 48 h under N_2. After cooling to room temperature, the reaction mixture was filtered through a Celite pad, and then filtrate was concentrated under reduced pressure. The product was purified by column chromatography on silica gel (eluent: hexane/chloroform = 3:1, v/v) to afford **1** as a white solid (yield = 1.60 g, 93%). ^1H NMR (400 MHz, DMSO-d_6): δ 9.03 (d, J = 8.4 Hz, 2H), 8.67 (s, 1H), 8.60-8.58 (m, 4H), 7.99 (d, J = 7.6 Hz, 2H), 7.78 (d, J = 8.4 Hz, 2H), 7.68-7.66 (m, 6H), 7.45 (td, J = 7.4 Hz, 1.3 Hz, 2H), 7.41 (d, J = 7.2 Hz, 2H), 7.33 (td, J = 7.2 Hz, 1.2 Hz, 2H),

6.80 (dd, *J* = 8.6 Hz, 1.8 Hz, 2H), 6.32 (d, *J* = 8.4 Hz, 2H), 6.04 (d, *J* = 1.6 Hz, 2H), 1.90 (s, 6H). ^{13}C NMR (100 MHz, $CDCl_3$): δ 165.04, 164.02, 156.52, 143.81, 139.24, 139.22, 138.16, 137.39, 131.38, 131.19, 130.98, 129.48, 129.03, 128.40, 128.00, 127.87, 127.45, 127.34, 125.86, 124.63, 119.83, 114.52, 110.55, 56.92, 20.40. MS (MALDI-TOF): *m*/*z* calcd 665.28 $[M]^+$; found 665.18. Anal. calcd (%) for $C_{49}H_{35}N_3$: C 88.39, H 5.30, N 6.31; found: C 88.35, H 5.23, N 6.34.

MXAc-PPM (2): This compound was synthesized according to the same procedure as described above for the synthesis of **1**, except that **9** (0.97 g, 2.58 mmol) was used as the reactant instead of **8**, yielding **2** as a white solid (yield = 1.60 g, 91%). ^{1}H NMR (400 MHz, DMSO-d_6): δ 9.01 (d, *J* = 8.8 Hz, 2H), 8.66 (s, 1H), 8.60-8.57 (m, 4H), 7.73 (d, *J* = 8.8 Hz, 2H), 7.67-7.66 (m, 6H), 7.26 (dd, *J* = 6.0 Hz, 1.6 Hz, 4H), 7.15 (dd, *J* = 8.8 Hz, 1.2 Hz, 2H), 7.08-7.04 (m, 2H), 6.76 (dd, *J* = 8.6 Hz, 1.4 Hz, 2H), 6.48 (d, *J* = 2.0 Hz, 2H), 6.24 (d, *J* = 8.4 Hz, 2H), 1.96 (s, 6H). ^{13}C NMR (100 MHz, $CDCl_3$): δ 165.06, 163.99, 148.44, 138.22, 137.38, 137.14, 132.54, 132.06, 131.54, 131.43, 131.25, 130.99, 129.74, 129.52, 129.04, 127.83, 127.45, 127.34, 123.69, 115.85, 114.06, 110.58, 44.74, 20.48. MS (MALDI-TOF): *m*/*z* calcd 681.28 $[M]^+$; found 681.11. Anal. calcd (%) for $C_{49}H_{35}N_3O$: C 86.32, H 5.17, N 6.16; found: C 86.45, H 5.11, N 6.31.

MFAc-PM (3): A mixture of **7** (1.00 g, 4.25 mmol), **8** (1.55 g, 4.31 mmol), $Pd(OAc)_2$ (0.03 g, 0.14 mmol), P(*t*-Bu)$_3$HBF$_4$ (0.03 g, 0.1 mmol), and K_2CO_3 (1.80 g, 13.0 mmol) in dry toluene (80 mL) was refluxed for 12 h under N_2. After cooling to room temperature, the reaction mixture was filtered through a Celite pad, and then filtrate was concentrated under reduced pressure. The product was purified by column chromatography on silica gel (eluent: hexane/chloroform = 3:1, v/v) to afford **3** as a white solid (yield = 2.01 g, 92%). ^{1}H NMR (400 MHz, DMSO-d_6): δ 9.02 (d, *J* = 4.8 Hz, 2H), 8.77 (dd, *J* = 6.4 Hz, 2.0 Hz, 2H), 7.98 (d, *J* = 7.6 Hz, 2H), 7.71 (dd, *J* = 6.8 Hz, 2.0 Hz, 2H), 7.55 (t, *J* = 4.8 Hz, 1H), 7.44 (td, *J* = 7.2 Hz, 1.2 Hz, 2H), 7.39 (d, *J* = 7.2 Hz, 2H), 7.32 (td, *J* = 7.2 Hz, 1.2 Hz, 2H), 6.78 (dd, *J* = 8.8 Hz, 1.9 Hz, 2H), 6.26 (d, *J* = 8.4 Hz, 2H), 6.03 (d, *J* = 2.0 Hz, 2H), 1.89 (s, 6H). ^{13}C NMR (100 MHz, $CDCl_3$): δ 164.24, 157.44, 156.51, 144.01, 139.24, 139.14, 137.55, 131.58, 130.86, 129.52, 128.39, 127.98, 127.89, 127.45, 125.84, 124.61, 119.82, 119.39, 114.45, 56.88, 20.39. MS (MALDI-TOF) *m*/*z*: calcd 513.22

[*M*]$^+$; found 514.04. Anal. calcd (%) for $C_{37}H_{27}N_3$: C 86.52, H 5.30, N 8.18; found: C 86.64, H 5.06, N 8.23.

MXAc-PM (4): This compound was synthesized according to the same procedure as described above for the synthesis of **3**, except that **9** (1.60 g, 4.26 mmol) was used as the reactant instead of **8**, yielding **4** as a white solid (yield = 2.03 g, 90%). ^{1}H NMR (400 MHz, DMSO-d_6): δ 9.01 (d, J = 5.2 Hz, 2H), 8.75 (dd, J = 6.4 Hz, 2.0 Hz, 2H), 7.67 (d, J = 8.4 Hz, 2H), 7.55 (t, J = 5.0 Hz, 1H), 7.25-7.23 (m, 4H), 7.12 (dd, J = 7.6 Hz, 1.2 Hz, 2H), 7.06-7.04 (m, 2H), 6.74 (dd, J = 8.8 Hz, 1.9 Hz, 2H), 6.46 (d, J = 1.6 Hz, 2H), 6.18 (d, J = 8.8 Hz, 2H), 1.95 (s, 6H). ^{13}C NMR (100 MHz, $CDCl_3$): δ 164.18, 157.44, 148.41, 143.91, 137.60, 137.04, 132.55, 132.03, 131.62, 131.51, 130.91, 129.77, 129.50, 127.79, 127.43, 123.66, 119.40, 115.83, 113.98, 44.70, 20.46. MS (MALDI-TOF): *m*/*z* calcd 529.22 [*M*]$^+$; found 529.12. Anal. calcd (%) for $C_{37}H_{27}N_3O$: C 83.91, H 5.14, N 7.93; found: C 83.84, H 5.03, N 8.02.

Ac-PM (5): This compound was synthesized according to the same procedure as described above for the synthesis of **3**, except that **10** (0.89 g, 4.25 mmol) was used as the reactant instead of **8**, yielding **5** as a white solid (yield = 1.45 g, 94%). ^{1}H NMR (400 MHz, DMSO-d_6): δ 8.99 (d, J = 5.2 Hz, 2H), 8.69 (d, J = 8.4 Hz, 2H), 7.55-7.50 (m, 5H), 6.99 (td, J = 7.7 Hz, 1.3 Hz, 2H), 6.93 (td, J = 7.5 Hz, 1.3 Hz, 2H), 6.24 (dd, J = 8.0 Hz, 1.2 Hz, 2H), 1.64 (s, 6H). ^{13}C NMR (100 MHz, $CDCl_3$): δ 164.19, 157.40, 143.66, 140.69, 137.49, 131.55, 130.74, 130.08, 126.38, 125.25, 120.66, 119.35, 114.12, 36.00, 31.28. MS (MALDI-TOF): *m*/*z* calcd 363.17 [*M*]$^+$; found 362.99. Anal. calcd (%) for $C_{25}H_{21}N_3$: C 82.61, H 5.82, N 11.56; found: C 82.61, H 5.75, N 11.65.

The synthetic routes for intermediates **6–9** are outlined in **Schemes 4-2–5**, respectively. The detailed synthetic procedures and characterization data for intermediates **6–9** are described below.

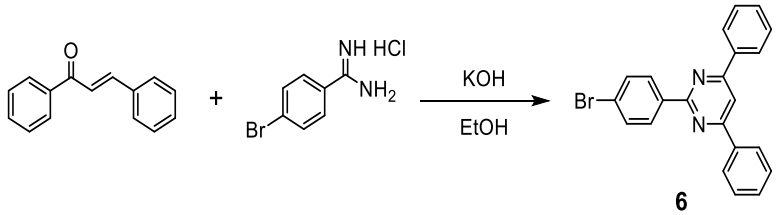

Scheme 4-2. Synthesis of 2-(4-bromophenyl)-4,6-diphenylpyrimidine (**6**).

Compound 6: To a stirred mixture of chalcone (8.84 g, 42.5 mmol) and 4-bromobenzamidine hydrochloride (5.00 g, 21.2 mmol) in ethanol (200 mL) was added dropwise a solution of potassium hydroxide (2.38 g, 42.4 mmol) in ethanol (100 mL) at room temperature. The mixture was then refluxed for 3 h. After cooling to room temperature, the formed precipitate was collected by filtration, washed with a large amount of water, and dried under vacuum to afford **6** as a white solid (yield = 16.0 g, 97%). ^{1}H NMR (400 MHz, $CDCl_3$): δ 8.61 (dd, J = 6.8 Hz, 2.0 Hz, 2H), 8.29-8.26 (m, 4H), 8.04 (s, 1H), 7.66 (dd, J = 6.8 Hz, 2.0 Hz, 2H), 7.59-7.55 (m, 6H). MS (MALDI-TOF): m/z calcd 386.04 $[M]^+$; found 386.68.

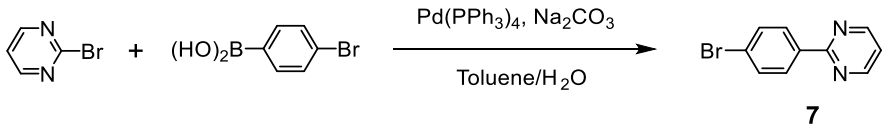

7

Scheme 4-3. Synthesis of 2-(4-bromophenyl)pyrimidine (**7**).

Compound 7: 2-Bromopyrimidine (10.0 g, 62.9 mmol) and $Pd(PPh_3)_4$ (0.73 g, 0.63 mmol) were dissolved in toluene (100 mL) under N_2 at room temperature. 4-Bromophenylboronic acid (12.6 g, 62.7 mmol) and an aqueous solution (50 mL) of sodium carbonate (20.0 g, 189 mmol) were then added to the solution. The mixture was stirred for 24 h at 90 °C under N_2. After cooling to room temperature, the reaction mixture was added in to water, and the product was extracted with chloroform. The combined organic layers were washed with water and dried over anhydrous Na_2SO_4. After filtration and evaporation, the product was purified by column chromatography on silica gel (eluent: hexane/ethyl acetate = 20:1, v/v) to yield **7** as a white solid (yield = 4.4 g, 30%). ^{1}H NMR (400 MHz, $CDCl_3$): δ 8.74 (d, J = 4.8 Hz, 2H), 8.27 (d, J = 9.0 Hz, 2H), 7.56 (d, J = 9.0 Hz, 2H), 7.15 (t, J = 4.8 Hz, 1H).

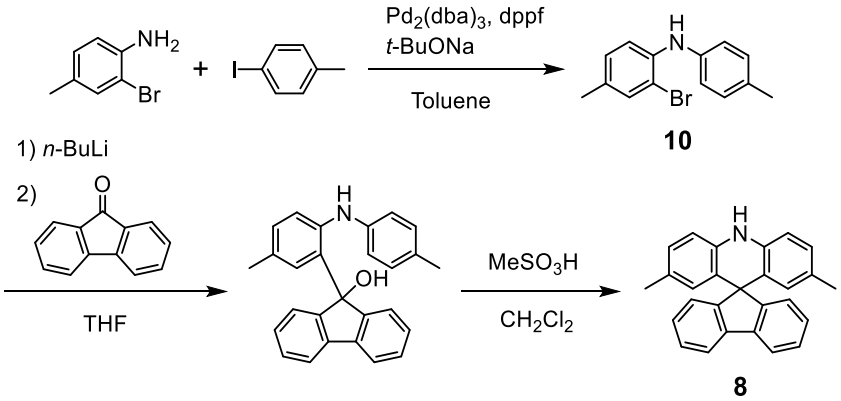

10 **8**

Scheme 4-4. Synthesis of spiro[2,7-dimethylacridine-9,9'-fluorene] (**8**).

Compound 10: To a stirred solution of 2-bromo-4-methylaniline (48.4 g, 260 mmol), sodium *tert*-butoxide (37.5 g, 390 mmol) in dry toluene (520 mL) were added 1-iodo-4-methylbenzene (64.2 g, 286 mmol), $Pd_2(dba)_3$ (2.38 g, 2.6 mmol), and 1,1'-bis(diphenylphosphino)ferrocene (dppf, 1.44 g, 2.6 mmol) at room temperature. The mixture was refluxed for 8 h under N_2. After cooling to room temperature, the reaction mixture was filtered through a Celite pad with chloroform, and the filtrate was concentrated under reduced pressure. The crude product was purified by column chromatography on silica gel (eluent: hexane/dichloromethane = 9:1, v/v) to give **10** as a white solid (yield = 54.8 g, 74%). ^{1}H NMR (400 MHz, $CDCl_3$): δ 7.56 (d, J = 8.3 Hz, 1H), 7.34 (d, J = 1.4 Hz, 1H), 7.10 (d, J = 8.0 Hz, 2H), 7.07 (d, J = 8.3 Hz, 1H), 7.00 (d, J = 8.4 Hz 2H), 6.96-6.91 (m, 1H), 2.32 (s, 3H), 2.25 (s, 3H). MS (MALDI-TOF): m/z calcd 275.03 $[M]^+$; found 275.71.

Compound 8: To a stirred solution of **10** (21.0 g, 76.0 mmol) in dry THF (300 mL) was added dropwise *n*-butyllithium (1.6 M, 97.4 mL, 156 mmol) at −78 °C under N_2. The mixture was stirred for 1 h at that temperature. After heating up to 0 °C, fluorenone (15.1 g, 83.6 mmol) was added to the solution, and the mixture was further stirred for 6 h at room temperature. The reaction was quenched by addition of a large amount of water. Then, the product was extracted with chloroform and dried over anhydrous Na_2SO_4. After filtration and evaporation, the product was used in the next reaction without further purification.

This crude product was dissolved in dichloromethane (300 mL), and methanesulfonic acid (14.6 g, 152 mmol) was added to the solution at room temperature. The mixture was refluxed for 1 h under air. After cooling to room temperature, the mixture was concentrated under reduced pressure. The residue was purified by column chromatography on silica gel (eluent: hexane/dichloromethane = 4:1, v/v) to afford **8** as a white solid (yield = 12.2 g, 45%). ^{1}H NMR (400 MHz, $CDCl_3$): δ 7.78 (br, 1H), 7.37-7.18 (m, 14H). MS (MALDI-TOF): m/z calcd 359.17 $[M]^+$; found, 358.98.

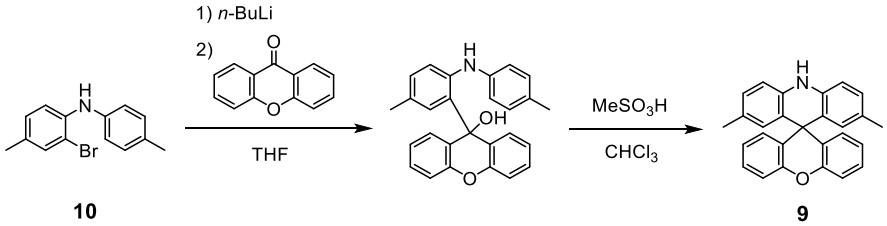

Scheme 4-5. Synthesis of spiro[2,7-dimethylacridine-9,9'-xanthene] (**9**).

Compound 9: To a stirred solution of **10** (20.0 g, 72.4 mmol) in dry THF (300 mL) was added dropwise *n*-butyllithium (2.6 M, 61.4 mL, 159 mmol) at −78 °C under N_2. The mixture was stirred for 1 h at that temperature. After heating up to 0 °C, xanthone (15.6 g, 79.5 mmol) was slowly added to the solution, and the mixture was further stirred for 1 h at 0 °C and for 2 h at room temperature. The reaction was quenched by addition of a large amount of water. Then, the product was extracted with chloroform and dried over anhydrous Na_2SO_4. After filtration and evaporation, the product was used in the next reaction without further purification.

This crude product was dissolved in chloroform (300 mL), and methanesulfonic acid (7.7 g, 80.1 mmol) was added to the solution at room temperature. The mixture was refluxed for 1 h under air, and then further reacted for 12 h at room temperature. The mixture was concentrated under reduced pressure. The residue was purified by column chromatography on silica gel (eluent: hexane/chloroform = 3:1, v/v) to afford **9** as a white solid (yield = 18.5 g, 68%). ^{1}H NMR (400 MHz, DMSO-d_6): δ 8.99 (s, 1H), 7.18 (dd, J = 6.7, 1.6 Hz), 6.95 (t, J = 3.8 Hz), 6.9 (d, J = 7.8 Hz, 2H), 6.82 (d, J = 8.3 Hz, 2H), 6.78 (d, J = 8.2 Hz, 2H), 6.31 (s, 2H), 1.95 (s, 6H). MS (MALDI-TOF): m/z calcd 375.16 $[M]^+$; found 374.86.

4. 5. 3. Quantum Chemical Calculations

Quantum chemical calculations were performed using the Gaussian 09 program package. The molecular geometries in the ground state were optimized using the PBE1PBE functional with the 6-31G(d) basis set in the gas phase. The lowest singlet and triplet excited states were computed using the optimized structures with time-dependent density functional theory (TD-DFT) at the same level.

4. 5. 4. Photophysical Measurements

UV–vis absorption and photoluminescence (PL) spectra were measured with a V-670 spectrometer (Jasco) and a FP-8600 spectrophotometer (Jasco), respectively, using degassed spectral grade solvents. The absolute PL quantum yields (Φ_{PL}) were determined using an ILF-835 integrating sphere system (Jasco). The transient PL decay measurements were carried out using a C11367 Quantaurus-tau fluorescence lifetime spectrometer (Hamamatsu Photonics; λ = 340 nm, pulse width = 100 ps, and repetition rate = 20 Hz) under N_2, and a C9300 Streak camera (Hamamatsu Photonics) with an N_2 gas laser (λ = 337 nm, pulse width = 500 ps, and repetition rate = 20 Hz) under vacuum ($< 4 \times 10^{-1}$ Pa). The HOMO energies of materials in neat films were determined using

an AC-2 ultraviolet photoelectron spectrometer (Riken-Keiki). The LUMO energies were estimated by subtracting the optical energy gaps (E_g) from the measured HOMO energies; the E_g values were determined from the onset positions of the PL spectra of thin films.

4. 5. 5. OLED Fabrication and Characterization

ITO-coated glass substrates were cleaned with detergent, deionized water, acetone, and isopropanol. The substrates were then subjected to UV–ozone treatment for 30 min before they were loaded into an E-200 vacuum evaporation system (ALS Technology). The organic layers and a cathode aluminum layer were thermally evaporated on the substrates under vacuum (<6 × 10^{-5} Pa) with an evaporation rate of <0.3 nm s^{-1} through a shadow mask. The layer thickness and deposition rate were monitored in situ during deposition by an oscillating quartz thickness monitor. OLED characteristics were measured using a 2400 source meter (Keithley) and a CS-2000 spectroradiometer (Konica Minolita).

4. 6. Conclusions

A new family of deep-blue TADF emitters, consisting of pre-twisted acridan–pyrimidine D–A motifs, were designed and synthesized. All of these emitters in doped thin films showed excellent PL properties with quantum yields of 69–91% accompanied by prominent TADF originating from their small ΔE_{ST}. By employing these TADF emitters for OLEDs, considerably high maximum external EL quantum efficiencies of up to 20.4% with CIE coordinates of (0.16, 0.23) were achieved. Deep-blue EL with CIE coordinates of (0.15, 0.15) could also be obtained through rational molecular design in this platform. These results validate a versatile design strategy to utilize pyrimidine derivatives as a universal platform for the further development of efficient deep-blue organic emitters.

References

[1] a) M. A. Baldo, S. Lamansky, P. E. Burrows, M. E. Thompson, S. R Forrest, Appl. Phys. Lett. 1999, 75, 4; b) C. Adachi, M. A. Baldo, M. E. Thompson, S. R. Forrest, J. Appl. Phys. 2001, 90, 5048; c) S. Reineke, F. Lindner, G. Schwartz, N. Seidler, K. Walzer, B. Lüssem, K. Leo, Nature 2009, 459, 234; d) H. Yersin, Highly Efficient OLEDs with Phosphorescent Materials; Wiley-VCH: Weinheim, Germany, 2008.

[2] K. S. Yook, J. Y. Lee, Adv. Mater. 2012, 24, 3169.

[3] M. Zhu, C. Yang, Chem. Soc. Rev. 2013, 42, 4963.

[4] a) S. Hirata, Y. Sakai, K. Masui, H. Tanaka, S. Y. Lee, H. Nomura, N. Nakamura, M. Yasumatsu, H. Nakanotani, Q. Zhang, K. Shizu, H. Miyazaki, C. Adachi, *Nat. Mater.* **2015**, *14*, 330; b) M. Kim, S. K. Jeon, S.-H. Hwang, J. Y. Lee, *Adv. Mater.* **2015**, *27*, 2515;

c) J. W. Sun, J. Y. Baek, K.-H. Kim, C.-K. Moon, J.-H. Lee, S.-K. Kwon, Y.-H. Kim, J.-J. Kim, *Chem. Mater.* **2015**, *27*, 6675; d) T.-A. Lin, T. Chatterjee, W.-L. Tsai, W.-K. Lee, M.-J. Wu, M. Jiao, K.-C. Pan, C.-L. Yi, C.-L. Chung, K.-T. Wong, C.-C. Wu, *Adv. Mater.* **2016**, *28*, 6976.

[5] a) Q. Zhang, B. Li, S. Huang, H. Nomura, H. Tanaka, C. Adachi, *Nat. Photon.* **2014**, *8*, 326; b) Q. Zhang, J. Li, K. Shizu, S. Huang, S. Hirata, H. Miyazaki, C. Adachi, *J. Am. Chem. Soc.* **2012**, *134*, 14706; c) S. Wu, M. Aonuma, Q. Zhang, S. Huang, T. Nakagawa, K. Kuwabara, C. Adachi, *J. Mater. Chem. C* **2014**, *2*, 421; d) M. Liu, Y. Seino, D. Chen, S. Inomata, S.-J. Su, H. Sasabe, J. Kido, *Chem. Commun.* **2015**, *51*, 16353; e) I. Lee, J. Y. Lee, *Org. Electron.* **2016**, *29*, 160; f) S. Y. Lee, C. Adachi, T. Yasuda, *Adv. Mater.* **2016**, *28*, 4626.

[6] a) S. Y. Lee, T. Yasuda, Y. S. Yang, Q. Zhang, C. Adachi, *Angew. Chem. Int. Ed.* **2014**, *53*, 6402; b) P. Rajamalli, N. Senthilkumar, P. Gandeepan, C.-Z. Ren-Wu, H.-W. Lin, C.-H. Cheng, *J. Mater. Chem. C* **2016**, *4*, 900; c) P. Rajamalli, N. Senthilkumar, P. Gandeepan, P.-Y. Huang, M.-J. Huang, C.-Z. Ren-Wu, C.-Y. Yang, M.-J. Chiu, L.-K. Chu, H.-W. Lin, C.-H. Cheng, *J. Am. Chem. Soc.* **2016**, *138*, 628; d) Z. Wang, Y. Li, X. Cai, D. Chen, G. Xie, K. Liu, Y.-C. Wu, C.-C. Lo, A. Lien, Y. Cao, S.-J. Su, *ACS Appl. Mater. Interfaces* **2016**, *8*, 8627.

[7] a) H. Uoyama, K. Goushi, K. Shizu, H. Nomura, C. Adachi, *Nature* **2012**, *492*, 234; b) I. S. Park, S. Y. Lee, C. Adachi, T. Yasuda, *Adv. Funct. Mater.* **2016**, *26*, 1813; c) Y. J. Cho, K. S. Yook, J. Y. Lee, *Sci. Rep.* **2015**, *5*, 7859; d) D. Zhang, M. Cai,

Y. Zhang, D. Zhang, L. Duan, *Mater. Horiz.* **2016**, *3*, 145; e) D. Zhang, M. Cai, Z. Bin, Y. Zhang, D. Zhang, L. Duan, *Chem. Sci.* **2016**, *7*, 3355; f) Y. J. Cho, S. K. Jeon, B. D. Chin, E. Yu, J. Y. Lee, *Angew. Chem. Int. Ed.* **2015**, *54*, 5201; g) W. Liu, C.-J. Zhang, K. Wang, Z. Chen, D.-Y. Chen, F. Li, X.-M. Ou, Y.-P. Dong and X.-H. Zhang, *ACS Appl. Mater. Interfaces* **2015**, *7*, 18930.

[8] a) M. Numata, T. Yasuda, C. Adachi, *Chem. Commun.* **2015**, *51*, 9443; b) T. Hatakeyama, K. Shiren, K. Nakajima, S. Nomura, S. Nakatsuka, K. Kinoshita, J. Ni, Y. Ono, T. Ikuta, *Adv. Mater.* **2016**, *28*, 2777; c) I. S. Park, M. Numata, C. Adachi, T. Yasuda, *Bull. Chem. Soc. Jpn.* **2016**, *89*, 375; d) Y. Kitamoto, T. Namikawa, D. Ikemizu, Y. Miyata, T. Suzuki, H. Kita, T. Sato, S. Oi, *J. Mater. Chem. C* **2015**, *3*, 9122; e) K. Suzuki, S. Kubo, K. Shizu, T. Fukushima, A. Wakamiya Y. Murata, C. Adachi, H. Kaji, *Angew. Chem. Int. Ed.* **2015**, *54*, 15231.

[9] I. S. Park, J. Lee, T. Yasuda, *J. Mater. Chem. C* **2016**, *4*, 7911.

[10] P. A. Vecchi, A. B. Padmaperuma, H. Qiao, L. S. Sapochak, P. E. Burrows, *Org. Lett.* **2006**, *8*, 4211.

[11] a) C. Murawski, K. Leo, M. C. Gather, *Adv. Mater.* **2013**, *25*, 6801; b) M. A. Baldo, C. Adachi, S. R. Forrest, *Phys. Rev. B. Condens. Matter Mater. Phys.* **2000**, *62*, 10967.

[12] C. Adachi, M. A. Baldo, S. R. Forrest, *J. Appl. Phys.* **2000**, *87*, 8049.

[13] T. Takahashi, K. Shizu, T. Yasuda, K. Togashi, C. Adachi, *Sci. Technol. Adv. Mater.* **2014**, *15*, 034202.

Chapter 5

A High-Efficiency Blue Delayed Fluorescence Material Based on Phenazaborin

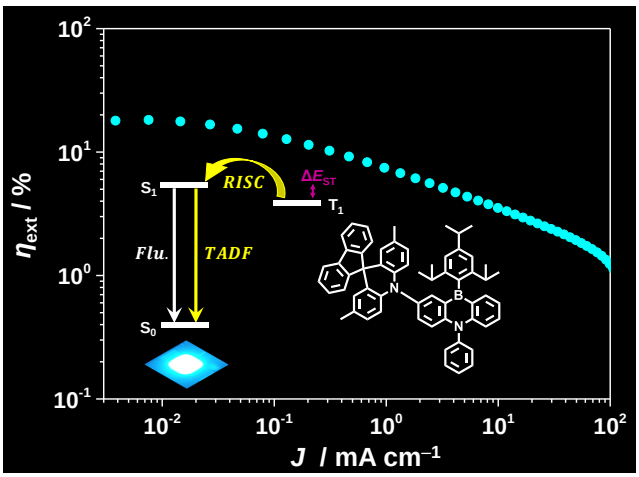

5. 1. Introduction

Versatile TADF molecular systems, including phthalonitrile,[1] triazine,[2] benzophenone,[3] diphenylsulfone,[4] and spirofluorene derivatives[5] have been developed for the last couple of years, and high η_{int} and external quantum efficiency (η_{ext}) have been achieved for OLEDs using these efficient TADF emitters, which are approaching the best performance of phosphorescent OLEDs. Among the key chromaticity components (i.e., red, green, and blue emitters), it is very challenging to explore highly efficient and stable blue TADF molecules because of their intrinsic wide energy gap and high T_1 excited energy levels. So far there have been only a few reports on blue TADF emitters exhibiting both the high electroluminescence (EL) efficiency and color purity.[4a,6]

Boron-containing luminescent π-conjugated molecules have been investigated intensively as optoelectronic functional materials,[7] as unique electronic interactions between the vacant 2p orbital of boron and the π* orbital can lead to produce new electron-accepting materials. Kawashima and coworkers reported that functionalized phenazaborins bearing boron and nitrogen atoms on the central π-conjugated framework, exhibit excellent photoluminescent (PL) properties with the PL quantum yields (Φ_{PL}) of up to 100%.[7a] Nevertheless, phenazaborin derivatives have not yet been applied to emitters in OLEDs, and their EL performance has not been clarified up to now. In view of this, utilizing a phenazaborin acceptor unit in TADF molecular design will provide blue TADF emitters with high PL and EL efficiencies.

In this chapter, a new high-efficiency blue TADF luminophore, MFAc-AzB (**Figure 5-1**) based on angular-linked phenazaborin acceptor and spiroacridan donor units, was designed and synthesized, that accomplishes a remarkably high η_{ext} of 18.2% for blue TADF-based OLEDs with a color coordinate of (0.15, 0.23). TADF emission originates from singlet intramolecular charge transfer (ICT) excited state,[1-5] so the emission wavelength should depend on electronic donor and acceptor strength. Aiming at TADF emission at a short wavelength, MFAc-AzB is designed to weaken the ICT effect by combining a relatively weak phenazaborin acceptor with a spiroacridan donor unit. The phenyl-substituted amino moiety in phenazaborin unit can weaken the electron-withdrawing property of a boron atom owing to participation of a lone pair of nitrogen in π-system, and hence lead to blue shift of ICT emission.

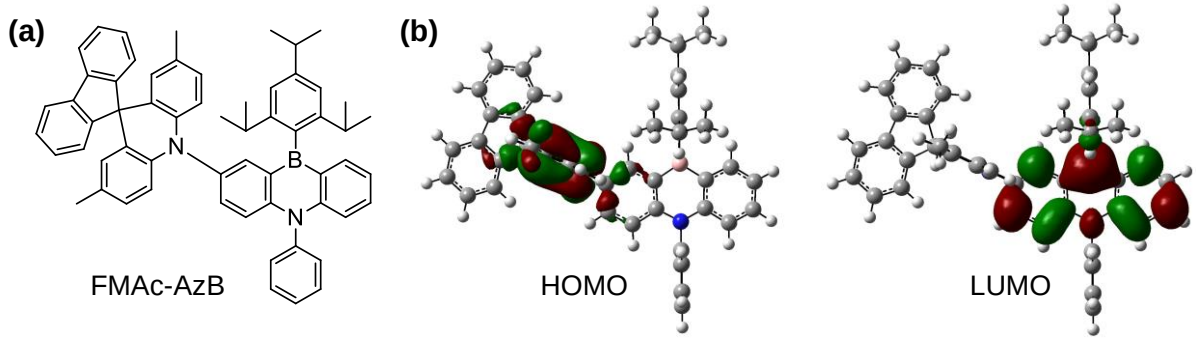

Figure 5-1. (a) Molecular structure and (b) HOMO (−4.66 eV) and LUMO (−1.51 eV) distributions of MFAc-AzB calculated at the B3LYP/6-31G(d) level. The calculated S_1 and T_1 energies are 2.62 and 2.59 eV, respectively.

5. 2. Molecular Geometric and Electronic Structures

Time-dependent density functional theory (TD-DFT) calculations were performed at the B3LYP/6-31G(d) level for understanding the electronic and geometrical structures of MFAc-AzB. As shown in **Figure 5-1b**, the calculated highest occupied molecular orbital (HOMO) and lowest unoccupied molecular orbital (LUMO) are well separated and distributed on spiroacridan donor and phenazaborin acceptor units, respectively, on account of a large dihedral angle of 89.1° between these units. As a result, this clear spatial separation of the frontier orbitals leads to a very small energy gap between the S_1 and T_1 states (ΔE_{ST}) of 0.03 eV, which is required to promote TADF, because the RISC rate constant (k_{RISC}) is inversely proportional to the exponential ΔE_{ST}, following a Boltzmann relationship: $k_{RISC} \propto \exp(-\Delta E_{ST}/k_B T)$.

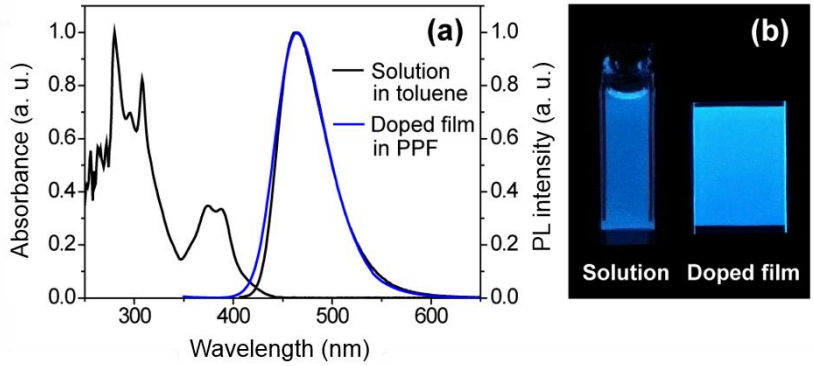

Figure 5-2. (a) Absorption and PL spectra of MFAc-AzB in toluene solution and 20 wt% doped film in PPF at room temperature. (b) Photographs of luminescence recorded under UV irradiation at 365 nm.

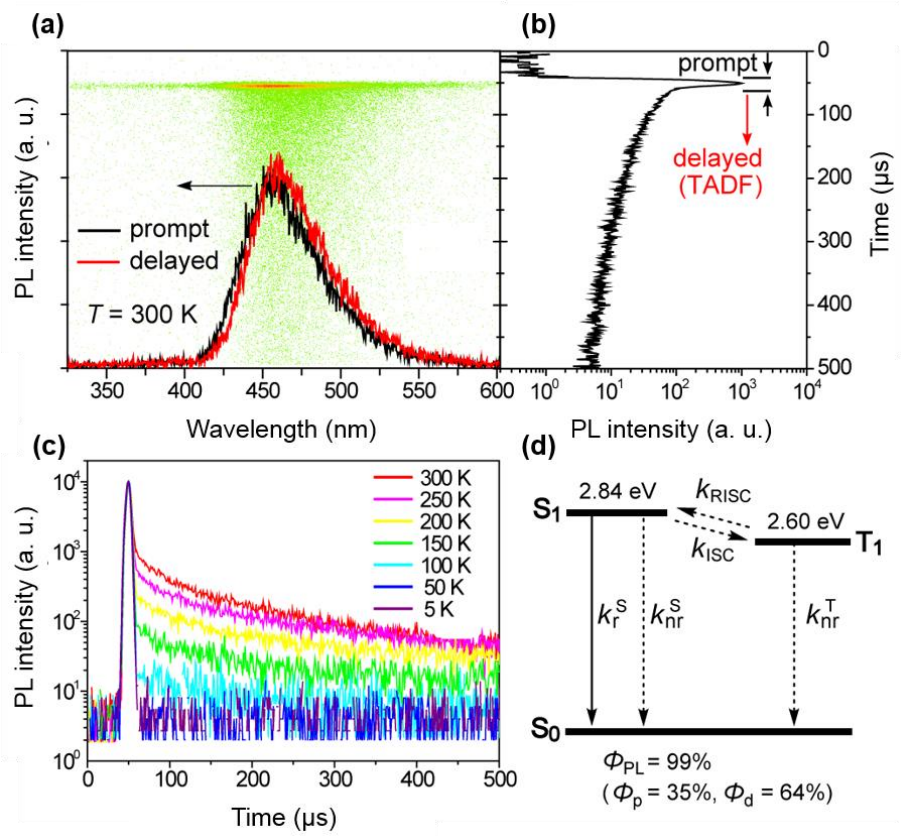

Figure 5-3. (a) Streak image and time-dependent PL emission spectra showing the prompt (black) and delayed (red) components, and (b) transient PL decay curve of a 20 wt%-MFAc-AzB:PPF doped film at 300 K. (c) Temperature dependence of transient PL decay ranging from 5 to 300 K. (d) Postulated PL decay processes for MFAc-AzB; k_r^S and k_{nr}^S are the radiative and non-radiative decay rate constants of the S_1 state, k_{ISC} and k_{RISC} are the ISC ($S_1 \rightarrow T_1$) and RISC ($T_1 \rightarrow S_1$) rate constants, respectively, and k_{nr}^T is the non-radiative rate constant of the T_1 state.

5. 3. Photophyscial Properties

Figure 5-2 presents the UV–vis absorption and PL spectra of MFAc-AzB. The lowest-energy absorption was observed at around 390 nm in toluene solution, which is assigned to the ICT transition mainly associated with electron transfer from the spiroacridan to phenazaborin moieties**.** MFAc-AzB emitted blue PL light with an emission peak (λ_{PL}) at 464 nm, and the absolute Φ_{PL} of MFAc-AzB in toluene increased from 13% to 26% after N_2 bubbling. The PL spectrum of a 20 wt%-MFAc-AzB:PPF (PPF = 2,8-bis(diphenylphosphine oxide)dibenzofuran)[8] doped film showed almost the same blue PL emission (λ_{PL} = 467 nm) solely from the MFAc-AzB emitter without the emission from the PPF host, suggesting that energy transfer from the host to emitter is efficient in the doped film. Remarkably, the absolute Φ_{PL} of an MFAc-AzB neat film and MFAc-AzB:PPF doped film reached to 53% and 99% under N_2 at room temperature, respectively, which are much higher than that in dilute solution,

because of reduced torsional and vibrational non-radiative relaxations in the solid states. Such remarkable enhancement of the PL properties in the neat film, compared to its dilute solution, reveals the aggregation-induced emission (AIE)[9] characteristics of MFAc-AzB. In the doped film, further suppression of concentration quenching effect seems to enhance the Φ_{PL} to almost 100%.

To gain further insight into the photophysical properties, the transient PL decay and its temperature dependence were analyzed for a 20 wt%-MFAc-AzB:PPF doped film by using a streak camera (**Figure 5-3**). At room temperature (300 K), the transient PL decay can be evidently classified into two components (**Figures 5-3a, b**). The first one corresponds to nanosecond-scale prompt fluorescence (lifetime τ_p = 19 ns) from the S_1 to the ground state (S_0). The second one is assigned to microsecond-scale TADF (τ_d = 91 μs). The time-dependent PL spectra for the prompt and delayed components are coincident each other. While the TADF component is almost negligible below 50 K, the intensity of TADF obviously increased with increasing temperature to 300 K (**Figure 5-3c**). Thus, it can be estimated that the overall Φ_{PL} of 99% in the doped film is composed of 35% for the prompt component (Φ_p) and 64% for the delayed component (Φ_d). The Φ_p and Φ_d efficiencies were derived from the emission intensity proportions of the prompt and delayed components in the transient PL signals. The experimental ΔE_{ST} of MFAc-AzB in the doped film was estimated to be 0.24 eV from the S_1 and T_1 energy levels of 2.84 and 2.60 eV determined by the measured fluorescence (300 K) and phosphorescence (5 K) spectra (**Figure 5-4** and **Table 5-2**). From the experimentally obtained PL efficiency and lifetime data, the radiative decay rate constant for $S_1 \rightarrow S_0$ (k_r^S), the intersystem crossing rate constant for $S_1 \rightarrow T_1$ (k_{ISC}), and the RISC rate constant for $T_1 \rightarrow S_1$ (k_{RISC}) of MFAc-AzB in the doped film are calculated to be 6.4×10^6, 1.2×10^7, and 2.0×10^4 s^{-1}, respectively (**Figure 5-3d** and **Table 5-3**).

Table 5-2. Photophysical data of MFAc-AzB.

Compound	λ_{asb} [nm] sol[a)]	λ_{PL} [nm] sol[a)] / film[b)]	Φ_{PL} [%][c)] sol[a)] / film[b)]	τ_p [ns][d)] / τ_d [μs][d)]	HOMO [eV][e)]	LUMO [eV][f)]	E_S / E_T [eV][g)]	ΔE_{ST} [eV][h)]
MFAc-AzB	307, 373, 387	464 / 464	26 / 99	19 / 91	−5.85	−2.90	2.84 / 2.60	0.24

[a)]Measured in oxygen-free toluene solution at room temperature; [b)] 20 wt%-doped thin film in a host matrix (host = PPF); [c)]Absolute PL quantum yield evaluated using an integrating sphere under a nitrogen atmosphere; [d)]PL lifetimes of prompt (τ_p) and delayed (τ_d) decay components for the 20 wt%-doped film measured using a streak camera at 300 K; [e)]Determined by photoelectron yield spectroscopy in pure neat films; [f)]Deduced from the HOMO and optical energy gap (E_g); [g)]Singlet (E_S) and triplet (E_T) energies estimated from onset wavelengths of the emission spectra at 300 and 5 K in the doped films, respectively; [h)]$\Delta E_{ST} = E_S - E_T$.

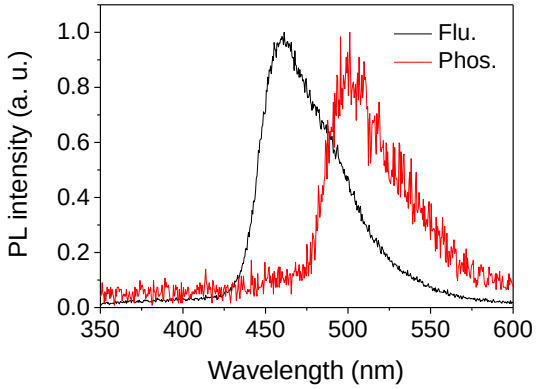

Figure 5-4. PL spectra for prompt fluorescence in the range of 0–300 ns at 300 K (black) and phosphorescence in the range of 1–10 ms at 5 K (red) for 20 wt%-MFAc-AzB-doped film in a PPF host matrix. The lowest excited singlet (S_1) and triplet energy (T_1) levels of MFAc-AzB were determined from the high energy onsets of the fluorescence and phosphorescence, respectively.

Table 5-3. Rate constants and quantum efficiencies for decay processes of MFAc-AzB in the 20 wt%-doped film.

Compound	k_r^S [s^{-1}]	k_{ISC} [s^{-1}]	k_{RISC} [s^{-1}]	Φ_p [%]	Φ_d [%]	Φ_{ISC} [%]	Φ_{RISC} [%]
MFAc-AzB	6.8×10^6	5.6×10^6	2.3×10^6	17	62	83	75

[a)]Abbreviations: k_r^S, radiative rate constant ($S_1\rightarrow S_0$); k_d, delayed-radiative rate constant ($S_1\rightarrow T_1\rightarrow S_1\rightarrow S_0$); k_{ISC}, intersystem-crossing (ISC) rate constant ($S_1\rightarrow T_1$); k_{RISC}, reverse ISC rate constant ($T_1\rightarrow S_1$); Φ_p, quantum efficiency for prompt fluorescence component; Φ_d, quantum efficiency for delayed fluorescence component; Φ_{ISC}, ISC quantum efficiency; Φ_{RISC}, RISC quantum efficiency.

5. 4. Electroluminescence Performance

Next, the performance of MFAc-AzB as a blue TADF emitter was studied by fabricating a multilayer OLED with the following device configuration (**Figure 5-5a**): ITO (100 nm)/HAT-CN (10 nm)/αc-NPD (40 nm)/mCP (10 nm)/20 wt%-MFAc-AzB:PPF (20 nm)/PPF (10 nm)/TPBi (30 nm)/Liq (0.8 nm)/Al (80 nm). In this device, HAT-CN (2,3,6,7,10,11-hexacyano-1,4,5,8,9,12-hexaazatriphenylene) and α-NPD (4,4'-bis[*N*-(1-naphthyl)-*N*-phenylamino]-1,1'-biphenyl) were used as a hole-injection layer and hole-transporting layer; whereas TPBi (1,3,5-tris(*N*-phenylbenzimidazol-2-yl)benzene) and Liq (8-hydroxyquinoline lithium) were employed as an electron-transporting layer and electron-injection material, respectively. In addition, thin layers of mCP (1,5-bis(9-carbazolyl)benzene) and PPF with high T_1 energies (T_1 = 2.9 eV[10] and 3.1 eV,[8] respectively) were inserted to suppress triplet exciton quenching at the neighboring interfaces and to confine the excitons in the MFAc-AzB:PPF emitting layer.

The current density–voltage–luminance (*J*–*V*–*L*) characteristics, η_{ext} plots, and EL spectrum of the MFAc-AzB-based TADF OLED are depicted in **Figure 5-5**. The device exhibited bright blue EL emission with the peak at 473 nm, and the EL spectrum was similar to the corresponding PL spectra (**Figure 5-2a**). Moreover, the MFAc-AzB-based TADF OLED achieved a high η_{ext} of 18.2%, current efficiency (η_c) of 32.6 cd A^{-1}, and power efficiency (η_p) of 25.6 lm W^{-1} at low current densities. Commission Internationale de l'Éclairage (CIE) color coordinates of the device were (0.15, 0.23). In general for TADF OLEDs, the T_1 excitons are directly formed by carrier recombination and then converted to the emissive S_1 excited state through efficient RISC. Therefore, the theoretical maxima of η_{int} and η_{ext} can be estimated by equations **1-18** and **1-19**. Based on the foregoing equations, η_{int} of the MFAc-AzB-based device can be estimated to be 98–99%, which is nearly four times higher than the 25% limit of η_{int} of conventional fluorescent OLEDs. This study has thus achieved a highly efficient blue TADF OLED with η_{ext} over 18%, which is the highest level among blue-emitting TADF OLEDs ever reported.[4a,6]

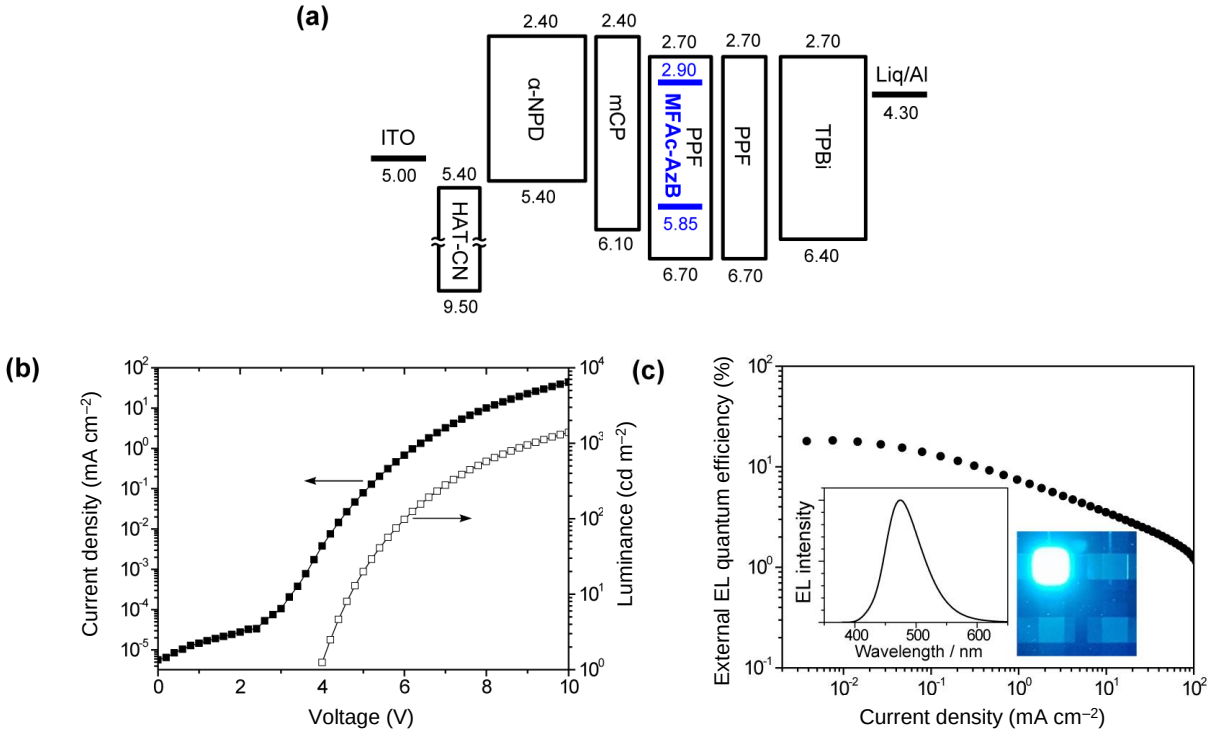

Figure 5-5. (a) Energy-level diagram, (b) current density–voltage–luminance (*J*–*V*–*L*) plots, and (c) external EL quantum efficiency as a function of current density for a blue TADF OLED based on MFAc-AzB as an emitter. The insets in (c) show and an EL spectrum and a photograph of blue EL emission from the device taken at 10 mA cm^{-2}.

Table 5-4. EL performance of the TADF-based OLED.[a)]

TADF emitter	Host	λ_{EL} [nm]	V_{on} [V]	L_{max} [cd m^{-2}]	η_{ext} [%]	η_c [cd A^{-1}]	η_p [lm W^{-1}]	CIE (x, y)
MFAc-AzB	PPF	473	4.0	1,900	18.2	32.6	25.6	(0.15, 0.23)

[a)]Abbreviations: λ_{EL} = EL emission maximum, V_{on} = turn-on voltage at 1 cd m^{-2}, L_{max} = maximum luminance, η_{ext} = maximum external EL quantum efficiency, η_c = maximum current efficiency, η_p = maximum power efficiency, CIE = Commission Internationale de l'Éclairage color coordinates measured at 10 mA cm^{-2}, PPF = 2,8-bis(diphenylphosphoryl)dibenzofuran.

5. 5. Experimental Section

5. 5. 1. General Methods

Quantum chemical calculation for MFAc-AzB was performed using the Gaussian 09 program package. Geometries in the ground state were optimized using the B3LYP functional with the 6-31G(d) basis set. Low-lying excited singlet and triplet states were computed using the optimized structures with time-dependent density functional theory (TD-DFT) at the same level. NMR spectra were recorded on a Bruker Avance III 500 or Avance III 400 spectrometer. Chemical shifts of ^{1}H and ^{13}C NMR signals were quoted to tetramethylsilane (δ = 0.00) and $CDCl_3$ (δ = 77.0) as internal standards, respectively. Matrix-assisted laser desorption ionization time-of-flight (MALDI-TOF) mass spectra were collected on an Autoflex III spectrometer (Bruker Daltonics) using dithranol as the matrix. Organic thin films for photophysical measurements were vacuum-deposited under high vacuum (~ 7 × 10^{-5} Pa) onto quartz glass and Si (100) substrates, which were pre-cleaned by acetone and isopropanol. UV–vis absorption spectra and photoluminescence (PL) spectra were measured with a Jasco V-670Y spectrometer and a Jasco FP-8600Y spectrophotometer, respectively, in degassed spectral grade solvents. The photoluminescence quantum yields (Φ_{PL}) were determined using a Jasco ILF-835Y and calibrated integrating sphere system. The transient PL properties of doped films were evaluated using a Hamamatsu Photonics C9300 Streak camera with an N_2 gas laser (λ = 337 nm, pulse width = 500 ps, repetition rate = 20 Hz) under vacuum (< 4 × 10^{-1} Pa). The HOMO energy level of the sample was determined using a Riken-Keiki AC-2 ultraviolet photoelectron spectrometer. The LUMO energy level was estimated by subtracting the optical energy gap (E_g) from the measured HOMO energy; the E_g value was determined from the onset position of the PL spectrum of a neat film.

5. 5. 2. Preparation of Materials

All regents and anhydrous solvents were purchased from Sigma-Aldrich, Tokyo Chemical Industry (TCI), or Wako Pure Chemical Industries, and were used as received unless otherwise noted. A host material, 2,8-bis(diphenylphosphine oxide)dibenzofuran (PPF) was prepared according to the literature procedure,[16] and then further purified by vacuum sublimation twice. Other OLED materials were purchased from Luminescence Technology Corporation. The detailed synthetic routes for MFAc-AzB are outlined in **Scheme 5-1**.

5. 5. 3. Synthesis

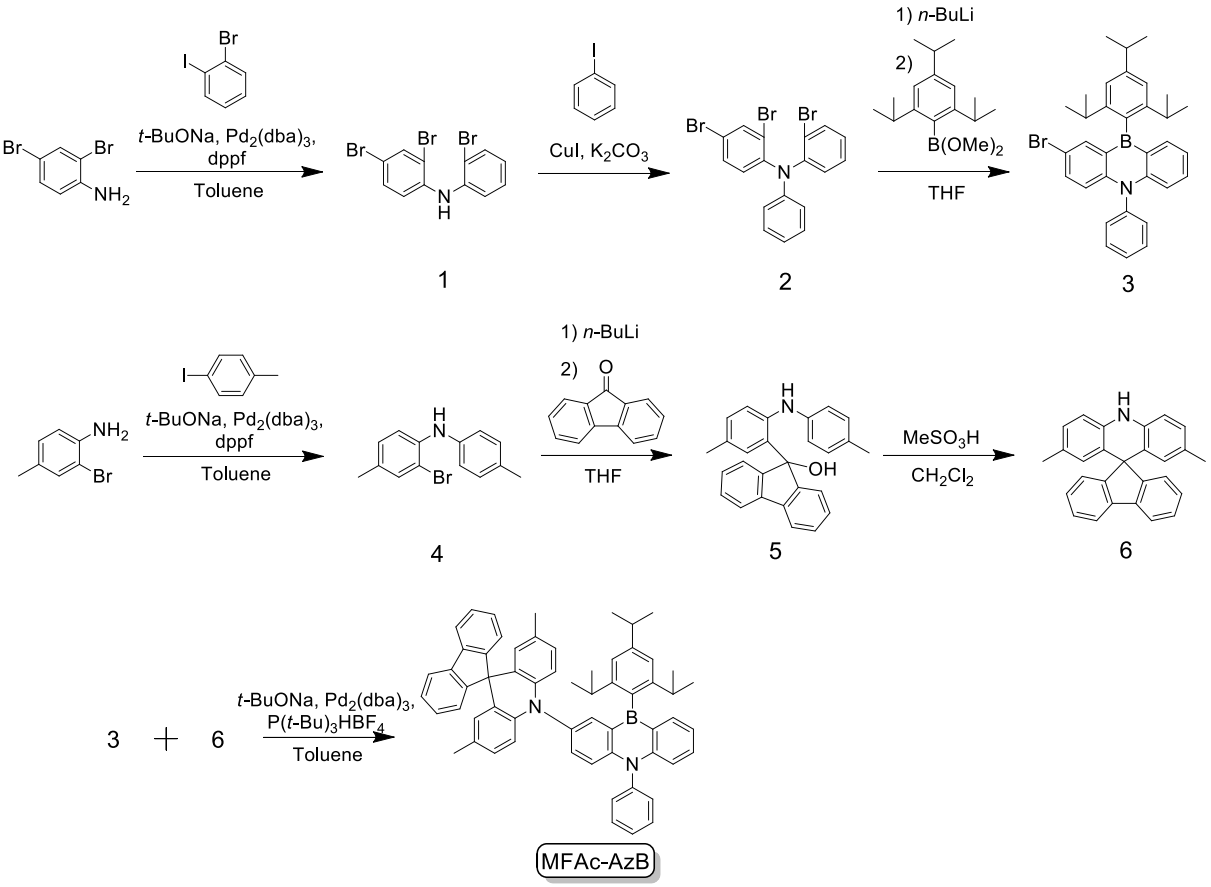

Scheme 5-1. Synthetic routes of MFAc-AzB.

MFAc-AzB was synthesized using Buchwald–Hartwing amination of a bromo-phenazoborin precursor (**3**) with spiroacridan (**6**) by employing $Pd_2(dba)_3/P(t\text{-}Bu)_3HBF_4$ catalytic system in 77% yield without affecting the boron center. The final product was purified by column chromatography, followed by temperature-gradient vacuum sublimation. Therefore, the chemical and thermal stability of MFAc-AzB are high enough for OLED applications because of effective steric protection of the 2,4,6-triisopropylphenyl group on the boron center.

Synthesis of 2,4-dibromo-*N*-(2-bromophenyl)aniline (1): A solution of 2,4-dibromoaniline (25.1 g, 100 mmol), sodium *tert*-butoxide (14.4 g, 150 mmol) in toluene (250 mL) was stirred for 30 min under nitrogen atmosphere at room temperature. Then, 1-bromo-2-iodobenzene (28.3 g, 100 mmol), $Pd_2(dba)_3$ (0.46 g, 0.5 mmol), and 1,1'-bis(diphenylphosphino)ferrocene (dppf, 0.54 g, 1.0 mmol) were added to the solution. The mixture was refluxed for 6 h. After cooling to room temperature, the precipitate was filtered through a Celite pad with chloroform, and the filtrate was concentrated under reduced pressure. The product was purified by column chromatography on silica gel (hexane/CH_2Cl_2 = 9:1, v/v), and recrystallized from hexane to give 1 as a white solid (yield = 31.3 g, 77%). ^{1}H NMR (500 MHz, $CDCl_3$): δ 7.71 (d, *J* = 2.2 Hz, 1H), 7.59 (dd, *J* = 8.0 Hz, 1.2 Hz, 1H), 7.31 (dd, *J* = 8.7 Hz, 2.2 Hz, 1H), 7.27-7.22 (m, 2H), 7.13 (dd, *J* = 8.7 Hz, 2.2 Hz, 1H), 6.90-6.86 (m, 1H), 6.38 (br, 1H); MS (MALDI-TOF) *m*/*z*: 402.98 $[M]^+$, calcd 402.82.

Synthesis of 2,4-dibromo-*N*-(2-bromophenyl)-*N*-phenylaniline (2): A mixture of **1** (30.8 g, 75.8 mmol), iodobenzene (77.3 g, 379 mmol), CuI (14.4 g, 75.8 mmol), and K_2CO_3 (21.0 g, 151.6 mmol) was stirred for 72 h at 190 °C under nitrogen atmosphere. After cooling to room temperature, the precipitate was filtered through a Celite pad with toluene, and the filtrate was concentrated under reduced pressure. The product was purified by column chromatography on silica gel (hexane/CH_2Cl_2 = 9:1, v/v) to give **2** as a white solid (yield = 28.5 g, 78%). ^{1}H NMR (500 MHz, $CDCl_3$): δ 7.75 (d, *J* = 2.3 Hz, 1H), 7.63 (dd, *J* = 8.0 Hz, 1.5 Hz, 1H), 7.36 (dd, *J* = 8.6 Hz, 2.3 Hz, 1H), 7.28-7.20 (m, 3H), 7.09 (dd, *J* = 8.0 Hz, 1.6 Hz, 1H), 7.06 (td, *J* = 7.4 Hz, 1.60 Hz, 1H), 6.99 (dd, *J* = 7.4 Hz, 1.1 Hz, 1H), 6.95 (d, *J* = 8.6 Hz, 1H), 6.72 (dd, *J* = 7.8 Hz, 1.1 Hz, 2H); MS (MALDI-TOF) *m*/*z*: 479.07 $[M]^+$, calcd 478.85.

Synthesis of 2-bromo-5-phenyl-10-(2,4,6-triisopropylphenyl)-5,10-dihydrodibenzo[*b*,*e*][1,4]azaborine (3): To a solution of **2** (28.0 g, 58.0 mmol) in dry THF (290 mL) was added dropwise *n*-butyllithium (1.6 M, 72.5 mL, 31.8 mmol) at −78 °C under nitrogen atmosphere. The mixture was stirred for 30 min at that temperature. Then, a solution of dimethyl (2,4,6-triisopropylphenyl)boronate (16.0 g, 58.0 mmol) in dry THF (30 mL) was added dropwise to the solution at −78 °C. The reaction mixture was allowed to react for 1 h at −78 °C, and then further reacted for 2 h at room temperature. After that, the mixture was reflux for 1 h. After heating up to room temperature, the reaction was quenched by addition of a large amount of water. The product was extracted with chloroform and dried over anhydrous magnesium

sulfate. After filtration and evaporation, the crude product was purified by column chromatography on silica gel (hexane/CH_2Cl_2 = 9:1, v/v), and then recrystallized from acetonitrile to afford **3** as a white solid (yield = 21.4 g, 69%). ^{1}H NMR (500 MHz, $CDCl_3$): δ 8.02 (d, *J* = 2.5 Hz, 1H), 7.90 (dd, *J* = 7.6 Hz, 1.5 Hz, 1H), 7.73 (t, *J* = 7.2 Hz, 2H), 7.65 (tt, *J* = 7.4 Hz, 1.1 Hz, 1H), 7.53-7.47 (m, 2H), 7.44 (dd, *J* = 8.4 Hz, 1.0 Hz, 2H), 7.12-7.09 (m, 3H), 6.80 (d, *J* = 8.7 Hz, 1H), 6.72 (d, *J* = 9.2 Hz, 1H), 3.02 (sep., *J* = 6.9 Hz, 1H), 2.42 (sep., *J* = 6.8 Hz, 2H), 1.39 (d, *J* = 6.9 Hz, 6H), 1.05 (d, *J* = 6.8 Hz, 6H), 1.02 (d, *J* = 6.8 Hz, 6H); MS (MALDI-TOF) *m*/*z*: 535.46 $[M]^+$, calcd 535.20.

Synthesis of 2-bromo-4-methyl-*N*-(*p*-tolyl)aniline (4): A solution of 2-bromo-4-methylaniline (48.4 g, 260 mmol), sodium *tert*-butoxide (37.5 g, 390 mmol) in dry toluene (520 mL) was stirred for 30 min under nitrogen atmosphere at room temperature. Then, 1-iodo-4-methylbenzene (64.2 g, 286 mmol), $Pd(OAc)_2$ (2.38 g, 2.6 mmol), and 1,1'-bis(diphenylphosphino)ferrocene (dppf, 1.44 g, 2.6 mmol) were added to the solution. The mixture was refluxed for 8 h. After cooling to room temperature, the precipitate was filtered through a Celite pad with chloroform, and the filtrate was concentrated under reduced pressure. The product was purified by column chromatography on silica gel (hexane/CH_2Cl_2 = 9:1, v/v) to give **4** as a white solid (yield = 54.8 g, 74%). ^{1}H NMR (500 MHz, $CDCl_3$): δ 7.56 (d, *J* = 8.3 Hz, 1H), 7.34 (d, *J* = 1.4 Hz, 1H), 7.10 (d, *J* = 8.0 Hz, 2H), 7.07 (d, *J* = 8.3 Hz, 1H), 7.00 (d, *J* = 8.4 Hz 2H), 6.96-6.91 (m, 1H), 2.32 (s, 3H), 2.25 (s, 3H); MS (MALDI-TOF) *m*/*z*: 275.71 $[M]^+$, calcd 275.03.

Synthesis of 9-(5-methyl-2-(*p*-tolylamino)phenyl)-9*H*-fluoren-9-ol (5): To a solution of **4** (21.0 g, 76.0 mmol) in dry THF (300 mL) was added dropwise *n*-butyllithium (1.6 M, 97.4 ml, 156 mmol) at −78 °C under nitrogen atmosphere. The mixture was stirred for 1 min at room temperature. After heating up to 0 °C, 9*H*-fluorenone (15.1 g, 83.6 mmol) was added to the mixture, and the mixture was further stirred for 6 h at room temperature. The reaction was quenched by addition of a large amount of water. The product was extracted with chloroform and dried over anhydrous magnesium sulfate. After filtration and evaporation, the product was used in the next reaction without further purification.

Synthesis 2,7-dimethyl-10*H*-spiro[acridine-9,9'-fluorene] (6): To a solution of crude **5** in dichloromethane (300 mL) was added methanesulfonic acid (14.6 g, 152 mmol) at room temperature. The mixture was refluxed for 1 h under air. After cooling to room temperature,

the mixture was concentrated under reduced pressure. The residue was purified by column chromatography on silica gel (hexane/CH_2Cl_2 = 4:1, v/v) to give **6** (yield = 12.2 g, 45%). ^{1}H NMR (400 MHz, $CDCl_3$): δ 7.78 (br, 1H), 7.37-7.18 (m, 14H); MS (MALDI-TOF) *m*/*z*: 358.98 $[M]^+$ calcd 359.17; found, 358.98.

Synthesis of 2,7-dimethyl-10-(5-phenyl-10-(2,4,6-triisopropylphenyl)-5,10-dihydrodibenzo[*b*,*e*][1,4]azaborin-2-yl)-10*H*-spiro[acridine-9,9'-fluorene] (MFAc-AzB): A solution of 6 (1.58 g, 4.4 mmol), sodium *tert*-butoxide (0.77 g, 8.0 mmol) in dry toluene (40 mL) was stirred for 30 min under nitrogen atmosphere at room temperature. To the solution were added 3 (2.15 g, 4.0 mmol), $Pd_2(dba)_3$ (0.073 g, 0.08 mmol), and P(*t*-Bu)$_3$HBF$_4$ (0.093 g, 0.32 mmol). The mixture was refluxed for 14 h. After cooling to room temperature, the precipitate was filtered through a Celite pad with chloroform, and the filtrate was concentrated under reduced pressure. The product was purified by column chromatography on silica gel (hexane/CH_2Cl_2 = 7:3, v/v), and recrystallized from acetonitrile to give MFAc-AzB as a light yellow solid (yield = 2.5 g, 77%). ^{1}H NMR (500 MHz, $CDCl_3$): δ 8.06 (d, *J* = 2.0 Hz, 1H), 7.97 (dd, *J* = 7.5 Hz, 1.2 Hz, 1H), 7.79-7.75 (m, 4H), 7.69 (t, *J* = 7.5 Hz, 1H), 7.59 (d, *J* = 7.3 Hz, 2H), 7.56-7.50 (m, 2H), 7.41 (d, *J* = 7.6 Hz, 2H), 7.34 (t, *J* = 7.3 Hz, 2H), 7.20-7.11 (m, 4H), 7.06 (s, 2H), 6.90 (d, *J* = 8.7 Hz, 1H), 6.61 (d, *J* = 8.4 Hz, 2H), 6.26 (d, *J* = 8.4 Hz, 2H), 6.13 (s, 2H), 2.97 (sep., *J* = 6.8 Hz, 1H), 2.57 (sep., *J* = 6.7 Hz, 2H), 1.90 (s, 6H), 1.35 (d, *J* = 6.9 Hz, 6H), 1.06 (d, *J* = 6.8 Hz, 6H), 1.03 (d, *J* = 6.8 Hz, 6H); ^{13}C NMR (125 MHz, $CDCl_3$, δ): 156.05, 150.41, 147.90, 146.31, 145.57, 141.64, 139.93, 139.66, 137.74, 134.89, 132.89, 132.52, 131.00, 130.41, 129.12, 129.04, 128.29, 127.83, 127.42, 127.34, 125.80, 124.77, 120.07, 119.92, 119.72, 116.90, 114.60, 56.97, 35.26, 34.24, 24.48, 24.44, 24.19, 20.38; HRMS (FAB) *m*/*z*: 814.44584 $[M]^+$, calcd 814.44583.

5. 5. 4. OLED Fabrication and Measurements

Indium tin oxide (ITO)-coated glass substrates were cleaned with detergent, deionized water, acetone, and isopropanol, and then treated with UV-ozone treatment for 15 min, before being loaded into a vacuum evaporation system. The organic layers were thermally evaporated on the substrates under vacuum (< 6×10^{-5} Pa) with an evaporation rate of < 0.3 nm s^{-1}. A cathode aluminum layer was then deposited through a shadow mask. The layer thickness and deposition rate were monitored in situ during deposition by an oscillating quartz thickness

monitor. OLED device properties were measured using a Keithley source meter 2400 and a Konica Minolita CS-2000

5. 6. Conclusion

A new phenazaborin-based luminophore, MFAc-AzB, have been presented for OLED application. A highly efficient blue TADF material exhibiting a high Φ_{PL} of 99% has been successfully developed by combining phenazaborin acceptor and spiroacridan donor units. An OLED employing MFAc-AzB as a blue TADF emitter has achieved a notably high maximum η_{ext} of 18.2%. The molecular design featuring the phenazaborin core can provide a promising way for further developing sophisticated high-efficiency blue TADF molecules for OLED applications.

References

[1] H. Uoyama, K. Goushi, K. Shizu, H. Nomura, C. Adachi, *Nature* **2012**, *492*, 234.

[2] a) S. Y. Lee, T. Yasuda, H. Nomura, C. Adachi, *Appl. Phys. Lett.* **2012**, *101*, 093306; b) S. Hirata, Y. Sakai, K. Masui, H. Tanaka, S. Y. Lee, H. Nomura, N. Nakamura, M. Yasumatsu, H. Nakanotani, Q. Zhang, K. Shizu, H. Miyazaki, C. Adachi, *Nat. Mater.* **2015**, *14*, 330.

[3] a) S. Y. Lee, T. Yasuda, Y. S. Yang, Q. Zhang, C. Adachi, *Angew. Chem. Int. Ed.* **2014**, *126*, 6520; b) S. Y. Lee, T. Yasuda, I. S. Park, C. Adachi, *Dalton Trans.* **2015**, *44*, 8356.

[4] a) Q. Zhang, B. Li, S. Huang, H. Nomura, H. Tanaka, C. Adachi, *Nat. Photon.* **2014**, *8*, 326; b) Q. Zhang, J. Li, K. Shizu, S. Huang, S. Hirata, H. Miyazaki, C. Adachi, *J. Am. Chem. Soc.* **2012**, *134*, 14706.

[5] K. Nasu, T. Nakagawa, H. Nomura, C.-J. Lin, C.-H. Cheng, M.-R. Tseng, T. Yasuda, C. Adachi, *Chem. Commun.* **2013**, *49*, 10385.

[6] a) M. Numata, T. Yasuda, C. Adachi, *Chem. Commun.* **2015**, *51*, 9443; b) W. Sun, J. Y. Baek, K.-H. Kim, C.-K. Moon, J.-H. Lee, S.-K. Kwon, Y.-H. Kim, J.-J. Kim, *Chem. Mater.* **2015**, 27, 6675; c) M. Kim, S. K. Jeon, S.-H. Hwang, J. Y. Lee, *Adv. Mater.* **2015**, *27*, 2515.

[7] a) T. Agou, J. Kobayashi, T. Kawashima, *Chem. Commun.* **2007**, 3204; b) T. Ago, J. Kobayashi, T. Kawashima, *Org. Lett.* **2006**, *8*, 2241; c) T. Agou, M. Sekine, J. Kobayashi, T. Kawashima, *Chem. Commun.* **2009**, 1894; d) T. Agou, T. Kojima, J. Kobayashi, T. Kawashima, *Org. Lett.* **2009**, *11*, 3534; e) A. Wakamiya, K. Mori, S. Yamaguchi, *Angew. Chem. Int. Ed.* **2007**, *46*, 4273; f) C.-H. Zhao, A. Wakamiya, Y. Inukai, S. Yamaguchi, *J. Am. Chem. Soc.* **2006**, *128*, 15934; g) T. Noda, Y. Shirota, *J. Am. Chem. Soc.* **1998**, *120*, 9714; b) H. Doi, M. Kinoshita, K. Okumoto, Y. Shirota, *Chem. Mater.* **2003**, *15*, 1080; h) N. Matsumi, K. Naka, Y. Chujo, *J. Am. Chem. Soc.* **1998**, *120*, 5112; i) C. D. Entwistle, T. B. Marder, *Chem. Mater.* **2004**, 16, 4574; j) W. L. Jia, X. D. Feng, D. R. Bai, Z. H. Lu, S. Wang, G. Vamvounis, *Chem. Mater.* **2005**, *17*, 164.

[8] P. A. Vecchi, A. B. Padmaperuma, H. Qiao, L. S. Sapochak, P. E. Burrows, *Org. Lett.* **2006**, *8*, 4211.

[9] A. Qin, B. Z. Tang, *Aggregation-Induced Emission: Fundamentals*, Wiley, United Kingdom, **2013**.

[10] R. J. Holmes, S. R. Forrest, Y.-J. Tung, R. C. Kwong, J. J. Brown, S. Garon, M. E. Thompson, *Appl. Phys. Lett.* **2003**, *82*, 2422.

Chapter 6

Linear-Shaped Delayed Fluorescence Materials Based on Terephthalonitrile with Horizontally Oriented Dipoles for High-Efficiency Electroluminescence

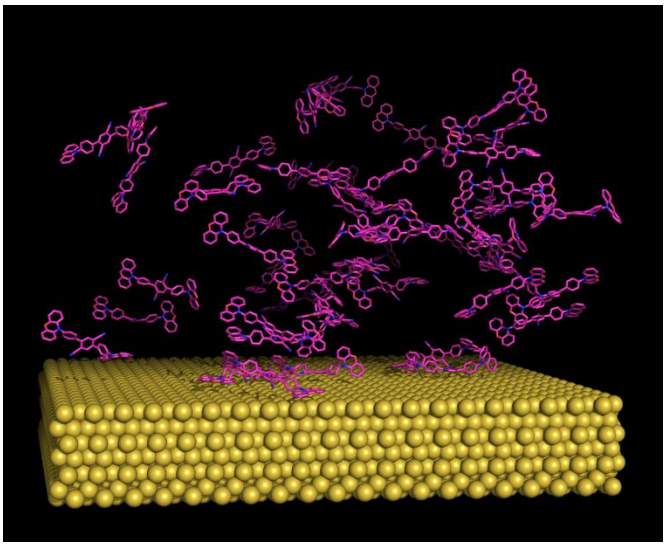

6. 1. Introduction

As mentioned in General Introduction, the light out-coupling efficiency (η_{out}) is considered to be 20% due to the fact that the emission takes place in a high refractive index (n) material and the energy of an excited emitter can be radiated into different optical channels of the OLED layered system.[1] Hence, only a small fraction of the light emission is finally extracted from the device into the outside medium air. Thus, various approaches have been introduced to enhance η_{out} such as scattering methods,[2] microcavity structures,[3] low-index grids,[4] and surface corrugations.[5] Although these approaches show high efficiencies by the enhancement of η_{out}, requiring extra efforts during production and leading to overall expensive fabrication cost. An alternative way to enhance η_{out} is to introduce an advanced molecular design with horizontally oriented dipoles, because molecules emit the light in vertical direction to its transition dipole moment,[6] and hence induce high η_{out} with conventional fluorescent,[7] organometallic phosphorescent,[8] and even TADF emitters.[9]

In this chapter, a strategy to realize a high external electroluminescence (EL) quantum efficiency (η_{ext}) are reported through advanced molecular design of donor–acceptor–donor (D–A–D) type molecules, which consist of a central terephthalonitrile (TPN) acceptor moiety with three donor moieties, benzo[*a*]carbazole (BCz), 9,9-dimethylacridan (Ac), and phenoxazine (Px), linked by π-conjugated phenylene bridges by employing a linear shaped molecular structure (**Figure 6-1a**), which is well known to have large transition dipole moments owing to their long molecular axis, and hence these materials horizontally oriented onto the substrate in vacuum-deposited neat films or even doped films with a host material, leading to enhancement of η_{out}. The electron-withdrawing TPN moiety was selected in consideration of its good electron-accepting ability, whereas, the electron-donating moieties were adopted owing to substantially different strength of electron-donating ability in order of BCz < Ac < Px for fine color tuning from light-blue to yellow. These electron donor and acceptor moieties are linked via the π-conjugated phenylene bridges for enhancing a radiative decay constant, maintaining a small ΔE_{ST}. These newly designed TADF emitters with light-blue (BCz-TPN), green (Ac-TPN), and yellow (Px-TPN) emissions demonstrated high η_{out} values of up to 30.9% through their horizontally oriented dipoles of TPN-based molecules and hence exhibited high η_{ext} of up to 23.4% in TADF-based OLEDs.

6. 2. Molecular Design and Quantum Chemical Calculations

The geometric and electronic structures of TPN molecules were calculated by time-dependent density functional theory (TD-DFT) at B3LYP/6-31G(d,p) level using the Gaussian 09 program. As shown in **Figure 6-1b**, all of the molecules exhibit proper separation of the HOMO and LUMO distributions. The HOMOs of TPN molecules are predominantly distributed over the peripheral electron-donating donor moieties, whereas the LUMOs are mainly located on the central electron-accepting TPN core as well as the π-conjugated phenylene bridges, because the proton atoms of donor moieties in the *peri*-position lead to highly twisted geometry between the π-conjugated phenylene bridges and donor units, decreasing the exchange interaction integral of the HOMO and LUMO wavefunctions of a molecule. Consequently, the calculated dihedral angles between the peripheral donor unit and the π-conjugated phenylene bridge were to be 71–72˚ for BCz-TPN, 88–89˚ for Ac-TPN, and 89–90˚ for Px-TPN, and hence induce the extremely small calculated ΔE_{ST} values of less than 0.034 eV. The calculation results are depicted in **Table 6-1** for more detail.

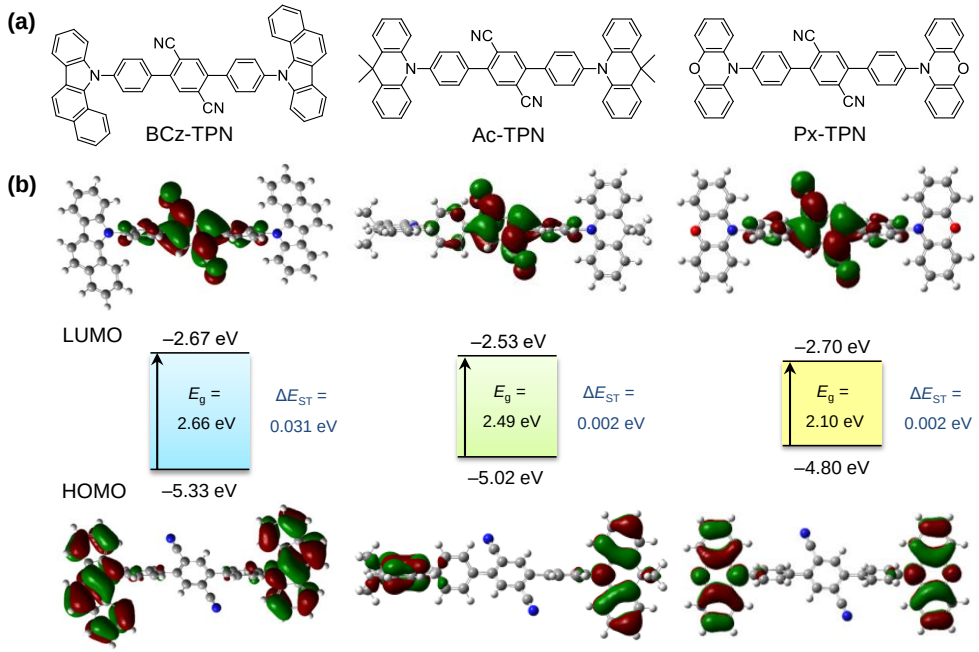

Figure 6-1. (a) Molecular structures, (b) HOMO–LUMO distributions and energy levels characterized by TD-DFT calculation at the B3LYP/6-31G(d,p) level of TPN-based TADF molecules.

To better understand molecular geometries of TPN derivatives in a solid state, the single crystal structures are also depicted in **Figure 6-2**. The single crystals were obtained from a mixture of chloroform and methanol at room temperature, and the structures were determined

by X-ray single crystal analysis. Molecules of TPN derivatives show the symmetric molecular geometry and large dihedral angles between the peripheral donor unit and the π-conjugated phenylene bridge of 63–64˚ for BCz-TPN, 75–76˚ for Ac-TPN, and 78–79˚ for Px-TPN, which show practically corresponding to the calculated dihedral angles. In consequence of our molecular design, both optical- and electrical-generated singlet and triplet excitons can be utilized for the emission through efficient up-conversion from the T_1 state to the emissive S_1 state, leading to ICT transition from peripheral donor moieties to a central acceptor core by highly distorted geometries of TPN molecules.

Table 6-1. TD-DFT calculation results. The lowest excited singlet (S_1) and triplet energy (T_1) energies (vertical transition), oscillator strength (*f*), and transition configurations of the TPN derivatives calculated by TD-DFT at the B3LYP/6-31G(d,p).

Compound	State	*E* (eV)	*f*	Main configuration		ΔE_{ST} (eV)
BCz-TPN	S_1	2.316	0.0479	H → L	0.695	0.034
				H−1 → L	0.119	
	S_2	2.332	0.0040	H−1 → L	0.696	
				H → L	−0.120	
	T_1	2.282	0	H → L	0.659	
				H−1 → L	0.200	
	T_2	2.307	0	H−1 → L	0.665	
				H → L	−0.206	
Ac-TPN	S_1	2.035	0.0002	H → L	0.679	0.002
				H−1 → L	−0.186	
	S_2	2.035	0	H−1 → L	0.679	
				H → L	0.186	
	T_1	2.033	0	H → L	0.685	
				H−1 → L	−0.163	
	T_2	2.033	0	H−1 → L	0.703	
				H → L	0.163	
Px-TPN	S_1	1.726	0.0004	H → L	0.704	0.002
	S_2	1.727	0	H−1 → L	0.704	
	T_1	1.724	0	H → L	0.704	
	T_2	1.726	0	H−1 → L	0.704	

H → L represents the HOMO to LUMO transition. Excitation configurations with the highest contributions are presented, together with the corresponding transition symmetry and nature of the involved orbitals.

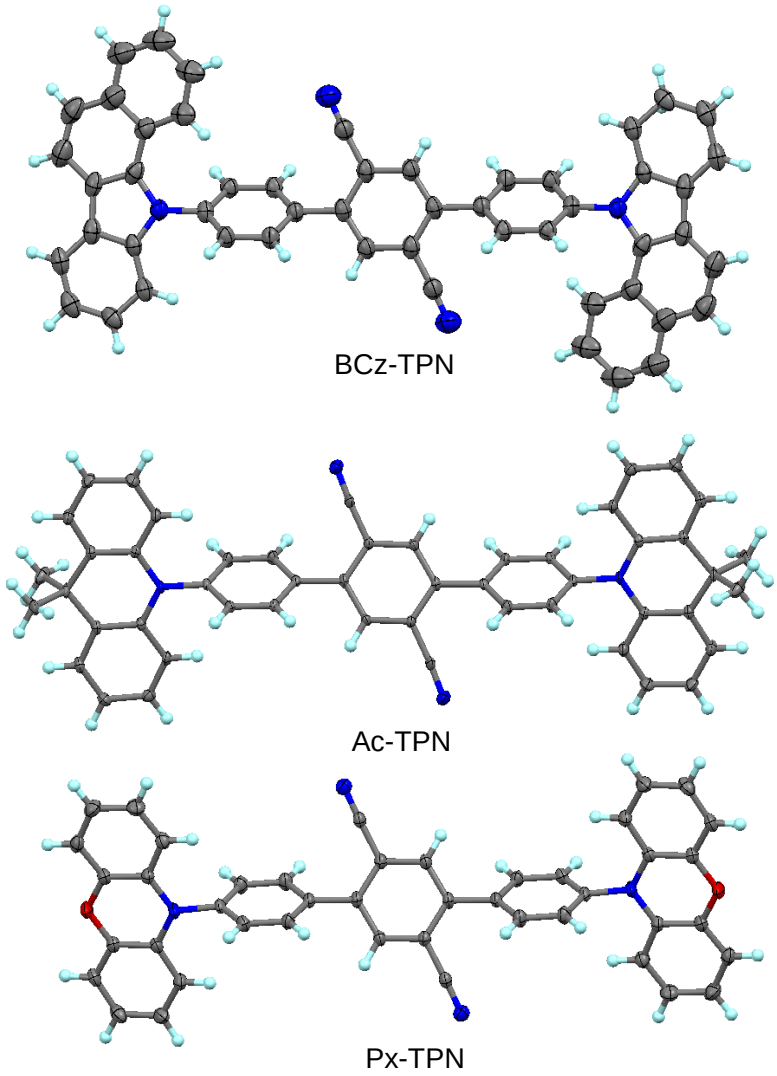

Figure 6-2. ORTEP diagram of TPN-based molecules with 50% probability ellipsoids. Atom color code: C, gray; N, blue; H, light-blue; O, red.

6. 3. Photophysical Properties

The molecular orbital distributions are well matched in the photophysical properties of the TPN-based emitters. As shown in **Figure 6-3**, the lowest energy absorption of TPN-based emitters in toluene at around 350–450 nm is attributed to the ICT transition from the peripheral donor moieties to the central acceptor core. Moreover, TPN-based emitters exhibit light-blue, green, and orange emission with a peak wavelength of 486, 528, and 600 nm, respectively, which color-tunable results are corresponding to the calculated molecular energy gap (E_g) between the HOMO and LUMO, in accordance with the different strengths of electron-donating ability of the donor units.

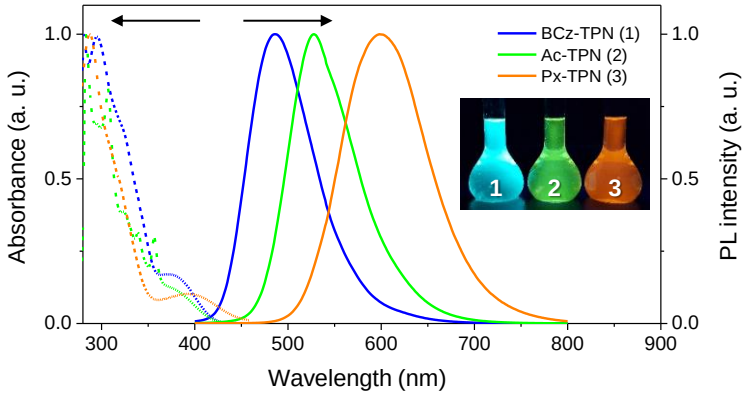

Figure 6-3. UV–vis absorption and PL spectra of TPN-based TADF emitters in toluene. The inset shows luminescent images under UV irradiation at 365 nm

Next, we turn our attention to the photophysical and TADF characteristics in solid state. Here, we prepared doped films of TPN-based emitters with a suitable host matrix. Each of host materials was selected to suppress non-radiative energy transfer of triplet excitons from the excited TADF emitter to the T_1 state of a host material and to confine the T_1 excitons within the emitting molecules (i.e., E_T; BCz-TPN = 2.72 eV < 2,8-bis(diphenylphosphoryl)dibenzofuran (PPF) = 3.1 eV,[10] Ac-TPN = 2.57 eV < 3,3'-bis(carbazol-9-yl)-1,1'-biphenyl (mCBP) = 2.9 eV,[11] and Px-TPN = 2.42 eV < 4,4'-bis(*N*-carbazolyl)-1,1'-biphenyl (CBP) = 2.56 eV)[12]. **Figure 6-4a** shows the emission colors of doped films ranging from light-blue to yellow with the emission maximum of 480, 507, and 556 nm, respectively. Moreover, their doped films exhibited the high absolute Φ_{PL} of nearly 80%.

Figures 6-4b as exemplified figure displays a streak image of a 6 wt%-Px-TPN:CBP doped film, which indicate a prompt component with a nanosecond-scale transient decay time (τ_p) of 25 ns and a delayed component with a micro-scale transient decay time (τ_d) of 1.2 μs in the time scale of 10 μs at 300 K. Corresponding to the prompt and delayed lifetimes, prompt (Φ_p) and delayed (Φ_p) PL quantum efficiencies were estimated 17% and 62%, respectively. Moreover, PL spectra of the prompt and delayed components show similar behavior (**Figure 6-4b**), which are indicated that the delayed emission is originated from S_1 to ground state (S_0) via the RISC process. As other evidence of up-conversion, the delayed PL intensity increases with increasing temperature from 5 to 300 K by thermal activation of the RISC process (**Figure 6-4c**). Similar transient behavior was obviously observed in the other TPN-based emitters (**Figure 6-5**).

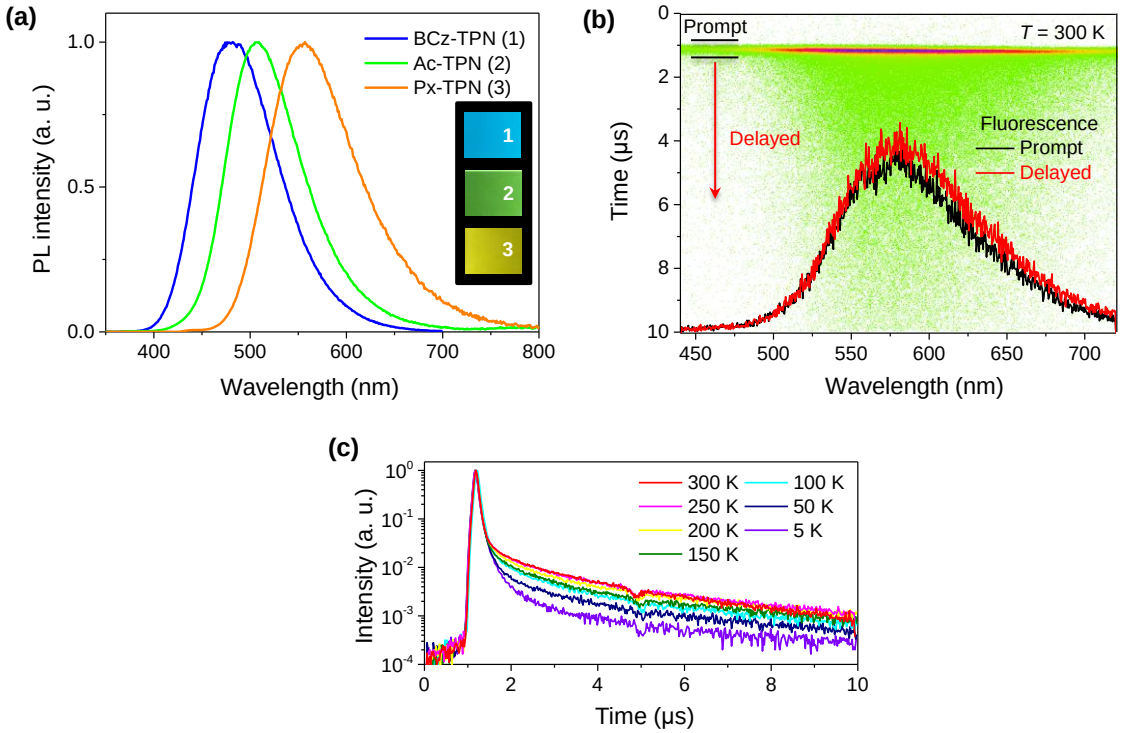

Figure 6-4. (a) PL spectra and the inset shows photographs under UV irradiation of 6 wt%-TPN TADF emitter-based doped films with a host matrix. (b) Streak image (measured 300 K and green dots represent PL photon counts) and (c) temperature dependence of transient PL decay (measured at 5–300 K) of a 6 wt%-Px-TPN:CBP doped film under vacuum.

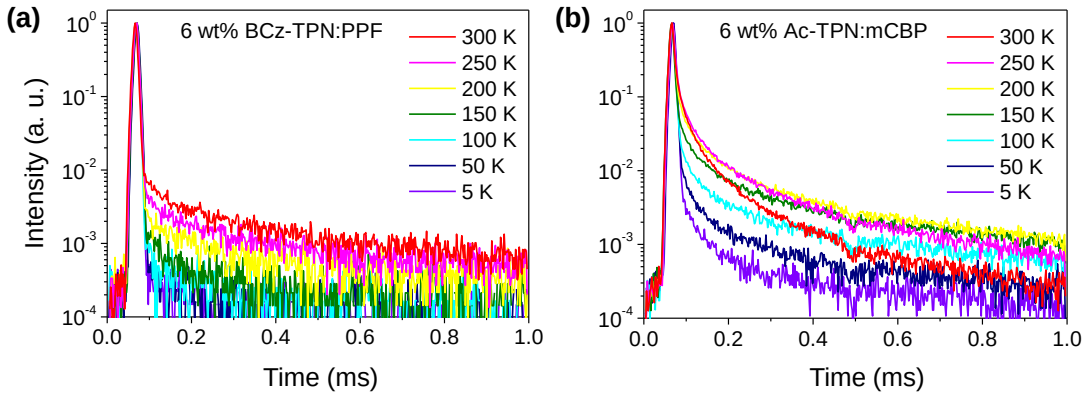

Figure 6-5. Temperature dependent transient PL decay of 6 wt%-doped films of BCz-TPN:PPF and (b) Ac-TPN:mCBP in a host matrix measured from 5 to 300 K.

From the experimental results of room temperature-fluorescence (300 K) and low temperature-phosphorescence (5 K) spectra of the doped films, ΔE_{ST} values of TPN-based TADF emitters are established to be 0.28 eV for BCz-TPN, 0.25 eV for Ac-TPN, and 0.13 eV for Px-TPN (**Figure 6-6**), which show practically inversely proportional to the delayed exciton lifetimes in order of 196 μs for BCz-TPN, 77 μs for Ac-TPN, and 1.2 μs for PxTPN. The more

detail photophysical properties of TPN-based TADF emitters are summarized in **Tables 6-2** and **3**.

Table 6-2. Photophysical properties of TPN-based TADF materials.

Compound	λ_{abs} [nm] sol[a)]	λ_{PL} [nm] sol[a)] / film[b)]	Φ_{PL}[%][c)] sol[a)] / film[b)]	τ_p [ns][d)] / τ_d [μs][d)]	HOMO[e)] [eV]	LUMO[f)] [eV]	E_S / E_T [eV][g)]	ΔE_{ST} [eV][h)]
BCz-TPN	294, 372	486 / 480	52 / 79	27 / 196	−6.10	−3.25	3.00 / 2.72	0.28
Ac-TPN	307, 356, 376[i)]	528 / 507	~100 / 78	23 / 77	−6.10	−3.50	2.82 / 2.57	0.25
Px-TPN	287, 318[i)], 393	600 / 556	30 / 79	25 / 1.2	−5.80	−3.50	2.55 / 2.42	0.13

[a)]Measured in oxygen-free toluene solution at room temperature; [b)]6 wt%-doped film in a host matrix (host = PPF for BCz-TPN; mCBP for Ac-TPN; CBP for Px-TPN); [c)]Absolute PL quantum yield evaluated using an integrating sphere under a nitrogen atmosphere; [d)]PL lifetimes of prompt (τ_p) and delayed (τ_d) decay components for the 6 wt%-doped film measured using a streak camera at 300 K; [e)]Determined by photoelectron yield spectroscopy in pure neat films; [f)]Deduced from the HOMO and optical energy gap (E_g); [g)]Singlet (E_S) and triplet (E_T) energies estimated from onset wavelengths of the emission spectra at 300 K and 5 K in the doped films, respectively; [h)]$\Delta E_{ST} = E_S - E_T$; [i)]Shoulder peak.

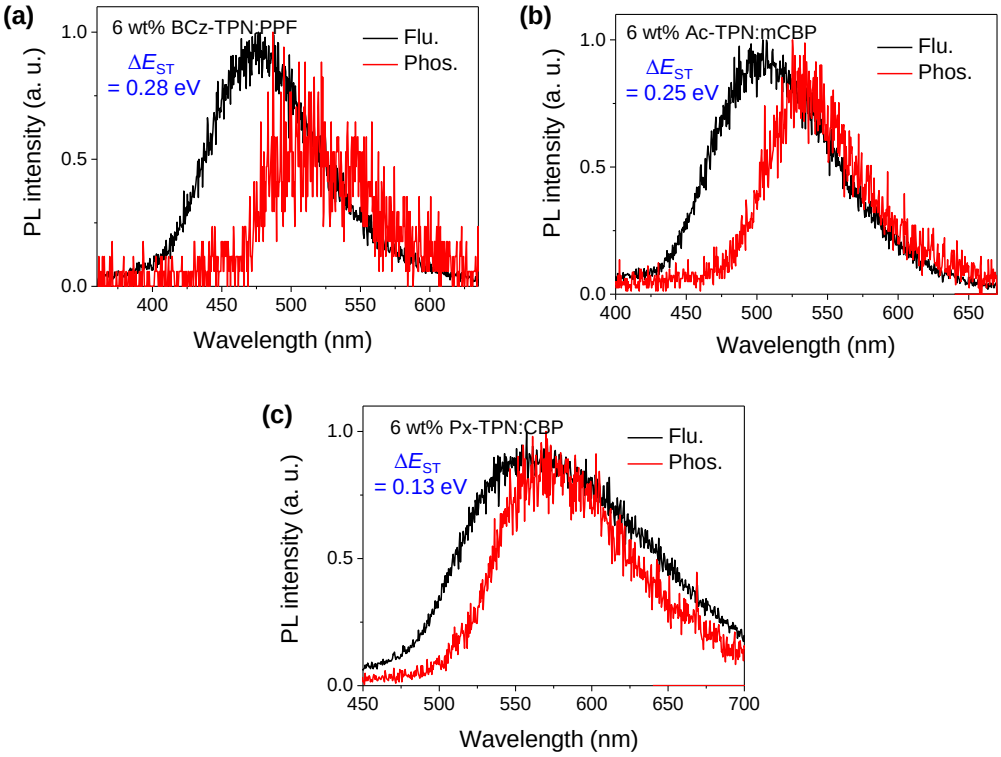

Figure 6-6. PL spectra of fluorescence at 300 K (black) and phosphorescence at 5 K (red) for 6 wt%-doped films in a host matrix. (a) BCz-TPN:PPF, (b) Ac-TPN:mCBP, and (c) Px-TPN:CBP. The lowest excited singlet (S_1) and triplet energy (T_1) levels of the TADF emitters were determined from the high energy onsets of the fluorescence and phosphorescence, respectively.

Table 6-3. Rate constants and quantum efficiencies for decay processes of the TPN derivatives in 6 wt%-doped films.[a)]

Compound	k_r^S [s^{-1}]	k_{ISC} [s^{-1}]	k_{RISC} [s^{-1}]	Φ_p [%]	Φ_d [%]	Φ_{ISC} [%]	Φ_{RISC} [%]
BCz-TPN	6.2×10^6	3.2×10^7	2.4×10^4	16	63	86	75
Ac-TPN	5.2×10^6	3.8×10^7	8.1×10^4	12	66	88	75
Px-TPN	6.8×10^6	3.3×10^7	3.7×10^6	17	62	83	75

[a)]Abbreviations: k_r^S, radiative rate constant ($S_1\rightarrow S_0$); k_{ISC}, intersystem-crossing (ISC) rate constant ($S_1\rightarrow T_1$); k_{RISC}, reverse ISC rate constant ($T_1\rightarrow S_1$); Φ_p, quantum efficiency for prompt fluorescence component; Φ_d, quantum efficiency for delayed fluorescence component; Φ_{ISC}, ISC quantum efficiency; Φ_{RISC}, RISC quantum efficiency.

6. 4. Electroluminescence Properties

Multilayer OLEDs were fabricated using the TPN-based TADF materials as emitters of the 6 wt%-doped EML with a corresponding host material. The architectures and energy levels used in the devices were shown in **Figure 6-7**. The device architecture for a light-blue-TADF-based OLED was prepared, Device **A**: glass/indium tin oxide (ITO; 100 nm)/α-NPD (40 nm)/mCP (10 nm)/6 wt%-BCz-TPN:PPF (20 nm)/PPF (10 nm)/TPBi (30)/Liq (1 nm)/Al (80 nm), whereas green- and yellow-TADF-based OLEDs were fabricated followed configuration, Device B: ITO (100 nm)/TAPC (35 nm)/6 wt%-Ac-TPN:mCBP or Px-TPN:CBP (15 nm)/PPF (10 nm)/TPBi (40 nm), Liq (1 nm)/Al (80 nm), where α-NPD (4,4'-bis[*N*-(1-naphthyl)-N-phenylamino]-1,1'-biphenyl) for Device **A** and TAPC (4,4'-(cyclohexane-1,1-diyl)bis(*N*,*N*-di-*p*-tolylaniline)) for Device **B** were employed as a hole-transporting layer (HTL), whereas TPBi (1,3,5-tris(*N*-phenylbenzimidazol-2-yl)benzene) and Liq (8-hydroxyquinoline lithium) for both devices were employed as an electron-transporting layer (ETL) and electron-injection material, respectively. To suppress triplet exciton quenching and confine the excitons within the EML, thin layers 1,5-bis(9-carbazolyl)benzene (mCP, E_T = 2.9 eV)[13] for Device **A** in a HTL/EML interface and PPF for both devices in the EML/ETL interfaces were inserted.

The TADF-based OLEDs containing TPN-based TADF emitters exhibited the light-blue, green and yellow emission with a peak EL wavelength of 493, 519, and 560 nm, respectively (**Figure 6-8a**). **Figures 6-8b** and **8c** show the current density–voltage–luminance (*J*–*V*–*L*) characteristics and the η_{ext} versus current density of OLEDs, respectively. The turn–on voltages (V_{on}) of the TADF-based OLEDs at 1 cd m^{-2} were in the range of 3.6–4.2 V. All of the devices demonstrated the high maximum η_{ext} of over 20%. Moreover, TADF-based OLEDs achieved high maximum power efficiencies (η_p) of 46.3–59.6 lm W^{-1} and current efficiencies (η_c) of 60.9–72.1 cd A^{-1} (**Figure 6-8d** and **Table 6-4**). The EL efficiency of the BCz-TPN-

based device drastically decreased with increasing current density, whereas Px-TPN-based device showed the high η_{ext} of 20% even at 1000 cd m^{-2}, which phenomenon is well known as the efficiency roll-off. In general, the efficiency roll-off is influenced by long lived triplet excitons, which lead to high probability of triplet quenching in the devices such as triplet-triplet annihilation and/or triplet-polaron annihilation.[14] Therefore, efficiency of the OLED based on BCz-TPN (τ_d = 196 μs) dramatically decreased with increasing current density compared to that of the OLED based on Px-TPN (τ_d = 1.2 μs).

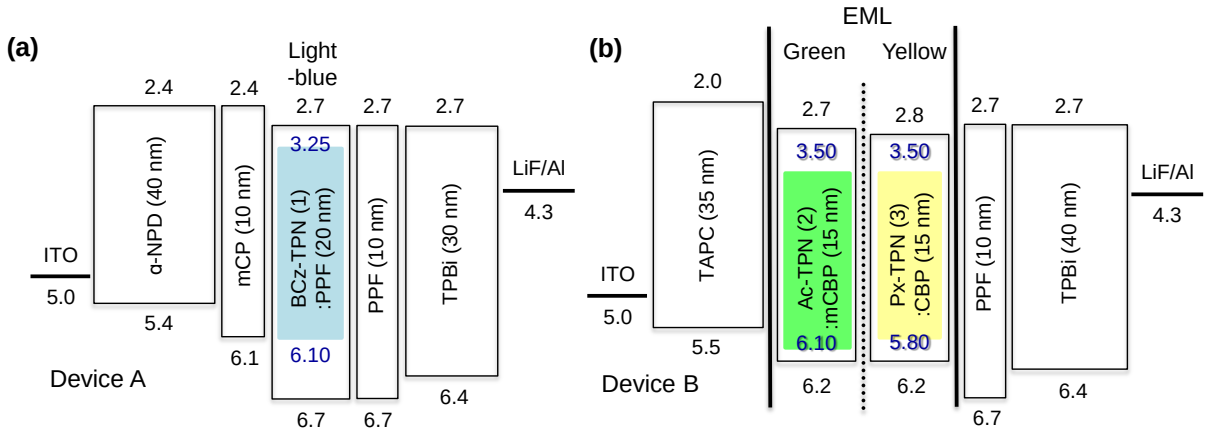

Figure 6-7. Schematic representation of the TADF-OLED structures (a) Device **A** for a BCz-TPN-based OLED and (b) Device **B** for Ac-TPN and Px-TPN-based OLEDs, and energy level diagrams of the materials used.

The high η_{out} values of TPN-based OLEDs were calculated to be 26.5% for BCz-TPN, 27.2% for Ac-TPN, and 30.9% for Px-TPN by the combination of equations **1-18** and **1-19** from the experimental results (**Table 6-3**). The more detailed information of the performance for the TADF-based OLEDs is summarized in **Table 6-4**.

Table 6-4. EL performance of the TADF-based OLEDs.[a)]

TADF emitter	Host	λ_{EL} [nm]	V_{on} [V]	L_{max} [cd m^{-2}]	η_{ext} [%]	η_c [cd A^{-1}]	η_p [lm W^{-1}]	η_{out} [%]	CIE (x, y)
BCz-TPN	PPF	493	3.8	5,000	20.1	60.9	50.3	26.5	(0.21, 0.36)
Ac-TPN	mCBP	519	4.2	9,300	20.6	65.2	46.3	27.2	(0.28, 0.55)
Px-TPN	CBP	560	3.6	29,000	23.4	72.1	59.6	30.9	(0.44, 0.54)

[a)]Abbreviations: λ_{EL}, EL emission maximum; V_{on}, turn–on voltage at 1 cd m^{-2}; L_{max}, maximum luminance; η_{ext}, maximum external EL quantum efficiency; η_c, maximum current efficiency; η_p, maximum power efficiency; η_{out}, light out-coupling efficiency; CIE, Commission Internationale de l'Éclairage color coordinates measured at 10 mA cm^{-2}; PPF, 2,8-bis(diphenylphosphoryl)dibenzofuran; mCBP, 3,3'-bis(carbazol-9-yl)-1,1'-biphenyl; CBP, 4,4'-bis(carbazol-9-yl)-1,1'-biphenyl.

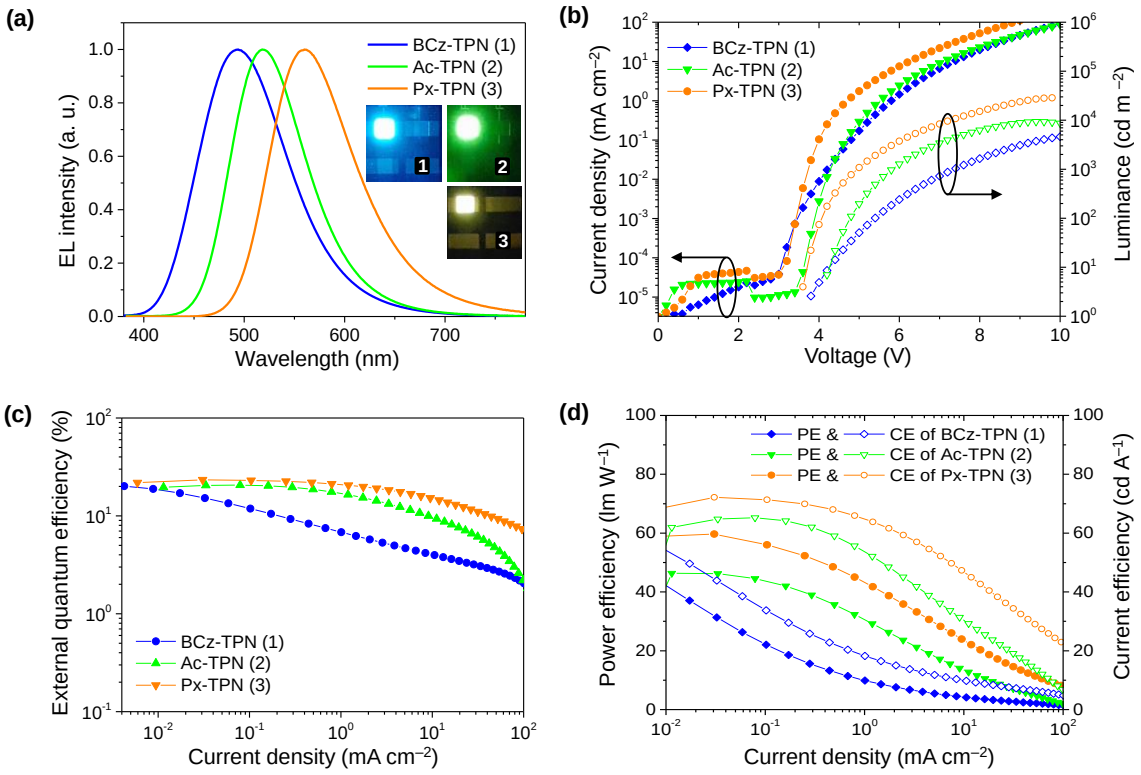

Figure 6-8. (a) EL spectra (inset is photographs of each device at 10 mA cm^{-2}), (b) current–voltage–luminance (*J*–*V*–*L*) plots, (c) external EL quantum efficiency (η_{ext}) against current density characteristics, and (d) power efficiency (η_p)–current density–current efficiency (η_c) characteristics of the TADF-based OLEDs.

6. 5. Molecular Orientation

To confirm the extent to which variation in orientation of transition dipole moments of TPN-based TADF molecules affects η_{out} of their OLEDs, we investigated an orientation of the transition dipole moments using the variable angle spectroscopic ellipsometry (VASE) and angle-dependent *p*-polarized PL measurement of the EML.[8b,16] **Figure 6-9a** shows electric dipole moments of TPN-based molecules from the HOMO to LUMO vertical transition calculated by TD-DFT, which present the same direction with ICT transition and long axis of linear-shaped molecules. As exemplified in **Figure 6-9b**, the orientation of transition dipole moments in a pure thin film of Px-TPN was quantified using an orientation order parameter (*S*), which is defined as:

$$S = \frac{3(\cos^2\theta) - 1}{2} = \frac{k_e^{max} - k_o^{max}}{k_e^{max} + k_o^{max}} \qquad \textbf{(7-1)}$$

where $\cos^2\theta$ indicates the ensemble average, θ is the angle between the axis of the transition dipole moment and the direction perpendicular to the substrate surface, and k_o^{max} and k_e^{max} are the ordinary and extraordinary extinction coefficients at the peak of the band attributed to the

transition dipole moments, respectively. Accordingly, the oriented order parameter of the pure neat film of Px-TPN was calculated to be nearly $S = -0.5$, which indicates the linear-shaped Px-TPN molecule in the pure neat film are perfectly horizontally oriented against the substrate surface. Moreover, a pure neat film of Ac-TPN shows similar manner with that of Px-TPN (**Figure 6-10**).

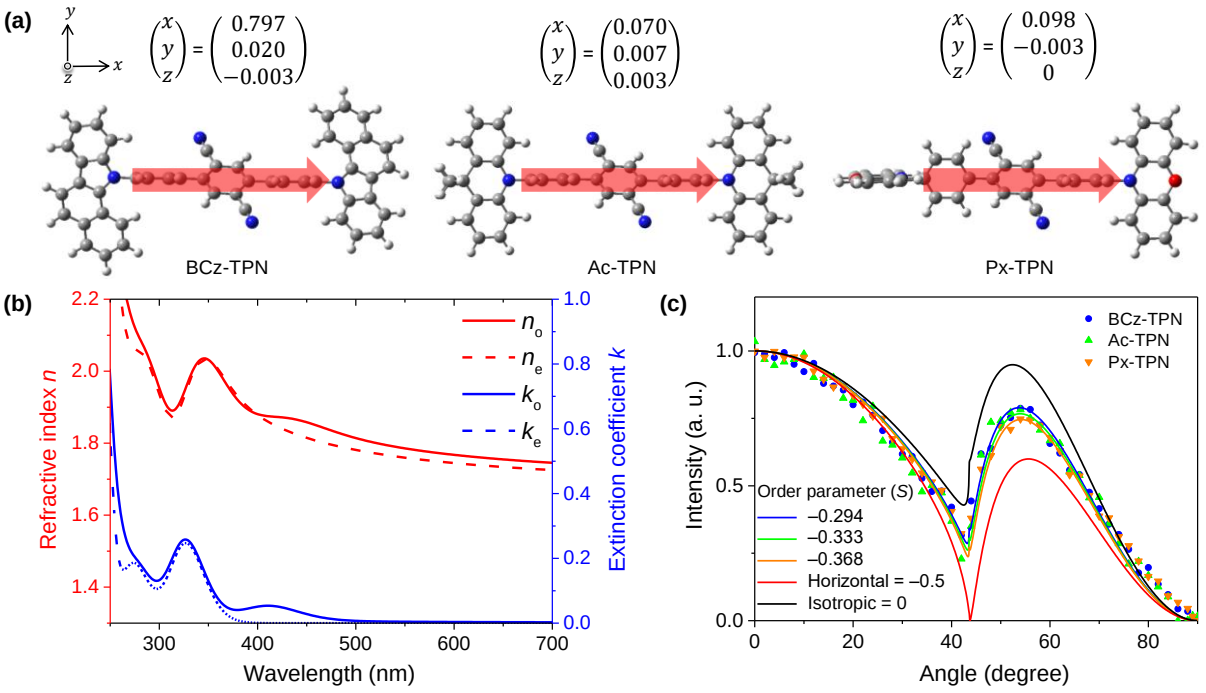

Figure 6-9. (a) Molecular structures of TPN-based molecules calculated by TD-DFT. Parenthesis part indicates electric transition dipole moments (a. u.) from HOMO to LUMO vertical transition. (b) Anisotropies in the refractive indices (red lines) and the extinction coefficients (blue lines) of a pure thin film of Px-TPN. The solid and broken lines indicate the horizontal and perpendicular components of the optical constants, respectively. (c) Angle-dependent PL spectra of 6 wt%-TPN-based materials in a host matrix (PPF for BCz-TPN, mCBP for Ac-TPN, and CBP for Px-TPN) and simulated spectra of perfectly horizontal (red line, $S = -0.5$) and isotropic (black line, $S = 0$) orientations.

We also examined minutely for 6 wt%-TPN-based materials in a corresponding host matrix with the EML in each device by employing angle-dependent *p*-polarized PL measurement. 15 nm thickness-samples of 6 wt%-emitters in a host matrix were prepared onto a glass substrate by thermal evaporation and angle-dependent PL spectra of these doped films were collected with corresponding a maximum PL wavelength of 6 wt%-emitter-doped films in the range of 0°–90°. **Figure 6-9c** shows experimental results of angle-dependent *p*-polarized PL measurement, *S* values of doped films of TPN materials were estimated to be –0.294 for

BCz-TPN, –0.333 for Ac-TPN, and –0.368 for Px-TPN, which results suggest that relatively horizontally oriented dipoles of TPN-based molecules exhibits strong PL intensity in vertical direction against a substrate (0°) because the emission light is emitted through the vertical direction to the transition dipole moments. Consequently, TPN-based TADF molecules exhibiting primarily horizontally oriented even in a host matrix lead to high η_{out} when emitting light from the dipoles.

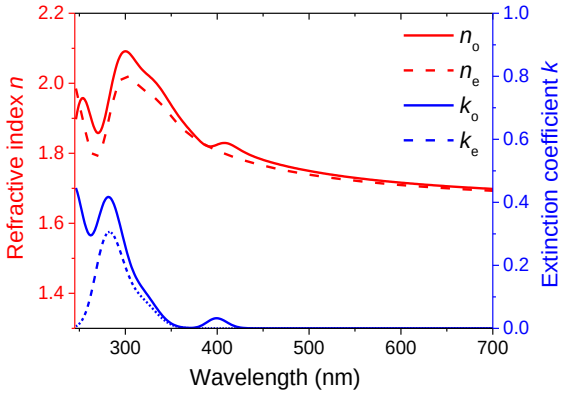

Figure 6-10. Anisotropies in the refractive indices (red lines) and the extinction coefficients (blue lines) of a 50 nm thickness pure film of Ac-TPN. The solid and broken lines indicate the horizontal and perpendicular components of the optical constants, respectively. The oriented order parameter was calculated to be nearly S = –0.5.

6. 6. Experimental Section

6. 6. 1. General Methods

All regents and anhydrous solvents were purchased from Sigma-Aldrich, Tokyo Chemical Industry (TCI), or Wako Pure Chemical Industries, and were used without further purification unless otherwise indicated. 9,9-dimethyl-10-(4-(4,4,5,5-tetramethyl-1,3,2-dioxaborolan-2-yl)-phenyl-acridan (**9**),[17] 10-(4-(4,4,5,5-tetramethyl-1,3,2-dioxaborolan-2-yl)phenyl)-phenoxazine (**10**),[17] and 2,8-bis(diphenylphosphine oxide)dibenzofuran (PPF)[10] were prepared by a procedure in the paper. PPF was further purified by sublimation twice. Other OLED materials were purchased from Luminescence Technology Corporation. All reactions were performed under a nitrogen atmospheres in dry solvents. The final products were fully characterized by ^{1}H and ^{13}C NMR spectroscopy, MALDI-TOF mass spectrometry, and elemental analysis. NMR spectra were recorded on a Bruker Avance III 500 spectrometer. Chemical shifts of ^{1}H and ^{13}C NMR signals were quoted to tetramethylsilane (δ = 0.00) and $CDCl_3$ (δ = 77.0) as internal standards. Matrix-assisted laser desorption ionization time-of-

flight (MALDI-TOF) mass spectra were collected on an Autoflex III spectrometer (Bruker Daltonics) using dithranol as the matrix. Elemental analyses were carried out with a Yanaco MT-5 CHN corder. All final compounds were purified by temperature-gradient sublimation under vacuum before measurements and device fabrication.

6. 6. 2. Synthesis

The synthetic scheme of TPN-based materials is shown in Scheme. 1, and the detail synthetic methods and characterization data are described in Supporting Information. The TPN derivatives were synthesized by Suzuki-Miyaura cross-coupling reactions of 2,5-dibromoterephthalonitrile with boronic esters in high yields (83–98%) by employing a $Pd(PPh_3)_4/Na_2CO_3$ catalytic system. All of the final compounds were purified by column chromatography, and then further purification was executed by temperature-gradient sublimation under high vacuum condition to obtain highly pure organic materials.

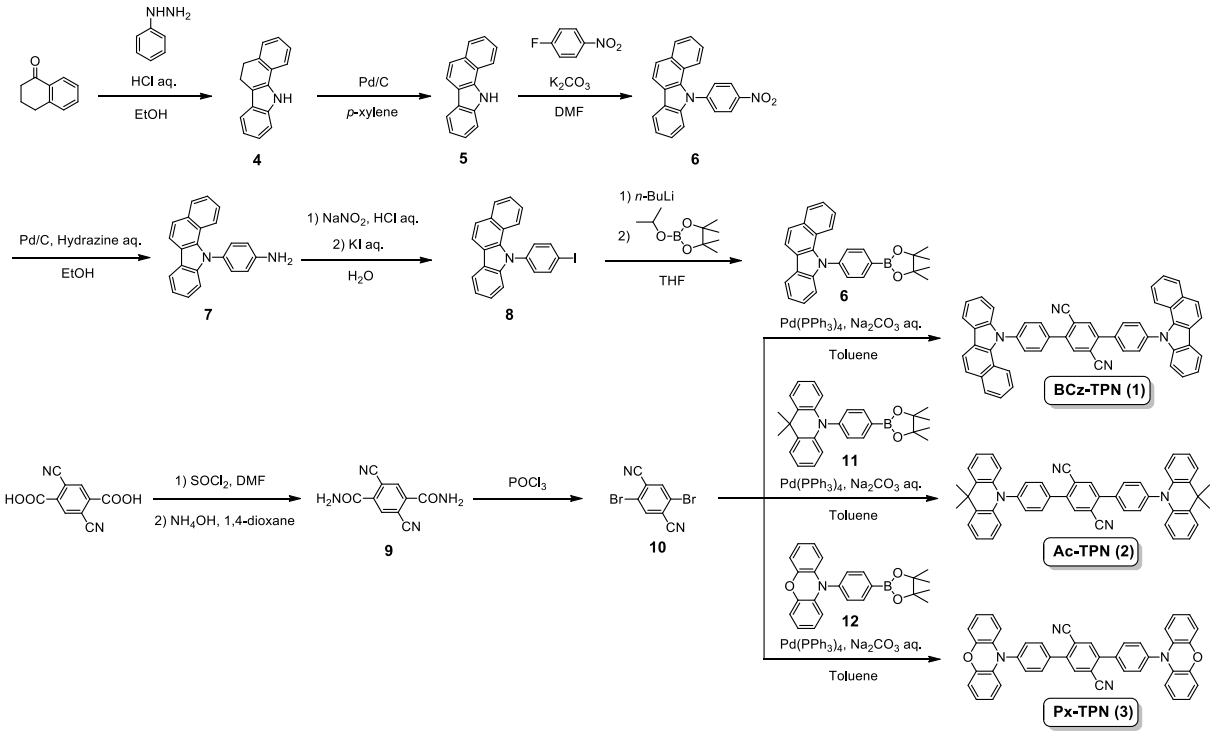

Scheme 6-1. Synthesis procedures for BCz-TPN, Ac-TPN, and Px-TPN

Synthesis of 6,11-dihydro-5*H*-benzo[*a*]carbazole (4): A mixture of phenylhydrazine (10.0 g, 92.5 mmol) and α-tetralone (13.5 g, 92.4 mmol) in ethanol (100 mL) was stirred at room temperature under a nitrogen atmosphere, and then HCl (36%, 15 mL) was added to the mixture.

The mixture was stirred for 3 h at 60 °C under a nitrogen atmosphere. Upon cooling to room temperature, the precipitate was filtered with methanol to give **4** (yield = 18.3 g, 90%) as a white solid. ^{1}H NMR (500 MHz, $CDCl_3$, δ): 8.20 (br, s, 1H), 7.55 (d, J = 7.8 Hz, 1H), 7.39 (d, J = 8.0 Hz, 1H), 7.34 (d, J = 7.5 Hz, 1H), 7.28-7.25 (m, 2H), 7.20-7.15 (m, 2H), 7.12 (td, J = 7.4 Hz, 1H), 3.07 (t, J = 7.6 Hz, 2H), 3.00-2.97 (m, 2H). MS (MALDI-TOF) m/z: $[M]^+$ calcd 219.10, found 219.61.

Synthesis of 11*H*-benzo[*a*]carbazole (5): A solution of **4** (10.0 g, 45.6 mmol) in *p*-xylene (100 mL) was stirred at room temperature under a nitrogen atmosphere, and then palladium on carbon (10 wt.%, 0.5 g) was slowly added to the solution. The mixture was refluxed for 24 h under a nitrogen atmosphere. Upon cooling at room temperature, the precipitate was filtered with $CHCl_3$ through a Celite pad. The solvent was removed under reduced pressure, and then the crude powder was filtered with methanol to give **4** (yield = 8.9 g, 90%) as a white solid. ^{1}H NMR (500 MHz, $CDCl_3$, δ): 8.81 (br, s, 1H), 8.14 (t, J = 7.4 Hz, 3H), 8.02 (d, J = 8.1 Hz, 1H), 7.67 (d, J = 8.5 Hz, 1H), 7.61 (td, J = 6.7, 1.3 Hz, 2H), 7.54 (td, J = 7.5 Hz, 1.2 Hz, 1H), 7.45 (td, J = 7.6, 1.1 Hz 1H), 7.31 (td, J = 7.5, 0.8 Hz, 1H). MS (MALDI-TOF) m/z: $[M]^+$ calcd 217.09, found 216.56.

Synthesis of 11-(4-nitrophenyl)-11*H*-benzo[*a*]carbazole (5): A mixture of **4** (8.0 g, 36.8 mmol) and K_2CO_3 (15.3 g, 111 mmol) in DMF (80 mL) was stirred for 30 min at room temperature under a nitrogen atmosphere. After 1-fluoro-4-nitrobenzene (5.7 g, 40.4 mmol) was added into the mixture, the reaction mixture was refluxed for 24 h under a nitrogen atmosphere. Upon cooling at room temperature, the mixture was added into methanol (50 mL) and ice water (50 mL) mixture, and then the precipitate was filtered with methanol to give **5** (yield = 12.0 g, 96%) as a yellow solid. ^{1}H NMR (500 MHz, $CDCl_3$, δ): 8.53 (dd, J = 6.9 Hz, 2.2 Hz, 2H), 8.22 (d, J = 8.5 Hz, 1H), 8.20 (dd, J = 6.5 Hz, 1.3 Hz, 1H), 8.02 (d, J = 8.1 Hz, 1H), 7.79 (d, J = 8.5 Hz, 1H), 7.74 (dd, J = 6.8 Hz, 2.1 Hz, 2H), 7.47 (td, J = 7.5 Hz, 1.2 Hz, 1H), 7.44-7.36 (m, 3H), 7.30-7.25 (m, 2H). MS (MALDI-TOF) m/z: $[M]^+$ calcd 338.11, found 338.86.

Synthesis of 4-(11*H*-benzo[*a*]carbazol-11-yl)aniline (6): A solution of **5** (10.0 g, 29.6 mmol) in ethanol (100 mL) was stirred under nitrogen atmosphere, and then palladium on carbon (10 wt%, 0.4 g) was slowly added to the solution. An aqueous solution (5 mL) of hydrazine (35

wt%) was added dropwise to the mixture, and then the mixture was refluxed for 5 h under nitrogen atmosphere. Upon cooling to room temperature, the crude product was filtered and recrystallized with ice water, and then the precipitate was filtered with water to afford **6** (yield = 9.0 g, 99%) as a white solid. ^{1}H NMR (500 MHz, $CDCl_3$, δ): 8.14 (dd, J = 8.5 Hz, 0.8 Hz, 1H), 8.11 (d, J = 7.8 Hz, 1H), 7.90 (d, J = 8.1 Hz, 1H), 7.62 (d, J = 8.5 Hz, 1H), 7.53 (d, J = 8.6 Hz, 1H), 7.35 (t, J = 7.5 Hz, 1H), 7.30 (t, J = 7.6 Hz, 1H), 7.26-7.16 (m, 4H), 7.12 (d, J = 8.1 Hz, 1H), 6.86-6.83 (m, 2 H), 3.89 (br, s, 2H). MS (MALDI-TOF) m/z: $[M]^+$; calcd 308.13, found 307.86.

Synthesis of 11-(4-iodophenyl)-11*H*-benzo[*a*]carbazole (7): A mixture of **5** (8.0 g, 25.9 mmol) and sodium nitrite (2.3 g, 33.3 mmol) in H_2O (100 mL) were stirred at 0 °C. After HCl (36%, 4 mL) was added dropwise to the solution, the mixture was stirred for 1 h at 0 °C. An aqueous solution (50 mL) of potassium iodide (5.6 g, 33.8 mmol) was added dropwise to the mixture at 0 °C, and then the mixture was further reacted for 1 h at 0 °C. The reaction mixture was neutralized by an aqueous solution of sodium thiosulfate, and then extracted with CH_2Cl_2. The combined organic layers were dried over anhydrous $MgSO_4$ and evaporated under the reduced pressure, and then the crude product was purified by column chromatography on silica gel (hexane/CH_2Cl_2 = 19:1, v/v) to give **5** (yield = 7.9 g, 73%) as a white solid. ^{1}H NMR (500 MHz, $CDCl_3$, δ): 8.21 (d, J = 8.5 Hz, 1H), 8.18 (d, J = 7.6 Hz, 1H), 8.00-7.97 (m, 4H), 7.73 (d, J = 8.5 Hz, 1H), 7.47-7.42 (m, 2H), 7.39 (t, J = 7.7 Hz, 1H), 7.35 (t, J = 7.2 Hz. 1H), 7.32-7.27 (m, 2H), 7.17 (d, J = 7.7 Hz, 1H). MS (MALDI-TOF) m/z: $[M]^+$ calcd 419.02. found 418.92.

Synthesis of 11-(4-(4,4,5,5-tetramethyl-1,3,2-dioxaborolan-2-yl)phenyl)-11*H*-benzo[*a*]carbazole (8): A solution of **7** (5.0 g, 11.9 mmol) in THF (50 mL) was stirred at −78 °C under a nitrogen atmosphere, and then *n*-butyllithium (2.6 M, 5.1 mL, 13.1 mmol) in THF (50 mL) was added dropwise and followed by stirring for 1 h at that temperature. After that 2-isopropoxy-4,4,5,5-tetramethyl-1,3,2-dioxaborolane (2.7 g, 14.3 mmol) was added dropwise at −78 °C, and then the mixture was further reacted for 3 h at room temperature. A large amount of water was added to the mixture to quench the reaction. After stirring for 30 min, extraction with $CHCl_3$ and drying over anhydrous $MgSO_4$. After filtration and evaporation, the crude product was purified by column chromatography on silica gel (hexane/ethyl acetate = 5:1, v/v) to afford **8** (yield = 4.0 g, 80%) as a white solid. ^{1}H NMR (500 MHz, $CDCl_3$, δ): 8.15 (d, J = 8.5 Hz, 1H), 8.11 (dd, J = 6.9 Hz, 1.4 Hz, 1H), 8.02 (d, J = 8.2 Hz, 2H), 7.91 (d, J

= 7.8 Hz, 1H), 7.65 (d, *J* = 8.5 Hz, 1H), 7.48 (d, *J* = 8.2 Hz, 2H), 7.40 (d, *J* = 8.6 Hz, 1H), 7.35 (td, *J* = 7.5, 1.1 Hz, 1H), 7.31-7.24 (m, 2H), 7.15 (td, *J* = 7.7, 1.2 Hz, 1H), 7.11 (dd, *J* = 7.3 Hz, 0.8 Hz, 1H), 1.37 (s, 12H). MS (MALDI-TOF) *m*/*z*: $[M]^+$ calcd 419.21, found 419.12.

Synthesis of 2,5-dibromobenzene-1,4-dinitrile (10): 2,5-dibromotetrephthalic acid (14.7 g, 68.0 mmol), thionyl chloride (16.6 g, 140 mmol), and a few drops of DMF were refluxed for 3 h under a nitrogen atmosphere. After toluene (50 mL) was added into the mixture, thionyl chloride was removed by co-evaporation under reduced pressure. A precipitate was dissolved 1,4-dioxane (20 mL), and then the solution was added dropwise into NH_4OH (60 mL). After that, the mixture was reacted for 1 h at room temperature. A precipitate was filtered to give 2,5-dibromobenzene-1,4-diamide (**9**) (yield = 12.2 g, 94%) as a white solid.

9 (12.2 g, 57.0 mmol) and phosphoryl chloride (40 mL) were reacted for 8 h at 135 °C under a nitrogen atmosphere. Upon cooling to room temperature, the mixture was added dropwise into ice water, and then the precipitate was filtered with H_2O to give **10** (yield = 14.7 g, 90%) as a light yellow solid. ^{1}H NMR (500 MHz, $CDCl_3$, δ): 8.60 (s, 2H). ^{13}C NMR (125 MHz, $CDCl_3$, δ): 138.31, 124.11, 120.10, 115.27. MS (MALDI-TOF): *m*/*z*: $[M]^+$ calcd 285.86, found 285.83.

Synthesis of BCz-TPN: A mixture of **10** (0.50 g, 1.75 mmol), **8** (1.60 g, 3.82 mmol)**,** and $Pd(PPh_3)_4$ (0.04 g, 0.035 mmol) in toluene (50 mL) were stirred under a nitrogen atmosphere. After that, an aqueous solution (20 mL) of Na_2CO_3 (0.74 g, 6.99 mmol) was added to the mixture, and then the mixture was reacted for 72 h at 80 °C under nitrogen atmosphere. Upon cooling to room temperature, the reaction mixture was filtered through a Celite pad and then extracted with $CHCl_3$. The combined organic layers were washed with water and dried over anhydrous $MgSO_4$. After filtration and evaporation, the crude product was purified by column chromatography on silica gel (hexane/ethyl acetate = 5:1, v/v) to give BCz-TPN as a light beige solid (yield = 1.19 g, 96%). ^{1}H NMR (500 MHz, $CDCl_3$, δ): 8.26 (d, *J* = 8.6 Hz, 2H), 8.24-8.22 (m, 4H), 8.03 (d, *J* = 7.9 Hz, 2H), 7.97 (dd, *J* = 6.4, 1.9 Hz, 4H), 7.81-7.77 (m, 6H), 7.52 (d, *J* = 8.7 Hz, 2H), 7.49-7.44 (m, 4H), 7.40 (t, *J* = 6.9 Hz, 2H), 7.32 (td, *J* = 7.0, 1.1 Hz, 4H). ^{13}C NMR (125 MHz, $CDCl_3$, δ): 143.89, 141.81, 135.82, 135.28, 135.22, 133.54, 130.45, 129.83, 129.34, 125.30, 124.94, 123.78, 122.16, 121.86, 121.78, 120.80, 120.10, 119.72, 119.05, 116.85, 115.98, 110.26. MS (MALDI-TOF) *m*/*z*: $[M]^+$ calcd 710.25, found 710.36. Anal. calcd (%) for $C_{58}H_{38}N_4$: C, 88.07; H, 4.84; N, 7.08; found: C, 88.16; H, 4.74; N, 7.07.

Synthesis of Ac-TPN: Ac-TPN was synthesized according to the same procedure as described above for the synthesis of BCz-TPN, except that **11** (1.58 g, 3.84 mmol) was used as the reactant instead of **8**, yielding a light yellow solid (yield = 1.01 g, 83%). ^{1}H NMR (500 MHz, $CDCl_3$, δ): 8.13 (s, 2H), 7.91 (d, J = 8.0 Hz, 4H), 7.57 (d, J = 8.0 Hz, 2H), 7.49 (d, J = 7.7 Hz, 4H), 7.03 (t, J = 7.3 Hz, 2H), 6.97 (t, J = 7.5 Hz, 2H), 6.35 (d, J = 8.2 Hz, 4H), 1.72 (s, 12H). ^{13}C NMR (125 MHz, $CDCl_3$, δ): 143.79, 143.08, 140.61, 135.35, 135.32, 132.24, 131.21, 130.40, 126.50, 125.35, 121.01, 116.92, 115.66, 114.14, 36.05, 31.16. MS (MALDI-TOF) *m/z*: $[M+H]^+$ calcd 695.32, found 695.24. Anal. calcd (%) for $C_{50}H_{38}N_4$: C, 86.42; H, 5.51; N 8.06; found: C, 86.38; H, 5.52; N, 8.13.

Synthesis of Px-TPN: Px-TPN was synthesized according to the same procedure as described above for the synthesis of BCz-TPN, except that **12** (1.48 g, 3.84 mmol) was used as the reactant instead of **8**, yielding a light yellow solid (yield = 1.10 g, 98%). ^{1}H NMR (500 MHz, $CDCl_3$, δ): 8.07 (s, 2H), 7.87 (d, J = 8.85 Hz, 4H), 7.58 (d, J = 8.25 Hz, 4H), 6.75-6.64 (m, 12H), 6.02 (dd, J_1 = 6.6 Hz, J_2 = 1.25 Hz, 4H). ^{13}C NMR (125 MHz, $CDCl_3$, δ): 144.01, 143.69, 140.85, 135.58, 135.24, 133.89, 131.86, 131.40, 123.36, 121.81, 116.80, 115.70, 115.65, 113.34, 53.42. MS (MALDI-TOF) *m/z*: $[M]^+$ calcd 642.21, found 642.34. Anal. calcd (%) for $C_{44}H_{26}N_4O_2$: C, 82.23; H, 4.08; N, 8.72; found: C, 82.14; H, 3.94; N, 8.77.

6. 6. 3. Photoluminescence Measurements

Organic films for optical measurements were co-deposited under high vacuum (~ 5×10^{-4} Pa) onto quartz, Si(100), and glass substrates, which were pre-cleaned by detergent, acetone, and isopropanol. UV−vis absorption spectra and fluorescence spectra measurement were performed with a Shimadzu UV-2550 spectrometer and a Horiba Scientific Fluoromax-4 spectrophotometer, respectively, in degassed spectral grade solvents. The photoluminescence quantum yields (PLQY) were determined with a Hamamatsu Photonic C9920-02, PMA-11 calibrated integrating sphere system coupled with a photonic multichannel analyzer. The luminescence intensities and lifetimes were measured using a Hamamatsu Photonics C4334 Streak camera with an N_2 gas laser (λ = 337 nm, pulse width = 500 ps, repetition rate = 20 Hz) under vacuum (< 4×10^{-1} Pa). The HOMO energy levels for thin films were determined using a Riken-Keiki AC-3 ultraviolet photoelectron spectrometer. The LUMO energy levels were estimated by subtracting the optical energy gap (E_g) from the measured HOMO energies; E_g values were determined from the onset position of the PL spectra of pure neat films. Pure neat

films for the variable-angle spectroscopic ellipsometry (VASE) measurements were deposited onto Si(100) substrates. VASE was performed using a fast spectroscopic ellipsometer (M-2000U, J. A. Woollam Co. Inc.). Seven different angles of the incident light from 45° to 75° with steps of 5° were used. At each angle, the experimental ellipsometric parameters Ψ and Δ were obtained simultaneously in 1.6 nm steps from 245 to 1000 nm. The VASE data were analyzed using WVASE32 software. Samples for angle-dependent PL spectrum were prepared 6 wt%-emitters in a host matrix doped films on glass substrates and encapsulated with the same glass substrate under an inert nitrogen atmosphere and then were attached to an antireflection-coated half cylinder prism, which refractive index is 1.5, using matching oil in a rotation stage (SGSP-120YAW, Sigma Koki) and excited by a lager with a wavelength of 375 nm (DPS-5004, Neoarc). The emission from the sample was gathered by a calibrated multichannel spectrometer (PMA-11, Hamamatsu Photonics). This measurement collects only the p-polarized emission about orientation from 0° to 90°. The angle-dependent PL spectra were analyzed using Setfos 4.3 software, which provided a direction cosine of the transition dipole moment (μ) along with the direction against to the substrate of 0.22 for BCz-TPN, 0.20 for Ac-TPN, and 0.18 for Px-TPN, corresponding to $p_z : p_x = 0.56 : 1$, where p_z and p_x are μ of perpendicular and horizontal to the substrate, respectively. By using μ values, S can be estimated according to the following equations.[9c]

$$\frac{p_z}{p_x} = \frac{2\mu}{1-\mu} \quad \textbf{(7-2)}$$

$$S = \frac{4\mu^2-(1-\mu)^2}{4\mu^2+2(1-\mu)^2} \quad \textbf{(7-3)}$$

6. 6. 4. OLED Device Fabrication and Measurements

Indium tin oxide-coated glass substrates were cleaned with detergent, deionized water, acetone, and isopropanol. They were then treated with UV-ozone treatment for 15 min, before being loaded into a vacuum evaporation system. The organic layers were thermally evaporated on the substrates under vacuum (< 6×10^{-5} Pa) with an evaporation rate of < 0.3 nm/s. All of the layers were deposited through a shadow mask. The layer thickness and deposition rate were monitored in situ during deposition by an oscillating quartz thickness monitor. OLED properties were measured using a Keithley source meter 2400 and a Konica Minolita CS-2000.

6. 7. Conclusion

New metal-free linear-shaped TADF emitters blending a central terephthalonitrile acceptor core and several donor units linked by phenylene bridges, were designed and synthesized. Their well-separated HOMO–LUMO geometry provides a small ΔE_{ST} and high Φ_{PL}, simultaneously, which lead to efficient TADF characteristics with light-blue, green, and yellow emissions in doped films. These TADF-based OLEDs demonstrated high maximum EL efficiencies of up to 23.4% owing to their high internal quantum efficiencies of approximately 80% and light out-coupling efficiencies of up to 30.9%. We anticipate that these results will boost efficient TADF molecular design for future OLED applications.

References

[1] a) S. Nowy, B. C. Krummacher, J. Frischeisen, N. A. Reinke, W. Brütting, *J. Appl. Phys.* **2008**, *104*, 123109; b) J.-S. Kim, P. K. H. Ho, N. C. Greenham, R. H. Friend, *J. Appl. Phys.* **2000**, *88*, 1073.

[2] T. Yamasaki, K. Sumioka, T. Tsutsui, *Appl. Phys. Lett.* **2000**, *76*, 1243.

[3] a) S. Möller, S. R. Forrest, S. R. *J. Appl. Phys.* **2002**, *91*, 3324; b) Y. Sun, S. R. Forrest, *J. Appl. Phys.* **2006**, *100*, 073106.

[4] Y. Sun, S. R. Forrest, *Nat. Photon.* **2008**, *2*, 483.

[5] W. H. Koo, S. M. Jeong, F. Araoka1, K. Ishikawa1, S. Nishimura, R. Toyooka, H. Takezoe, *Nat. Photon.* **2010**, *4*, 222.

[6] a) J.-S. Kim, P. K. H. Ho, N. C. Greenham, R. H. Friend, *J. Appl. Phys.* **2000**, *88*, 1073; b) D. Yokoyama, *J. Mater. Chem.* **2012**, *21*, 19187.

[7] a) J. Frischeisen, D. Yokoyama, A. Endo, C. Adachi, W. Brütting, *Org. Electron.* **2011**, *12*, 809; b) H. S. Bang, S. Y. Seo, D. C. Choo, T. W. Kim, S. J. Lee, J. H. Seo, Y. K. Kim, C. Chu, J. Ha, *Thin Solid Films* **2009**, *517*, 5314.

[8] K.-H. Kim, S. Lee, C.-K. Moon, S.-Y. Kim, Y.-S. Park, J.-H. Lee; J. W. Lee, J. Huh, Y. You, J.-J. Kim, *Nat. Commun.* **2014**, *5*, 4769; b) M. J. Jurow, C. Mayr, T. D. Schmidt, T. Lampe, P. I. Djurovich, W. Brütting, M. E. Thompson, *Nat. Mater.* **2016**, *15*, 85.

[9] a) C. Mayr, S. Y. Lee, T. D. Schmidt, T. Yasuda, C. Adachi, W. Brütting, *Adv. Funct. Mater.* **2014**, *24*, 5232; b) J. W. Sun, J.-H. Lee, C.-K. Moon, K.-H. Kim, H. Shin, J.-J. Kim, *Adv. Mater.* **2014**, *26*, 5684; c) H. Kaji, H. Suzuki, T. Fukushima, K. Shizu, K. Suzuki, S. Kubo, T. Komino, H. Oiwa, F. Suzuki, A. Wakamiya, Y. Murata, C. Adachi, *Nat. Commun.* **2015**, *6*, 8476; d) T.-A. Lin, T. Chatterjee, W.-L. Tsai, W.-K Lee, M.-J. Wu, M. Jiao, K.-C. Pan, C.-L. Yi, C.-L. Chung, K.-T. Wong, C.-C. Wu, *Adv. Mater.* **2016**, *28*, 6976.

[10] P. A. Vecchi, A. B. Padmaperuma, H. Qiao, L. S. Sapochak, P. E. A. Burrows, *Org. Lett.* **2006**, *8*, 4211.

[11] S. Gong, X. He, Y. Chen, Z. Jiang, C. Zhong, D. Ma, J. Qin, C. Yang, *J. Mater. Chem.* **2012**, *22*, 2894.

[12] C. Adachi, R. C. Kwong, P. Djurovich, V. Adamovich, M. A. Baldo, M. Thompson, S. R. Forrest, *Appl. Phys. Lett.* **2001**, *79*, 2082.

[13] R. J. Holmes, S. R. Forrest, Y.-J. Tung, R. C. Kwong, J. J. Brown, S. Garon, M. E. Thompson, *Appl. Phys. Lett.* **2003**, *82*, 2422.

[14] C. Murawski, K. Leo, M. C. Gather, *Adv. Mater.* **2013**, *25*, 6801; b) Y. Zhang, S. R. Forrest, *Phys. Rev. Lett.* **2012**, *113*, 267404; c) M. A. Baldo, C. Adachi, S. R. Forrest, *Phys. Rev. B* **2000**, *62*, 10967.

[15] S. Y. Lee, T. Yasuda, H. Nomura, C. Adachi, *Appl. Phys. Lett.* **2012**, *101*, 093306

[16] J. Frischeisen, D. Yokoyama, C. Adachi, W. Brütting, *Appl. Phys. Lett.* **2010**, *96*, 073302.

[17] I. S. Park, S. Y. Lee, C. Adachi, T. Yasuda, *Adv. Funct. Mater.* **2016**, *26*, 1813

Chapter 7

Cyclohexane-Coupled Bipolar Host Materials with High Triplet Energies for Organic Light-Emitting Diodes Based on Delayed Fluorescence

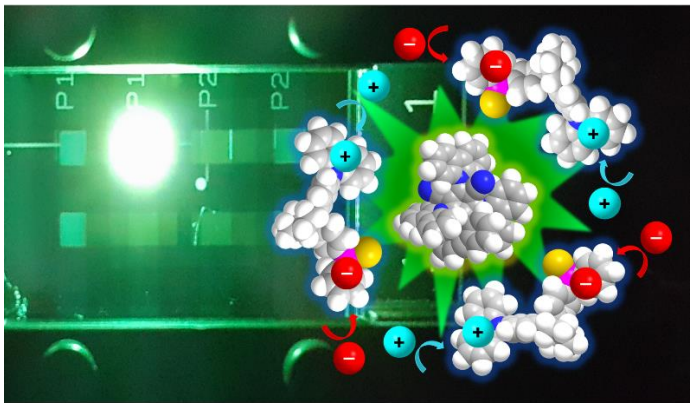

7. 1. Introduction

Similar to existing phosphorescent OLEDs, most TADF-OLEDs use a composite guest–host emitting layer (EML), where the TADF emitters as a guest are dispersed in a suitable host matrix at a low concentration to reduce concentration quenching and triplet–triplet annihilation.[1] Hence, the exploration of high-performance host materials is vital to the production of highly efficient and stable TADF-OLEDs. In this regard, there are several intrinsic physical requirements for host materials;[1c,1d,2] they are: (i) sufficiently higher T_1 energy (E_T) than the TADF emitter to prevent reverse energy transfer from the guest emitter to the host, (ii) properly aligned highest occupied molecular orbital (HOMO) and lowest unoccupied molecular orbital (LUMO) energy levels with the adjacent layers for effective charge injection, (iii) bipolar charge transport ability for balanced hole and electron fluxes in the EML, and (iv) high thermal and morphological stabilities to guarantee prolonged device operation.

Although numerous host materials have been developed, carbazole derivatives in OLED host materials still occupy a prominent research position,[3] owing to their intrinsic high E_T and good hole-transporting properties. For instance, 4,4'-bis(carbazole-9-yl)-1,1'-biphenyl (CBP)[3a,3b] is among the most widely used host material for green and red phosphorescent and TADF-OLEDs. However, CBP itself possesses a relatively low E_T of 2.66 eV,[3a,3b] which limits its application in blue-emitting devices. By removing one phenylene unit and modifying two carbazole units at the meta-linkage instead of the para-linkage, 1,3-bis(9-carbazolyl)benzene (mCP), with a high E_T of 2.90 eV, has been demonstrated to be an effective host material for blue OLEDs.[3c,3d] However, mCP as well as CBP suffers from poor morphological stability, originating from their low glass-transition temperature (T_g), which results in unfavourable crystallization or aggregation within the devices. Moreover, the propensity of mCP and CBP for unipolar hole transport causes charge recombination near the interface between the EML and the electron-transporting layer, which is detrimental to device efficiency and lifetime. Therefore, it is a significant challenge to develop novel bipolar host materials for the future of high-efficiency full-color TADF-OLEDs that simultaneously possess high E_T (>3.0 eV), high T_g (>100 °C), and balanced hole and electron transport capability. We recently reported a six-carbazole-decorated cyclotriphosphazene with a high E_T of 3.0 eV as a universal bipolar host material, achieving high η_{ext} for both blue and green TADF-OLED.[3e] To obtain bipolar, high-triplet-energy host materials, the design strategies such as introducing non-conjugated building

blocks[3f–3j] or using ortho or meta-phenylene linkages[3k–3u] to limit the π-conjugation between the electron-donating and accepting moieties have been commonly employed.

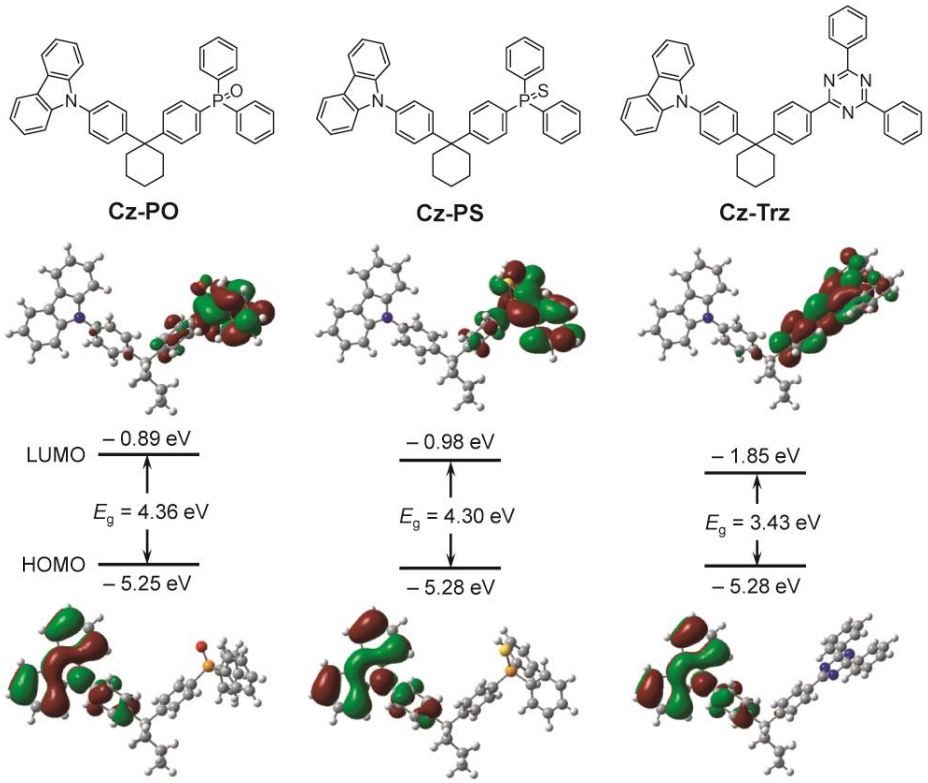

Figure 8-1. Molecular structures (top), and HOMO and LUMO distributions (bottom) of the cyclohexane-containing bipolar host materials, Cz-PO, Cz-PS, and Cz-Trz, calculated at the B3LYP/6-31G(d,p) level in a gas phase. E_g = HOMO–LUMO energy gap.

In this Chapter, a new series of bipolar host materials, Cz-PO, Cz-PS, and Cz-Trz, by integrating an electron-donating 9-phenylcarbazole (Cz) unit with an electron-accepting triphenylphosphine oxide (PO), triphenylphosphine sulfide (PS), or 2,4,6-triphenyl-1,3,5-triazine (Trz) unit through a non-conjugated cyclohexane core (**Figure 7-1**), were designed and synthesized. The effect of different electron-accepting units on the thermal, photophysical, and electrical properties of this set of materials was systematically studied. As expected, these new host materials exhibited high E_T values of over 3.0 eV and good bipolar charge transport characteristics. Among these three host materials, Cz-PS demonstrated the best OLED device performance with a maximum η_{ext} of up to 21.7% and reduced efficiency roll-off for TADF-OLEDs containing 1,2,3,5-tetrakis(carbazol-9-yl)-4,6-dicyanobenzene (4CzIPN)[4] as a green TADF emitter. The incorporation of the central cyclohexane core linked through a sp^3-hybridized carbon atom could provide spatial separation of the electron density distribution

between the peripheral units, contributing to enhancing the bipolar property and thermal stability, while maintaining the high E_T level of the resulting materials.

7. 2. Molecular Geometric and Electronic Structures

To reveal the electronic structures of Cz-PO, Cz-PS, and Cz-Trz, time-dependent density functional theory (TD-DFT) calculations were performed at the B3LYP/6-31G(d,p) level. As depicted in **Figure 7-1**, the HOMOs of these molecules are located on the electron-donating Cz units, whereas the LUMOs are mainly distributed over the electron-accepting PO, PS, and Trz moieties, which implies that these materials possess bipolar characteristics. Moreover, it was found that the central cyclohexane core effectively disrupts π-conjugation between the peripheral electron-donating and accepting moieties, leading to high values of the calculated E_T, approximately 3.0 eV (**Table 7-1**).

Table 7-1. TD-DFT calculation results for Cz-PO, Cz-PS, and Cz-Trz using the B3LYP/6-31G(d,p).[a)]

Compound	HOMO [eV]	LUMO [eV]	E_g [eV]	f	E_S / E_T [eV]	ΔE_{ST} [eV]
Cz-PO	–5.25	–0.89	4.36	0.1333	3.94 / 3.18	0.76
Cz-PS	–5.28	–0.98	4.30	0.1067	3.90 / 3.18	0.72
Cz-Trz	–5.28	–1.85	3.43	0.0307	3.13 / 2.97	0.16

[a)]Abbreviations: E_g = energy gap between HOMO and LUMO, f = oscillator strength, E_S = lowest-excited singlet energy, E_T = lowest-excited triplet energy, $\Delta E_{ST} = E_S - E_T$.

7. 3. Thermal and Photophysical Properties

As shown in **Figure 7-2**, the thermal properties of Cz-PO, Cz-PS, and Cz-Trz were characterized by thermogravimetric analysis (TGA) and differential scanning calorimetry (DSC). The decomposition temperatures (T_d), corresponding to 5% weight loss upon heating, are as high as 409, 404, and 434 °C for Cz-PO, Cz-PS, and Cz-Trz, respectively. In addition, all these compounds have a high T_g between 104 and 112 °C, which is indicative of rather high thermal and morphological stabilities as host materials. These T_d and T_g values are comparable or substantially higher than those of commonly used host materials in TADF-OLEDs, including CBP (T_d = 440 °C, T_g = 62 °C),[3a,3e,5] mCP (T_d = 370 °C, Tg = 60 °C),[3c–3e,5] and DPEPO (T_d = 322 °C).[6] Such high thermal and morphological stabilities should contribute in suppressing

unfavorable morphological change, and hence, ensuring an amorphous nature in the solid thin-film states within the devices.

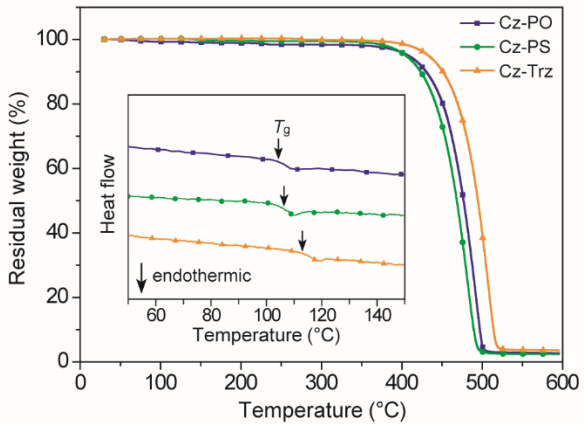

Figure 7-2. TGA and DSC (inset) curves for Cz-PO, Cz-PS, and Cz-Trz recorded at a heating rate of 10 °C min^{-1} under N_2.

The UV–vis absorption and photoluminescence (PL) spectra of neat thin films of Cz-PO, Cz-PS, and Cz-Trz are shown in **Figure 7-3a**, and the relevant photophysical data are summarized in **Table 7-2**. The three host materials exhibit strong absorption bands with peaks (λ_{abs}) below 300 nm, which are assigned to the π–π * transitions of the peripheral aromatic moieties. The lower-energy weak absorption bands ranging from 330 to 350 nm can be attributed to the n–π * transitions of the 9-phenylcarbazole unit. While the neat films of Cz-PO and Cz-PS exhibit almost the same PL emission in the UV region with peaks (λ_{PL}) at 355 nm, the neat film of Cz-Trz gives a broad structureless PL emission centered at 422 nm, suggesting that the excited state of Cz-Trz has charge-transfer characteristics that arise from the strong electron-withdrawing Trz unit. It should be noted here that efficient Förster energy transfer from the excited host materials to the 4CzIPN TADF emitter is expected since there is a considerably large spectral overlap between the emission of each host material and the absorption of 4CzIPN (**Figure 7-3a**).

Figure 7-3b shows the phosphorescence spectra of Cz-PO, Cz-PS, and Cz-Trz in frozen 2-methyltetrahydrofuran solutions obtained at 77 K, revealing well-structured emission bands with the highest-energy vibronic peaks at 409, 409, and 422 nm, respectively. Thus, the triplet energies (E_T) are determined to be 3.03, 3.03, and 2.94 eV for Cz-PO, Cz-PS, and Cz-Trz, respectively. It should be noted that the phosphorescence spectra and the E_T values of Cz-PO and Cz-PS are almost the same as those of the constituting 9-phenylcarbazole itself (**Figure 7-**

4). Therefore, the lowest excited T_1 states of both Cz-PO and Cz-PS are mainly governed by the 9-phenylcarbazole constituent. In phosphorescence spectrum of Cz-Trz, however, the emission from the 9-phenylcarbazole unit is no longer observed, presumably because of excited energy transfer from the 9-phenylcarbazole unit to the lower-energy 2,4,6-1,3,5-triazine unit. These results suggest that the respective electron-donating and accepting moieties can act as electronically-independent functional entities by virtue of the non-conjugated cyclohexane core, leading to high E_T values of the resulting bipolar materials. The E_T values of these bipolar molecules are high enough to host the green-emitting 4CzIPN (E_T = 2.4 eV)[4,7] and light-blue-emitting 2CzPN (E_T = 2.6 eV).[4,8] Such a high E_T of these host materials can be ascribed to the disruption of π-conjugation by the central cyclohexane core between the peripheral aromatic moieties.

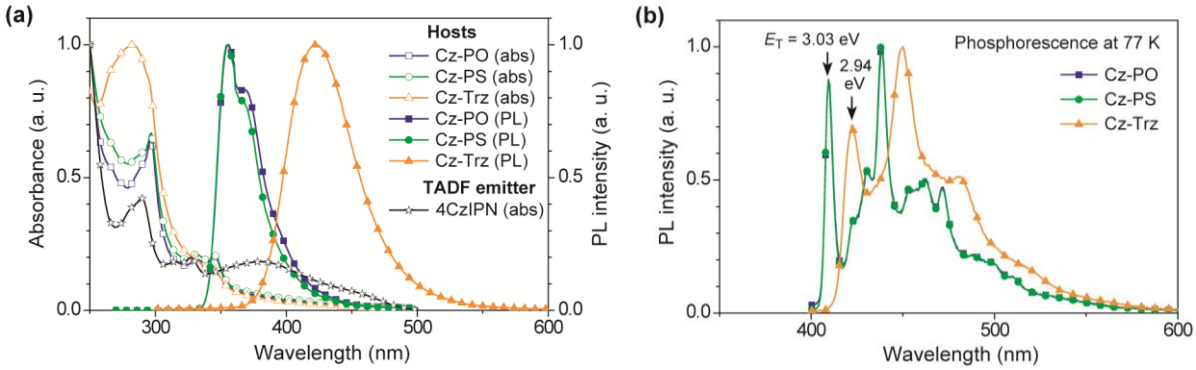

Figure 7-3. (a) UV–vis absorption and PL spectra of Cz-PO, Cz-PS, and Cz-Trz in neat thin films, and absorption spectrum of the 4CzIPN emitter in a neat thin film. (b) Phosphorescence spectra of Cz-PO, Cz-PS, and Cz-Trz in 2-methyltetrahydrofuran solutions at 77 K.

Table 7-2. Physical Parameters for Cyclohexane-Coupled Bipolar Host Materials.

Host	Photophysical properties						Thermal properties	
	λ_{abs}[a)] (nm)	λ_{PL}[a)] (nm)	HOMO[b)] (eV)	LUMO[c)] (eV)	E_g[c)] (eV)	E_T[d)] (eV)	T_g[e)] (°C)	T_d[f)] (°C)
Cz-PO	297, 331, 345	355	−6.00	−2.35	3.65	3.03	104	409
Cz-PS	297, 331, 345	355	−6.00	−2.35	3.65	3.03	107	404
Cz-Trz	283, 330, 343	422	−6.00	−2.75	3.25	2.94	112	434

[a)]Absorption and PL emission maxima measured in neat thin films. [b)]Determined by photoelectron yield spectroscopy in neat thin films. [c)]LUMO = HOMO + E_g, the values of E_g were deduced from the highest-energy onsets in the PL spectra of the neat films. [d)]Determined from the highest-energy vibronic peaks of phosphorescence spectra measured in frozen 2-methyltetrahydrofuran solutions at 77 K. [e)]Glass-transition temperature measured by DSC. [f)]Decomposition temperature (corresponding to 5% weight loss) determined by TGA.

To further study the photophysical processes between the host materials and 4CzIPN, we measured the PL spectra, quantum yields (Φ_{PL}), and transient lifetimes of the thin films with 6 wt% 4CzIPN doped in Cz-PO, Cz-PS, or Cz-Trz. As can be seen in **Figure 7-5a**, all these doped films display intense green PL emissions solely from 4CzIPN with a high Φ_{PL} of 98–99% upon photoexcitation. In addition, the transient PL decay characteristics of these doped films clearly indicate two exponential decay components (**Figure 7-5b**) consisting of a prompt fluorescence ($S_1 \rightarrow$ ground state (S_0)) with a transient lifetime (τ_p) of 14–15 ns and a delayed fluorescence ($S_1 \rightarrow T_1 \rightarrow S_1 \rightarrow S_0$) with a lifetime ($\tau_d$) of 3.5–4.3 μs at room temperature (300 K) under N_2 atmosphere.

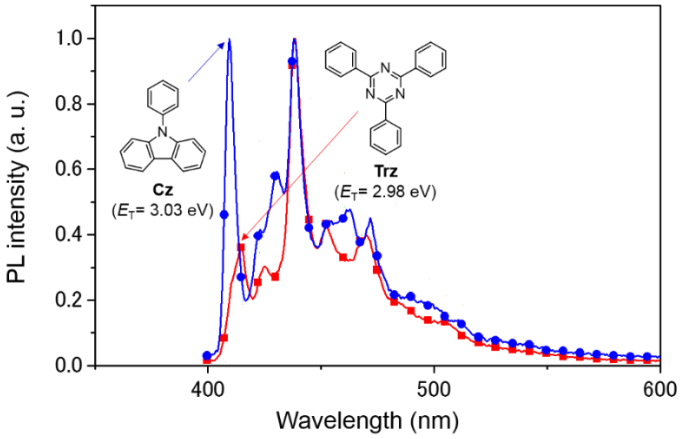

Figure 7-4. Phosphorescence spectra of 9-phenylcarbazole (Cz) and 2,4,6-triphenyl-1,3,5-triazine (Trz) in 2-methyltetrahydrofuran at 77 K.

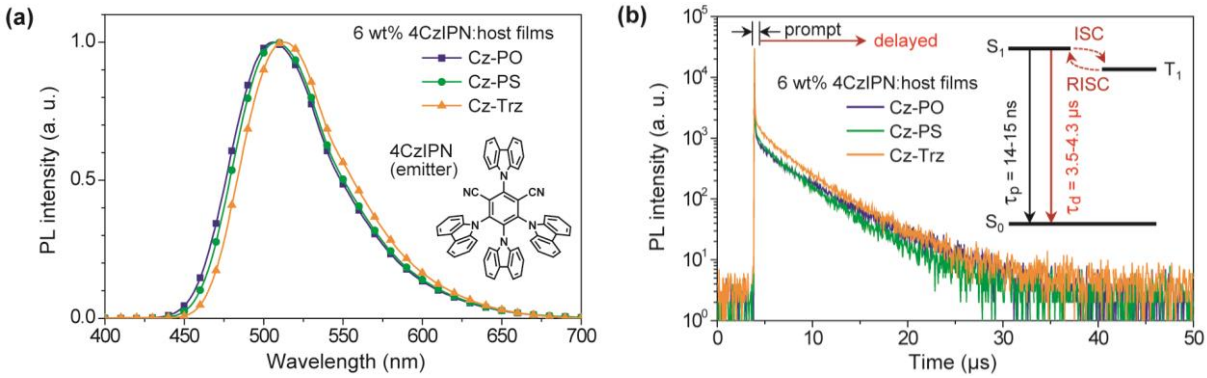

Figure 7-5. (a) Steady-state PL spectra and (b) transient PL decay curves for 6 wt%-4CzIPN:host doped thin films (host = Cz-PO, Cz-PS, and Cz-Trz) measured at 300 K under N_2. Insets: (a) chemical structure of 4CzIPN TADF emitter; (b) schematic representation of transient PL decay processes (ISC = intersystem crossing ($S_1 \rightarrow T_1$), RISC = reverse intersystem crossing ($T_1 \rightarrow S_1$), τ_p = prompt fluorescence lifetime, τ_d = delayed fluorescence lifetime).

7. 4. Electroluminescence Performance

Using the highly luminescent 4CzIPN:host TADF systems as an EML, green TADF-OLEDs were fabricated for comparing the overall device performance of the three host materials. The device configuration was ITO (100 nm)/HAT-CN (10 nm)/TAPC (40 nm)/6 wt%-4CzIPN:host (20 nm)/TPBi (50 nm)/Liq (1 nm)/Al (80 nm), as illustrated in **Figure 7-6a**. In this architecture, HAT-CN (2,3,6,7,10,11-hexacyano-1,4,5,8,9,12-hexaazatriphenylene) and TAPC (1,1-bis(4-ditolylaminophenyl)cyclohexane) act as a hole-injection layer and a hole-transporting layer (HTL), respectively. TPBi (1,3,5- tris(*N*-phenylbenzimidazol-2-yl)benzene) and Liq (8-hydroxyquinoline lithium) serve as an electron-transporting layer (ETL) and an electron-injection material, respectively. It is noted that reverse energy transfer from the doped 4CzIPN emitter to the host materials as well as unfavorable exciton quenching at the HTL/EML and EML/ETL interfaces can be effectively suppressed in the devices because all these host materials, TAPC (E_T = 2.87 eV),[3b] and TPBi (E_T = 2.74 eV)[9] have triplet energy levels higher than that of 4CzIPN.

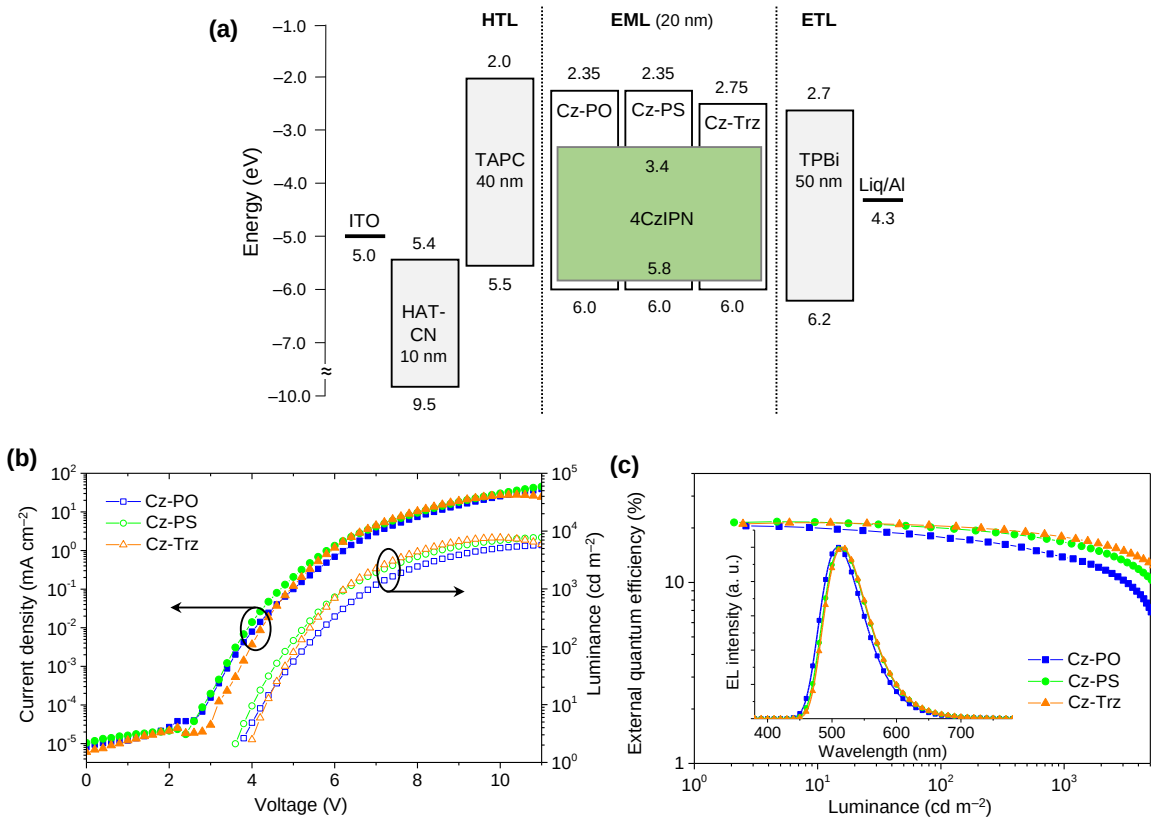

Figure 7-6. (a) Energy-level diagram of 4CzIPN-based TADF-OLEDs hosted by Cz-PO, Cz-PS, and Cz-Trz. (b) Current density–voltage–luminance (*J*–*V*–*L*) and (c) external EL quantum efficiency (η_{ext})–*L* curves of the TADF-OLEDs. The inset displays the EL spectra measured at 10 mA cm^{-2}.

Figure 7-6b and **6c** present the current density–voltage–luminance (*J*–*V*–*L*) and external quantum efficiency–luminance (η_{ext}–*L*) characteristics of the 4CzIPN-based TADF-OLEDs, respectively, and the device performances are summarized in **Table 7-3**. All the devices using Cz-PO, Cz-PS, and Cz-Trz as hosts achieved rather high OLED performances with a maximum η_{ext} of 20.5–21.7%, maximum current efficiencies (η_c) of 62.1–68.7 cd A^{-1}, and maximum power efficiencies (η_p) of 51.3–59.5 lm W^{-1}, without special light out-coupling enhancements. More importantly, the Cz-PS and Cz-Trz-hosted devices exhibited reduced efficiency roll-off characteristics at high luminance compared to the Cz-PO-hosted device. Indeed, at a practical luminance of 100 cd m^{-2} for display applications, the Cz-PS and Cz-Trz-hosted devices still had a high η_{ext} of over 20% (**Figure 7-6c** and **Table 7-3**), which suggests the superiority of Cz-PS and Cz-Trz over Cz-PO as the host for the 4CzIPN-based TADF-OLEDs.

Table 7-3. Electroluminescence Performances of 4CzIPN-Based TADF-OLEDs.[a)]

Host	λ_{EL} (nm)	η_{ext} (%)	η_c (cd A^{-1})	η_p (lm W^{-1})
		max / @100 cd m^{-2} / @1000 cd m^{-2} / @5000 cd m^{-2}	max / @100 cd m^{-2} / @1000 cd m^{-2} / @5000 cd m^{-2}	max / @100 cd m^{-2} / @1000 cd m^{-2} / @5000 cd m^{-2}
Cz-PO	510	20.5 / 17.8 / 13.8 / 6.8	62.1 / 54.9 / 42.1 / 20.1	51.3 / 33.8 / 20.1 / 6.8
Cz-PS	514	21.7 / 20.0 / 16.6 / 10.2	68.7 / 64.2 / 53.6 / 33.7	59.5 / 43.0 / 27.6 / 12.3
Cz-Trz	515	21.4 / 20.5 / 17.8 / 12.6	68.6 / 66.7 / 58.5 / 41.8	53.1 / 42.9 / 30.4 / 16.4

[a)]Abbreviations: λ_{EL} = EL emission maximum at 10 mA cm^{-2}; η_{ext} = external EL quantum efficiency; η_c = current efficiency; η_p = power efficiency.

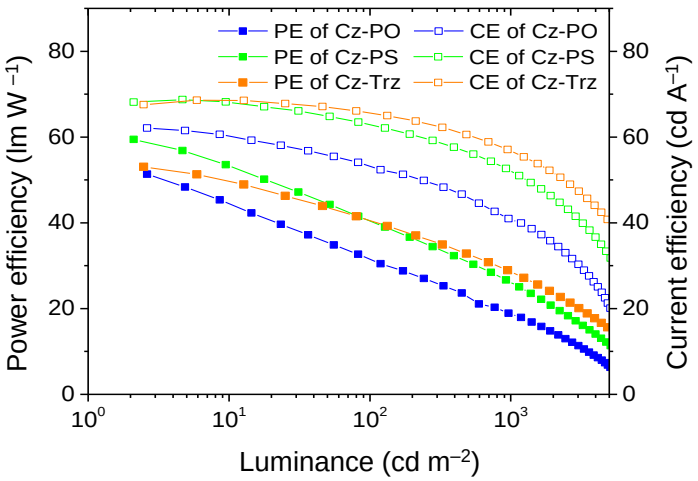

Figure 7-7. Power efficiency and current efficiency characteristics of 4CzIPN-based TADF-OLEDs employing Cz-PO, Cz-PS, and Cz-Trz as host materials.

Such superior OLED performances for the Cz-PS and Cz-Trz-hosted devices could not be explained by the magnitude of the E_T values of these host materials, since the E_T values of Cz-PO and Cz-PS (3.03 eV) are higher than that of Cz-Trz (2.94 eV). We, thus, anticipated that hole and electron balance in the EML should play an essential role in improving the device efficiencies. To evaluate the hole and electron densities in the EML, we fabricated hole-only devices (HODs) and electron-only devices (EODs) employing the 4CzIPN:host layer. The device configurations were ITO/HAT-CN (10 nm)/4,4'-bis[*N*-(1-naphthyl)-*N*-phenylamino]-1,1'-biphenyl (α -NPD, 20 nm)/6 wt%-4CzIPN:host (60 nm)/α-NPD (20 nm)/Al (100 nm) for the HODs and ITO/TPBi (20 nm)/6 wt%-4CzIPN:host (60 nm)/TPBi (20 nm)/Liq (1 nm)/Al (100 nm) for the EODs. **Figure 7-8** shows the *J*–*V* curves of these fabricated HODs and EODs. The hole current density was very similar among the three HODs (**Figure 7-8a**) because the hole-transport properties are dominated by the 9-phenylcarbazole unit, which is present in all the three host materials, as well as by the doped 4CzIPN emitter molecules. In contrast, for EODs, the highest electron current density was obtained with Cz-PS, and the order of electron current density was Cz-PS > Cz-Trz > Cz-PO (**Figure 7-8b**). This result suggests that the electron-transport ability of Cz-PO is much lower than that of Cz-PS and Cz-Trz. Therefore, the aforementioned high EL efficiencies and reduced roll-off characteristics of the Cz-PS and Cz-Trz-hosted TADF-OLEDs are primarily attributed to the appropriate bipolar nature of Cz-PS and Cz-Trz, which can lead to well-balanced charge fluxes and a broad distribution of the charge-recombination zone within the EML. Accordingly, substituting the widely used phosphine oxide (P=O) units by phosphine sulfide (P=S) units can be an effective way to develop advanced bipolar, high-triplet-energy host materials for TADF and phosphorescent OLEDs.

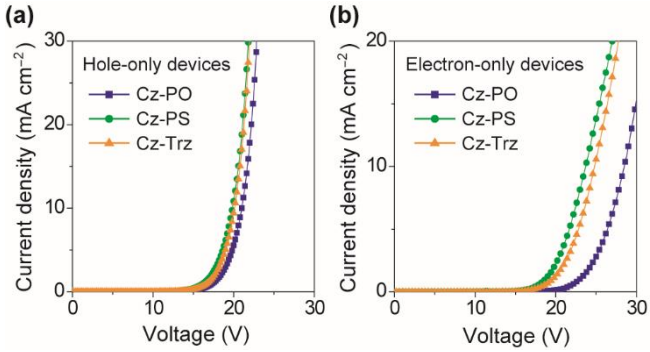

Figure 7-8. Current density–voltage (*J*–*V*) characteristics of (a) hole-only devices (HODs) and (b) electron-only devices (EODs) based on the Cz-PO, Cz-PS, and Cz-Trz hosts. HODs: ITO/HAT-CN (10 nm)/α-NPD (20 nm)/6 wt%-4CzIPN:host (60 nm)/ α -NPD (20 nm)/Al (100 nm). EODs: ITO/TPBi (20 nm)/6 wt%-4CzIPN:host (60 nm)/TPBi (20 nm)/Liq (1 nm)/Al (100 nm).

7. 5. Experimental Section

7. 5. 1. General Methods

NMR spectra were recorded on an Avance III 500 spectrometer (Bruker). Chemical shifts of ^{1}H and ^{13}C NMR signals were quoted to tetramethylsilane (δ = 0.00) and CDCl3 (δ = 77.0) as internal standards, respectively. Matrix-assisted laser desorption ionization time-of-flight (MALDI-TOF) mass spectra were collected on an Autoflex III spectrometer (Bruker Daltonics) using dithranol as the matrix. Elemental analyses were carried out with an MT-5 CHN corder (Yanaco). Thermogravimetric analysis (TGA) and differential scanning calorimetry (DSC) were performed on a DTG-60 analyzer (Shimadzu) and a DSC 204 F1 Phoenix analyzer (Netzsch), respectively, at a heating rate of 10 °C min^{-1} under N_2 atmosphere. UV–vis absorption and photoluminescence (PL) spectra were measured with a V-670 spectrometer (Jasco) and a FP-8600 spectrophotometer (Jasco), respectively, using degassed spectral grade solvents. The absolute PL quantum yields (Φ_{PL}) were measured using an ILF-835 integrating sphere system (Jasco). The transient PL measurements of doped thin films were performed using a Quantaurus-Tau C11367 lifetime spectrometer (Hamamatsu Photonics) (λ_{ex} = 340 nm, pulse width = 100 ps, and repetition rate = 20 Hz) under N_2. The HOMO energy levels of the materials in thin films were determined using an AC-2 ultraviolet photoelectron spectrometer (Riken-Keiki). The LUMO energy levels were estimated by subtracting the optical energy gap (E_g) from the measured HOMO energies; E_g values were determined from the high energy onset position of the PL spectra of the thin films. Density functional theory (DFT) calculations were performed using the Gaussian 09 program package. Geometries in the ground state were optimized using the B3LYP functional with the 6-31G(d,p) basis set. The lowest singlet and triplet excited states were computed using the optimized structures with time-dependent DFT (TD-DFT) at the same level.

7. 5. 2. Materials and Synthesis

All regents and solvents for the synthesis were purchased from Sigma-Aldrich, Tokyo Chemical Industry, or Wako Pure Chemical Industries, and were used as received unless otherwise noted. 1,2,3,5-Tetrakis(carbazol-9-yl)-4,6-dicyanobenzene (4CzIPN)[4] was prepared according to the literature procedure, and was purified by temperature-gradient vacuum sublimation. 2,3,6,7,10,11-Hexacyano-1,4,5,8,9,12-hexaazatriphenylene (HAT-CN) was donated by the Nippon Soda Co., Ltd. and was purified by vacuum sublimation before use.

Other OLED materials were purchased from E-Ray Optoelectronics Technology Co., Ltd. and were used for the device fabrication without further purification.

The synthetic routes for Cz-PO, Cz-PS, and Cz-Trz are outlined in **Scheme 7-1–3**, and the detailed synthetic procedures and characterization data are described as below. The mono-carbazolyl intermediate **2** was prepared from 1,1-bis(4-aminophenyl)cyclohexane using the Sandmeyer reaction followed by the Ullmann reaction with carbazole. Cz-PO was then synthesized via the C–P coupling reaction between **2** and diphenylphosphine oxide in the presence of catalytic amounts of $Pd_2(dba)_3$ and Xantphos (4,5-bis(diphenylphosphino)-9,9-dimethylxanthene) with 61% yield. The synthesis of Cz-PS was accomplished by treating Cz-PO with Lawesson's reagent, achieving a high yield (81%). Cz-Trz was prepared through the Suzuki–Miyaura cross-coupling reaction between **3** and **4** using $Pd(PPh_3)_4$ as a catalyst with 83% yield. The final products, Cz-PO, Cz-PS, and Cz-Trz, were further purified by temperature-gradient vacuum sublimation, and their chemical structures were confirmed by ^1H and ^{13}C nuclear magnetic resonance (NMR) spectroscopy, matrix-assisted laser desorption ionization time-of-flight (MALDI-TOF) mass spectrometry, and elemental analysis.

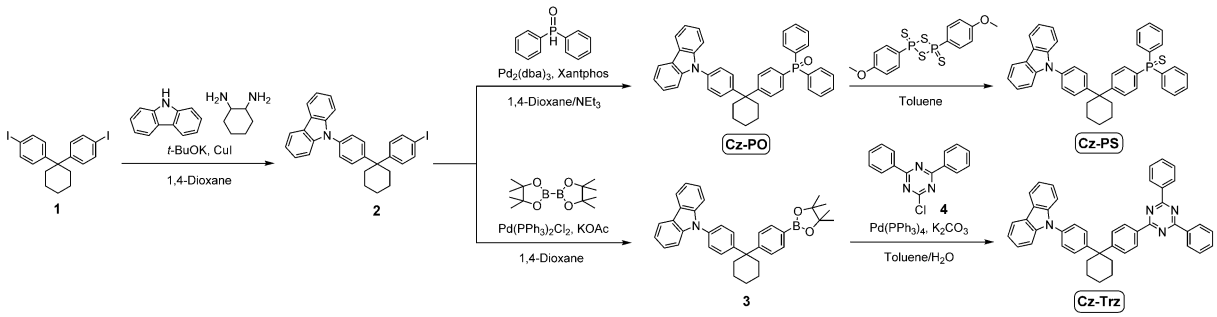

Scheme 8-1. Synthetic routes for Cz-PO, Cz-PS, and Cz-Trz.

Synthesis of Cz-PO: To a mixture of **2** (3.38 g, 6.41 mmol) and diphenylphosphine oxide (1.30 g, 6.43 mmol) in dry 1,4-dioxane (60 mL) were added triethylamine (1.5 mL), $Pd_2(dba)_3$ (0.27 g, 0.30 mmol), and 4,5-bis(diphenylphosphino)-9,9-dimethylxanthene (Xantphos; 0.34 g, 0.59 mmol) under N_2. The mixture was stirred for 12 h at 80 °C. After cooling to room temperature, the reaction mixture was added into water, filtered through a Celite pad, and then extracted with ethyl acetate. The combined organic layers were washed with water and dried over anhydrous $MgSO_4$. After filtration and evaporation, the crude product was purified by column chromatography on silica gel (eluent: CH_2Cl_2/hexane = 1:1, v/v) and recrystallization from toluene to afford Cz-PO as a white solid (yield = 2.35 g, 61%). This compound was further

purified by temperature-gradient sublimation under vacuum before use. ^{1}H NMR (500 MHz, $CDCl_3$): δ 8.13 (d, J = 7.7 Hz, 2H), 7.72-7.67 (m, 4H), 7.62 (d, J = 8.5 Hz, 1H), 7.59 (d, J = 8.5 Hz, 1H), 7.54 (td, J = 7.4 Hz, 1.5 Hz, 2H), 7.49-7.45 (m, 10H), 7.42-7.37 (m, 4H), 7.29-7.27 (m, 2H), 2.38-2.36 (m, 4H), 1.68-1.55 (m, 6H). ^{13}C NMR (125 MHz, $CDCl_3$): δ 152.58, 146.92, 140.83, 135.24, 133.01, 132.32, 132.24, 132.18, 132.15, 132.07, 131.90, 131.88, 130.06, 129.22, 128.54, 128.44, 127.54, 127.45, 126.77, 125.85, 123.31, 120.25, 119.84, 109.87, 46.51, 37.04, 26.23, 22.85. MS (MALDI-TOF): *m/z* calcd 602.26 $[M+H]^+$; found, 602.31. Anal. calcd for $C_{42}H_{36}NOP$: C 83.84, H 6.06, N 2.33; found: C 83.88, H 5.99, N 2.34.

Synthesis of Cz-PS: To a solution of Cz-PO (1.20 g, 1.99 mmol) in dry toluene (100 mL) was added 2,4-bis(4-methoxyphenyl)-1,3,2,4-dithiadiphosphetane-2,4-disulfide (Lawesson's reagent; 1.61 g, 3.98 mmol) under N_2. The mixture was refluxed for 12 h. After cooling to room temperature, the solvent was removed under reduced pressure. Then, the crude product was purified column chromatography on silica gel (eluent: CH_2Cl_2/hexane = 1:1, v/v) and recrystallization from toluene to give Cz-PS as a white solid (yield = 1.00 g, 81%). This compound was further purified by temperature-gradient sublimation under vacuum before use. ^{1}H NMR (500 MHz, $CDCl_3$): δ 8.13 (d, J = 7.8 Hz, 2H), 7.76-7.72 (m, 4H), 7.66 (d, J = 8.5 Hz, 1H), 7.64 (d, J = 8.5 Hz, 1H), 7.51 (td, J = 7.4 Hz, 2.0 Hz, 2H), 7.47-7.43 (m, 10H), 7.41-7.38 (m, 4H), 7.29-7.26 (m, 2H), 2.38-2.36 (m, 4H), 1.64-1.56 (m, 6H). ^{13}C NMR (125 MHz, $CDCl_3$): δ 146.70, 140.82, 135.26, 133.28, 132.61, 132.40, 132.35, 132.31, 132.26, 131.53, 131.51, 130.28, 129.59, 128.59, 128.54, 128.44, 127.53, 127.43, 126.78, 125.85, 123.31, 120.25, 119.84, 109.88, 46.43, 37.05, 26.23, 22.85. MS (MALDI-TOF): *m/z* calcd 618.24 $[M+H]^+$; found, 618.40. Anal. calcd for $C_{42}H_{36}NPS$: C 81.66, H 5.87, N 2.27; found: C 81.59, H 5.81, N 2.24.

Synthesis of Cz-Trz: To a mixture of **3** (3.00 g, 5.69 mmol), **4** (1.68 g, 6.28 mmol), and $Pd(PPh_3)_4$ (0.20 g, 0.17 mmol) in dry toluene (30 mL) and ethanol (20 mL) was added an aqueous solution (10 mL) of potassium carbonate (1.58 g, 11.4 mmol) under N_2. The mixture was refluxed for 12 h. After cooling to room temperature, the reaction mixture was added into water, filtered through a Celite pad, and the extracted with CH_2Cl_2. The combined organic layers were washed with water, and dried over anhydrous $MgSO_4$. After filtration and evaporation, the crude product was purified by column chromatography on silica gel (eluent: CH_2Cl_2/hexane = 1:5, v/v) and recrystallization from toluene to afford Cz-Trz as a white solid

(yield = 3.00 g, 83%). This compound was further purified by temperature-gradient sublimation under vacuum before use. ^{1}H NMR (500 MHz, $CDCl_3$): δ 8.78 (dd, *J* = 8.2 Hz, 1.4 Hz, 4H), 8.74 (d, *J* = 8.6 Hz, 2H), 8.12 (d, *J* = 7.7 Hz, 2H), 7.63-7.53 (m, 10H), 7.48 (d, *J* = 8.7 Hz, 2H), 7.42 (d, *J* = 7.9 Hz, 2H), 7.38 (td, *J* = 7.5 Hz, 1.1 Hz, 2H), 7.28-7.25 (m, 2H), 2.54-2.51 (m, 2H), 2.43-2.35 (m, 2H), 1.72-1.58 (m, 6H). ^{13}C NMR (125 MHz, $CDCl_3$): *δ* 171.60, 152.86, 147.70, 140.87, 136.29, 135.14, 133.79, 132.48, 129.17, 128.94, 128.63, 128.49, 127.73, 126.77, 125.82, 123.28, 120.22, 119.78, 109.91, 46.64, 37.15, 26.32, 22.96. MS (MALDI-TOF): *m/z* calcd 632.29 $[M]^+$; found, 632.55. Anal. calcd for $C_{45}H_{36}N_4$: C 85.41, H 5.73, N 8.85; found: C 85.49, H 5.70, N 8.88.

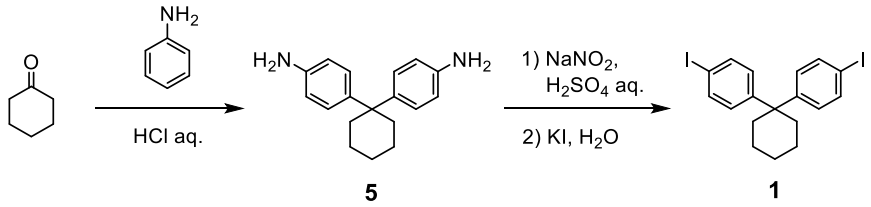

Scheme 8-2. Synthesis of compound **1**.

Synthesis of 1,1-bis(4-aminophenyl)cyclohexane (5): To a mixture of cyclohexanone (15.0 g, 153 mmol) in hydrochloric acid (36%, 60 mL) was added to aniline (56.9 g, 611 mmol). The reaction mixture was refluxed for 20 h. After cooling to room temperature, an aqueous solution of sodium hydroxide (20%) was added to the mixture to adjust the pH to ~10, and then the product was extracted with ethyl acetate. The combined organic layers were washed with water, and dried over anhydrous magnesium sulfate. After filtration and evaporation, the crude product was purified by column chromatography on silica gel (eluent: ethyl acetate/hexane = 1:1, v/v) to give **5** as a pale yellow solid (yield = 30.1 g, 74%). ^{1}H NMR (500 MHz, $CDCl_3$): *δ* 7.04 (d, *J* = 8.5 Hz, 4H), 6.60 (d, *J* = 8.5 Hz, 4H), 3.51 (s, br, 4H), 2.16 (t, *J* = 5.5 Hz, 4H), 1.55-1.46 (m, 6H).

Synthesis of 1,1-bis(4-iodophenyl)cyclohexane (1): To a mixture of **5** (29.8 g, 112 mmol) in an aqueous sulfuric acid (25%, 300 mL) was added dropwise an aqueous solution (160 mL) of sodium nitrite (31.1 g, 450 mmol) at 0 °C. The mixture was stirred for 2 h at the same temperature. Then, formed precipitates were filtered and washed with distilled water. The precipitates were added slowly to an aqueous solution (750 mL) of potassium iodide (74.7 g, 450 mmol). The mixture was stirred for 12 h at 50 °C. After cooling to room temperature, an

aqueous solution of sodium thiosulfate was added to the reaction mixture to remove remained iodine. The product was extracted with dichloromethane. The combined organic layers were washed with water, and dried over anhydrous magnesium sulfate. After filtration and evaporation, the crude product was purified by column chromatography on silica gel (eluent: hexane) to afford **1** as a white solid (yield = 26.0 g, 47%). ^{1}H NMR (500 MHz, $CDCl_3$): δ 7.58 (d, J = 8.6 Hz, 4H), 6.99 (d, J = 8.6 Hz, 4H), 2.19 (t, J = 5.5 Hz, 4H), 1.53-1.48 (m, 6H).

Synthesis of 1-[4-(carbazol-9-yl)phenyl]-1-(4-iodophenyl)cyclohexane (2): A mixture of **1** (20.0 g, 41.0 mmol), carbazole (5.48 g, 32.8 mmol), copper iodide (4.69 g, 24.6 mmol), potassium *tert*-butoxide (12.9 g, 115 mmol), and 1,2-diaminocyclohexane (2.34 g, 20.5 mmol) in dry 1,4-dioxane (400 mL) was refluxed for 48 h under N_2. After cooling to room temperature, the reaction mixture was added into water, and then filtered through a Celite pad. The product was extracted with dichloromethane. The combined organic layers were washed with water, and dried over anhydrous magnesium sulfate. After filtration and evaporation, the crude product was purified by column chromatography on silica gel (eluent: dichloromethane/hexane = 1:5, v/v) to afford **2** as a white solid (yield = 10.8 g, 50%). ^{1}H NMR (500 MHz, $CDCl_3$): δ8.13 (d, J = 7.7 Hz, 2H), 7.66 (d, J = 8.6 Hz, 2H), 7.45 (s, 4H), 7.40-7.38 (m, 4H), 7.28-7.26 (m, 2H), 7.13 (d, J = 8.6 Hz, 2H), 2.35-2.31 (m, 4H), 1.65-1.56 (m, 6H). MS (MALDI-TOF): m/z calcd 527.11 $[M]^+$; found 527.12.

Synthesis of 1-[4-(carbazole-9-yl)phenyl]-1-[4-(4,4,5,5-tetramethyl-1,3,2-dioxaborolan-2-yl)phenyl]cyclohexane (3): To a mixture of **2** (5.00 g, 9.5 mmol) and potassium acetate (2.80 g, 28.5 mmol) in dry 1,4-dioxane (50 mL) were added $Pd(PPh_3)_2Cl_2$ (0.20 g, 0.29 mmol) and 4,4,4',4',5,5,5',5'-octamethyl-2,2'-bi(1,3,2-dioxaborolane) (4.30 g, 16.9 mmol) under N_2. The mixture was stirred for 48 h at 90 °C. After cooling to room temperature, the reaction mixture was added into water, and then filtered through a Celite pad. The product was extracted with dichloromethane. The combined organic layers were washed with water, and dried over anhydrous magnesium sulfate. After filtration and evaporation, the crude product was purified by column chromatography on silica gel (eluent: dichloromethane/hexane = 1:3, v/v) to afford **3** as a white solid (yield = 4.0 g, 80%). ^{1}H NMR (500 MHz, $CDCl_3$): δ 8.12 (d, J = 7.8 Hz, 2H), 7.80 (d, J = 8.3 Hz, 2H), 7.48-7.37 (m, 10H), 7.27-7.24 (m, 2H), 2.47-2.43 (m, 2H), 2.34-2.29 (m, 2H), 1.66-1.58 (m, 6H), 1.34 (s, 12H). MS (MALDI-TOF): m/z calcd 527.30 $[M]^+$; found 527.16.

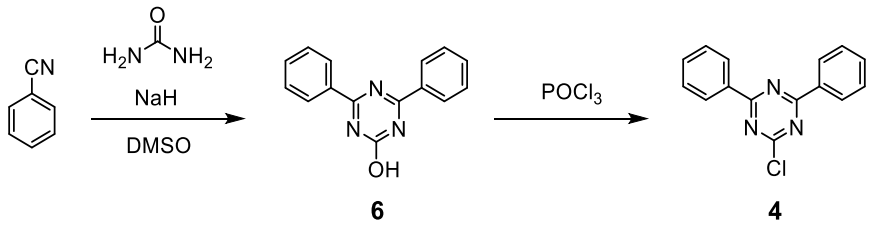

Scheme 7-3. Synthesis of compound **4**.

Synthesis of 4,6-diphenyl-1,3,5-triazin-2-ol (6): A mixture of benzonitrile (3.43 g, 33.3 mmol) and urea (5.10 g, 84.9 mmol) in dry dimethyl sulfoxide (100 mL) was stirred at room temperature under N_2. After cooling to 0 °C, sodium hydride (4.00 g, 167 mmol) was slowly added to the mixture. The reaction mixture was further stirred for 12 h at room temperature to form precipitates. The precipitates were collected by filtration, washed with water and hexane, and then dried under vacuum to give **6** as a white solid (5.20 g, 63%). ^{1}H NMR (500 MHz, $CDCl_3$): δ 8.59 (d, J =7.4 Hz, 4H), 7.68 (t, J = 7.1 Hz, 2H), 7.61 (t, J = 7.4 Hz, 4H). MS (MALDI-TOF): m/z calcd 249.09 $[M]^+$; found 249.63.

Synthesis of 2-chloro-4,6-diphenyl-1,3,5-triazine (4): A mixture of **6** (5.00 g, 20.1 mmol) and phosphoryl chloride (50 mL) was stirred for 3 h at 90 °C under N_2. After cooling to room temperature, the phosphoryl chloride was removed under reduced pressure with heating. Ice-water was slowly added into the resulting crude product, and then the precipitates were collected by filtration. The product was washed with water, and recrystallized from methanol to give **4** as a gray solid (yield = 3.10 g, 58%). ^{1}H NMR (500 MHz, $CDCl_3$): δ8.63 (dd, J = 8.4 Hz, 1.3 Hz, 4H), 7.66-7.62 (m, 2H), 7.56 (t, J = 7.7 Hz, 4H). MS (MALDI-TOF): m/z calcd 267.06 $[M]^+$; found 267.61.

8. 5. 3. OLED Fabrication and Measurements

Indium tin oxide (ITO)-coated glass substrates were cleaned with detergent, deionized water, acetone, and isopropanol. The substrates were then subjected to UV–ozone treatment for 15 min before they were loaded into a vacuum evaporation system. The organic layers and a cathode aluminum layer were thermally evaporated on the substrates with an evaporation rate of <0.3 nm s^{-1} under vacuum (<6 × 10^{-5} Pa) through a shadow mask. The layer thickness and deposition rate were monitored in situ during deposition by an oscillating quartz thickness

monitor. OLED properties were measured using a Keithley 2400 source meter and a Konica Minolta CS-2000 spectroradiometer.

8. 6. Conclusions

In summary, three bipolar host materials, Cz-PO, Cz-PS, and Cz-Trz, have been designed and synthesized by incorporating the electron-donating 9-phenylcarbazole unit and various electron-accepting aromatic units into a central cyclohexane core. The introduction of the non-conjugated cyclohexane core in the molecular design produced novel host materials with a high glass-transition temperature of over 100 °C and a high triplet energy level of about 3.0 eV. By using Cz-PS and Cz-Trz as a host and 4CzIPN as a green TADF emitter, we have developed high-performance OLEDs exhibiting high external electroluminescence quantum efficiencies that exceed 20% even at a high luminance of 100 cd m^{-2}. Among the three host materials, Cz-PS, bearing a triphenylphosphine sulfide unit, has been demonstrated to show superior bipolar transport ability, offering well-balanced current densities for holes and electrons in the emitting layer. Thus, our study can promote further design and the development of high-performance universal host materials for TADF and phosphorescent emitters.

References

[1] a) R. Czerwieniec, J. Yu, H. Yersin *Inorg. Chem.* **2011**, *50*, 8293; b) Z.-Q. Zhu, T. Fleetham, E. Turner, J. Li, *Adv. Mater.* **2015**, *27*, 2533; c)Y. Tao, C. Yang, J. Qin, *Chem. Soc. Rev.* **2011**, *40*, 2943; d) L. Xiao, Z. Chen, B. Qu, J. Luo, S. Kong, Q. Gong, J. Kido, *Adv. Mater.* **2011**, *23*, 926.

[2] a) A. Chaskar, H.-F. Chen, K.-T. Wong, *Adv. Mater.* **2011**, *23*, 3876; b) S. K. Yook, J. Y. Lee, *Adv. Mater.* **2012**, *24*, 3169.

[3] M. A. Baldo, S. Lamansky, P. E. Burrows, M. E. Thompson, S. R. Forrest, *Appl. Phys. Lett.* **1999**, *75*, 4; b) K. Goushi, R. Kwong, J. J. Brown, H. Sasabe, C. Adachi, *J. Appl. Phys.* **2004**, *95*, 7798; c) V. Adamovich, J. Brooks, A. Tamayo, A. M. Alexander, P. I. Djurovich, B. W. D'Andrade, C. Adachi, S. R. Forrest, M. E. Thompson, *New J. Chem.* **2002**, *26*, 1171; d) R. J. Holmes, S. R. Forrest, Y.-J. Tung, R. C. Kwong, J. J. Brown, S. Garon, M. E. Thompson, *Appl. Phys. Lett.* **2003**, *82*, 2422; e) T. Nishimoto, T. Yasuda, S. Y. Lee, R. Kondo, C. Adachi, *Mater. Horiz.* **2014**, *1*, 264; f) F. M. Hsu, C.-H. Chien, P. I. Shih, C.-F. Shu, *Chem. Mater.* **2009**, *21*, 1017; g) L. Zeng, T. Y.-H. Lee, P. B. Merkel, S. H. Chen, *J. Mater. Chem.* **2009**, *19*, 8772; h) H.-H. Chou, C.-H. Cheng, *Adv. Mater.* **2010**, *22*, 2468; i) W.-Y. Hung, T.-C. Wang, H.-C. Chiu, H.-F. Chen, K.-T. Wong, *Phys. Chem. Chem. Phys.* **2010**, *12*, 10685; j) S. Gong, Y.-L. Chang, K. Wu, R. White, Z.-H. Lu, D. Song, C. Yang, *Chem. Mater.* **2014**, *26*, 1463; k) S.-J. Su, H. Sasabe, T. Takeda, J. Kido, *Chem. Mater.* **2008**, *20*, 1691; l) Y. Tao, Q. Wang, C. Yang, Q. Wang, Z. Zhang, T. Zou, J. Qin, D. Ma, *Angew. Chem. Int. Ed.* **2008**, *47*, 8104; m) S. Q. Jeon, K. S. Yook, C. W. Joo, J. Y. Lee, *Adv. Funct. Mater.* **2009**, *19*, 3644; n) Y. Tao, Q. Wang, C. Yang, C. Zhong, K. Zhang, J. Qin D. Ma, *Adv. Funct. Mater.* **2010**, *20*, 304; o) Y.-M. Chen, W. Y. Hung, H.-W. You, A. Chaskar, H.-C. Ting, H.-F. Chen, K.-T. Wong, Y.-H. Liu, *J. Mater. Chem.* **2011**, *21*, 14971; p) H. Sasabe, N. Toyota, H. Nakanishi, T. Ishizuka, Y.-J. Pu, J. Kido, *Adv. Mater.* **2012**, *24*, 3212; q) M.-S. Lin, S.-J. Yang, H.-W. Chang, Y.-H. Huang, Y.-T. Tsai, C.-C. Wu, S.-H. Chou, E. Mondal, K.-T. Wong, *J. Mater. Chem.* **2012**, *22*, 16114; r) Y. Im, J. Y. Lee, *Chem. Commun.* **2013**, *49*, 5948; s) B. Pan, B. Wang, Y. Wang, P. Xu, L. Wang, J. Chen, D. Ma, *J. Mater. Chem. C* **2014**, *2*, 2466; t) M. Kim, J. Y. Lee, *Adv. Funct. Mater.* **2014**, *24*, 4164; u) W. Li, J. Li, F. Wang, Z. Gao, S. Zhang, *ACS Appl. Mater. Interfaces* **2015**, *7*, 26206.

[4] H. Uoyama, K. Goushi, K. Shizu, H. Nomura, C Adachi, *Nature* **2012**, *492*, 234.

[5] M.-H. Tsai, Y.-H. Hong, C.-H. Chang, H.-C. Su, C.-C. Wu, A. Matoliukstyte, J. Simokaitiene, S. Grigalevicius, J. V. Grazulevicius, C.-P. Hsu, *Adv. Mater.* **2007**, *19*, 862.

[6] a) C. Han, Y. Zhao, H. Xu, J. Chen, Z. Deng, D. Ma, Q. Li, P. Yan, P. *Chem. Eur. J.* **2011**, *17*, 5800; b) J. Zhang, D. Ding, Y. Wei, H. Xu, *Chem. Sci.* **2016**, *7*, 2870.

[7] H. Nakanotani, K. Masui, J. Nishide, T. Shibata, C. Adachi, *Sci. Rep.* **2013**, *3*, 2127.

[8] K. Masui, H. Nakanotani, C. Adachi, *Org. Electron.* **2013**, *14*, 2721.

[9] a) Y. T. Tao, E. Balasubramaniam, A. Danel, P. Tomasik, *Appl. Phys. Lett.* **2000**, *77*, 933; b) M. E. Kondakova, T. D. Pawlik, R. H. Young, D. J. Giesen, D. Y. Kondakov, C. T. Brown, J.-C. Deaton, J.-R. Lenhard, K. P Klubek, *J. Appl. Phys.* **2008**, *104*, 094501.

Chapter 8

Summary and Perspective

In this dissertation, new molecules were designed and synthesized for high-performance TADF-OLEDs.

In **Chapter 2**, luminescent wedge-shaped molecules, which comprise a central phthalonitrile or 2,3-dicyanopyrazine acceptor core coupled with various donor units, were designed and synthesized as TADF emitters. This set of materials allows systematic fine tuning of the band gap and exhibits TADF emission that cover the entire visible range from blue to red. Full-color TADF-OLEDs with high maximum external EL quantum efficiencies of up to 18.9% have been demonstrated by using these phthalonitrile and 2,3-dicyanopyrazine-based TADF emitters.

In **Chapter 3**, high-performance blue TADF molecules based on a central pyrimidine acceptor (A) core with peripheral diphenylacridan donor (D) units, have been developed. A design motif of highly twisted donor–acceptor–donor (D–A–D) architectures having a small singlet–triplet energy splitting allows for the production of efficient pure blue TADF with high quantum efficiencies exceeding 90%. An OLED based on the blue pyrimidine-based TADF emitter exhibited a high maximum external quantum efficiency of 20.8% and a high power efficiency of 31.5 lm W^{-1}.

In **Chapter 4**, a simple and versatile donor–acceptor (D–A) system combining acridan-based donors and pyrimidine-based acceptors has been developed as a new platform for high-efficiency deep-blue TADF emitters. The designed pre-twisted acridan–pyrimidine D–A molecules exhibit small singlet–triplet energy splitting and high photoluminescence quantum yields, functioning as efficient deep-blue TADF emitters. OLEDs utilizing these TADF emitters display bright blue electroluminescence with external EL quantum efficiencies of up to 20.4%, maximum current efficiencies of 41.7 cd A^{-1}, maximum power efficiencies of 37.2 lm W^{-1}, and color coordinates of (0.16, 0.23). The design strategy featuring such acridan–pyrimidine D–A motifs can offer great prospects for further developing high-performance deep-blue TADF emitters and TADF-OLEDs.

In **Chapter 5**, a highly efficient blue emitter based on phenazaborin acceptor and spiroacridan donor units was developed by weakening the intramolecular charge-transfer (ICT) effect. This new emitter were exhibited efficient TADF properties with a high PL quantum efficiency of nearly 100% in its doped film. A blue-emitting OLED containing the phenazaborin derivative as a TADF emitter exhibited a high external EL quantum efficiency of 18.2% with CIE color coordinates of (0.15, 0.23).

In **Chapter 6**, new linear-shaped TADF emitters, which consists of a central

terephthalonitrile acceptor core and three donor moieties linked by π-conjugated phenylene bridges were designed and synthesized. A D–A–D type linear-shaped molecular architecture allows to exhibit efficient TADF properties as well as horizontally oriented dipoles against to a substrate in a host matrix, which induce efficient light-blue, green, and yellow emission with small singlet–triplet energy splitting of less than 0.28 eV. Multilayer OLEDs based on these TADF emitters with a suitable host material exhibit both high internal quantum efficiencies of nearly 80% and extremely high light out-coupling efficiencies of over 30%, which lead to high maximum external electroluminescence quantum efficiencies of up to 23.4%.

In **Chapter 7**, novel bipolar host materials consisting of an electron-donating 9-phenylcarbazole unit and an electron-accepting triphenylphosphine oxide, triphenylphosphine sulfide, or 2,4,6-triphenyl-1,3,5-triazine unit linked by a non-conjugated cyclohexane core, have been developed. These bipolar host materials possess high glass-transition temperatures of over 100 °C and high lowest triplet values of approximately 3.0 eV. TADF-OLEDs employing these bipolar host materials with 1,2,3,5-tetrakis(carbazol-9-yl) -4,6-dicyanobenzene (4CzIPN) as a green TADF emitter achieved high external EL quantum efficiencies of up to 21.7% together with reduced efficiency roll-off characteristics. This is because of expansion of the charge-recombination zone within the emission layer arising from the bipolar charge transport ability of these host materials.

At the beginning of molecular design for full-color TADF materials based on the wedge-shaped molecular structure, various design strategies were introduced, including high-efficiency blue TADF emitters employing new acceptors of pyrimidine or phenazaborin, linear-shaped TADF materials with horizontally oriented dipoles for high EL efficiencies, and even bipolar host materials possessing high triplet energies and glass-transition temperatures by a non-conjugated cyclohexane core. This dissertation will be helpful in designing new high-efficiency TADF materials for future lighting applications

Finally, the author would like to introduce a new approach for highly efficient pure blue TADF materials. Up to date, highly efficient TADF materials have been reported with three primary colors (red, green, and blue) as mentioned in previous chapters. Although TADF-based OLEDs achieved high external quantum EL efficiencies of over 20%, several problems are awaiting solution as follows: (i) wide full width at half maximum (FWHM) of TADF emitters in the range of 80–120 nm (0.4–0.5 eV) because of their intramolecular charge transfer transition behavior between the donor and acceptor units, which disturbs the high color purity, especially in the blue region; (ii) the long emission lifetimes of blue

TADF emitters over 10 μs, which lead to decreasing the EL efficiency with increasing current density by undergoing the exciton deactivation processes such as triplet-triplet annihilation (TTA) and singlet-triplet annihilation (STA); (iii) TADF emitters normally have to be dispersed in a suitable host matrix due to their tendency to concentration quenching behavior at a high concentration of the emitter, which complicate the fabrication process of the device as well as need to additional molecular design for a suitable host material. Moreover, such a low concentrated emitting layer in the device decreases reliability of the device in comparison with the heavily doped or non-doped devices. Therefore, the author notes that upper mentioned requirements should be fulfilled for practical applications of blue TADF materials as OLEDs and lighting.

List of Publications

■ Original Papers

[1] In Seob Park, Sae Youn Lee, Chihaya Adachi, and Takuma Yasuda,
"Full-Color Delayed Fluorescence Materials Based on Wedge-Shaped Phthalonitriles and Dicyanopyrazines: Systematic Design, Tunable Photophysical Properties, and OLED Performance",
Advanced Functional Materials **2016**, *26*, 1813–1821. (**Chapter 2**)

[2] In Seob Park, Jiyoung Lee, and Takuma Yasuda,
"High-Performance Blue Organic Light-Emitting Diodes with 20% External Quantum Efficiency Based on Pyrimidine-Containing Thermally Activated Delayed Fluorescence Emitters",
Journal of Materials Chemistry C **2016**, *4*, 7911–7916. (**Chapter 3**)

[3] In Seob Park, Hideaki Komiyama, and Takuma Yasuda,
"Pyrimidine-Based Twisted Donor–Acceptor Delayed Fluorescence Molecules: A New Universal Platform for Highly Efficient Blue Electroluminescence",
Chemical Science **2017**, *8*, (DOI: 10.1039/C6SC03793C) in press. (**Chapter 4**)

[4] In Seob Park, Masaki Numata, Chihaya Adachi, and Takuma Yasuda,
"A Phenazaborin-Based High-Efficiency Blue Delayed Fluorescence Material",
Bulletin of the Chemical Society of Japan **2016**, *89*, 375–377. (**Chapter 5**)

[5] In Seob Park, Ryosuke Kondo, Naoya Aizawa, Chihaya Adachi, and Takuma Yasuda,
"Design of Highly Efficient Linear-Shaped Thermally Activated Delayed Fluorescent Emitters with Horizontally Oriented Dipoles",
in preparation. (**Chapter 6**)

[6] In Seob Park, Hongwook Seo, Hiroki Tachibana, Joung Uk Kim, Jinbo Zhang, Se Mo Son, and Takuma Yasuda,
"Cyclohexane-Coupled Bipolar Host Materials with High Triplet Energies for Organic Light-Emitting Diodes Based on Thermally Activated Delayed Fluorescence",
ACS Applied Materials & Interfaces **2017**, *9*, (DOI: 10.1021/acsami.6b13002) in press. (**Chapter 7**)

■ Joint Papers

[1] Jiyoung Lee, In Seob Park, and Takuma Yasuda,
"Thermally Activated Delayed Fluorescence Properties of Regioisomeric Xanthone-Based Twisted Intramolecular Charge-Transfer Luminophores"
Bulletin of the Chemical Society of Japan **2017**, *90*, (DOI: 10.1246/bcsj.20160380) in press.

[2] Naoya Aizawa, Chao-Jen Tsou, In Seob Park, and Takuma Yasuda,
"Aggregation-Induced Delayed Fluorescence from Phenothiazine-Containing Donor–Acceptor Molecules for High-Efficiency Non-Doped Organic Light-Emitting Diodes",
Polymer Journal **2017**, *49*, 197–202.

[3] Sunbin Hwang, William J. Potscavage, Jr., Yu Seok Yang, In Seob Park, Toshinori Matsushima, and Chihaya Adachi,
"Solution-Processed Organic Thermoelectric Material Exhibiting Doping-Concentration-Dependent Polarity",
Physical Chemistry Chemical Physics **2016**, 18, 29199–29207.

[4] Ryuhei Furue, Takuro Nishimoto, In Seob Park, Jiyoung Lee, and Takuma Yasuda,
"Aggregation-Induced Delayed Fluorescence Based on Donor/Acceptor-Tethered Janus Carborane Triads: Unique Photophysical Properties for Non-Doped OLEDs",
Angewandte Chemie International Edition **2016**, *55*, 7171–7175.

[5] Naoya Aizawa, In Seob Park, and Takuma Yasuda,
"Design of Thermally Activated Delayed Fluorescence Materials for Organic Light-Emitting Diodes",
AAPPS Bulletin **2016**, *26*, 9–19.

[6] Sae Youn Lee, Takuma Yasuda, In Seob Park, and Chihaya Adachi,
"X-Shaped Benzoylbenzophenone Derivatives with Crossed Donors and Acceptors for Highly Efficient Thermally Activated Delayed Fluorescence",
Dalton Transactions **2015**, *44*, 8356–8359.

List of Symposium

■ International Symposium

[1] In Seob Park, Chihaya Adachi, and Takuma Yasuda,
"Highly Efficient Thermally Activated Delayed Fluorescence Emitters Based on Benzonitrile Derivatives and Their Application in organic Light-Emitting Diodes*"*,
International Union of Materials Research Societies-International Conference on Electronic Materials (IUMRS-ICEM2016), Suntec, Singapore (July 04–08, 2016), Poster presentation.

[2] In Seob Park, Takuma Yasuda, Sae Youn Lee and Chihaya Adachi,
"Design of Full-Color Thermally Activated Delayed Fluorescence Emitters Based on Benzonitrile Derivatives and Their Application in Organic Light-Emitting Diodes",
The International Chemical Congress of Pacific Basin Societies 2015, Honolulu, Hawaii, USA (December 15–20, 2015), Oral presentation.

[3] In Seob Park, Sae Youn Lee, Takuma Yasuda, and Chihaya Adachi,
"Highly Efficient Thermally Activated Delayed Fluorescence Emitters Based on Benzonitrile Derivatives and Their Application in OLEDs",
16th International Symposium on Novel Aromatic Compounds (ISNA16), Madrid, Spain (July 5–10, 2015), Poster presentation.

[4] In Seob Park, Sae Youn Lee, Takuma Yasuda, and Chihaya Adachi,
"Design of Thermally Activated Delayed Fluorescence Materials Based on Phthalonitrile Derivatives and Their Application in OLEDs",
6th Asian Conference on Organics Electronics (A-COE), Tainan, Taiwan (November 12–14, 2014), Poster presentation.

[5] In Seob Park, Sae Youn Lee, Takuma Yasuda, and Chihaya Adachi,
"Design of Thermally Activated Delayed Fluorescence Materials Based on Phthalonitrile Derivatives and Their Application in OLEDs",
International Conference on White LEDs and Solid state Lighting, Jeju, Korea (June 1–5, 2014), Poster presentation.

Acknowledgments

First of all, the author would like to dedicate his gratitude to Professor Chihaya Adachi and Professor Takuma Yasuda at Kyushu University for helpful advices to progress advanced research and a lot of opportunity to have invaluable experience during the doctoral course.

The author is grateful to thank members of Yasuda laboratory, Keiko Urakawa, Assistant Professor Hideaki Komiyama, Assistant Professor Naoya Aizawa, Dr. Kyohei Matsuo, Jiyoung Lee, Seiichi Furukawa, Ryuhei Furue, Tatsuya Ohyama, Hiroki Tachibana, Takahiro To, Kohei Isayama, Tatsuya Mori, Satoshi Uwagawa, and So Shikita, and also would like to thank to members of Adachi laboratory, Associate Professor Hajime Nakanotani, Assistant Professor Kenichi Goushi, Associate Professor Jean-Charles Ribierre, Associate Professor Toshinori Masushima, Assistant Professor Ryota Kabe, Dea Hyeon Kim, Sun Bin Hwang, Zhao Li, Hiroyuki Mieno, Hiroki Noda, Taro Furukawa, Hao Ye, and Jong Uk Kim, as well as alumni and past members of Yasuda laboratory and Adachi laboratory, Dr. Yu Seok Yang, Dr. Woong Shin, Dr. Sae Youn Lee, Assistant Professor Ju-Hyung Kim, Masaki Numata, Associate Professor Qisheng Zhang, Assistant Professor Katsuyuki Shizu, Dr. Jie Li, Dr. Bo Li, Dr. Gábor Méhes, Assistant Professor Takeshi Komino, Ryosuke Kondo, Issei Ohtani, Takuro Nishimto, Keisuke Asahi, Yuta Fukutomi, Yu Hidaka, Myung Eun Jang, and Chao-Jen Tsou, who have been very helpful, collaborative, and friendly inside and outside the laboratory during the doctoral course.

The author would like to appreciate Dr. Sae Youn Lee for helping with experiements and valuable discussion.

The author is deeply indebted to Professor Se Mo Son at Pukyong National University for invaluable advice and the great opportunity to study in Kyushu University, Japan, and also would like to thank to Professor Yeon-Tae Jeong at Pukyong National University who gave him the interest about organic chemistry and organic photochemistry through his wonderful lectures and advice.

This work was supported in part by the JST ACCEL project, and Grants-in-Aid for Scientific Research on Innovative Areas “3D Active-Site Science” (No. 15H01049), Young Scientists (A) (No.25708032), Challenging Exploratory Research (No. 26620168) from JSPS, the Cooperative Research Program of “Network Joint Research Center for Materials and Devices”, the Casio Science Promotion Foundation, the Ogasawara Foundation for the

Promotion of Science and Engineering, and the Kurata Memorial Hitachi Science and Technology Foundation.

Finally, the author would like to his deepest appreciation to his family members: parents, brother, and cousinry. Their emotional support, love, and encouragement have inspired him to complete his doctoral course.

January, 2017

In Seob Park